The Pennsylvania State University

The Graduate School

College of Engineering

ULTRASONIC GUIDED WAVE PROPAGATION IN PIPES WITH ELBOWS

A Dissertation in

Engineering Science and Mechanics

by

Luke J. Breon

Submitted in Partial Fulfillment

of the Requirements
for the Degree of

Doctor of Philosophy

May 2016

The dissertation of Luke J. Breon was reviewed and approved* by the following:

Judith A. Todd
Professor of Engineering Science and Mechanics
P.B. Breneman Department Head Chair
Head of the Department of Engineering Science and Mechanics
Dissertation Advisor
Chair of Committee

Bernhard R. Tittmann
Schell Professor of Engineering Science and Mechanics

Joseph Cusumano
Professor of Engineering Science and Mechanics

Kyusun Choi
Associate Professor of Computer Science and Engineering

Richard Tutwiler
Professor of Acoustics

*Signatures are on file in the Graduate School

ABSTRACT

Guided wave inspection of pipelines is an important and growing area of Non-Destructive Evaluation (NDE). This technique can be used for remote inspection or monitoring of buried pipelines, or pipelines with insulation. Guided waves are sensitive to flaws such as corrosion pits and cracks. They can be used to locate flaws existing on either the outer or the inner surface of a pipe. Guided wave energy focusing can be performed to concentrate guided wave energy at particular combinations of circumferential and axial locations in straight pipes. When it can be used, this practice enhances the circumferential resolution of defects.

Elbows in a piping system are sufficiently disruptive to guided wave energy that the focusing methods used in practical inspections of straight pipe have not been extended to the region beyond an elbow. Counter-intuitively, elbows with a 45 degree bend are more harmful to guided waves than those with a 90 degree bend. A simple and elegant explanation for this phenomenon is provided in this dissertation.

Theoretical advancements to guided wave physics propagating around an elbow have tended to be few and slow. This is at least partly due to the complexity of the mathematics involved in the conventional description of guided wave mechanics. Parametric focusing for pipes with bends has not been previously possible as it is for straight sections of pipes. While some techniques such as time-reversal mirrors and blind finite-element-method modeling have existed for focusing beyond elbows, these techniques have been limited and largely of academic value. Also, the understanding of wave behavior in a pipe elbow has in the past been generally unclear. Consequently, signal interpretation has also been very limited for guided waves initiating in, or returning from, the far side of an elbow.

A new approach to understanding guided wave propagation is developed in this work. This understanding consists of the idea that the pathway a guided wave will take across a waveguide can be predicted from the geometric features of the waveguide and a set of initial conditions pertaining to the wave. One such feature is the geometric cross-section in which the wave is propagating. This cross-section refers to a plane that contains both the propagation direction of the wave and the coinciding surface normal of one of the boundaries guiding the wave.

Thinking of guided waves from this perspective enables a clear answer to some important questions about wave propagation beyond an elbow that have not been effectively answered before. For example, before this work, it was not understood if and when full guided wave

coverage exists in a pipe beyond an elbow. This new thinking also enables the calculation of the elbow transfer function--the mapping of guided wave energy impinging on an elbow to the configuration it will have on the other side of the elbow. Each of these examples separately represents significant practical advancements in the guided wave community.

The new approach also introduces a forward focusing model for controlling and focusing guided wave energy in pipe sections in and beyond an elbow. It is believed that this is the first such forward-oriented apparatus for controlling guided wave energy beyond an elbow. It is expected that this will be of great practical consequence. In addition to these specific benefits, it is anticipated that this dissertation will serve as a foundation for a good deal of future work and contributions to guided wave understanding and non-destructive testing equipment.

Table of Contents

List of Figures

List of Tables

Acknowledgements

I would like to thank the Electric Power Research Institute (EPRI) for their funding of this work and for allowing me to pursue this work using their Charlotte facilities. I have greatly enjoyed the stimulating technical discussions and supportive interaction with staff at EPRI and with my friends and colleagues at Penn State. In particular, I wish to thank Dr. Padmakumar Puthillath and Dr. Ehsan Khajeh for the inspiration they have been to me by their technical brilliance packed into outstanding personalities. The privilege of my interaction with these individuals has added much to my life during the short time I spent with them while pursuing this and other work at Penn State.

Thanks to Dr. Eric Hauck and the others who provided lab support with computer equipment and other logistics that kept the work at Penn State running smoothly. Special thanks to Steve Swilley and Steve Kenefick, who supported and facilitated this work at EPRI. Thanks also to Greg Selby for the insightful comments and suggestions shared regarding this work.

Very special thanks to Dr. Michael Quarry at EPRI as well, whose guided wave leadership in the power generation industry has facilitated a substantial and positive impact on the responsible practical use of guided wave. His efforts played a significant role in the initiation and support of this work. Additionally Dr. Quarry's technical genius has been an inspiration to me and I greatly appreciate his insights, knowledge of guided wave, and practical wisdom.

I also wish to thank Dr. Joseph Rose for his initial involvement with logistical management. Beyond this contribution, Dr. Rose has shown me many valuable lessons about life in general and about the academic and professional world. Many thanks also to Dr. Judith Todd, for chairing this dissertation. Without her, the effort would surely have been in vain. Thanks also to the other members of my committee, for their support and careful review of this dissertation. Their questions and comments have helped to shape this dissertation and to bring out the value of the work described herein.

Most of all, I want to thank Christ my Savior for giving me meaning and purpose in life, and my family and friends for their unconditional love and support for me in this work. Without these, I would not have found it possible to complete this dissertation. Many thanks especially to Hannah, my beautiful and loving wife, for her support, understanding, and encouragement in this endeavor. She has brought a new joy to my life that has overflowed into every area, and has helped to renew my enthusiasm for this work.

Chapter 1 Dissertation Overview, Motivation, and Surrounding Literature

This dissertation describes a novel method for understanding key aspects of ultrasonic guided wave propagation in piping structures with elbows. There are two main aspects of this new approach. The first main element is the idea that a propagating guided wave mode will take some particular pathway across a waveguide. The second main element is the idea that this pathway can be predicted in a theoretical, or parametric, fashion. Together, these ideas constitute a new method, or technique, for approaching guided wave propagation that enables us to consider geometrically complex waveguides. This new method will be frequently referred to in this dissertation as *mode following* or *mode tracing*. The underlying ideas are first presented in Chapter 2 as hypothetical constructs. The ideas are then fleshed out, starting with intuitive considerations of how a propagating wave will behave in a waveguide. This is followed by linking the intuitive considerations with well established theories taken from differential geometry and particle mechanics. It is shown that the intuitive description converges with ideas from these established theories.

Further theoretical considerations are presented in Chapter 3. These considerations are accompanied by Finite Element Method (FEM) modeling. The modeling is used as an independent demonstration of how guided wave energy behaves in a bent pipe and other relevant geometries. Chapter 3 also discusses some limitations of the new technique. The technique is then applied in Chapters 4 and 5 to four major topics pertaining to guided wave propagation in pipes with elbows. These topics are summarized in the following bulleted list:

- the pipe elbow as a guided wave transfer function;
- the empirical observation that a 45-degree elbow is more disruptive to guided wave propagation than a 90-degree elbow;
- the possibility of deterministically predicting wave energy coverage in a pipe beyond an elbow; and
- forward techniques for focusing guided wave energy in and beyond an elbow in a pipe system. This topic includes a consideration of natural focusing in and beyond an elbow.

Numerical FEM experimentation is again used for each of these topics to demonstrate independent wave propagation methodology that test the scenarios discussed in these applications. Comparison between each excursion with the new method and the paralleling FEM exercises shows remarkable concurrence. The theoretical backing given in Chapter 2, combined with the further theoretical testing of mode tracing ideas in Chapter 3 and the investigations into practical topics given in Chapters 4 and 5, bring about a convincing validation of the new method introduced in this dissertation.

The exploration of each of these four topics with the new method yields information that has not been heretofore understood. Chapter 4 describes, for what is thought to be the first time, how to calculate the transfer function of an elbow. Also shown in Chapter 4 is how mode following demonstrates a clear and elegant answer as to why 45-degree elbows are more disruptive to guided wave propagation than 90-degree elbows. Previously, this question has lacked a satisfactory answer. The chapter then shows that the technique allows deterministic addressing of the wave coverage in regions in and beyond an elbow.

Finally, Chapter 5 discusses guided wave focusing in and beyond an elbow. This constitutes a very important practical advancement in guided wave inspection capability. This chapter demonstrates how the mode tracing can be used to focus energy in and beyond an elbow in what is also thought to be the first forward-focusing model for pipes with elbows.

Each of these four items represents a valuable contribution of this dissertation, but the most important contribution is the new understanding of wave propagation itself, the idea of mode following. This understanding can no doubt be applied to many more aspects of guided wave propagation in pipes with elbows and other complex geometries than there is room to present in this work. It is expected that this work will provide a foundation for future Masters theses and Ph.D. dissertations, advancements in guided wave signal processing and practical inspection apparatus, and more.

Before discussing and developing these items further, we will discuss the practical motivation for this work and why the contributions in the dissertation matter. Throughout the discussion, we will also take a look at surrounding literature and how other ideas relate to this one. All references to guided waves used in this dissertation will be understood to refer to ultrasonic guided waves unless otherwise stated. The first part of the discussion is an introduction to the use of guided waves in industry.

There is a host of literature regarding the use of guided waves for examining practical waveguides [1-40], some of which will be discussed later in this section. Much attention has been placed on the development of Lamb and Rayleigh waves [41-54], and guided methods for plates, laminar media, and composites [55-64]. Focus on structural health monitoring for various structures using guided waves can be found in references [65-68]. Much literature also focuses on studying the mechanics of guided waves in these and other types of waveguides, signal processing, and general wave behavior [69-84]. Practical attention is given to the use of multiple sources, or source arrays, working together to bring about a desired guided wave effect [85-87]. Such arrays, often called phased arrays, are used in this dissertation to discuss focusing of guided wave energy.

One of the important application types for guided wave inspections are pipes, or piping systems [88-107]. Literature related to guided waves traveling in pipeline elbows is provided in references [88 and 109-118]. Such work will be reviewed in later chapters. Lowe and Cawley [119] authored a snapshot state-of-the-art for industrial use of guided waves for pipe inspections in 2005.

In related studies to this dissertation, Lawrenson et al. [120] discussed sound propagation in a hollow toroidal structure, and Liu and Wang [121] discussed wave front design is discussed for bulk waves. However, their findings are tangential to this work, because our interest lies in examining wave behavior in the walls of a toroidal shape, and the wave fronts of guided waves rather than bulk waves.

As mentioned, pipelines are a very important subset of waveguides for inspections. An extensive network of pipes has been created throughout the world to service such industries as petroleum transit and distribution, water transport, and heat exchanging for power plants. Often, the pipes are buried. However, the importance of their function and the severe consequences of failures make it imperative that steps are taken to assess and protect the structural integrity of these pipes.

Many methods are currently used for non-destructive testing of pipelines. A few examples magnetic flux leakage, eddy currents, radiography, ultrasonic bulk waves, ultrasonic guided waves, and electric conductivity evaluation. References 122 to 135 provide examples of these techniques and their applications, the most relevant of which are [130-135]. A majority of these methods require that a structure is accessible to inspection tools from at least one surface.

Large transit pipelines with relatively straight configurations accommodate pigging devices that operate on the inside of the pipeline. This type of apparatus currently affords a versatile platform to facilitate evaluation of the pipe wall using such methods as magnetic flux leakage, eddy current, and ultrasonic bulk wave testing techniques. Short range guided wave tools are also now being tested for use with such devices. Bar-Cohen [136] provides an interesting overview of some nondestructive technologies.

There is, however, growing interest in the development of better capabilities for inspecting shorter runs of pipes and those that contain many features such as bends, flanges, welded supports, and branches, or otherwise prohibit the use of pigging devices. So far, ultrasonic guided waves provide one of the best-posed solutions for this kind of application, especially for the inspection of buried piping at power plants and other facilities. Guided waves propagate for very significant distances in a pipeline under some unburied conditions, but the effective distance of a guided wave inspection range can decrease significantly if the pipe is coated or is placed underground.

Currently, ultrasonic guided waves are used mostly as a screening tool to quickly locate regions of pipe that need to be examined more closely. This is because guided wave analyses can often locate damage but do not typically give highly accurate quantitative information about the damage size. While the development of guided waves for screening purposes is still ongoing, there is an increasing pull from industry to refine the use of guided waves into a tool that can more precisely quantify damage, and to provide complete and independent inspections of underground piping. It is anticipated that the ideas presented here can be used to produce better signal processing tools that will help close this practical gap in the technology.

Elbows, however, disrupt guided wave modes and present challenges to signal interpretation for waves that travel past the elbow. Moreover, energy focusing becomes difficult with the introduction of an elbow, and the conventional techniques used to focus energy in straight pipes cannot be used beyond the elbow. Since elbows are frequently found in real piping systems, they represent a significant issue for practical inspections. The ultimate motivation of the work represented by this dissertation is to improve our understanding of wave propagation past an elbow.

Any such improvements will provide highly meaningful and added value for the guided wave community, with the development of a forward apparatus for focusing guided wave energy in and

beyond an elbow having tremendous practical and academic implications. While the conventional procedures used in the guided wave community have so far failed to produce such a forward apparatus, the mode tracing approach developed here has provided the breakthrough needed for exactly that endeavor. Chapters 4 and 5 discuss the details of this novel approach.

In thinking of the elbow problem, an obvious first question to consider is how the elbow affects a guided wave. As an approach to this question, we will think of the elbow as a geometric feature that operates on a wave mode. The elbow can be thought of as taking energy that impinges on it from one side and maps it to another configuration on the other side of the elbow as the energy traverses it. So, another way of thinking of the elbow, is that it is constitutes a geometric transfer function for guided waves. Discovering this transfer function is significant. Since guided wave mechanics for straight pipes are well understood [88, 96, 102, 104], tools already exist for characterizing guided wave propagation in straight pipes. This means that if the energy configuration of the wave as it exits an elbow into such a straight section can be obtained, existing tools can potentially be employed to characterize wave propagation in a straight pipe *beyond* an elbow.

The elbow, then, represents a link between straight pipe sections adjacent to it. This link has not been understood, and, while several attempts have been made to explore it [88, 109, 112-114], the characterization of the elbow has remained elusive [109] until this work. The notion of mode following as introduced here has led to a patent application [116], and since the publication of that document, other researchers have started down the same trail [115]. Characterizing the transfer function of the elbow represents an attractive contribution to both the academic community and the practical world. This characterization is given in Chapter 4.

Another problem caused by the elbow, noted in [109], is that guided wave insonification of particular regions beyond an elbow cannot be deterministically assured. This has important consequences for practical examinations of pipelines beyond an elbow because it means that no guarantee can be made that energy will travel to each region of the pipe beyond an elbow. The implication of this is that there could be unpredictable blind spots beyond an elbow. Since it cannot be foretold with conventional understanding where guided wave energy will and will not go in the region beyond the elbow, it can also not be assured as to what kind of inspection integrity would be achieved with a guided wave inspection of this region.

The use of mode following immediately brings determination of where wave energy is destined to go in a suitable waveguide, including piping elbows and following regions. This is inherent in the very nature of mode following since the technique is based upon being able to predict the pathway a mode will take across a waveguide. Therefore, this work brings an answer to the important question of whether there are any regions that are blind to a practical inspection. This is discussed in more detail in Chapter 4.

The significance of the inability of conventional techniques to focus guided wave energy in and beyond an elbow with practical methods has already been established in this dissertation. Probably the most useful method for focusing beyond an elbow that can be accomplished with surrounding methodologies is the idea of Time Reversal Mirrors (TRM) [137-144]. This method, as applied to focusing guided wave energy in a waveguide, requires access to both the location where focusing is to happen, and to the location where the guided wave source actuators are to be placed.

Alternatively, a guided wave reflector in the test sample could be substituted for the sensor that would otherwise need to be placed at the location where the focusing is to take place. Such a reflector would need to be large enough to reflect sufficient energy as to be used for the determination of the inputs needed for the actual focusing experiment, as described in the next paragraph. However, one of the practical drivers for focusing guided wave energy in a pipe is to detect reflectors that are smaller than can be reliably detected with non-focusing techniques. This means that the reflectors of interest are not likely to be detected unless focusing techniques are not needed anyway.

To make use of time reversal techniques in guided wave testing, an experiment is first done that involves placing a guided wave source at the location where the *focusing* is to eventually occur. The experimental energy travels from the guided wave source at the focus area to a receiver placed at the location where the guided wave *source* will be placed in the second phase, after the first experiment. The information collected by the receiver in the first experiment will be used to design the actual focusing experiment. The information can be obtained by either a laboratory experiment using physical probes or by a numerical experiment in a software simulation. Neither method for obtaining the information required for the actual focusing test would be suitable for practical inspections.

When conducting a laboratory experiment to obtain the data, access must be available to the location where the focusing is to be performed. If a guided wave operator could have access to such a point, as well as the time needed to perform the experiment, it would be more efficient to use an alternative test rather than to use guided wave technology. An example of such an alternative test is normal-beam ultrasonic measurements. The time to perform a numerical model to obtain appropriate information for focusing is normally prohibitive. Consequently, the use of TRM for focusing guided wave energy beyond an elbow has been largely of academic value, since the technique did not appear to be useful in practical guided wave inspection systems.

The development of a forward-model for focusing guided wave energy beyond an elbow is attractive academically since it represents a more direct, theoretically driven approach. It will also be attractive for practical purposes if it can be done more rapidly than FEM or other numerical solutions. The mode following idea presented here is substantially faster than the FEM solutions used in this work at obtaining focusing parameters for guided waves beyond elbows.

In order for any focusing techniques to be valuable in practical inspections, the speed at which the necessary computations can be performed must be sufficient to make focusing economically or otherwise viable. While it is not clear how fast this must be, it does appear that FEM solutions are too slow. The order of time required to calculate focusing parameters via mode following is on the order of seconds to minutes, while FEM solutions typically require minutes to hours. Improvements in the calculation speeds of both methods will no doubt arise, but mode following is naturally computationally lighter than FEM.

Additionally, this dissertation presents a simple explanation of why 45-degree elbows are generally more disruptive to guided wave propagation than 90-degree elbows. This contribution brings substantial academic contribution in that it answers a counter-intuitive question that has haunted the guided wave community. It would be intuitively expected that, if a wave traversing a 45-degree bend in a pipe experiences disruption and other undesirable effects, that those effects would only increase the further the wave travels around the elbow.

From a practical point of view, it is known that 45-degree elbows disrupt guided waves more than 90-degree elbows, but it has not been understood why and what could be done to compensate for the added severity of the 45-degree over the 90-degree elbow. So, in addition to the academic significance of the explanation offered in this work, the knowledge gained may lead to changes in

guided wave inspection hardware and examination practices to help overcome the effects of the elbow.

With the motivation and main contributions of this dissertation in mind, we will begin comparing the idea of mode following to related literature and other existing approaches to guided waves. As will be shown later in this section, conventional methods for understanding guided wave propagation such as those represented by [88, 92, 96, 104, 109, 114] take the entire waveguide into account when describing wave behavior. One striking difference between this type of approach and the idea of mode following is analogous to the difference between Eulerian descriptions and Lagrangian descriptions for applications such as fluid flow.

Eulerian and Lagrangian descriptions are very widely used in many fields such as fluid dynamics [145]. Since they play only the part of an analogy in this work, no further attention will be given as to their origins or uses. Traditional methods of describing wave propagation would be Eulerian because these methods approach the subject by defining a wave field across the entire waveguide. Mode following, on the other hand, takes on a Lagrangian analogy since it is based on following the propagation of a particular mode across a subset of a waveguide.

Approaches involving wave propagation that reflect a Lagrangian viewpoint are ray tracing methods, which have been widely implemented for studying ultrasonic wave propagation and behavior [146-157]. Such methodologies determine the path an ultrasonic wave will take through a bulk material that contains interfaces such as inhomogeneities, layers, and reflectors. Ray methods have not been widely applied to guided wave propagation.

While Balvantin et al. [147] have used ray methods to look at wave scattering from a reflector for guided waves, the literature on the use of ray methods for guided waves is not extensive. Practical data collection systems for bulk wave ultrasonic testing, on the other hand, often contain processing algorithms for calculating ray paths through a complex bulk material. The corresponding computations can become intensive even for short propagation distances. Beam simulation and inspection parameter calculations, such as focal laws, are popular uses for ray tracing [146, 149, 150].

Ray tracing in its conventional presentation, is different from the focus of this work since it generally pertains to methods for bulk waves. Mode following has a distinctive flavor of ray methodology because it addresses the wave propagation pathway of guided wave modes. However, this method should not be confused with ray tracing for bulk waves even though the

two seem similar at first glance. Mode following is oriented toward studying ultrasonic waves that are guided by waveguide boundaries. An assumption in this work is that the waveguide of interest is homogeneous, and of uniform thickness throughout. The traditional notion of ray tracing uses Snell's law to calculate the change in propagation direction of a wave impinging on a material interface such as a reflector, change in material, or change in material properties. Snell's law is very familiar to those who deal with wave mechanics and is described in [131].

Perhaps the most closely related idea to the work that will be demonstrated in this dissertation comes from the field of guided wave tomography. In tomography, a set of sensors are positioned around or near some region of interest in a waveguide. Guided wave signals are transmitted from one sensor in the set to each of the other sensors, and after the signals are collected, a reconstruction algorithm is used to analyze the region of interest. For some purposes, the pathway taken from one sensor to another need not be fully known to get useful information. For example, Breon [158] examined wave propagation around an elbow, but treated the elbow as if it were a flat geometry for the purposes of reconstruction. However, for more sophisticated reconstruction algorithms, it would be necessary to understand the propagation pathway across the waveguide from one sensor to another.

In the case of flat plates, it is easy to realize that the pathway a wave will take from one sensor in an array to another is simply the straight line that connects the two sensors. The pathway followed in pipes is slightly more complicated, but still intuitive, since the pathways can be conceptualized as straight lines connecting relevant sensor pairs drawn on a flat plate that is then wrapped into the shape of a pipe. In this case, the pathways would be helices, as observed in [159-161].

It is much more difficult when moving from a pipe geometry to an elbow geometry, to intuitively understand the wave pathway between two sensors. It is thought that this has, in fact, not been developed for use in guided wave mechanics prior to this work. However, it is shown in this dissertation that guided waves propagating through a waveguide will take a path that can be calculated based on the geometric curvature of the waveguide. Three variations regarding the relevant pathways are formally introduced in chapter 2, and are summarized here as well. They are *geodesics*, principles of *Newtonian mechanics* used to observe the behavior of a particle, and a discrete approach that employs local geometric properties of the waveguide of interest.

The first two of these methods represent mature fields of understanding. Geodesics [162-168], and Newtonian mechanics [169]. While the methods of geodesics and the methods of Newtonian mechanics relevant to this dissertation are essentially the same, each is mentioned separately as they take on mutually different appearances. The use of geodesic principles provides a natural fit with the idea of tracing a wave pathway. On the other hand, methods of Newtonian mechanics are much more native to the traditional work surrounding guided wave propagation. The discussion on Newtonian mechanics and methods of geodesics facilitates a good bridge between the conventional thought process for understanding guided wave mechanics and the ideas presented in this dissertation.

In addition to all the methods described in this dissertation, FEM simulations or laboratory experiments can also yield the pathway information, although they may be time consuming and are may not be theoretically driven. Mode following offers a more theoretically driven and direct method of observing guided wave propagation. FEM simulations *are* used in this work extensively to validate the new ideas presented in this dissertation.

Previous approaches to understanding guided wave behavior in pipes has often taken the form of addressing the global elastic behavior of a waveguide [88, 92, 93, 95, 96, 98, 100-102, 104, 134, 170]. These have favored a direct solution of Navier's equation, with the work of Gazis [171, 172] providing the basic foundation. His technique involves determining the wave dispersion properties of the waveguide of interest for the entire waveguide. The underlying mechanism for this approach is well connected to mature theories such as elasticity, dynamics, and vibrations [169 and 173-175].

Mode following replaces the consideration of the elastic behavior of the entire waveguide with a consideration of a cross-sectional slice belonging to the waveguide and oriented so as always to include the direction of wave propagation. This slice is chosen carefully, and the choice requires that the slice include the surface normal of the boundary containing the wave as well as the tangent vector of the wave propagation direction.

This idea will be used to think of a specific cross-section of a waveguide as an independent subset of the whole structure. Our consideration of the elastic behavior of the waveguide will be restricted to the elastic behavior of this cross-section. This cross-section will be responsible for providing the transverse resonance a propagating guided wave needs to form modal order through the thickness of the waveguide. The transverse resonance is well understood in preceding guided

wave theory [134], and is used in this work in conjunction with the determination of the pathway a guided wave will take across a waveguide to explore the idea of mode following.

While for the sake of formality, the significance of this transverse resonance will be discussed briefly in Chapter 2, it is sufficiently related to contemporary ideas as to not present conceptual difficulty. The more interesting part of this work is the idea that the pathway a guided wave will take across a waveguide can be predicted based on the geometric features of the waveguide and some initial conditions of the wave. The idea of predicting this pathway and using it to understand wave propagation in a geometrically complex waveguide, such as a pipe elbow, is thought to be new in this work and introduced to the guided wave community here for the first time.

The theoretical scope of this work will be more or less restricted to waveguides that can be approximated as shells, although experimental numerical work is provided to demonstrate that the methods herein can be applied to real engineering structures with finite thicknesses, such as pipes and toroidal waveguides. It is noted again here, that the waveguides are assumed to be of constant thickness—that is, the surfaces of the waveguide bounding the thickness have a mutual center of curvature at each point.

We will now introduce some conventions to be used in this dissertation before moving to the next chapter, where we will look at the development of the mode following technique. Figure 1.1 of the following sketches shows a section of a straight pipeline and is labeled with the inner and outer radii and the cylindrical coordinates. The ϕ-direction will be used interchangeably with the term “circumferential direction,” and the θ-direction, or z-direction, will be considered interchangeable with the term "axial direction." Figure 1.2 illustrates a pipe with an elbow. A transducer array, while not shown on the figure, is indicated on one of the sections of straight pipe connected to the elbow. The straight pipe connected to the other side of the elbow (the side that does not contain the transducer array) will be referred to as the region beyond the elbow.

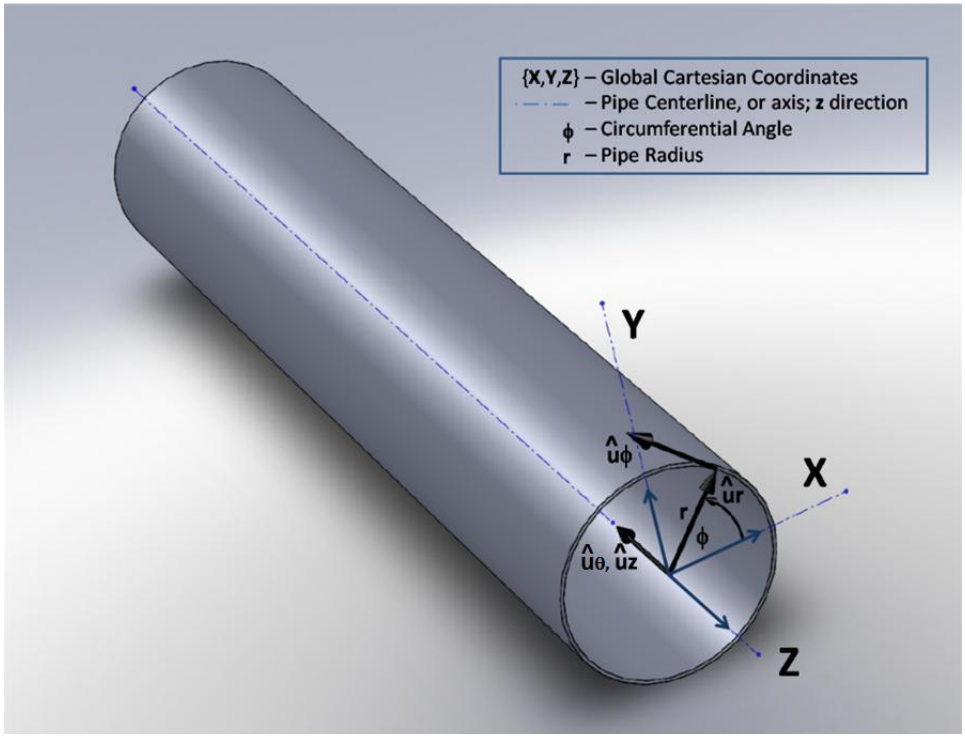

Figure 1.1
Sketch of straight pipe section. The inner radius is a, the outer radius is b. The radial direction is denoted as r and the circumferential direction is ϕ. The longitudinal direction is the -z direction.

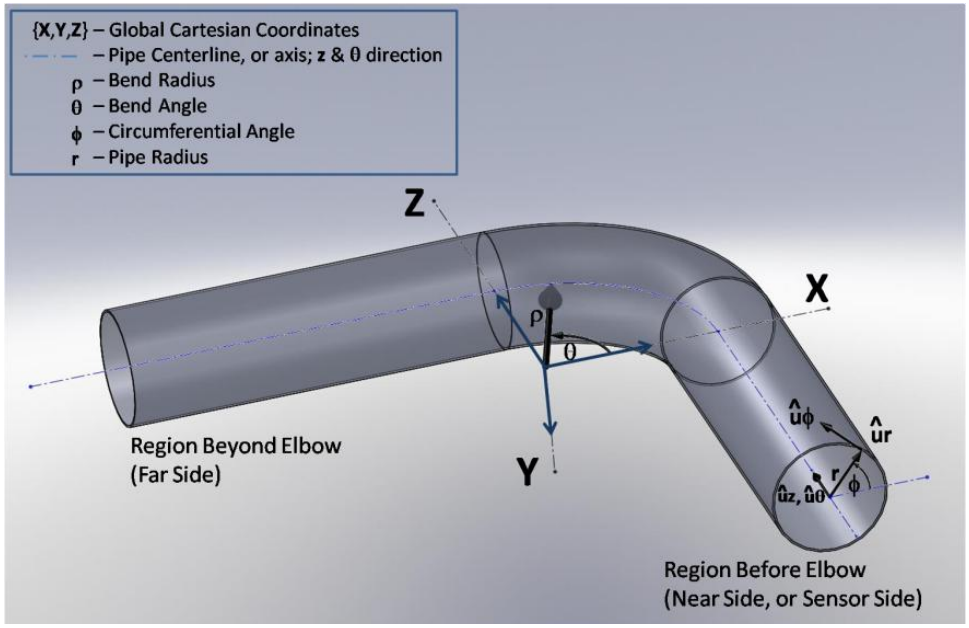

Figure 1.2
A bent pipe featuring a transducer array and a welded elbow. The straight section of pipe not containing a transmitter is considered to be "beyond the elbow."

The intrados and extrados of a generic pipe elbow are demonstrated in Figure 1.3. This figure also shows the pipe radius, r, the bend radius of the elbow, ρ, and the bend angle, θ. Generally, θ will be used to specify a position along the pipe axis. In straight runs of pipe, θ will coincide with the z-direction and will be measured in units of distance. In pipe bend regions, θ will be used to specify the bend angle, and will be assigned units of radians. Also, α will be used periodically to denote the angle going from the θ-direction to the ϕ-direction as shown in Figure 1.4. Figure 1.5 represents an array of transducers that has been placed around the circumference of a pipe. This figure also demonstrates the naming orientation of a transducer array that will be referred to in this work.

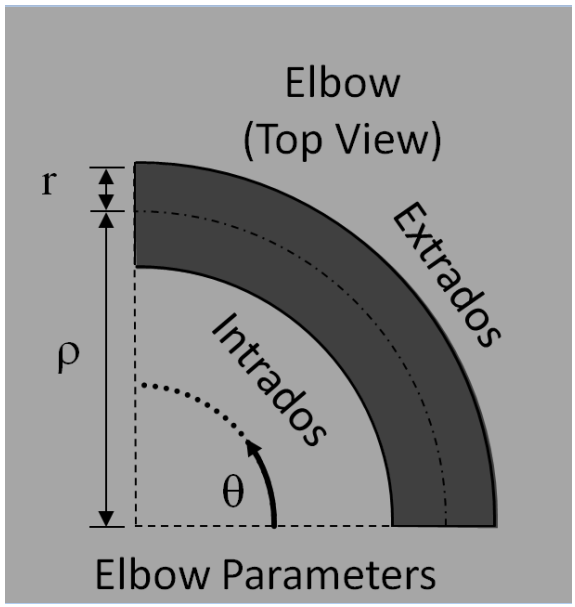

Figure 1.3
Top view of an elbow showing Intrados, Extrados, ρ, θ, and r.

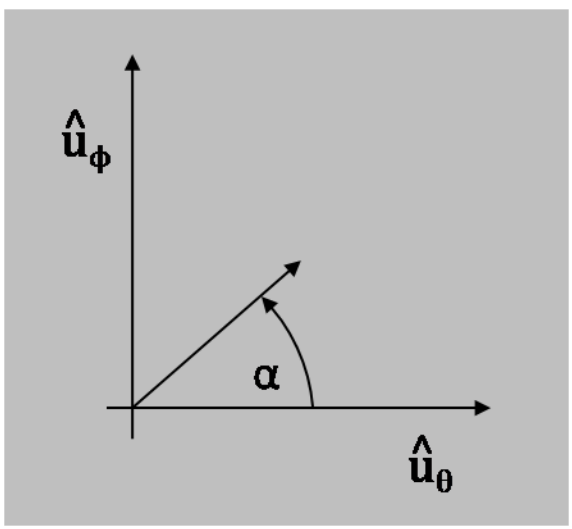

Figure 1.4
Definition of α as the angle between the θ-direction and the ϕ-direction.

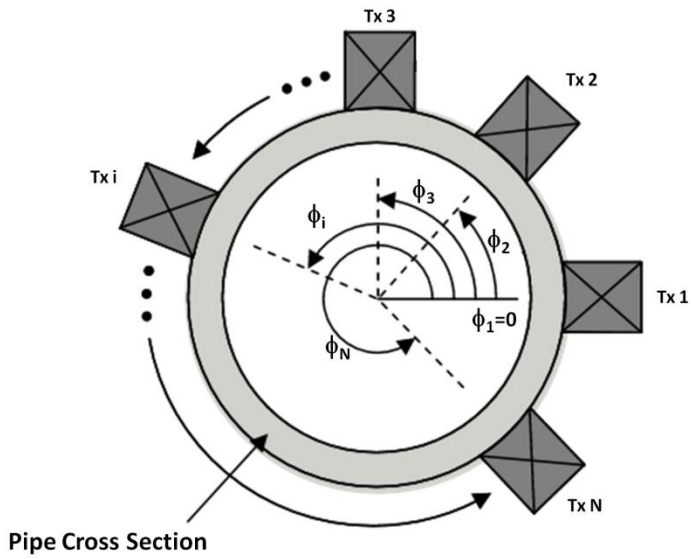

Figure 1.5
Cross-section of a pipe illustrating a set of N transducers placed around the circumference of the pipe. The transducers are designated Tx 1through Tx N, and are located at circumferential angles ϕ_1 through ϕ_N

Chapter 2 Development of a Novel Approach to Ultrasonic Guided Wave Mechanics

This chapter discusses the theoretical construction of the new approach to understanding guided wave propagation. The chapter begins with a consideration of the conventional approach and points out some important limitations of that methodology, then introduces the innovative premise of this dissertation. The development of the new methodology begins with an intuitive exercise in considering how a guided wave should behave, then fleshes out the idea by a mathematical description. Following that, the idea is further substantiated by looking at classical theory in Newtonian mechanics and linking that theory to the developing methodology of this chapter. Finally, the link between this work and the well understood field of geodesics is established and some comments are offered regarding the use of geodesic methods for guided wave propagation mechanics.

The developments of this chapter are explored in Chapters 4 and 5 by applying the ideas of mode following presented in this chapter to the four applications discussed in Chapter 1. Numerical demonstrations of the convergence of the theories in this chapter will be offered in Chapter 3, as well as some further theoretical explorations of the ideas in this chapter. Finite Element Method analyses are employed along with the theoretical discussions in Chapter 3, and the application of mode tracing in Chapters 4 and 5 demonstrate that the constructions of this chapter do indeed accurately predict guided wave propagation in practical structures such as pipe systems.

Before discussing the development of the new approach to understanding guided wave energy propagation, a review of traditional methods for describing guided waves is warranted. However, in order to focus this chapter on the contributions of this dissertation rather than on the existing theory, the bulk of the theoretical development of the conventional methods will be presented in Appendix A. The methods described in Appendix A can be found in [88, 102, 104, 134, 171].

The traditional method for approaching guided wave propagation problems is to begin with elasticity and vibrational principles to describe the collection of vibration modes on a waveguide, then build on this information to generate other constructs, such as dispersion curves. Modal expansion can then be used to examine wave behavior as a superposition of individual wave modes. As shown in Appendix A, these methods can be used to calculate mode excitation

functions and to superimpose derived mode energy profiles at desired spatial locations and time intervals.

In 1959, Gazis [171] solved Navier's equation for straight sections of pipe and provided the mathematical solutions necessary for determining the three-dimensional elastic wave behavior for domains of hollow cylinders. Importantly, Gazis [171] used the Helmholtz decomposition to accomplish his derivations. This work has underpinned much of the subsequent work in guided wave development for piping applications, as summarized in Appendix A. Conventional methods work elegantly for focusing guided wave energy in straight sections of pipe. The basic principles and theory discussed in Appendix A have been expanded over past decades for other purposes such as enhancing focusing techniques in multi-layered pipes. For example, when using guided waves in buried pipes and pipes with coatings [96].

However, the same approach has not been successfully paralleled for pipe elbow domains, possibly in part because of the complexity of the mathematics. For example, the Helmholtz decomposition of the wave equation by Gazis for pipe cannot be applied to the geometry of a pipe elbow, which is a subset of a torus, because the wave equation is not separable in toroidal coordinates [176]. This has ultimately meant that theoretically mature conventional understanding of guided wave propagation in piping systems has been limited to regions that do not involve elbows. In 2005, Rose et al. concluded that guided wave operations beyond an elbow were still not fully understood [109]. This dissertation will periodically refer to the state-of-the-art of guided wave as discussed in their paper.

Despite the lack of applicability of the conventional methods to pipe elbows, it is well known that guided wave energy is certainly able to traverse an elbow [109-114]. However, solid theoretical understanding of guided wave behavior in a pipe elbow has remained limited [109], with much of what is known about the elbow stemming from experimental observation, rather than from theory.

This dissertation offers a novel approach to understanding guided wave propagation. Instead of solving the analytical equations of elasticity on the pipe elbow geometry and determining dispersion curves and normal modes for the structure, it is assumed that there is some wave mode that will propagate across the structure, and the behavior of such a wave mode is examined. In the sense of an allegory, the conventional methodology can be thought of as being Eulerian in nature while the novel approach is more Lagrangian. The conventional methodology considers

the behavior of Navier's equation across a domain window, but the ideas presented here consider a particular wave mode as it travels across a domain.

As noted in the introduction, this idea is similar to the notion of *ray tracing*, a common technique employed in bulk wave propagation problems and beam scattering. [147, 148, 150-155, 157]. However, ray tracing is not thought to have been applied to guided wave mechanics before for determining the trajectory of a propagating wave mode as a whole.

Transverse Resonance and Transverse Resonance Pathway

To begin thinking in this new manner, two primary tools are highlighted. The first of the two tools is the fact that most guided waves require a transverse resonance [134]. Some guided waves such as Rayleigh-Lamb waves are a hybrid between bulk waves and guided waves. While such waves can behave as bulk waves, in that they can propagate in a half-space, they are also guided by the profile of the waveguide surface. Even though the idea of the transverse resonance is not new, it will be used in an innovative way for this development.

The other tool we use for this development is thought to be even more original in considering guided wave propagation. This tool is the idea that a propagating wave mode will not change direction without some type of constraining geometry, material in-homogeneity, or other feature of the waveguide to dictate that change in direction. This idea is presented first as an intuitive observation that will be fleshed out and validated throughout the development in this dissertation. We will begin with a discussion of the transverse resonance.

For sustained propagation, guided waves generally require that at least one of three dimensions of a waveguide is restricted so that the wave propagation is bounded by at least one set of two parallel surfaces. An example of a geometry with one set of parallel bounding surfaces is a thin plate. A square rod is a waveguide that has two sets of parallel bounding surfaces. A circular rod geometry can be thought of as having an infinite number of parallel bounding surfaces. In each of these cases, wave resonances can be established between each set of two parallel bounding surfaces.

This analysis can be extended to pipe geometries, which can be imagined as a plate geometry with one set of two parallel bounding surfaces. In this case, the lateral edges of the plate will not be present, as they will have been aligned with each other so as to present a continuous geometry

in the circumferential direction of the pipe. Also for the pipe case, the two parallel boundaries have a curvature differing from one another despite the fact that each will have a shared surface normal at any given axial and circumferential coordinate. This shared surface normal means that the two surfaces are parallel to one another.

If a pipe were sectioned by a plane containing its axial direction, the resulting cross-section of each intersection of the pipe with the cutting plane would look like the cross-section of a plate. The outer and inner radii of the pipe, then, would each trace straight and parallel lines across the cut separated by the thickness of the pipe wall. Dispersion curves are readily calculated for this type of geometry using the methods described by Rose [134].

If instead, the pipe were sectioned by a plane normal to the pipe axis, the resulting cross-section would result in an annulus. The outer and inner circles traced on the cutting plane by the respective outer and inner radii of the pipe would be parallel to one another, but would have mutually different curvatures. The dispersion curves for this type of cross-section have been developed in Appendix A.

More generic sectioning strategies, such as sectioning the pipe with a helix revolving about the axial direction, can also be considered. Any cut such that the surface normals of the inner and outer surface at each axial and circumferential location along the cut are collinear would again result in two parallel lines traced by the inner and outer radii that are separated by the thickness of the pipe. In such general sections, the resulting cross-section would be a planar section that is curved, or bent. Applying the same notion to another geometry such as a pipe elbow will result in a similar cross-section that could include twisting as well as bending. It is this generic, plane-like, cross-section that will provide the transverse resonance for the purposes of this dissertation.

Since ultrasonic guided waves are stress waves, they will exhibit beam spreading, and not all of the energy of a wave mode will exist in a single cross-section of transverse resonance such as was introduced in the previous paragraph. Some thoughts on how to handle this beam spreading are given later in this chapter, but as we will see in subsequent chapters, valuable conclusions can still be drawn without accounting for beam spreading. Expansion of the ideas introduced here will be left as a module for further development of this work. In this dissertation, we will, in most cases, consider the transverse resonance pathway that contains the highest amplitude of energy of a traveling wave packet. When another transverse resonance path is discussed, such as

the transverse resonance pathway of an energy null, or in the case where all transverse resonance pathways represent an identical amplitude of energy, it will be clear from the context.

Selecting the appropriate cross-section to use for considering the transverse resonance of a propagating wave mode is the purpose of the second major tool driving this work. This is the idea that a propagating wave mode will not change its direction of propagation without a mechanism in the waveguide that facilitates the change in direction. The two tools go hand-in-hand, since a propagating wave mode will need a transverse resonance, and the transverse resonance of interest will be the cross-section that always contains some feature of interest of the propagating wave mode, such as the part of the mode with the greatest amplitude. This dissertation will refer to the entire cross-section of the waveguide that always contains such a feature of interest as the *transverse resonance pathway*, or more simply, the *resonance pathway*. The determination of the particular transverse resonance pathway of arbitrary interest is one of the key developments of this work. These ideas are illustrated in Figure 2.1 for a simple plate geometry.

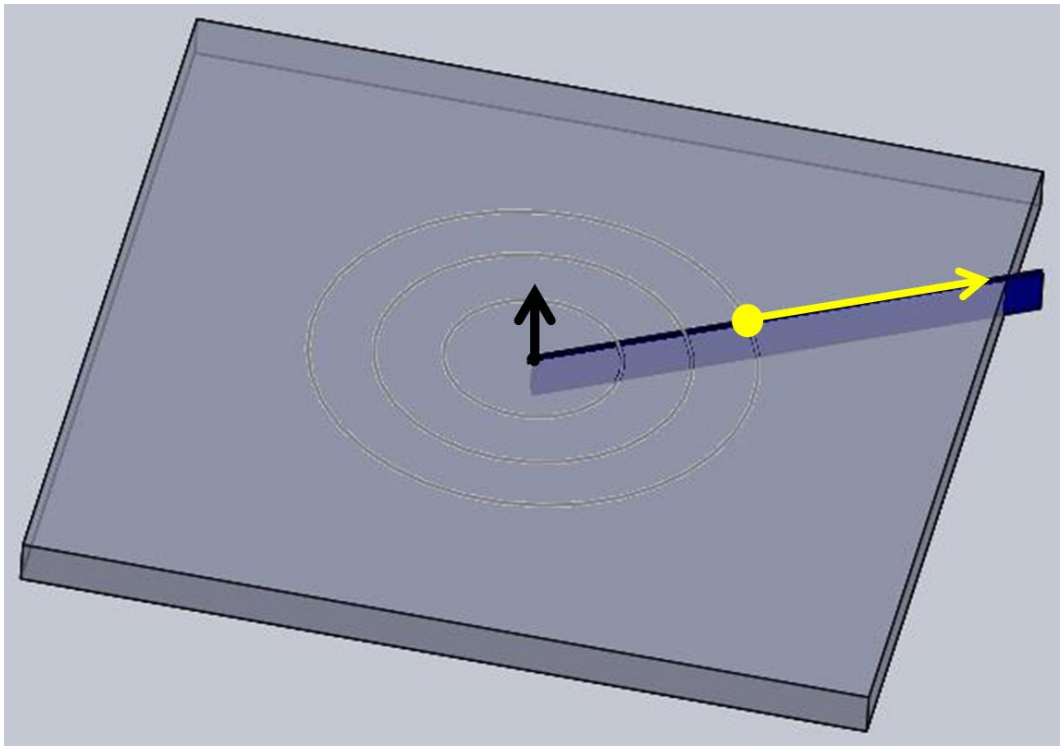

Figure 2.1
Illustration of the transverse resonance pathway used by a subset of a propagating guided wave mode on a plate. The source is a radially symmetric source at the location of the black arrow. The yellow dot represents a point on the leading edge of the wavefront moving in the direction of the yellow arrow, and the blue plane represents the transverse resonance pathway.

In Figure 2.1, a radially symmetric point wave source is depicted by a black arrow in the center of the top surface of a flat translucent plate. Light gray circles surrounding the wave source denote the zero-crossings of the wave amplitude for one wavelength of the wave. We now pick an arbitrary point on the leading edge of the wave front, and conceptually place a yellow dot at this location. We will allow this dot to move with the leading edge of the portion of the wave that coincided with the dot when we first conceptually placed it on the plate.

It is easy to visualize that the dot will simply move in a straight line across the plate away from the location of the source. Points on the surface of the plate will also theoretically move transversly to the direction of movement of the yellow dot as the non-zero and non-π phases of the wave traverse those points on the plate, but since the dot remains on the leading edge, or zero phase, of the wave, the dot itself does not oscillate as it moves. Furthermore, the conceptual construction of this exercise is meant to be independent of wave frequency, wave speed, and

wave amplitude, so we need not consider the elastic behavior of the plate in order to evaluate the trajectory of the yellow dot. We do assume, though, that the plate is homogeneous and isotropic.

The movement of the yellow dot is depicted in the figure by the yellow arrow, and the corresponding transverse resonance pathway is shown in the figure by a blue plane. We can apply the same thought experiment to a pipe geometry as well. While slightly more effort is required to state intuitively the resulting pathway of the leading edge of a portion of the wave front, it is still relatively straightforward to understand that the new pathway will trace a generic helix across the pipe surface. A pipe geometry can be thought of as a plate that has been wrapped into a cylinder, so a straight line drawn across a plate before such a wrapping takes place will map into a helix. This helical transverse resonance pathway is shown in Figure 2.2. In this figure, the source, yellow dot, direction arrow, and circular wave front are not rendered.

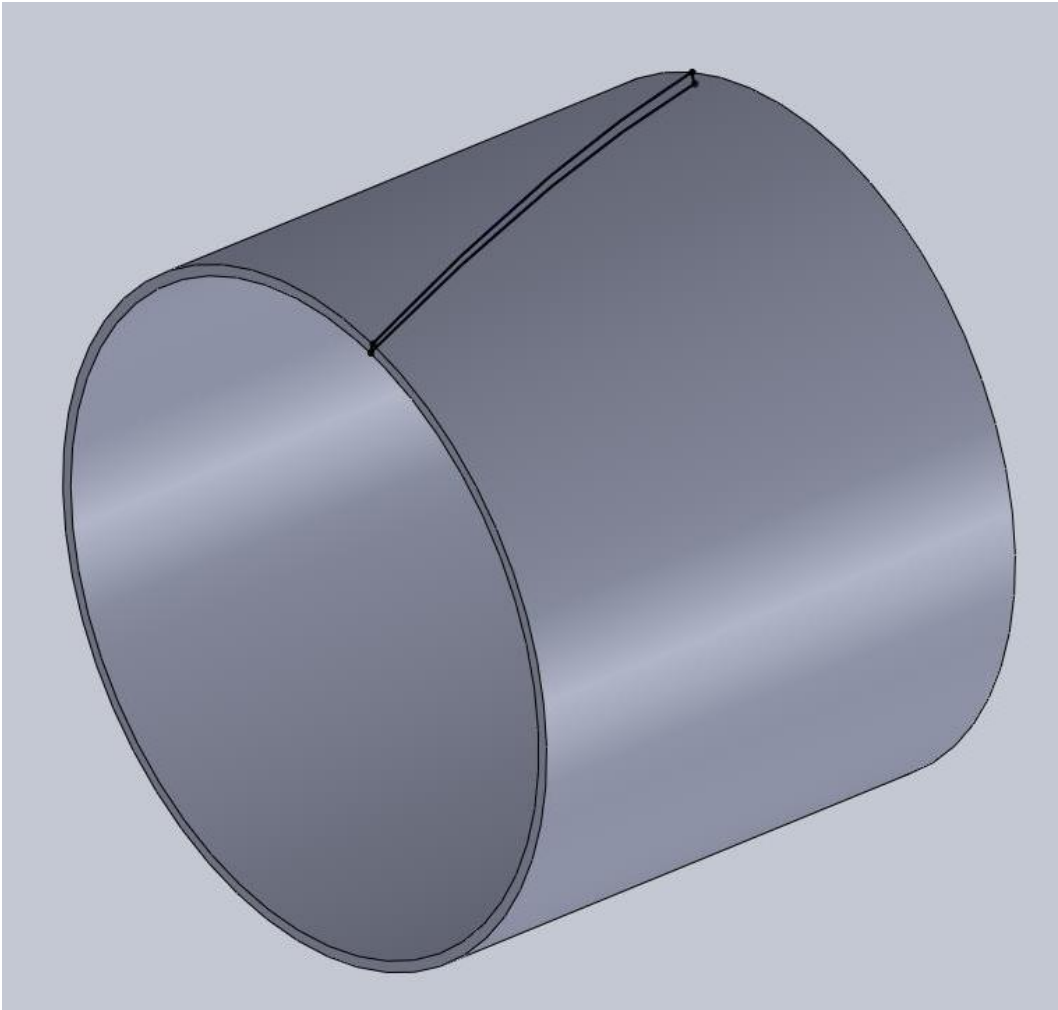

Figure 2.2
Illustration of a transverse resonance pathway across a pipe geometry.

The ideas introduced in this chapter may appear simple when first encountered, but predicting the exact pathway a guided wave will take across a geometrically complex waveguide such as an elbow is not intuitive and does not appear to have been explored in the literature before the work described in this dissertation. Given the requirement of a transverse resonance, we can intuitively observe that if the surface normals bounding a guided wave change orientation, the transverse resonance pathway and the wave mode dependent on this resonance pathway must also change orientation. If the surface normals change orientation by rotating slightly and smoothly about the tangent direction of the wave propagation, the transverse resonance and dependent wave mode must also follow suit.

On the other hand, it is also possible for the surface normals bounding a guided wave to change orientation but remain in the plane defined by the wave propagation direction and the original orientation of the surface normals. It is very straightforward to realize that, in such a case, the transverse resonance will merely bend about the center of curvature of the bounding surfaces at the point the surface normals change orientation.

Determining the Transverse Resonance Pathway for a Wave Mode

In conceptualizing the transverse resonance pathway on a complex waveguide, we might consider the trajectory of an ant intending to walk in a straight line across the surface of the waveguide. It is then possible to consider how the surface normal vectors change as the ant moves along the surface, and to study how changes in the curvature of the surface can ultimately cause the ant to walk a trajectory that is non-planar.

We can then hypothesize that the trajectory followed by the ant coincides with one bounding edge of the transverse resonance pathway taken by a mode propagating through the same waveguide, provided both the ant and the wave mode have the same starting location and initial direction. This edge is denoted in Figure 2.1 as a black line on the top edge of the blue plane representing the transverse resonance pathway. We note that since the transverse resonance is formed by the surface of the waveguide, the bounding edge of the transverse resonance pathway must always be tangential to the waveguide surface. The trajectory of the ant will, of course, also remain tangent to the surface of the waveguide. We also note that the surface normal vector is tangent to the transverse resonance plane at each point along the intersection of the resonance pathway and the waveguide surface. The surface normal vector and resonance pathway direction vector at a point, **P**, are illustrated in Figure 2.3 as **N** and **D** respectively. Also shown in the figure is a vector, **T**, that is orthogonal to the transverse resonance pathway at point **P**.

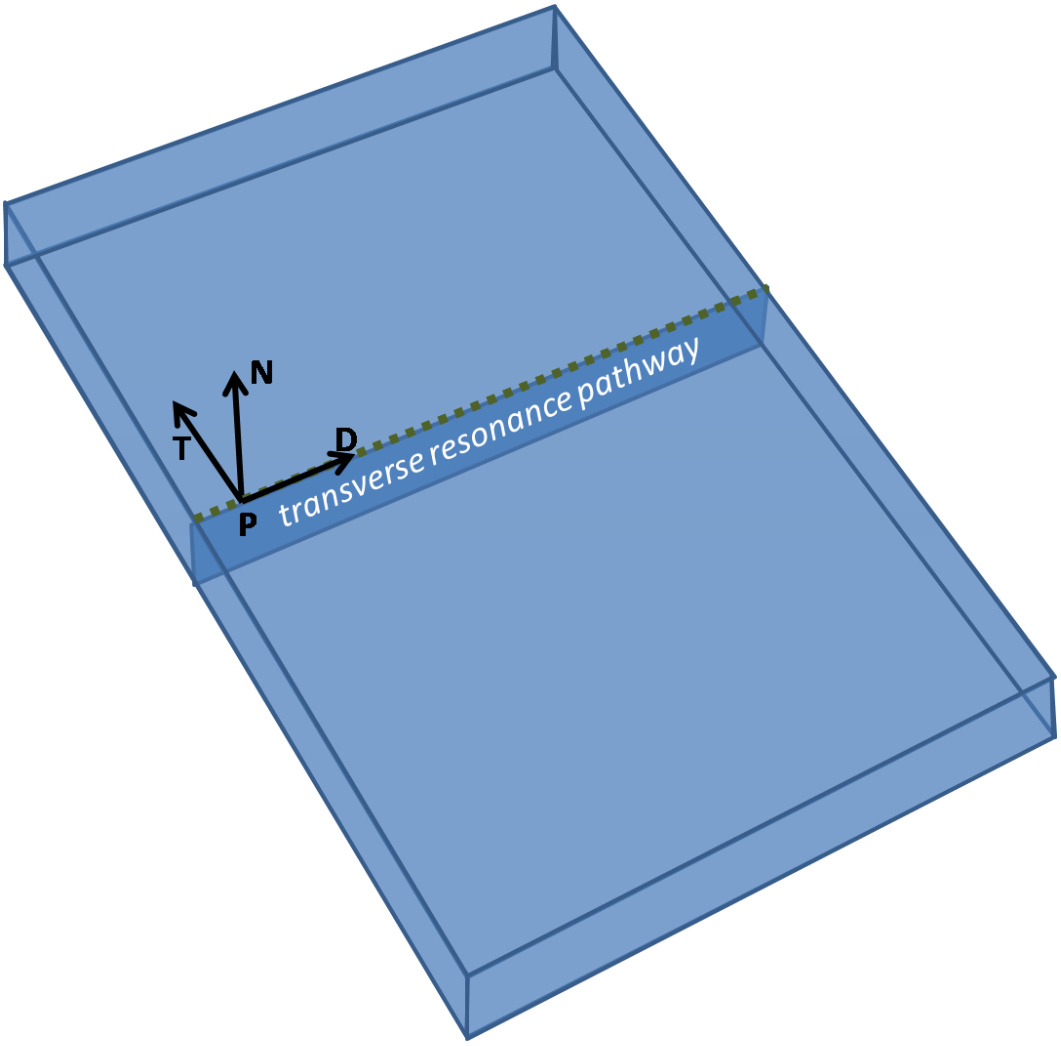

Figure 2.3
Schematic of transverse resonance pathway depicting an example surface normal vector, direction vector, and an orthogonal vector that can be obtained by crossing the normal vector with the direction vector.

To examine such a trajectory, a starting location, $\mathbf{P}_1$, is first chosen on the surface and an initial direction of motion, $\mathbf{D}_1$, is chosen. The choice of starting location can be arbitrary, but the choice of initial direction must be tangent to the surface of the waveguide at the starting location. Then an end location, $\mathbf{P}_2$, is calculated by moving a small distance, ds, from the starting point in the direction initially chosen. The transverse resonance pathway is then constrained to pass through both the starting location and the end location. Also, the transverse resonance pathway is oriented so that the surface normal is tangent to the pathway plane for each point considered. This construction will result in an iterative approach to determining the transverse resonance

pathway by replacing $\mathbf{P}_1$ with $\mathbf{P}_2$ and restarting the calculation. However, for all iterations other than the first one, the direction vector is no longer arbitrary.

Because of the constraint that both the surface normal **N** and the instantaneous direction vector **D** must be included in the plane of the transverse resonance pathway at each point, it is possible to calculate a unit vector, **T**, that is orthogonal to the transverse resonance pathway at each point. This can be done by crossing the normal vector with a vector aligned with the instantaneous propagation direction at each point and normalizing. Then when considering a point that is not the starting point, we can use this **T** vector to determine a new instantaneous direction vector for the transverse resonance pathway, by crossing the **T** vector with the new surface normal vector at the point $\mathbf{P}_2$. This construction provides a solution for the orientation of the transverse resonance pathway that meets all the constraints imposed. The process can be repeated as desired using the solutions obtained for the end point $\mathbf{P}_2$ as the starting location and initial direction for another step ds across the surface.

Since the step size ds used to move across the surface is arbitrary and could change with each iteration or be kept constant, it is convenient to normalize the direction vectors **D**, and apply a fixed ds for each iteration. This algorithm can be written simply in iterative form as Equation 2.1 and Equation 2.2.

$$\boldsymbol{P}_i = \boldsymbol{P}_{\boldsymbol{i-1}} + \boldsymbol{D}_{i-1} ds$$

Equation 2.1

$$\boldsymbol{D}_i = -\boldsymbol{N}_i \times (\boldsymbol{N}_i \times \boldsymbol{D}_{i-1})$$

Equation 2.2

In Equation 2.1, $\mathbf{P}_i$ is the new end position for the iteration, $\mathbf{P}_{i-1}$ is the starting position of the iteration, $\mathbf{D}_{i-1}$ is the initial direction vector for the iteration, and ds is the arbitrary step distance to move the solver for the iteration. The terms in Equation 2.2 are defined similarly, with $\mathbf{D}_i$ representing the final direction vector for the iteration, $\mathbf{N}_i$ being the surface normal at position $\mathbf{P}_i$, and $\mathbf{D}_{i-1}$ defined as in Equation 2.1. The vector **T** that is orthogonal to the transverse resonance pathway at the point of interest is represented in the equation as ($\mathbf{N}_i \times \mathbf{D}_{i-1}$). The negative in Equation 2.2 stems from switching the order of the second cross product from $\mathbf{T} \times \mathbf{N}$ as described earlier to $\mathbf{N} \times \mathbf{T}$. This technique will be referred to in subsequent discussion as the *digital method of surface normals*, or simply the *vector method*.

This construction is, so far, an intuitive attempt to determine the trajectory of the transverse resonance pathway. It stems from an analogy between an ant walking in what feels to be a straight line across a waveguide, and a guided wave mode behaving in an analogous fashion. The algorithm introduced here is inspired by considering how the curvature of the waveguide could bring about the effect of changing the direction of a propagating wave mode or a particle such as an ant while that moving entity would otherwise simply move straight ahead. However, at this point, the construction is still a hypothesis.

To bring life to this analogy, we will replace the ant walking on the waveguide surface by a particle traveling between two parallel, rigid, surfaces, or constraint surfaces, that take the shape of the waveguide in a zero-potential field. We then look at Newtonian principles in a discrete fashion to examine how the constraint surfaces cause the particle to change direction. The following discussion uses concepts described in textbooks on dynamics in engineering mechanics, such as Hibbler [177]. As for the pathway of the ant, we define a starting position and initial velocity direction for the particle. We will allow no forces other than the constraint forces to act on the particle.

The particle will only accelerate in directions normal to the surface. Thus the constraint force, **CF,** at any point is given by Equation 2.3, where **V** is the velocity vector, **N** is the surface normal vector, m is the mass of the particle, and ρ is the radius of curvature at the point of interest. Replacing acceleration with the time derivative of velocity results in Equation 2.4.

$$\boldsymbol{CF} = m\boldsymbol{a} = m\frac{\boldsymbol{V}\cdot\boldsymbol{V}}{\rho}\boldsymbol{N}$$

Equation 2.3

$$d\boldsymbol{V} = \frac{\boldsymbol{V}\cdot\boldsymbol{V}}{\rho}\boldsymbol{N}dt$$

Equation 2.4

To discretize the method for finite iteration sizes, the $d\boldsymbol{V}$ is replaced with $\Delta\boldsymbol{V}$, which can be written as $\Delta\boldsymbol{V} = \boldsymbol{V}_i - \boldsymbol{V}_{i-1}$, where $\boldsymbol{V}_{i-1}$ and $\boldsymbol{V}_i$ are the velocity vectors at the first and second points of the discretized interval respectively. Using this substitution and replacing ρ with ρ_i, dt with Δt_i, and **N** with $\mathbf{N}_i$ allows Equation 2.4 to be discretized as Equation 2.5.

$$\boldsymbol{V}_i = \boldsymbol{V}_{i-1} + \frac{\boldsymbol{V}_{i-1} \cdot \boldsymbol{V}_{i-1}}{\rho_i} \boldsymbol{N}_i \Delta t_i$$

Equation 2.5

Applying the constraint that the particle can have no velocity in the direction of the constraint normal yields Equation 2.6, which can be rewritten as Equation 2.7. This in turn allows Equation 2.5 to be written as Equation 2.8, then massaged into Equation 2.9 by multiplying the single $\mathbf{V}_{i-1}$ term by $\mathbf{N}_i$ dotted with $\mathbf{N}_i$, or unity, and factoring out a minus sign. Finally, by the vector triple product, $\boldsymbol{V}_i$ can be written as Equation 2.10.

$$\boldsymbol{V}_i \cdot \boldsymbol{N}_i = 0 = \boldsymbol{V}_{i-1} \cdot \boldsymbol{N}_i + \frac{\boldsymbol{V}_{i-1} \cdot \boldsymbol{V}_{i-1}}{\rho_i} \boldsymbol{N}_i \cdot \boldsymbol{N}_i \Delta t_i$$

Equation 2.6

$$\frac{\boldsymbol{V}_{i-1} \cdot \boldsymbol{V}_{i-1}}{\rho_i} \Delta t_i = -\boldsymbol{V}_1 \cdot \boldsymbol{N}_i$$

Equation 2.7

$$\boldsymbol{V}_i = \boldsymbol{V}_{i-1} - (\boldsymbol{V}_{i-1} \cdot \boldsymbol{N}_i)\boldsymbol{N}_i$$

Equation 2.8

$$\boldsymbol{V}_i = -[(\boldsymbol{V}_{i-1} \cdot \boldsymbol{N}_i)\boldsymbol{N}_i - (\boldsymbol{N}_i \cdot \boldsymbol{N}_i)\boldsymbol{V}_{i-1}]$$

Equation 2.9

$$\boldsymbol{V}_i = -\boldsymbol{N}_i \times (\boldsymbol{N}_i \times \boldsymbol{V}_{i-1})$$

Equation 2.10

Comparing this approach to the exercise of looking at surface curvature to bring about a change in direction of an ant moving across a surface, it can be recognized that the normal vector $\boldsymbol{N}_i$ in Equation 2.10 is the familiar normal vector $\boldsymbol{N}_i$ from Equation 2.2. Since only constraint forces act on the particle, the magnitude of the velocity vector does not change as it moves if the Δt becomes infinitesimally small. Because of the discretization used in this development, however,

the magnitude of the velocity could change with each iteration. If we confine the velocity magnitude to remain fixed by normalizing $\mathbf{V}_i$ at the end of each iteration, it would be analogous to normalizing the $\mathbf{D}_i$ vector from Equation 2.2. Also, each velocity term in equations Equation 2.5 through Equation 2.10 could have been replaced with the corresponding direction vector **D** multiplied by an additional Δt_i term. Doing so would have resulted in Equation 2.10 being the same as Equation 2.2.

This exercise shows that the construction of the transverse resonance pathway based on the intuitive requirements of that pathway does indeed converge to the pathway of a particle such as an ant moving along the same surface and having no motivation to change direction other than that caused by purely geometric properties. This brings credibility to the hypothesis that the transverse resonance pathway can be calculated via the intuitive means given in Equation 2.1 and Equation 2.2. Furthermore, this construction represents a straightforward algorithm for processing the transverse resonance pathway for digitally-defined geometries, so long as the surface normals can be found for any arbitrary point. The methods for calculating the transverse resonance pathway we will discuss next require smooth and parametric geometric definitions.

The discussion of discretized methods of Newtonian particle mechanics for investigating the transverse resonance pathway leads one to immediately think about more generalized approaches to the problem. For this, we will once again consider a particle constrained to move along a constraint surface W in a zero-potential field. The development will take a traditional approach to this class of problems and make use of well known theorems. In particular, this consideration will follow the style of Meirovitch [173].

The trajectory of the particle can be obtained given an initial position **P** and velocity vector **V**. Because this system has no potential energy, the Lagrangian $\boldsymbol{\mathcal{L}}$ will contain only kinetic energy. The Lagrangian with respect to global Cartesian coordinates {x,y,z} can be written as Equation 2.11. The Lagrangian can then be operated on by Equation 2.12, where q_i form a set of generalized coordinates and $\dot{q}_i$ indicates $\partial q_i/\partial t$.

$$\boldsymbol{\mathcal{L}} = T = \frac{1}{2}m\boldsymbol{V}\cdot\boldsymbol{V} = \frac{1}{2}m\left(\left(\frac{dx}{dt}\right)^2 + \left(\frac{dy}{dt}\right)^2 + \left(\frac{dz}{dt}\right)^2\right) = \frac{1}{2}m(\dot{x}^2 + \dot{y}^2 + \dot{z}^2)$$

Equation 2.11

$$\frac{\partial}{\partial t}\left(\frac{\partial \boldsymbol{\mathcal{L}}}{\partial \dot{q}_i}\right) - \frac{\partial \boldsymbol{\mathcal{L}}}{\partial q_i} = 0$$

Equation 2.12

Solving these equations for a cylindrical constraint surface of radius r, angular coordinate ϕ, and axial coordinate z such as defined by Equation 2.13 would produce a pair of ordinary differential equations representing the trajectory of a particle on W given an initial position and velocity.

$$x = r\cos\phi$$
$$y = r\sin\phi$$
$$z = z$$

Equation 2.13

In particular, fixing r to be constant, substituting Equation 2.13 into Equation 2.11, then solving Equation 2.12 for generalized coordinates ϕ and z results in trivial solutions for the second temporal derivatives for both z and ϕ. The coordinate r is held constant because the particle is constrained to lie on the surface of W. Therefore, the radial velocity and acceleration of the particle are automatically zero. The velocity of the particle in both the z and ϕ directions is constant because their accelerations are zero. These velocities are therefore equal to the respective components of the initial velocity **V** in the z and ϕ directions. The solutions for z and ϕ as functions of time can be written as Equation 2.14, where $\dot{z}$ and $\dot{\phi}$ are the time derivatives of z and ϕ respectively.

$$z(t) = z_0 + \dot{z}t; \;\; \phi(t) = \phi_o + \dot{\phi}t$$

Equation 2.14

Providing any initial position vector $\{\phi_o, z_0\}$ and initial velocity vector $\{\dot{\phi}, \dot{z}\}$ will result in the particle tracing a helix over the constraint surface W. Thus, the only motion the particle can have in W is that of a helix, with degenerate cases being a straight line along the axial direction when $\dot{\phi} = 0$, and circular motion about an axial location when $\dot{z} = 0$. This concurs with the intuitive observation that the transverse resonance pathway on a hollow cylinder will take the form of a helix. Similarly, while not shown here because of the extreme ease of proving it, if we apply this method to the geometry of a flat plate, we will find that a particle will move in a straight line across the plate. This also concurs with the intuitive observation made earlier.

While the solution of particle motion on a cylindrical or flat constraint surface are easy to solve analytically and not particularly interesting, the solutions obtained for a toroidal geometry such as found in a pipe elbow are much more intriguing. For the following consideration of particle motion on a torus, the intrados and extrados will be placed in the x-z plane of the global {x,y,z} Cartesian coordinates. The generalized coordinates θ and ϕ will be used to denote the angle lying in the x-z plane and the angle moving between the extrados and intrados respectively. Also, ρ will be used to denote the bend radius of the torus and r will denote the distance between the axis of revolution of the torus and the constraint surface. The surface of the torus will again be named W.

The generalized coordinates {r,θ,ϕ} can be mapped to the global coordinates {x,y,z} by Equation 2.15. As before, there will be no potential field for the particle, and the r coordinate is a constant, so its derivatives are automatically zero. This coordinate will consequently be excluded from the discussion in this derivation from here on.

$$x = (\rho + r\cos\phi)\cos\theta$$
$$y = r\sin\phi$$
$$z = (\rho + r\cos\phi)\sin\theta$$

Equation 2.15

The time derivatives of x, y, and z are given as Equation 2.16.

$$\dot{x} = -r\sin\phi\cos\theta\dot{\phi} - (\rho + r\cos\phi)\sin\theta\,\dot{\theta}$$
$$\dot{y} = r\cos\phi\,\dot{\phi}$$
$$\dot{z} = -r\sin\theta\sin\phi\dot{\phi} + (\rho + r\cos\theta)\cos\phi\,\dot{\theta}$$

Equation 2.16

The Lagrangian $\boldsymbol{\mathcal{L}}$ again consists only of kinetic energy and is defined as before. Substituting the values of $\{\dot{x}, \dot{y}, \dot{z}\}$ in Equation 2.16 into Equation 2.11 yields the Lagrangian given in Equation 2.17. Applying this equation to Equation 2.12 results in the two coupled ordinary differential equations shown in Equation 2.18 and Equation 2.19.

$$\boldsymbol{\mathcal{L}} = \frac{1}{2}m(\dot{r}^2 + (\rho + r\cos\phi)^2\dot{\theta}^2 + r^2\dot{\phi}^2)$$

Equation 2.17

$$\frac{d^2\phi}{dt^2} + \frac{(\rho + r\cos\phi)\sin\phi}{r}\left(\frac{\mathrm{d}\theta}{\mathrm{dt}}\right)^2 = 0$$

Equation 2.18

$$\frac{d^2\theta}{dt^2} - \frac{2r\sin\phi}{(\rho + r\cos\phi)}\frac{d\theta}{dt}\frac{d\phi}{dt} = 0$$

Equation 2.19

These two equations do not have known analytic solutions. The terms involving θ in Equation 2.18 can be separated from those involving ϕ and substituted into Equation 2.19 to obtain an equation for the acceleration of θ in terms of quantities of ϕ. Such an equation, however, also has no analytic solution. Furthermore, presenting θ motion in terms of ϕ does not appear interesting enough to discuss further in this dissertation.

As for the case of the cylindrical boundary surface, the solutions to the equations governing the particle motion require a vector of initial position and a vector of initial velocity. As will be shown in Chapters 3 and 4, numerical solutions to Equation 2.18 and Equation 2.19 demonstrate that a particle will travel along paths with substantially different trajectories for relatively small permutations of initial conditions.

Methods of Geodesics

Finally, we take the calculation of the transverse resonance pathway one more step by now discussing methods of *geodesics*. Geodesics are native to the field of differential geometry and are often used for handling exactly the type of problem discussed in this chapter; determining optimized pathways across various geometrical shapes. As is the case for Newtonian mechanics, geodesic theory is well understood and well developed [162-168].

Geodesics are included in this work because of the elegance they offer in considering the initial intuitive hypothesis that the transverse resonance pathway can be calculated by examining the surface normals of a waveguide. Methods involving geodesics appear to be rare in traditional guided wave literature. This dissertation will introduce the guided wave community to geodesic

methods as a mature tool for calculating the transverse resonance pathway for a guided wave mode propagating in a waveguide.

While essentially similar to a differential approach to the discrete methods for observing particles with Newtonian mechanics, geodesic methods do look very different. This discussion of geodesics will draw largely from the style of Zwillinger [167]. Since geodesics are well documented and understood, we will not concern ourselves with their introduction in this dissertation, but will move directly into a discussion of their relevance. However, for the sake of completeness, a full mathematical application of geodesics for the pipe elbow is given in Appendix B.

In their conventional form, geodesics are lines on the boundary of a given geometric shape that represent the shortest path between specified sets of endpoints [166]. While a single geodesic represents the shortest path between any two endpoints, we will not use geodesics in that context for this dissertation. Instead, we will replace one of the end point constraints with the constraint of an initial direction. In some cases, we may also consider the shortest path between two points on a waveguide, but often, we will not find this as useful for studying guided wave mechanics as the constraints of a starting location and an initial direction.

While there are many texts dealing with geodesic constructs, the following development will follow the synopsis provided by Zwillinger [167]. A geodesic on a manifold W with connection ∇ is a curve $\gamma(t)$ such that the tangent vector to $\gamma(t)$ is parallel along $\gamma(t)$. This requires that the geodesic equation given in Equation 2.20 be true.

$$\frac{\delta\dot{\gamma}}{\delta t} = 0$$

Equation 2.20

The notation $\dot{\gamma}$ will be used to imply the derivative of γ with respect to time. The covariant derivative of $\dot{\gamma}$ can be obtained by expanding $\dot{\gamma}$ to a continuously differentiable vector field on an open set. Using local coordinates on W, the geodesic equation can be written using the summation convention for surfaces with continuous spatial derivatives as in Equation 2.21.

$$\frac{d^2x_i}{dt^2} + \Gamma^{\mathrm{i}}_{\mathrm{jk}}\frac{dx_j}{dt}\frac{dx_k}{dt} = 0$$

Equation 2.21

In this equation, x_j are the coordinates of the curve γ(t) and Γ^i_{jk} are the Christoffel symbols of the connection ∇. Equation 2.21 will have a unique solution for a given set of initial position and initial velocity. Equation 2.20 means that there is no acceleration of the curve γ. However, the curve γ could still lie on a curved manifold. Such a manifold can be thought of as a constraint surface, and the motion can be determined by the curvature of the surface. The Christoffel symbols are defined in Equation 2.22, where the g_{ij} tensor is the metric, or covariant tensor, of the surface, and is constructed as shown in Equation 2.23. The g^{ij} tensor is the contravariant tensor, and produces the Kronecker delta tensor when multiplied with the covariant metric tensor.

$$\Gamma^i_{jk} = \frac{1}{2} g^{im} (g_{mj,k} + g_{mk,j} - g_{jk,m})$$

Equation 2.22

$$ds^2 = g_{ij} dx_i dx_j$$

Equation 2.23

For orthogonal coordinate systems, only the diagonal metric coefficients g_{11}, g_{22}, and g_{33} are non-zero, and they can be found by Equation 2.24.

$$g_{ii} = \left(\frac{dx_1}{du_i}\right)^2 + \left(\frac{dx_2}{du_i}\right)^2 + \left(\frac{dx_3}{du_i}\right)^2$$

Equation 2.24

Referring to Equation 2.15 and noting that the generalized coordinates for the torus constraint surface we chose before are {r,θ,ϕ}, the metric coefficients can be found. The variable r is a constant on the surface of a torus, and therefore has trivial derivatives only. However, r will be allowed to vary for the construction of the covariant tensor. Because toroidal coordinates are orthogonal [176], either Equation 2.23 or Equation 2.24 can be used to determine the metric tensor for a torus, which has the following values for g_{ii}.

$$g_{11} = 1; \;\; g_{22} = (\rho + r\cos\phi)^2; \;\; g_{33} = r^2$$

Equation 2.25

The contravariant tensor is effectively the inverse of the covariant tensor, and the covariant tensor found here is diagonal, so the coefficients of the contravariant tensor are:

$$g^{11} = 1; \;\; g^{22} = \frac{1}{(\rho + r\cos\phi)^2}; \;\; g^{33} = \frac{1}{r^2}$$

Equation 2.26

Because of the orthogonality of toroidal coordinates, all the off-diagonal entries in the g_{ij} and g^{ij} tensors are zero, and all the terms in Equation 2.22 with $i \neq m$ will be zero. Also, because r does not vary, each term involving a 1 in either the k or l term in Equation 2.22 will also be zero. Of course, since r is held constant, $\ddot{r}$ is automatically zero, and the case of i=1 need not be computed for Equation 2.21. Stepping through the remaining terms in Equation 2.21 and Equation 2.22 results in the following two equations, which are the same as obtained by Newtonian methods earlier. The intermediate mathematics involved in finding the Christoffel symbols are lengthy and are shown in Appendix B.

$$\frac{d^2}{dt^2} = \frac{(\rho + r\cos\phi)\sin\phi}{r}\left(\frac{d\theta}{dt}\right)^2$$

Equation 2.27

$$\frac{d^2\theta}{dt^2} - \frac{2r\sin\phi}{(\rho + r\cos\phi)}\frac{d\theta}{dt}\frac{d\phi}{dt} = 0$$

Equation 2.28

Since the development of methods using Newtonian Principles and Equation 2.12 result in identical solutions to those in the development of geodesics, this dissertation will not compare or differentiate between them in subsequent sections. Instead, the rest of this document will refer to both techniques as *parametric techniques*, or simply *geodesic methods*, since the field of geodesics is the more natural fit of the two to this work. Solutions to Equation 2.27 and Equation 2.28 will be sometimes referred to as *mode traces*.

This chapter has introduced the theoretical construction of the new approach to guided wave understanding. The development began with the observation that a propagating guided wave mode will not change direction as it moves unless there is a physical reason to do so. The goal of this chapter is to understand how the geometry of a particular waveguide can be the physical driver that makes a propagating wave mode change direction. To do this, we noted that a propagating wave mode takes *some* path across a waveguide and we developed a method for calculating this pathway. The developments of this chapter form the construction of the

methodologies for calculating this pathway, and we hypothesize that these algorithms are indeed methods of finding the pathway of interest.

This chapter has provided the reasoning behind the thought that the mathematics and systems discussed here actually can predict the trajectory of a propagating guided wave mode. However, the next chapters explore these methods and will show that numerical analyses done by FEM simulations indicate that this hypothesis is correct. As the chapters progress, we will apply the new approach to some important questions and problems surrounding guided wave propagation in pipes with elbows. As we do so, we will follow the new theory with FEM analysis to verify that the conclusions drawn by the new method are supported by independent numerical tests.

Chapter 3 Numerical Exploration and Practical Implementation of Mode Tracing

In this chapter, we explore some theoretical implications of the methods introduced in Chapter 2. These explorations are accompanied by FEM simulations that show modeling predictions for each of the scenarios explored by mode tracing. This chapter will lend further credibility to the aim given in Chapter 2. In the following two chapters, we will examine some guided wave propagation characteristics for the four important practical applications described in the introduction. The first three of these will be looked at in Chapter 4, and the last one will be kept for Chapter 5. For each of the four applications, FEM simulations will be done to parallel the scenarios of the mode tracing algorithms of Chapter 2. The FEM models will be constructed as described in Appendix C. The four applications are:

- the elbow as a guided wave transfer function;
- exploration of why a 45-degree elbow is more disruptive to guided wave than a 90-degree elbow;
- determinism for guided wave coverage of regions beyond an elbow; and
- forward focusing of guided waves beyond an elbow and natural focusing in bent pipes.

The results of the FEM validations used in this work are considered authoritative for two major reasons. The first reason is that the simulations use methods of continuum mechanics and are completely independent of the premise and methods of Chapter 2. The FEM solver is not programmed to take advantage of wave theory to make shortcuts in wave propagation analyses for guided wave. Instead, the solver blindly solves equations of continuum mechanics and produces time varying stress and displacement fields, etc. for each model. The second reason the FEM results are considered authoritative is that the same engine (ABAQUS) has been used extensively in the guided wave community for modeling guided waves and has been shown to match very well with laboratory experiments and guided wave theory, as shown in [8, 32, 88, 96].

Before investigating the four applications, the theoretical developments of Chapter 2 are extended. This starts with comparisons between the different sets of mathematics used in Chapter 2, and then discusses the notion of geodesic circles, or contours of constant distance from a point on a waveguide. This serves as a logical check on the validity of the mode tracing algorithm and the use of geodesic methods for studying guided wave propagation. Also, some practical

observations about the limitations of the new methodology and relevant discussions are offered. To compare the methods of Chapter 2, we will look at convergence between the two vector method and the parametric methods.

One easy test to apply the mode tracing algorithm to is geometries with known guided wave behavior. The simplest of these is a homogeneous, isotropic, flat plate with a circularly symmetric source. Because of symmetry, the wave will spread uniformly in all directions away from the source. The resulting relevant transverse resonance pathway will be a straight line, as discussed in Chapter 2. Even without computation, it can be realized that the digital method of surface normals will produce a straight line on a flat plate because the initial direction is orthogonal to the surface normal at that point, and the surface normals at each point are always mutually parallel. Therefore, there is no mathematical structure in Equation 2.2 to bend the pathway of the transverse resonance. Rather, crossing the direction vector with an orthogonal normal vector then crossing the same normal vector with the resulting vector from the first cross product will result in the final direction vector being exactly parallel with the original direction vector.

So instead of plotting the convergence of the digital method of surface normals for flat plate geometries, we will begin by looking at the convergence of the method for cylindrical geometries instead. Like the flat plate, the analytic solution for the transverse resonance pathway on a cylinder is readily available. This pathway is predicted to be a helix in 3-dimensional Cartesian space, or a straight line in the space of the generalized coordinates ϕ and z as defined and demonstrated in Chapter 2. The pipe used for this study is a schedule 20 pipe of 609.4 mm (24 in) outside diameter.

Figure 3.1 shows the results generated by the vector method on a cylindrical geometry. The selected helix pitch angle used in this computation is 30 degrees. This pitch angle represents the angle between the longitudinal axis of the pipe and the helical trace. The plot shows several results obtained by the vector method with different interval step sizes ds. This figure plots the circular coordinate ϕ multiplied by the pipe radius versus the longitudinal coordinate z.

Also, superimposed over this plot is the exact solution, which is merely a straight line with a slope of 30 degrees. While a pipe of 609.4 mm (24-in) diameter was used in this calculation, the solution is analytically valid for pipes of any diameter, since it is merely a helix with a fixed pitch angle of 30 degrees. Figure 3.2 shows a zoomed version of Figure 3.1. It can be observed that

the vector method is very close to the real solution for a significant distance, then falls away from the analytic solution as the trace distance, or distance of propagation increases. Reducing the step size ds results in the solution following the analytic solution for a greater distance away from the starting point. In practical implementations, though, the vector method would not likely be used for this problem because of the availability of fast, analytical means of determining the solution.

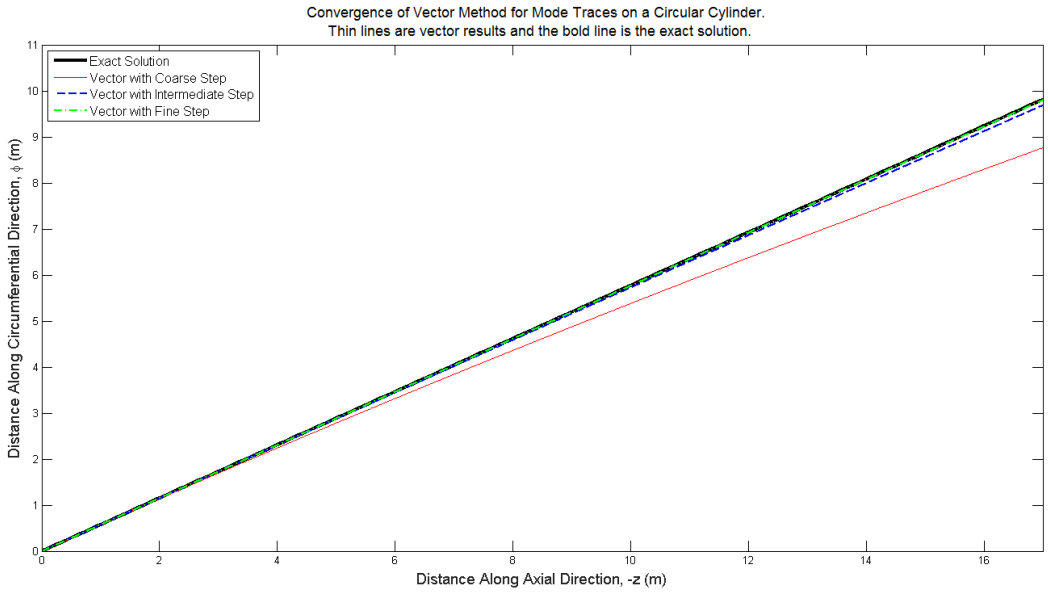

Figure 3.1
Plot showing convergence of the vector method for finding mode traces in a pipe to the exact solution. The launch angle of the solution is 30 degrees. The bold black line is the exact solution, and the red line, the dashed blue line, and the dash-dot green line are the results with a coarse ds, an intermediate ds, and a fine ds respectively. The pipe represented is a 609.4 mm (24 in) diameter schedule 20 pipe.

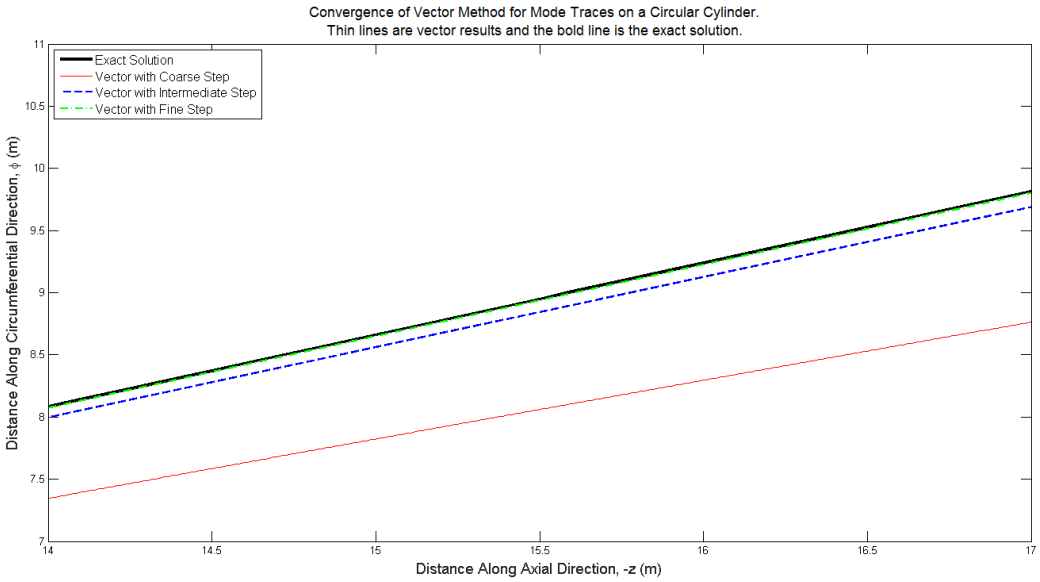

Figure 3.2
Zoomed plot showing convergence of the vector method for finding mode traces in a pipe to the exact solution. The bold black line is the exact solution, and the red line, the dashed blue line, and the dash-dot green line are the results with a coarse ds, an intermediate ds, and a fine ds respectively. The pipe represented is a 609.4 mm (24 in) diameter schedule 20 pipe.

Similarly, Figure 3.3 shows the results obtained on a torus, and Figure 3.4 shows a zoomed version of Figure 3.3. In the case of the torus, the exact solution does not exist analytically, other than as Equation 2.18 and Equation 2.19 themselves. Therefore, the results shown represent only the vector method and the numerical solutions of the system of coupled ODEs given in Equation 2.18 and Equation 2.19. The solutions of the ODEs are given by a thin line in the figure, and the solutions of the vector method are given in thick lines.

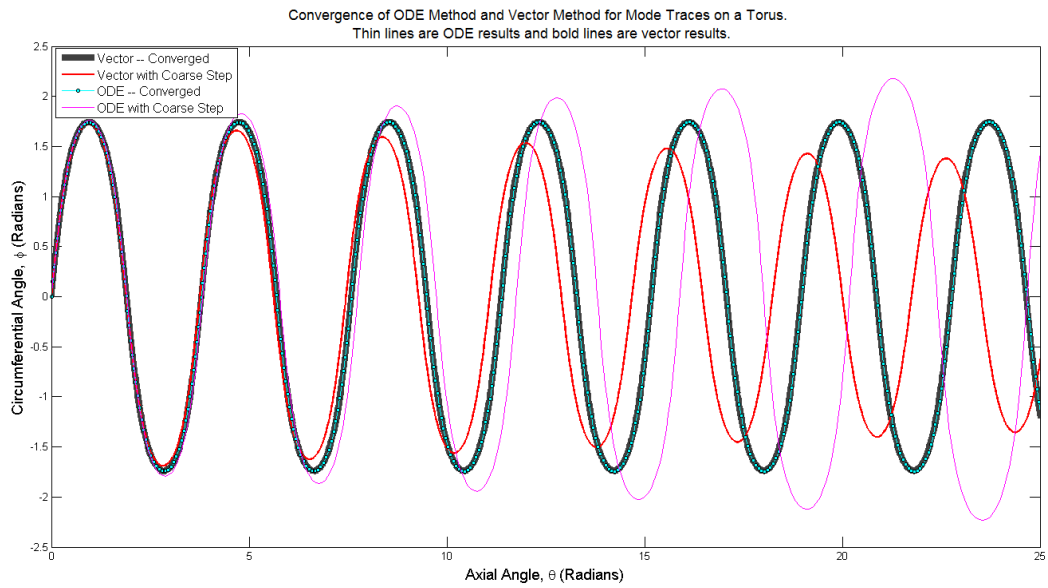

Figure 3.3
Plot showing convergence of both the ODE method and the vector method for finding mode traces on a torus. The launch angle of each solution is 45 degrees from the extrados. The thin magenta line is the solution from the ODE method when using a coarse step size. The bold red line is the solution of the vector method when using a coarse step size. The bold black line is the solution of the vector method when using a fine step size, and lying on top of this trace is the solution is a cyan line with circle markers representing the ODE method solution when using a fine step size.

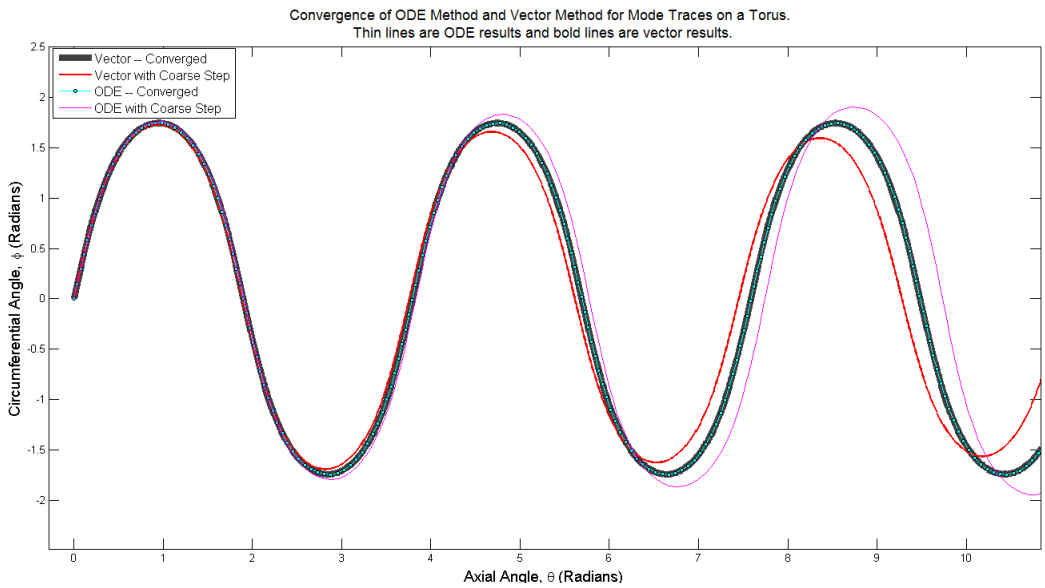

Figure 3.4
Zoomed plot showing convergence of both the ODE method and the vector method for finding mode traces on a torus. The launch angle of each solution is 45 degrees from the extrados. The thin magenta line is the solution from the ODE method when using a coarse step size. The bold red line is the solution of the vector method when using a coarse step size. The bold black line is the solution of the vector method when using a fine step size, and lying on top of this trace is the solution is a cyan line with circle markers representing the ODE method solution when using a fine step size.

The geometry of the torus represented by these solutions is a toroidal version of a 609.4 mm (24 in) diameter schedule 20 pipe elbow with a bend radius of 914.4 mm (36 in). As for the case of the cylinder just discussed, the solutions obtained start to drift away from a converged result as the calculation distance increases. Even when the iteration step size is coarse, both solutions converge to each other for short calculation distances, but they drift away from one another as the calculation distance grows. It can be seen, though, that both solutions converge to the same solution, given sufficient resolution in the step size.

It is interesting to notice that in this exercise, the two methods converge to the same solution from different directions. The vector method tends to decrease in amplitude and frequency as the calculation distance increases, and the ODE solver method tends to increase in amplitude and frequency as the calculation distance increases. This tendency of the two methods to drift in opposite directions from one another, if generally consistent, could be useful as a method of measuring the convergence of the solution. Checking the characteristics of the two solvers to see if they generally drift in opposite directions as they do here, though, is not a focus of this work.

In either case, redundant methods for calculating the transverse resonance pathway are good tools to have.

It can be seen that both the vector method and the method of solving differential equations converge to the same transverse resonance pathway. This is expected, however, from the discussion in Chapter 2. While this dissertation will continue to move the idea of mode following from an intuitive hypothesis to a demonstrated technique, it is worth remembering that this tool is brand new in this work. As such, it has not been developed yet to the same extent as the conventional approach outlined in Chapter 2 and Appendix A. Consequently, there is opportunity for future work with this method. This tool does, though, provide a useful invention that answers some important and interesting questions regarding guided wave propagation.

Geodesic Circles

Another idea that stems from the concept of mode tracing comes from Huygen's principle. This principle establishes that the wave radiating from a point source will move in all directions away from the source. If the source is symmetric, such as a 'breathing' sphere in an infinite homogeneous and isotropic medium, the energy will move away from the source with equal intensity in all directions. This means that the wave fronts of the energy will always be spherical. This principle can be applied to the mode tracing idea as well. Doing so results in the observation that a spherically symmetric wave front will move an equal distance over a given time interval along any direction. The analogous idea applies to a circularly symmetric wave front such as a symmetric point source generating a guided wave mode on a flat plate. As usual, we constrain the plate to be homogeneous and isotropic.

To investigate whether this is borne out in the use of geodesic methods, we conceptually place any two geodesics, or mode traces, on such a structure that each originate at the location of a symmetric point source and leave in mutually different directions. If the wave does indeed follow the geodesics, then at any given propagation time after the wave has been introduced into the structure, the wave front will be the same distance from the source on both geodesics.

If an infinite number of mode traces, therefore, were used to model energy spreading from a point source, each of a mutually different direction, each trace could be thought of as a carrier of the infinitesimal amount of energy coinciding with the initial direction of the trace. In practice, a

finite number of traces will be used, and each will have a finite starting angle between itself and its nearest neighboring mode trace.

For a point source in a homogeneous isotropic medium, the wave speed is identical in all directions, so according to Huygen's principle, the energy will exist at the same geodesic distance on each of the mode traces, at a particular time. For a guided wave on a plate excited by a point source, this means that the wave will travel with a circular wave front as it moves away from the source. In the general case, the same should hold, meaning that the wave front represents a geodesic circle on the surface of the waveguide. The location of where energy will exist at a given time, therefore, can be determined by finding the geodesic circle defined by a temporal radius around a point source. This is demonstrated using FEM simulations following a brief look at geodesic circles and how they can be obtained.

Because of the existence and simplicity of the analytical geodesic solutions for a straight pipe, the geodesic circles for straight pipes can be easily obtained. For this, the generalized coordinates {z, ϕ} will be used. The pipe radius, r, is held constant. The coordinate z is the axial coordinate of the pipe, and ϕ is the circumferential angle. The distance along z is simply z itself, and the distance along ϕ is the radius r times ϕ. Recall Equation 2.14, describing the geodesic solutions for a pipe. This equation is given again here for convenience as Equation 3.1.

$$z(t) = z_0 + \dot{z}t; \;\; \phi(t) = \phi_o + \dot{\phi}t$$

Equation 3.1

The differential increments of distance along z and ϕ are given in Equation 3.2.

$$dz = \dot{z}dt; \quad d\phi = r\dot{\phi}dt$$

Equation 3.2

The infinitesimal increment of distance, *ds*, along the pipe for a time of dt is then Equation 3.3, which can be integrated over time to get the total distance traveled, R, by the geodesic over a time T. Doing so, and integrating from time equals zero to time equals T results in Equation 3.4. Note that by the geodesic solutions for a circular cylinder the quantities $\dot{\phi}$ and $\dot{z}$ are constants.

$$ds = \sqrt{r^2\dot{\phi}^2 + \dot{z}^2}dt$$

Equation 3.3

$$R = T\sqrt{r^2\dot{\phi}^2 + \dot{z}^2}$$

Equation 3.4

The angle, α, made between the axial and circumferential distance directions can be introduced as Equation 3.5. Solving Equation 3.4 for T and making use of Equation 3.5 and an elementary trigonometric identity allows the calculation of the time T needed for a geodesic to reach a length of R as a function of the angle α. This is shown in Equation 3.6.

$$\tan\alpha = \frac{r\dot{\phi}}{\dot{z}}$$

Equation 3.5

$$T = \frac{R\cos\alpha}{\dot{z}}$$

Equation 3.6

This allows $z(T)$ and $\phi(T)$ to be obtained by substituting T in Equation 3.6 for t in Equation 3.1. Equation 3.5 can be used to simplify the results. These quantities represent the final values of the generalized coordinates z and ϕ for a geodesic originating from the origin of z and ϕ, and having length R and angle α. Following this process and letting $z_0 = \phi_o = 0$ leads to Equation 3.7.

$$z(T) = R\cos\alpha\,; \quad \phi(T) = \frac{R\sin\alpha}{r}$$

Equation 3.7

The equations mapping the generalized coordinates {r,z,ϕ} to global Cartesian coordinates {x,y,z} are shown in Equation 3.8.

$$x = r\cos\phi$$
$$y = r\sin\phi$$
$$z = z$$

Equation 3.8

It is easy enough to realize that geodesic circles on a flat structure are just circles in Cartesian space. Geodesic circles for pipes with elbows are not analytically available, but can be obtained numerically. Examples of geodesic circles for pipes and pipes with elbows derived from FEM simulations are given next.

In the first of these FEM simulations, a point source is placed on the top edge of one end of a straight pipe. This means that the source is located at an axial distance of 0 m and a circumferential location of $\pi/2$ radians. The guided wave is allowed to propagate in the simulation and four snapshots of the propagating wave fronts are taken, each at mutually different times. Even though the guided wave source used in the simulation is a point source, its placement on the model is not symmetric, since it is located on one end of the pipe.

Furthermore, the source is designed to actuate in a shear fashion rather than in a radial one. This means that motion of the source lies in the ϕ direction rather than the r direction. This type of point source generates shear waves polarized in the axial direction and longitudinal waves polarized in the circumferential direction. Consequently, both a shear mode and a longitudinal mode are seen in the simulation. Both move away from the source with a constant wave speed in all directions, but instead of the wave front of either mode being fully circular, the amplitude of the wave front for each mode drops off sharply as the launch angle α between the axial direction and the circumferential direction of the wave front approaches $\pm\pi/4$ radians.

To show whether the wave front of the propagating guided wave mode actually is circular in a geodesic sense, some special shapes are fabricated and superimposed with the pipe geometry in the results of the FEM simulation. These shapes are designed so that when they are superimposed on the pipe geometry, the intersection of the surface of the special shape and the outer pipe surface traces a geodesic circle on the pipe. The relevant equations of a geodesic circle for pipes are given in Equation 3.7. The special shape needed so that the superposition of the special shape with the pipe will trace a geodesic circle by the intersection of their boundaries can be obtained by projecting the geodesic circle of interest onto the x-z plane.

This is done directly by plugging in the results from Equation 3.7 for a particular geodesic radius R into the x and z map given in Equation 3.8 and extruding the resulting x-z cross-section into a 3-dimensional shape of sufficient height so as to appropriately intersect with the pipe geometry. For geodesic circles of small diameter on a pipe, the resulting special shape resembles a slightly fore-shortened circular peg. As the geodesic radius grows, however, the special shape takes on an increasingly innovative look.

An example of such a special shape for a geodesic circle of small diameter is shown in Figure 3.5. In this figure, the pipe geometry extends from the lower left corner of the figure toward the center of the right edge of the figure. The special shape resembles an extruded "D" shape and is

oriented so that the extrusion direction is orthogonal to the axis of the pipe. The geodesic radius of the special shape is 300 mm (11.8 in). Similarly, a special shape needed for representing a geodesic circle of larger diameter is shown in Figure 3.8. In Figure 3.8, the geodesic radius of the special shape is 900 mm (35.4 in). We will neglect the faster longitudinal mode produced by the loading source and compare only the wave front of the slower, shear, mode with the intersection of the pipe and the special shapes of relevant geodesic diameter.

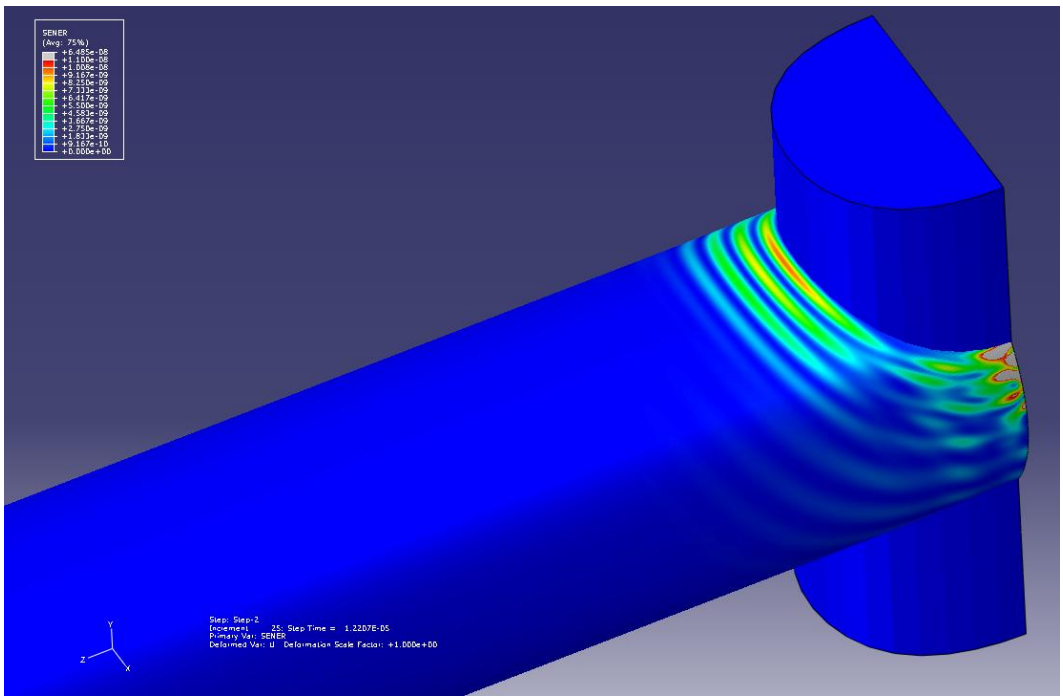

Figure 3.5
FEM simulation of a point source on a straight pipe. The superimposed shape on the drawing is a special shape that is designed such that the intersection of the special shape and the pipe geometry forms a geodesic half circle of 300 mm (11.8 in) radius. The shear mode wave fronts can be seen to follow the geodesic half circle denoted by this intersection.

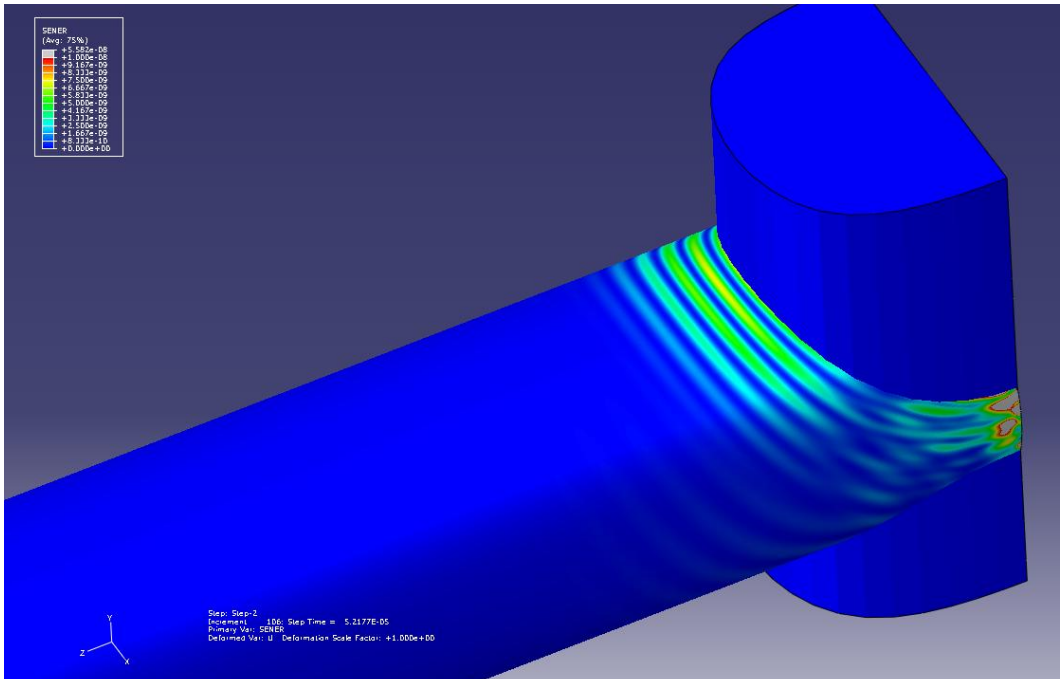

Figure 3.6
FEM simulation of a point source on a straight pipe. The superimposed shape on the drawing is a special shape that is designed such that the intersection of the special shape and the pipe geometry forms a geodesic half circle of 400 mm (15.7 in) radius. The shear mode wave fronts can be seen to follow the geodesic half circle denoted by this intersection.

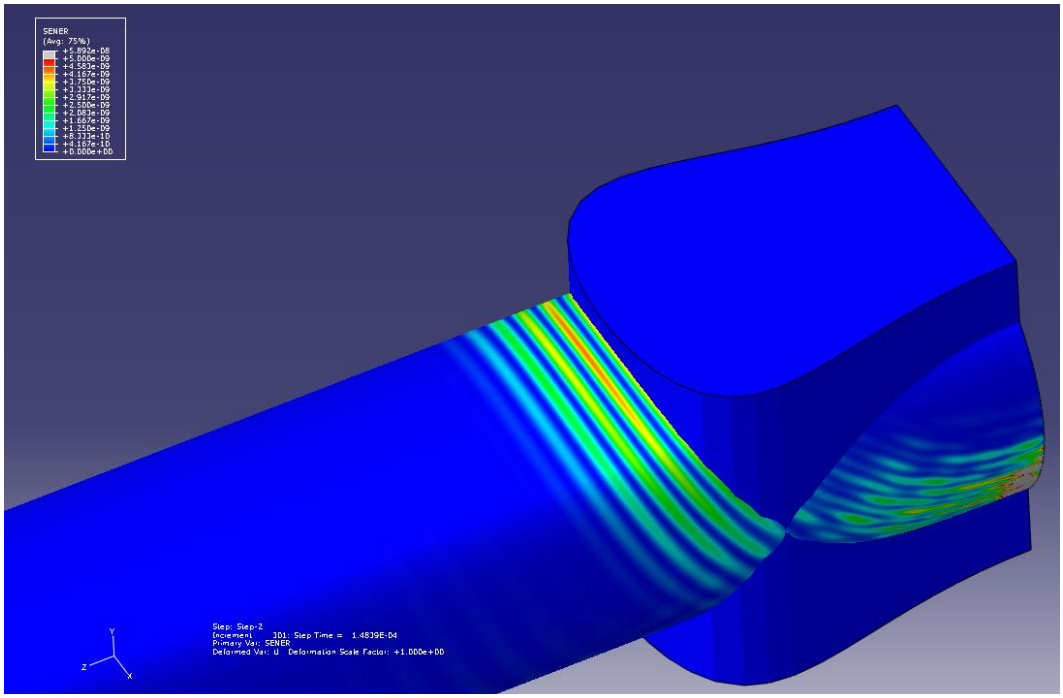

Figure 3.7
FEM simulation of a point source on a straight pipe. The superimposed shape on the drawing is a special shape that is designed such that the intersection of the special shape and the pipe geometry forms a geodesic half circle of 700 mm (27.6 in) radius. The shear mode wave fronts can be seen to follow the geodesic half circle denoted by this intersection.

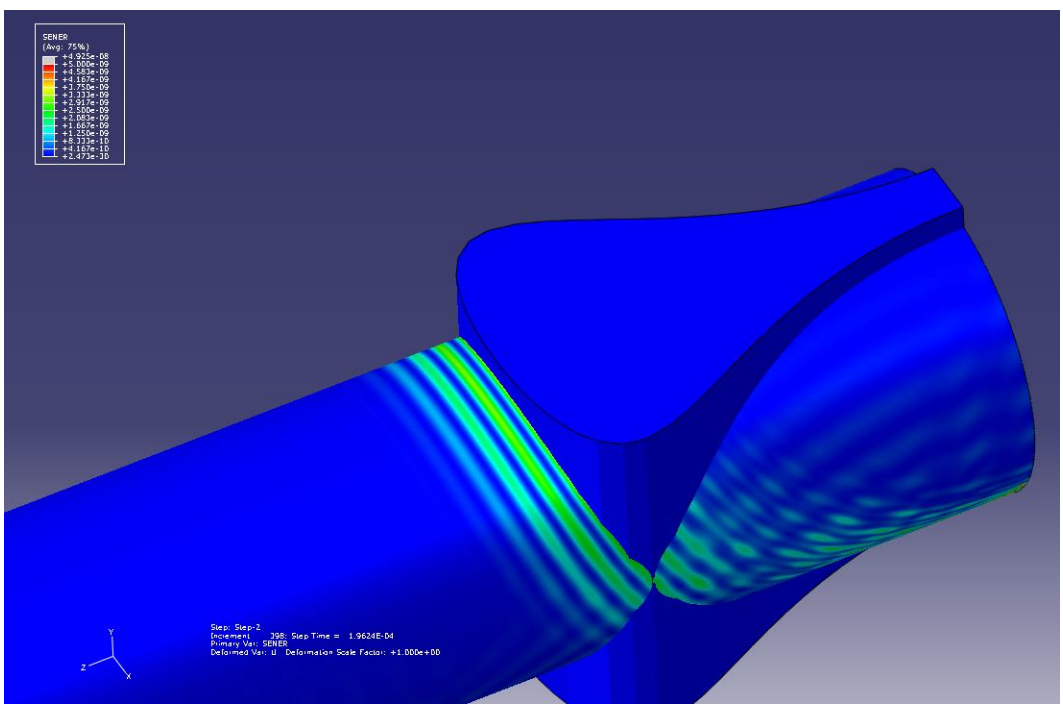

Figure 3.8
FEM simulation of a point source on a straight pipe. The superimposed shape on the drawing is a special shape that is designed such that the intersection of the special shape and the pipe geometry forms a geodesic half circle of 900 mm (35.4 in) radius. The shear mode wave fronts can be seen to follow the geodesic half circle denoted by this intersection.

While this exercise is qualitative in nature, it very convincingly shows that the wave front of the shear mode does indeed follow a geodesic circle. Inspection of Figure 3.5, for instance, shows that the wave fronts of the shear mode in this simulation very precisely follow the geometric intersection of the special shape and the pipe surfaces. The other images in Figure 3.6 through Figure 3.8 show the same wave at respectively increasing distances from the source. In particular, the geodesic radii of the special shapes shown are 400 mm (15.7 in), 700 mm (27.6 in), and 900 mm (35.4 in) respectively. In each of these figures, the wave front of the shear mode lies exactly along the intersection of the pipe and the relevant special shape.

The propagation distance of the wave used for each of these snapshots is chosen arbitrarily, other than to provide a good opportunity to compare the wave front with the profile of the special shape in each case. The x-z cross-section of each of the special shapes used in this exercise have been defined in a point-to-point fashion rather than as an analytical curve. Therefore, the boundaries of the special shapes are not smooth, but discrete in nature. The reason for this choice of boundary definition for the special shapes is due to the logistical difficulty of defining the analytically correct shape in ABAQUS, the FEM solver used for the simulation.

This phenomenon can also be simulated solely through the use of mode tracing, as seen in Figure 3.9. In this figure, a variety of geodesic circular segments are shown overlaid on a wire frame of a straight pipe. The circular segments are bounded on either side by a mode trace originating from the source and moving away from the source at some bounding angle. These two bounding mode traces provide an example of using geodesic boundary tracing to track beam spreading between two angles of interest leaving a source. This idea is further discussed later in this chapter.

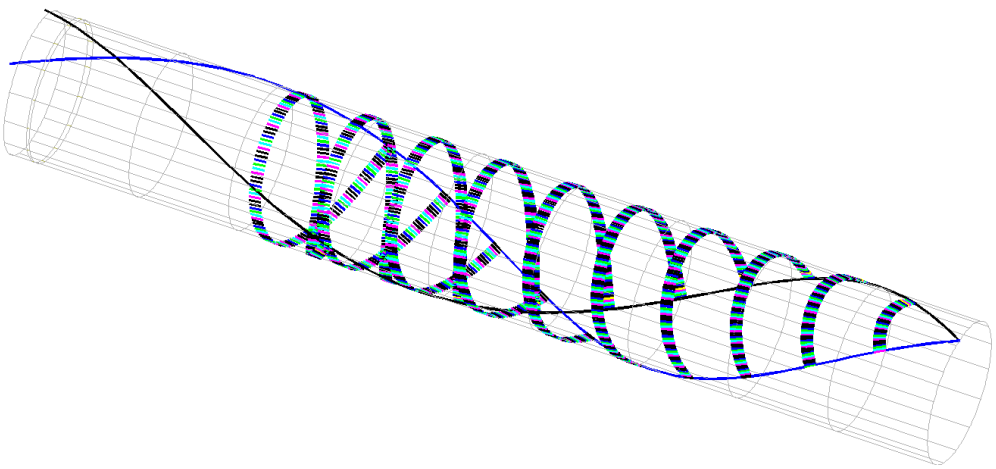

Figure 3.9
Depiction of geodesic circular segments bounded by two mode traces as a function of geodesic distance from a point source.

A series of FEM simulations is also used next to show guided wave energy spreading from a symmetric point source on a pipe elbow. For these models, a 609.4 mm (24 in) diameter pipe is used with damped ends. A 90-degree elbow is preceded in each model by 0.86 m (34 in) of straight pipe. There is an additional 0.86 m (34 in) of straight pipe beyond the elbow. In the resulting figures shown here, such as Figure 3.10, the plotted information represents an unwrapped pipeline. The two black vertical lines in the figures denote the entrance and the exit of the elbow in the piping system. The point source for each of these images is symmetric, that is, it actuates in the r direction. This source also does not suffer from the edge effects of the previous FEM simulation. The source for each FEM simulation is located at the zero angle of θ, meaning the beginning of the elbow. The source is located at mutually different angles of ϕ in the different plots, where ϕ varies as $n\pi/5$, with the integer n ranging from 0 to 5.

To the left of the leftmost black vertical line in each figure, the wave is moving leftward into a straight section of pipe. Similarly, to the right of the rightmost black vertical line, the wave is moving right through a straight section of pipe. Between the two lines, the wave is progressing through the elbow. In each case, the point source is located on the elbow entrance.

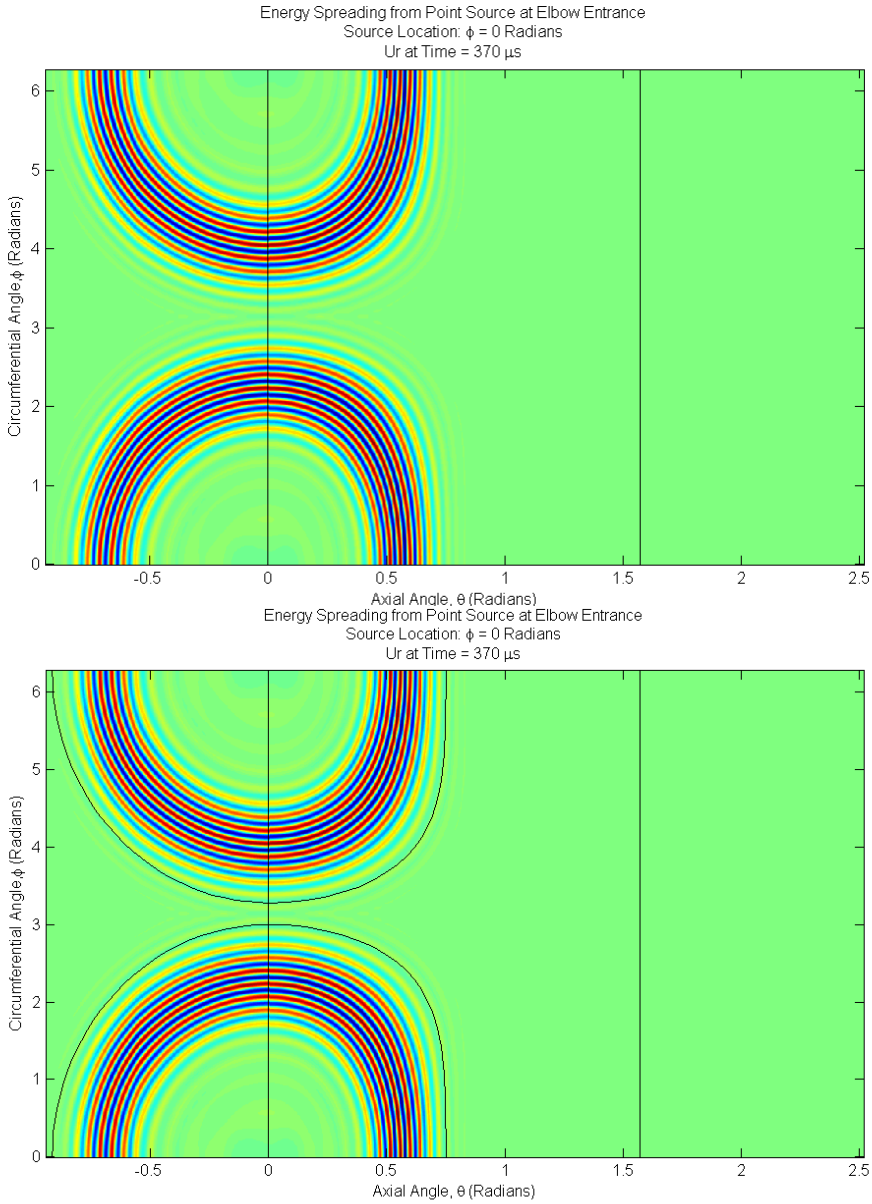

Figure 3.10
FEM simulation results showing energy spreading from a point source on a 609.4 mm (24 in) diameter pipe with a 1.5D elbow. The source is located at 0 radians. The region of the image between the two black vertical lines is an unwrapped representation of the elbow. The regions outside the black vertical lines are unwrapped straight pipe sections. The top panel shows only the FEM results. The bottom panel shows the same result but with a geodesic circle of 0.91 m (36 in) radius superimposed over the FEM output.

The first set of images from Figure 3.10 to Figure 3.15 show the energy after propagating for 370 μs. The second set of images from Figure 3.16 to Figure 3.21 show the same plots but after the energy has propagated for 650 μs. In all of these images, the top panel shows only the FEM

simulation output overlaid with the black vertical lines denoting the elbow entrance and exit. The bottom panel shows the same thing but also shows a geodesic circle plotted over the FEM data. As described earlier, the wave fronts of a symmetric point source such as the ones used here radiate away from the source in a circular fashion. The geodesic circles in these images allow the observation that the simulated waves conform to this circular pattern.

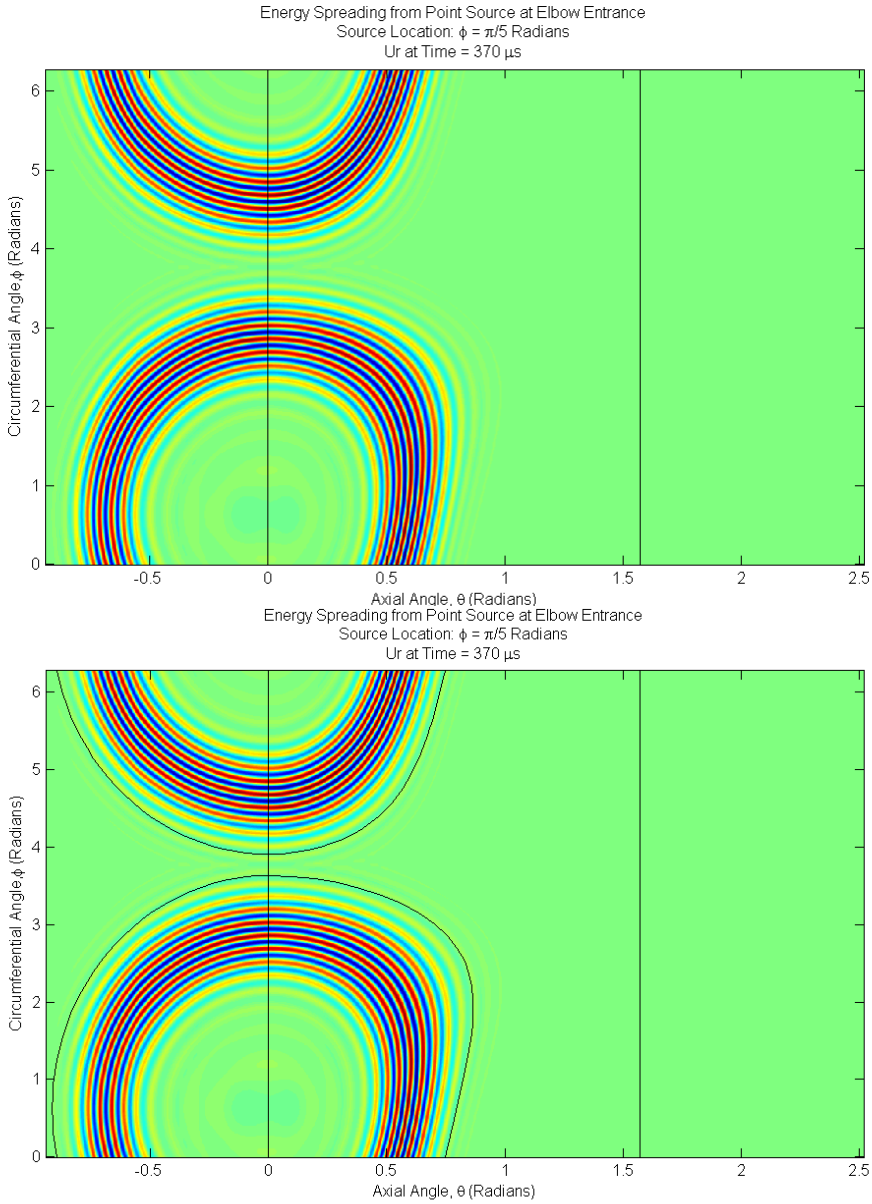

Figure 3.11
FEM simulation results showing energy spreading from a point source on a 609.4 mm (24 in) diameter pipe with a 1.5D elbow. The source is located at $\pi/5$ radians. The region of the image between the two black vertical lines is an unwrapped representation of the elbow. The regions outside the black vertical lines are unwrapped straight pipe sections. The top panel shows only the FEM results. The bottom panel shows the same result but with a geodesic circle of 0.91 m (36 in) radius superimposed over the FEM output.

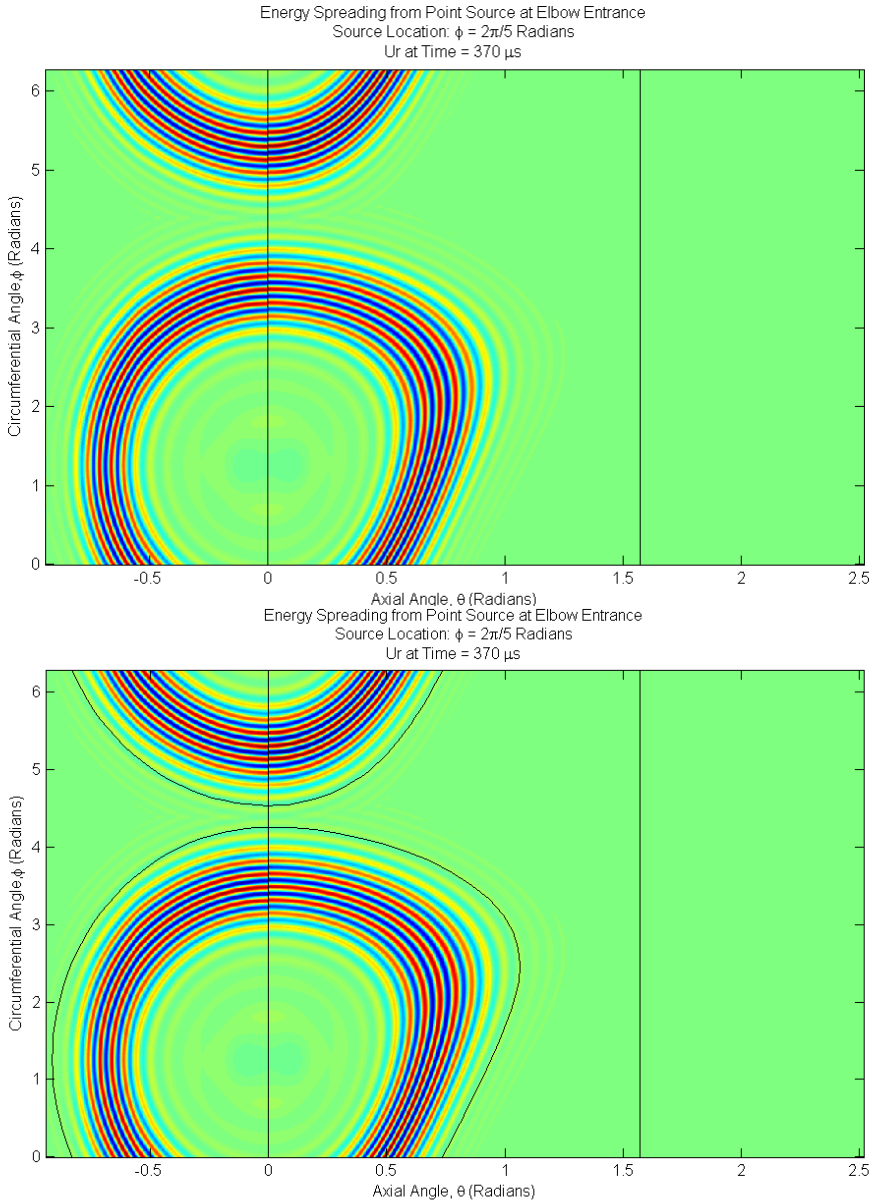

Figure 3.12
FEM simulation results showing energy spreading from a point source on a 609.4 mm (24 in) diameter pipe with a 1.5D elbow. The source is located at $2\pi/5$ radians. The region of the image between the two black vertical lines is an unwrapped representation of the elbow. The regions outside the black vertical lines are unwrapped straight pipe sections. The top panel shows only the FEM results. The bottom panel shows the same result but with a geodesic circle of 0.91 m (36 in) radius superimposed over the FEM output.

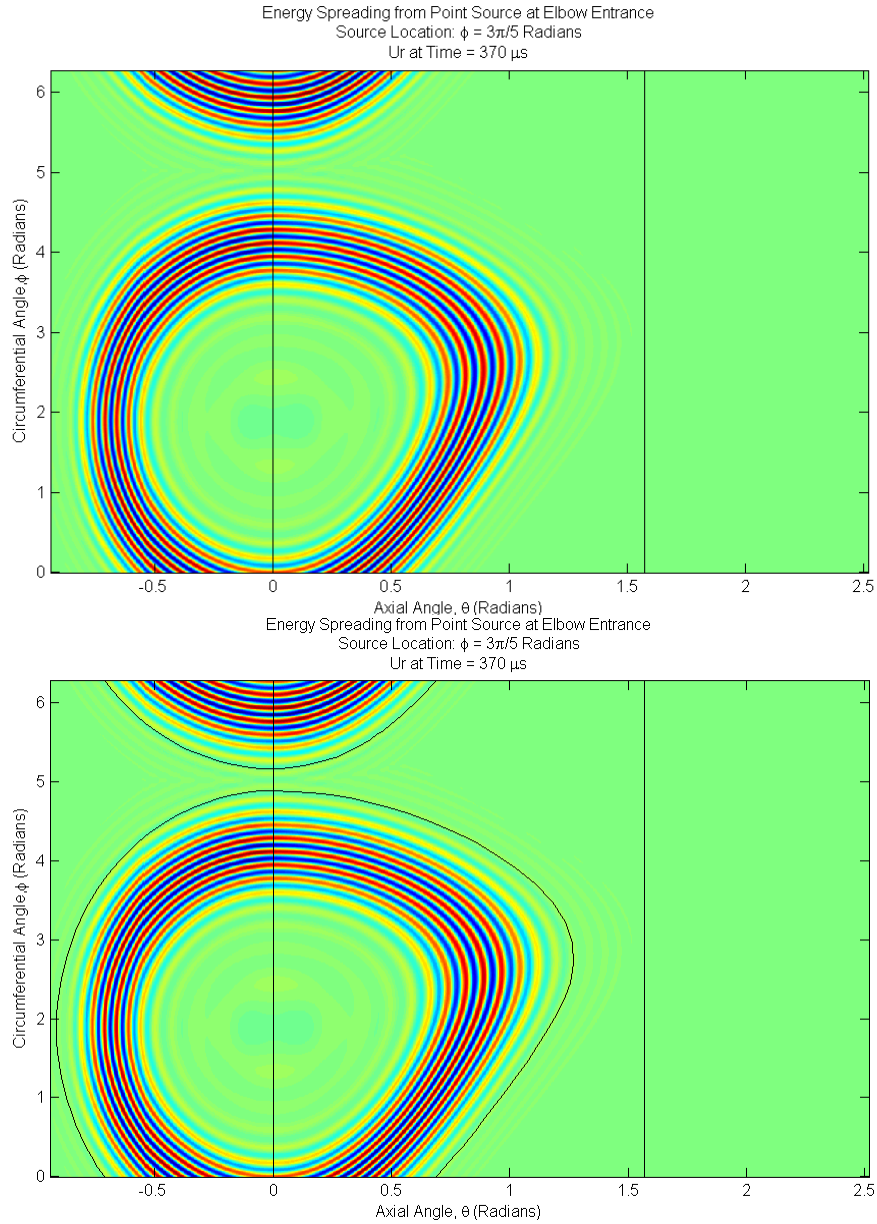

Figure 3.13
FEM simulation results showing energy spreading from a point source on a 609.4 mm (24 in) diameter pipe with a 1.5D elbow. The source is located at $3\pi/5$ radians. The region of the image between the two black vertical lines is an unwrapped representation of the elbow. The regions outside the black vertical lines are unwrapped straight pipe sections. The top panel shows only the FEM results. The bottom panel shows the same result but with a geodesic circle of 0.91 m (36 in) radius superimposed over the FEM output.

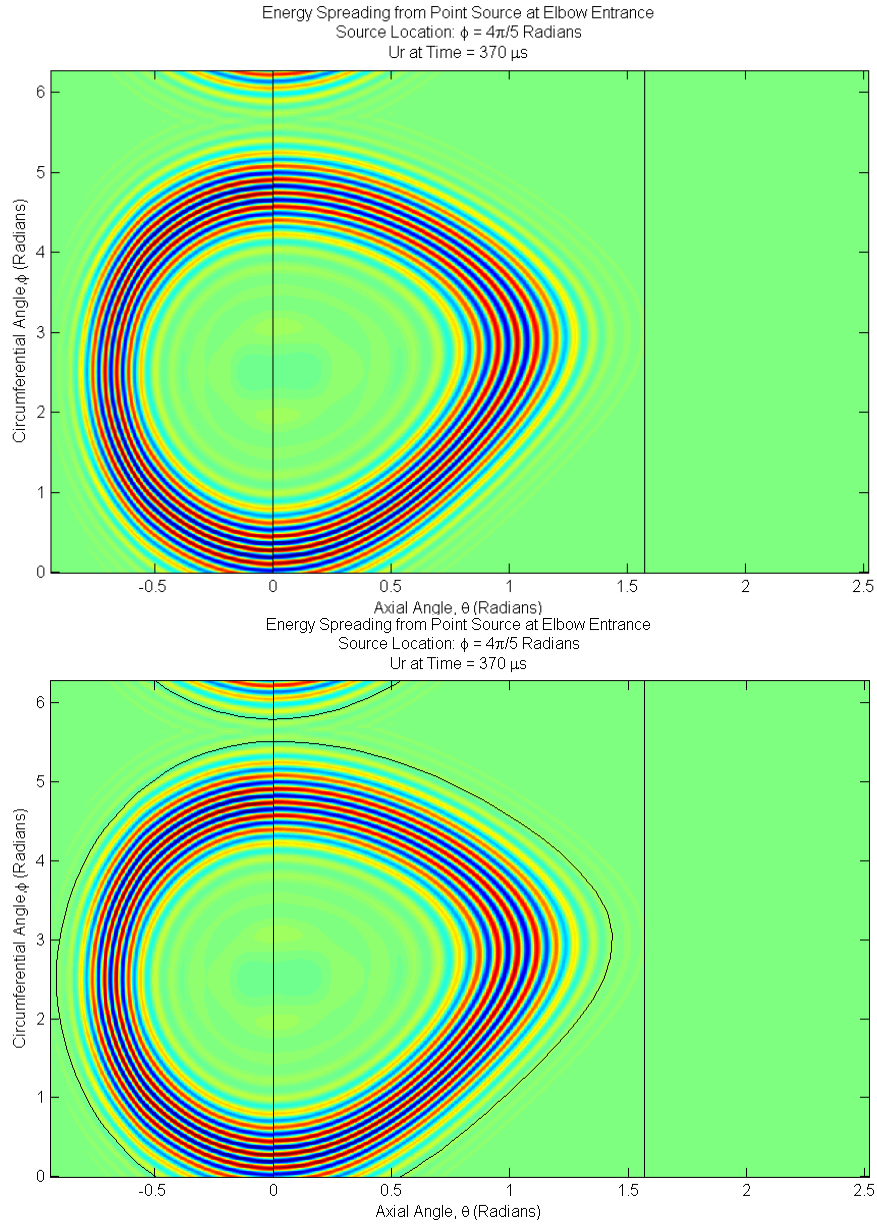

Figure 3.14
FEM simulation results showing energy spreading from a point source on a 0.61 m (24 in) diameter pipe with a 1.5D elbow. The source is located at $4\pi/5$ radians. The region of the image between the two black vertical lines is an unwrapped representation of the elbow. The regions outside the black vertical lines are unwrapped straight pipe sections. The top panel shows only the FEM results. The bottom panel shows the same result but with a geodesic circle of 0.91 m (36 in) radius superimposed over the FEM output.

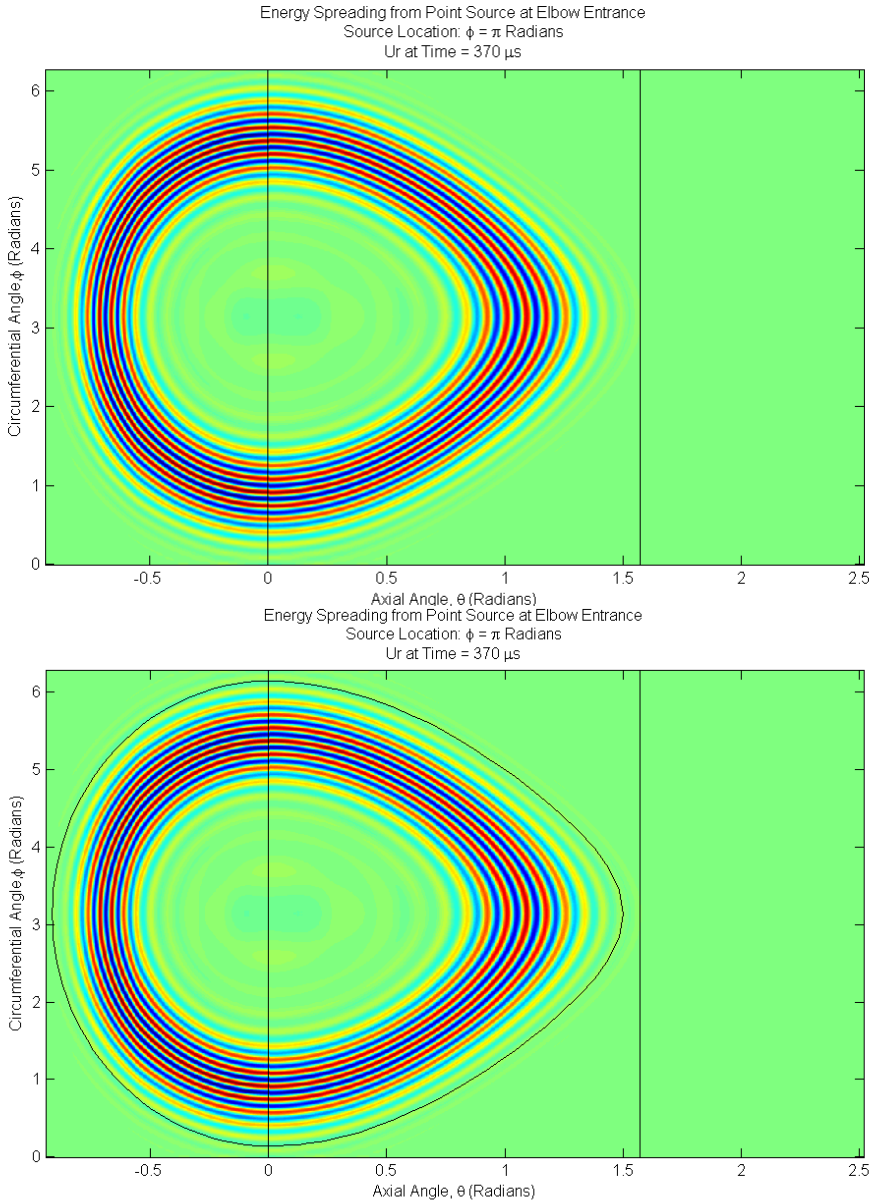

Figure 3.15
FEM simulation results showing energy spreading from a point source on a 0.61 m (24 in) diameter pipe with a 1.5D elbow. The source is located at π radians. The region of the image between the two black vertical lines is an unwrapped representation of the elbow. The regions outside the black vertical lines are unwrapped straight pipe sections. The top panel shows only the FEM results. The bottom panel shows the same result but with a geodesic circle of 0.91 m (36 in) radius superimposed over the FEM output.

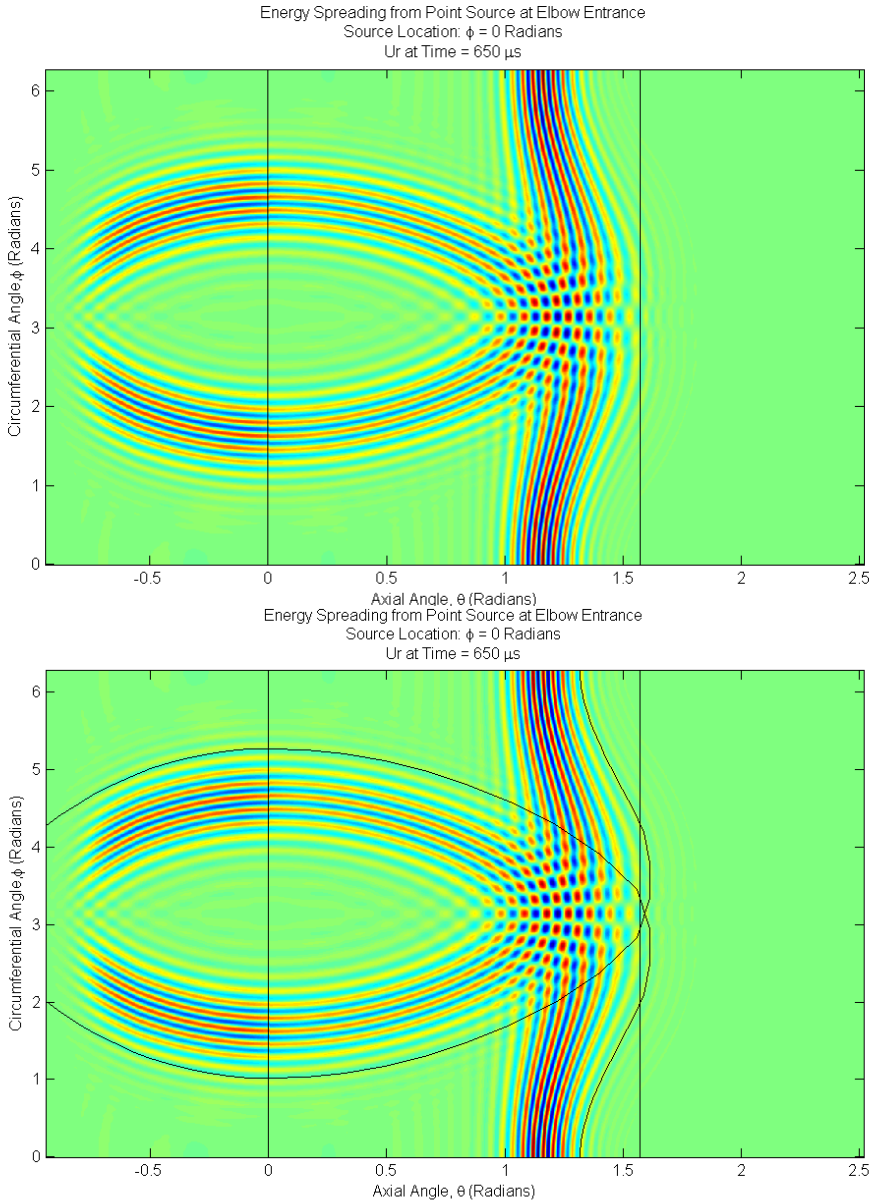

Figure 3.16
FEM simulation results showing energy spreading from a point source on a 0.61 m (24 in) diameter pipe with a 1.5D elbow. The source is located at 0 radians. The region of the image between the two black vertical lines is an unwrapped representation of the elbow. The regions outside the black vertical lines are unwrapped straight pipe sections. The top panel shows only the FEM results. The bottom panel shows the same result but with a geodesic circle of 1.6 m (63 in) radius superimposed over the FEM output.

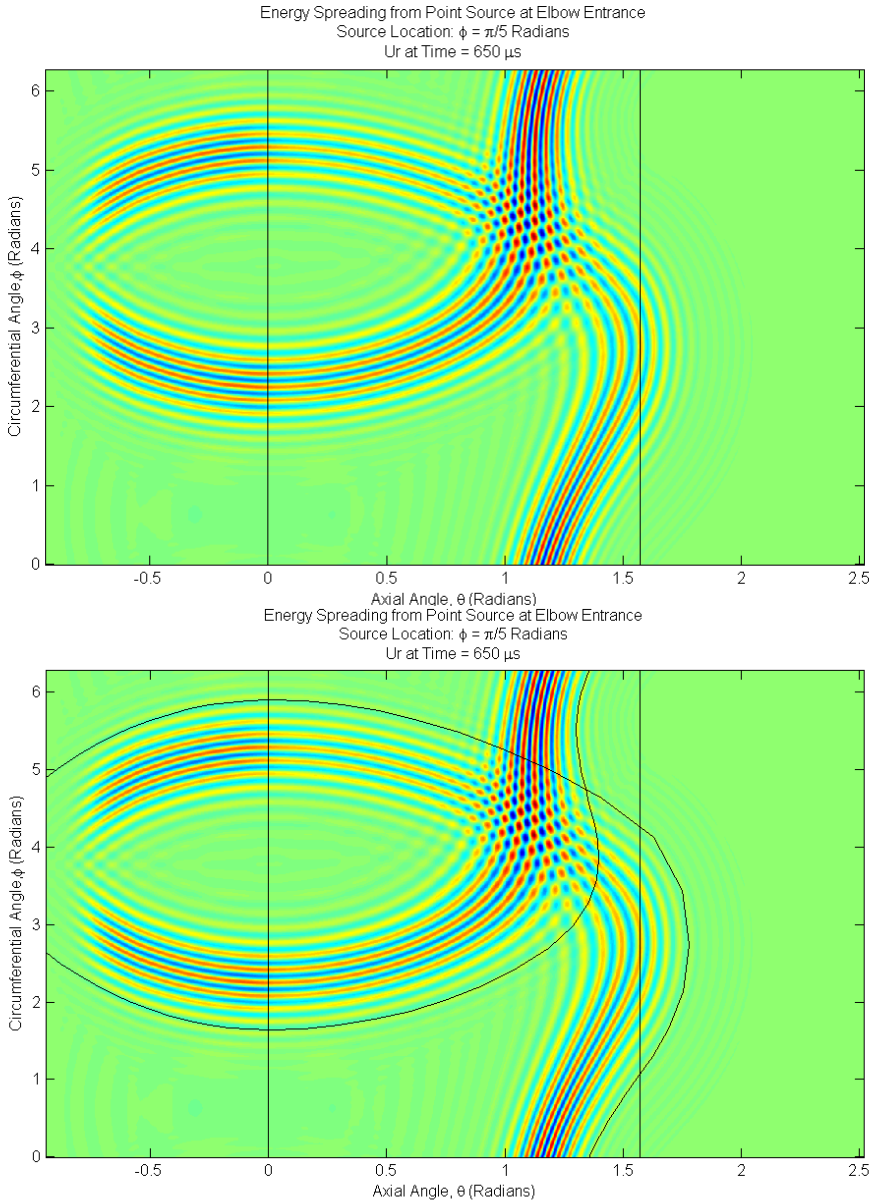

Figure 3.17
FEM simulation results showing energy spreading from a point source on a 0.61 m (24 in) diameter pipe with a 1.5D elbow. The source is located at $\pi/5$ radians. The region of the image between the two black vertical lines is an unwrapped representation of the elbow. The regions outside the black vertical lines are unwrapped straight pipe sections. The top panel shows only the FEM results. The bottom panel shows the same result but with a geodesic circle of 1.6 m (63 in) radius superimposed over the FEM output.

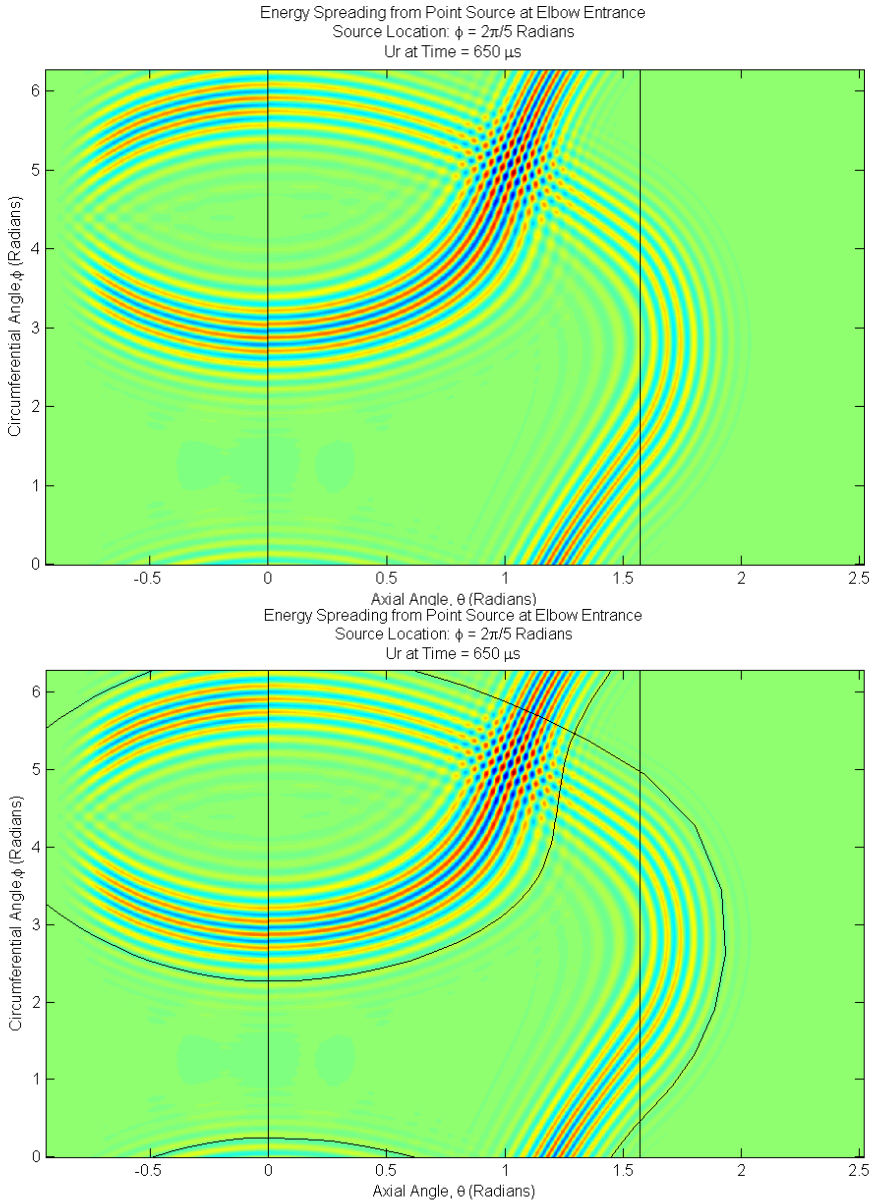

Figure 3.18
FEM simulation results showing energy spreading from a point source on a 0.61 m (24 in) diameter pipe with a 1.5D elbow. The source is located at $2\pi/5$ radians. The region of the image between the two black vertical lines is an unwrapped representation of the elbow. The regions outside the black vertical lines are unwrapped straight pipe sections. The top panel shows only the FEM results. The bottom panel shows the same result but with a geodesic circle of 1.6 m (63 in) radius superimposed over the FEM output.

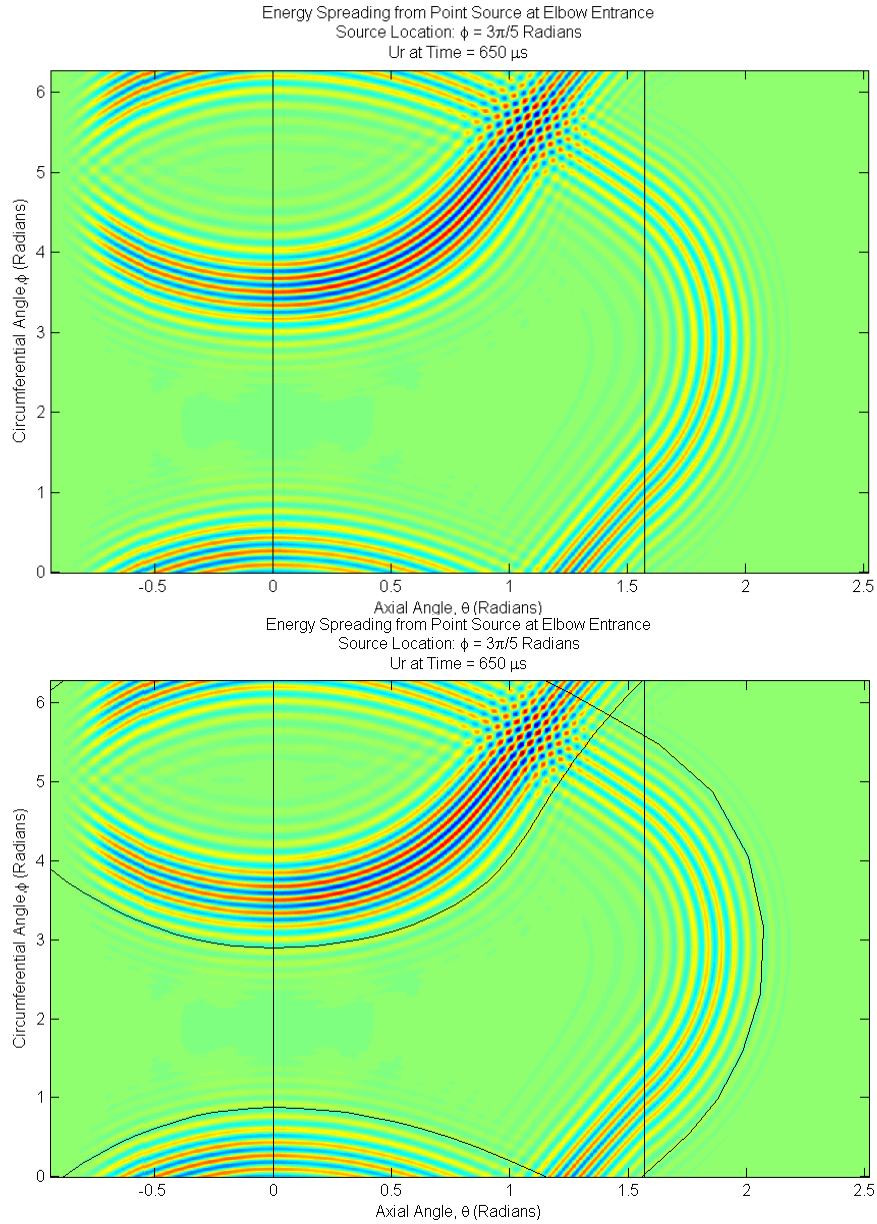

Figure 3.19
FEM simulation results showing energy spreading from a point source on a 0.61 m (24 in) diameter pipe with a 1.5D elbow. The source is located at $3\pi/5$ radians. The region of the image between the two black vertical lines is an unwrapped representation of the elbow. The regions outside the black vertical lines are unwrapped straight pipe sections. The top panel shows only the FEM results. The bottom panel shows the same result but with a geodesic circle of 1.6 m (63 in) radius superimposed over the FEM output.

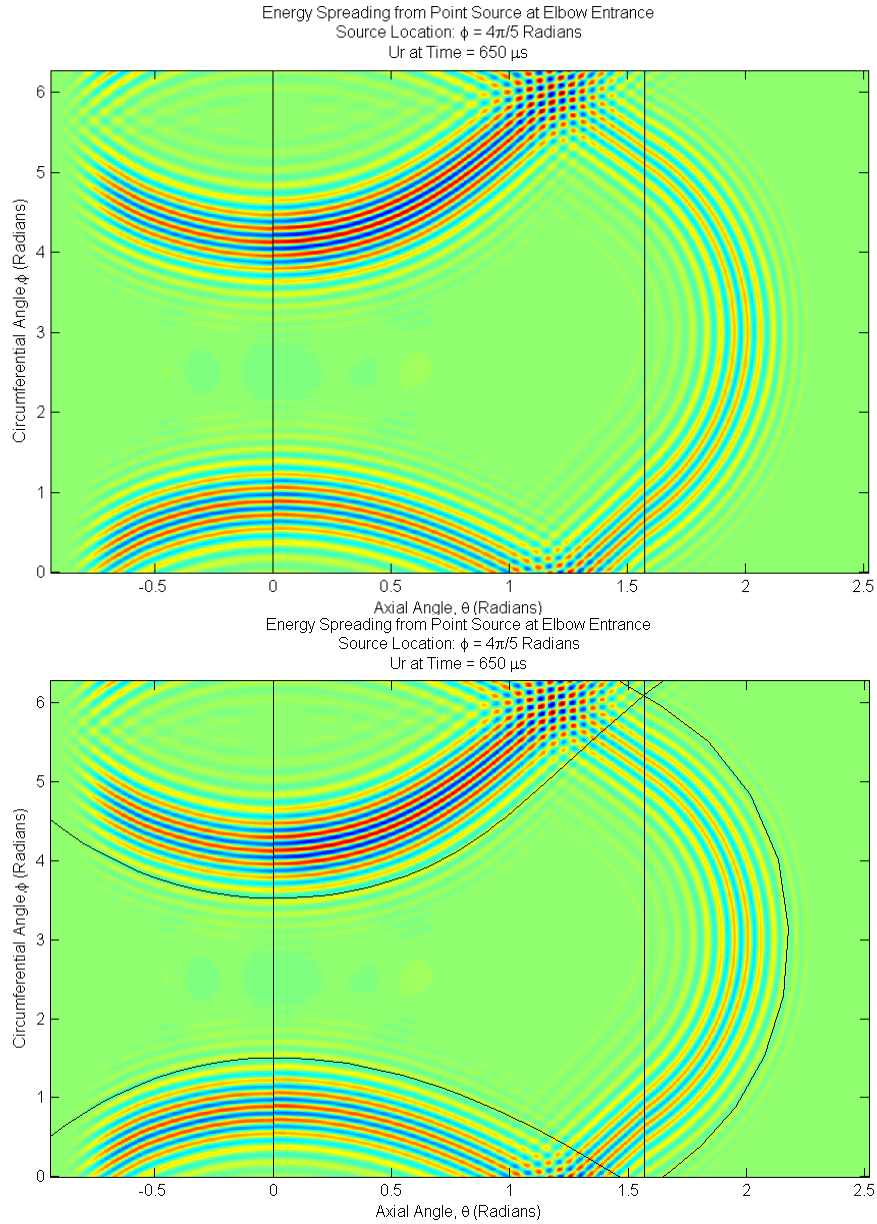

Figure 3.20
FEM simulation results showing energy spreading from a point source on a 0.61 m (24 in) diameter pipe with a 1.5D elbow. The source is located at $4\pi/5$ radians. The region of the image between the two black vertical lines is an unwrapped representation of the elbow. The regions outside the black vertical lines are unwrapped straight pipe sections. The top panel shows only the FEM results. The bottom panel shows the same result but with a geodesic circle of 1.6 m (63 in) radius superimposed over the FEM output.

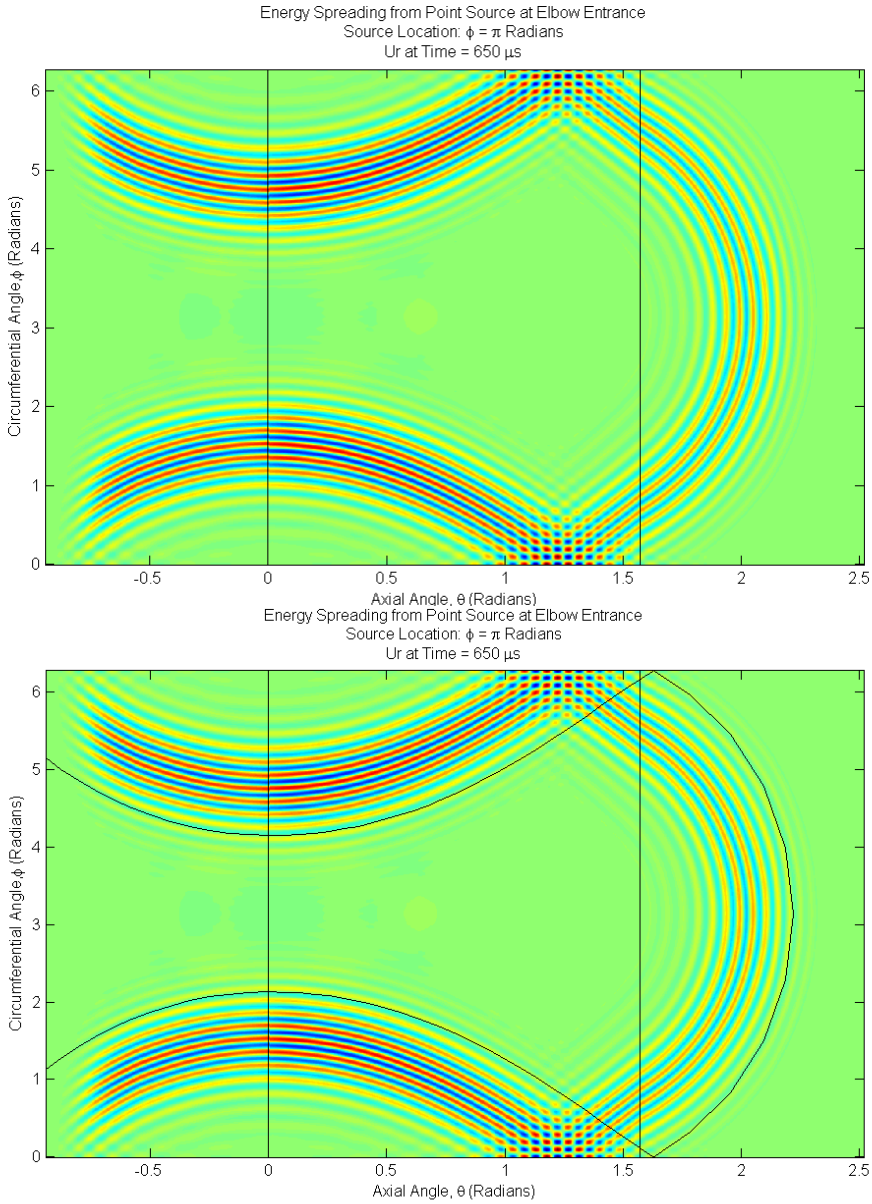

Figure 3.21
FEM simulation results showing energy spreading from a point source on a 0.61 m (24 in) diameter pipe with a 1.5D elbow. The source is located at π radians. The region of the image between the two black vertical lines is an unwrapped representation of the elbow. The regions outside the black vertical lines are unwrapped straight pipe sections. The top panel shows only the FEM results. The bottom panel shows the same result but with a geodesic circle of 1.6 m (63 in) radius superimposed over the FEM output.

Each of the geodesic circles in the figures from Figure 3.10 through Figure 3.21 is constructed with 242 points, each representing the tip of a mode trace originating from the location of the point source and moving in a mutually separate direction from all the other traces. The initial

angle between each pair of neighboring mode traces is mutually equal, or $2\pi/242$ radians. For the latter set of images, the discretization of the geodesic circles gives a sense of the density of mode traces that end at particular regions of the geodesic circle.

Regions of the circles that are very smooth, and consist of many points, are those with many mode traces landing there. This is indicative that a lot of energy from the point source is ultimately distributed there. Regions of the circles that are less smooth consist of fewer mode traces and represent places where the energy from the point source is more thinned out. It can be seen in all these cases, that the guided wave really does propagate away from the point source in a geodesically circular fashion. This exercise lends substantial credibility to the hypothetical idea of mode tracing introduced in Chapter 2.

From here, we move into a discussion of some limitations of the mode tracing approach to understanding guided wave propagation. We will also discuss the idea of thinking of beam spreading by tracing some feature of a wave mode, such as the 6 dB down point or a null point on the directivity function of a wave source. This idea was introduced in the discussion surrounding Figure 3.9. This concept is illustrated in Figure 3.22, which shows geodesic boundary tracing on a flat plate.

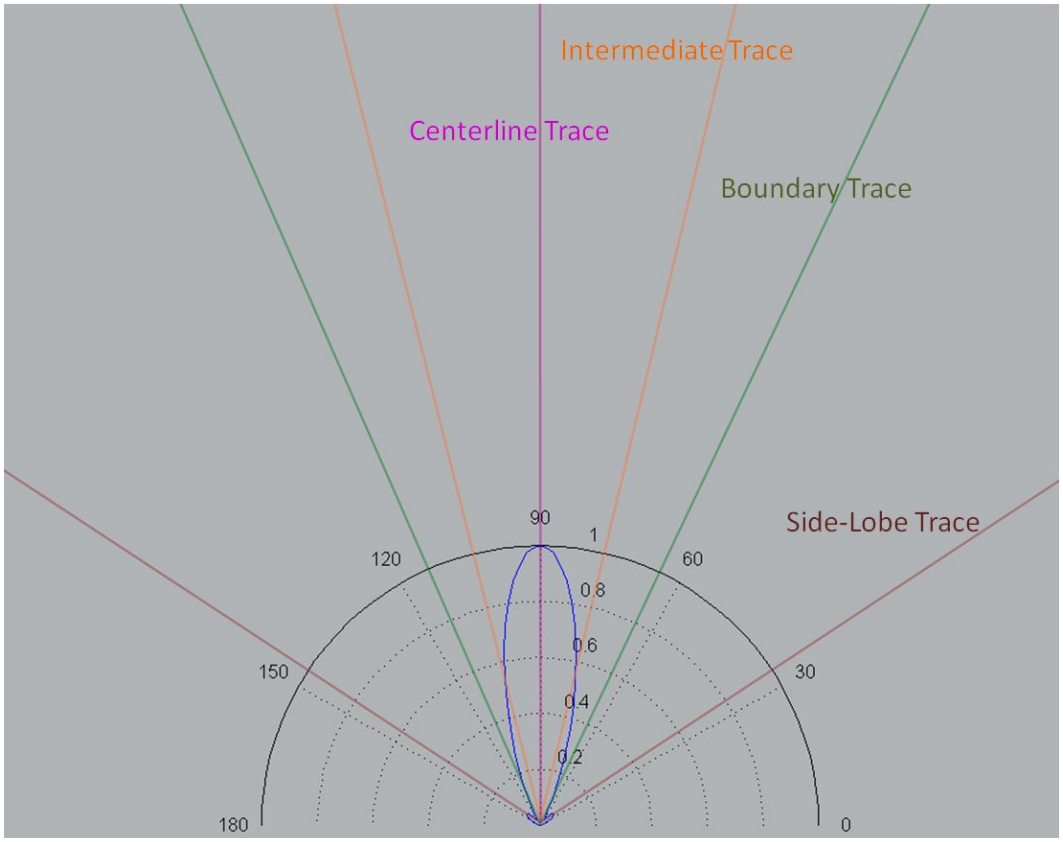

Figure 3.22
Illustration of geodesics on a flat plate representing the use of geodesic methods, or mode tracing, for tracking wave energy of various intensities. The geodesics are overlaid on an illustrational wave energy directivity plot. The magenta centerline geodesic represents the path taken by the highest intensity energy. The orange traces depict the path taken by the energy leaving the source at an angle corresponding to about 6 dB down from the maxim energy direction. The green traces show the path taken by the outer edge of the mode packet, and the brown traces show the propagation direction of the side lobes.

In Figure 3.22, the directivity function of a hypothetical guided wave source is shown in blue. The directivity function shows the normalized map of energy amplitude that will leave the source in a particular direction. For symmetric point sources such as those used in the FEM simulations shown in Figure 3.10 to Figure 3.21, the directivity function will be a circle, because the amplitude of energy leaving the source will be equal in all directions. Many real guided wave sensors, however, are directional, that is, they have a preferred energy direction.

Such a sensor will launch a larger percentage of energy in one direction than other directions. Generally, stand-alone guided wave sensors are bi-directional, that is, a directivity profile that includes all the angles around the sensor from 0 to 2π radians will exhibit a line of symmetry. Consequently, directivity functions usually only include the angles from 0 to π radians around the

sensor. Also, the directivity function is usually calculated so that the preferred direction of the sensor is oriented to be 90 degrees, or $\pi/2$ radians. The directivity function shown in Figure 3.22 conforms to this convention.

In this dissertation, we use mode tracing to determine the pathway a propagating guided wave mode will take across a wave guide. Often, we mean the part of the wave mode that represents the largest amplitude of energy leaving a source. Such a reference is shown in Figure 3.22 with a magenta line titled "Centerline Trace." The term *centerline geodesic* or *center pathway* could also be used to mean the same thing on more generic shapes. In some cases, though, we may wish to refer to other traces that leave the source in a different direction.

For example, Figure 3.22 shows orange lines on either side of the centerline trace. These lines have been selected because they represent the 6 dB down angles of the sensor, the angles where the energy leaving the sensor is half as strong as the strongest energy leaving the sensor. We may also wish to think about the green lines in Figure 3.22, which represent the first energy null on either side of the main sensor direction. More generically, though, we could pick any mode trace moving in any initial direction away from the source, or any set of such traces.

One idea that follows from Figure 3.22, is that it may be possible to account for meaningful beam spreading by looking not at the centerline geodesic, but rather by considering boundary mode traces that represent the majority of the energy that leaves a sensor. This is the idea used in Figure 3.9. Employing this strategy would allow us to watch the trajectory of the shear wave mode examined in Figure 3.5 through Figure 3.8 for example. While this idea does not aspire to completely account for beam spreading, it could be useful, and may be an initial start toward including beam spreading in the new methods described in this dissertation. For the most part, however, discussions of beam spreading are not the focus of this dissertation, as this work offers a broad contribution to guided wave understanding even without examining beam spreading.

The notion of geodesic boundary tracing leads to the immediate realization that the profile of energy moving away from a source along a homogeneous, infinite, and isotropic, flat plate will need to be the same regardless of the distance away from the source. This means that if a circle were drawn around a guided wave source and the wave energy introduced by the source that crosses the circle were measured and plotted as a function of angle around the sensor, the shape of the profile should be independent of the radius used to draw the circle. Otherwise, it could be difficult to implement the ideas surrounding Figure 3.22.

The directivity function of point sources have already been explored through the work presenting geodesic circles. However, FEM simulations are used next to explore the directivity plots of a source that exhibits directionality. The source we will look at is the familiar source used for the FEM simulation shown in Figure 3.5 through Figure 3.8. In this case, though, a flat plate is used instead of a pipe, and the source is of finite size, and is rectangular. The source is placed in the center of the plate and is actuated in a shear motion. The dimensions of the source are 9.8 mm (0.25 in) in the x-direction, and 25.4 mm (1 in) in the y-direction. The source behaves as a rigid actuator and is constrained to exhibit a motion in the y-direction only. The design of this sensor is intended to launch a guided shear wave that travels in the positive and negative x-directions.

The plate domain is aligned in the x-y plane in the FEM simulation with the plate thickness lying in the z-direction. The edges of the plate are damped as described in Appendix C. The purpose of this damping is to simulate the condition of a plate with infinite lateral dimensions. The energy is excited from the center of the plate, and several sets of simulated receivers are placed in circular footprints on the surface of the plate, concentric with the source. Several relevant FEM damping techniques are explored and discussed by Prahbu et al. [178].

Each node in the plate domain lying on one of these receiver rings is used to monitor the guided wave energy that crosses the node. In particular, every such node records the x and y displacements of the plate surface at the location of the node. These displacements are then used to calculate the directivity plot of the sensor as a function of wave propagation distance along the plate. Receivers are also discussed in Appendix C. Figure 3.23 shows an image of the simulation output approximately 106 micro seconds after the simulation begins.

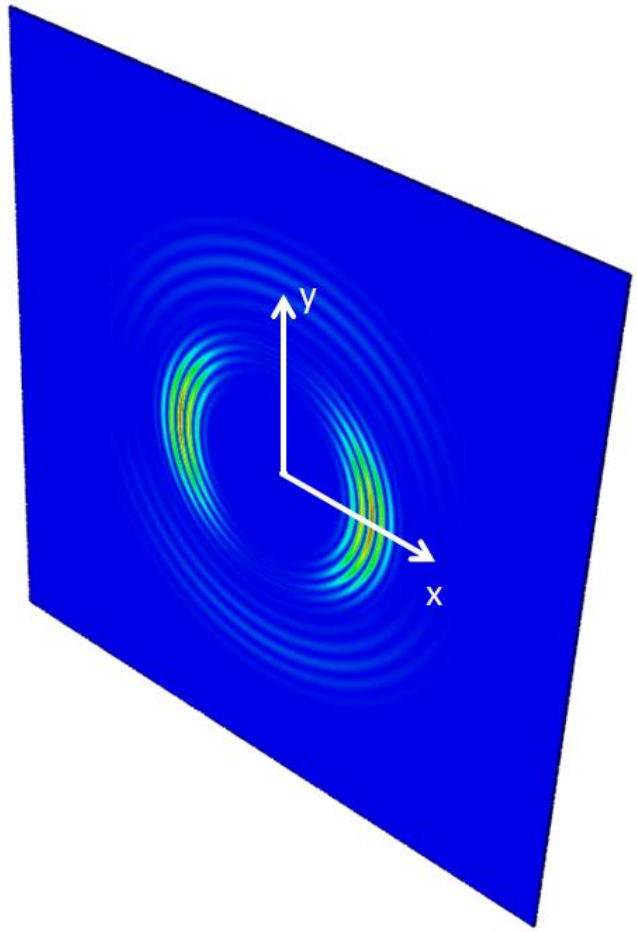

Figure 3.23
FEM simulation result showing longitudinal and shear wave modes radiating from a rectangular source on a flat plate at 106 us. An x-y coordinate system is superimposed on the figure to show the orientation used to discuss this simulation.

As discussed for the straight pipe, when investigating geodesic circles on pipes, the source used here generates both a longitudinal and a shear mode. The longitudinal mode is the faster of the two, and can be seen in Figure 3.23 as polarized in the y-direction. The amplitude of the longitudinal mode drops off as it approaches the plane containing the center of the source and lying orthogonal to the y-direction. Similarly, the shear mode can also be seen in the figure. This mode is polarized to move along the x-direction, and, like the longitudinal mode, drops off in amplitude as it approaches the plane containing the center of the source and lying orthogonal to the x-direction. This behavior is analogous to the behavior of the respective longitudinal and shear modes generated by the source used for the exploration of the geodesic circle on a pipe.

Because of the activation characteristics of the source, a rigid rectangular displacement on the surface of the plate, the resulting energy is not at all circularly symmetric. The source moves only in the y-direction, but guided wave energy leaves the source in all directions. By design, most of the energy will be launched from the long edges of the source and will travel in the x-direction with particle motion in the y-direction. This constitutes a transverse wave, often referred to as a shear wave.

However, the energy launched by the short edges of the sensor will travel in the y-direction with particle motion still in the y-direction. This constitutes a longitudinal wave. Energy that leaves the source in other directions consist of some combination of these wave types. Also, due to the Poisson effect, the corners of the source generate particle motion in the x-direction. This energy will radiate away from the corners and will have the greatest amplitude along the diagonal directions of the plate. Displacement fields demonstrating the y-polarized and x-polarized displacements are given in Figure 3.24 and Figure 3.25 respectively.

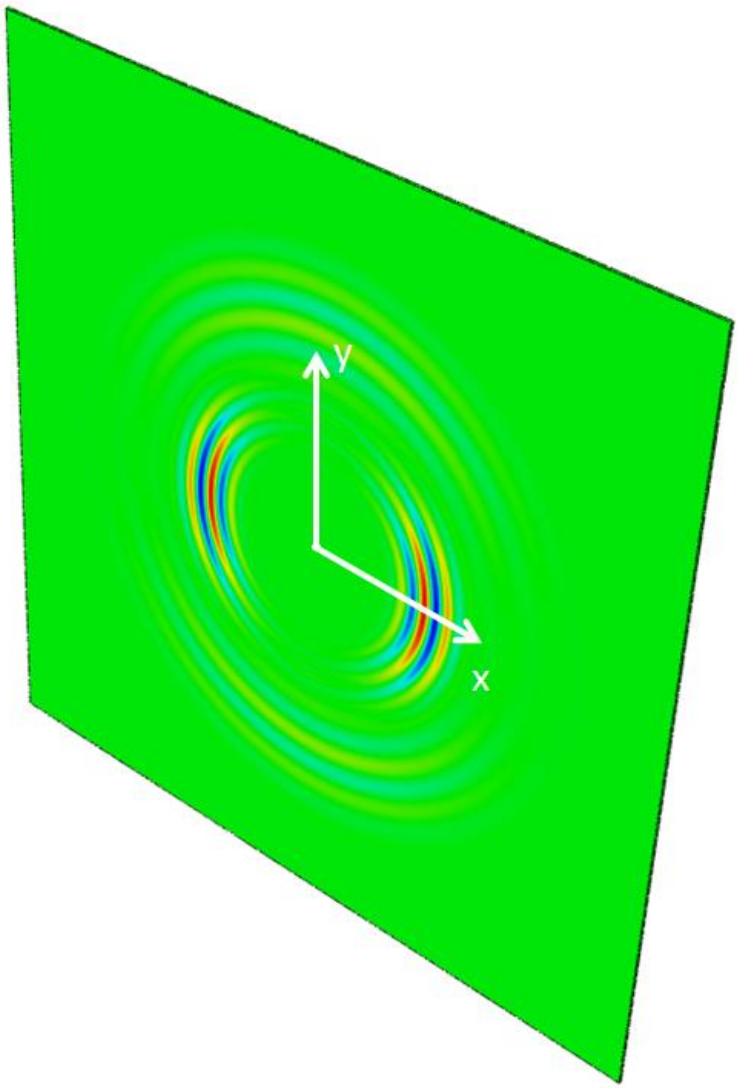

Figure 3.24
Surface displacements polarized in the y-direction after about 106 μs of propagation time from a rectangular source on a flat plate actuated in the y-direction.

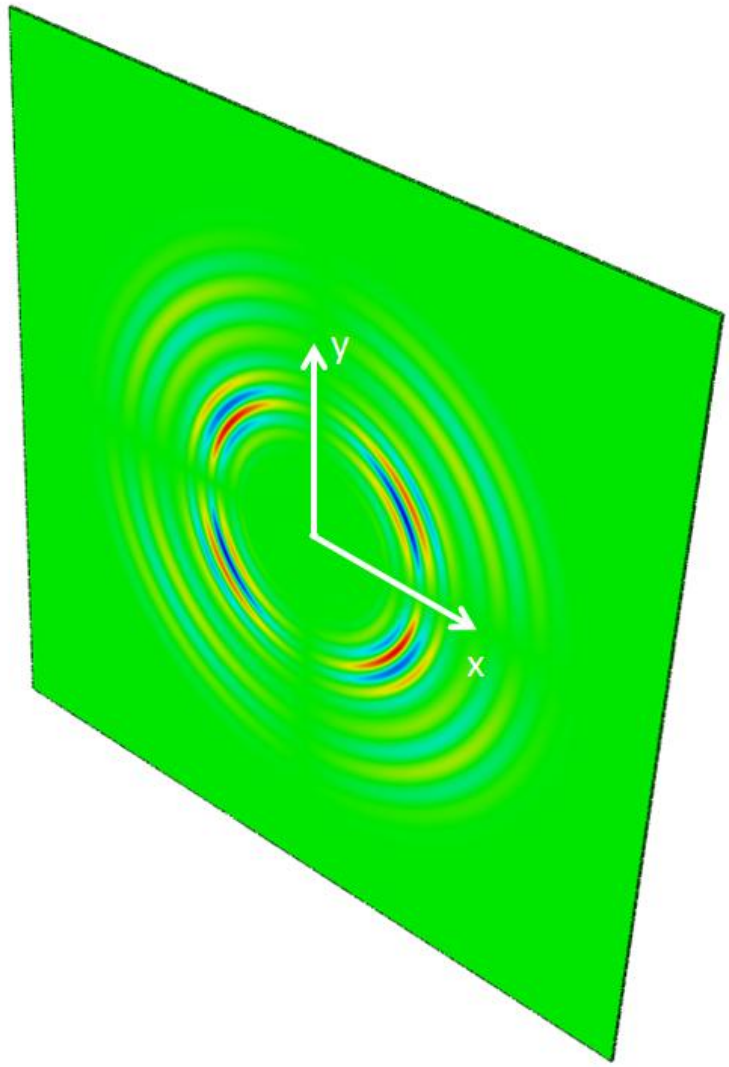

Figure 3.25
Surface displacements polarized in the x-direction after about 106 μs of propagation time from a rectangular source on a flat plate actuated in the y-direction.

Two types of directivity plots of the wave as functions of distance are given in Figures 3.26 through 3.29. In each of these plots, an angle of zero corresponds with the positive x-axis, and an angle of 90 degrees corresponds to the positive y-axis. One of the two types of directivity plot measures only displacements that take place in the y-direction, as this is the type of motion exhibited by the source. An image showing the relevant y-polarized displacement field is shown in Figure 3.24. The image represents the simulation after about 106 μs of propagation time. The results for this directivity function type are given in Figure 3.26 as individual, normalized,

directivity functions representing each of the receiver rings. In Figure 3.27, each of these plots are superimposed on one another in an un-normalized fashion. Those directivity functions that are measured near the source have higher overall amplitudes than ones measured further away from the source. This is because the wave amplitude decreases as the wave spreads away from the source.

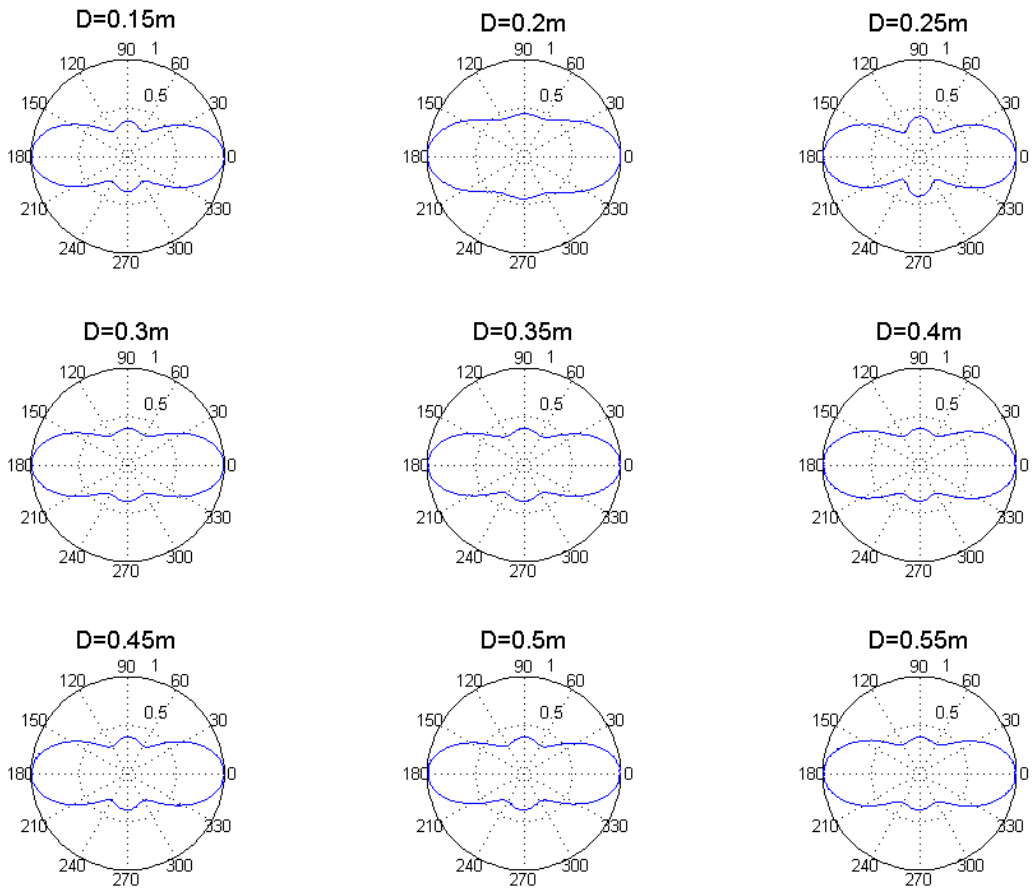

Figure 3.26
Results of an FEM model showing normalized y-displacement directivity properties of a guided wave for various distances of propagation. The functions can be seen to be invariant in shape except for the top center one, at D=0.15m from the source. This discrepancy is caused by the interference of the various wave modes near the source.

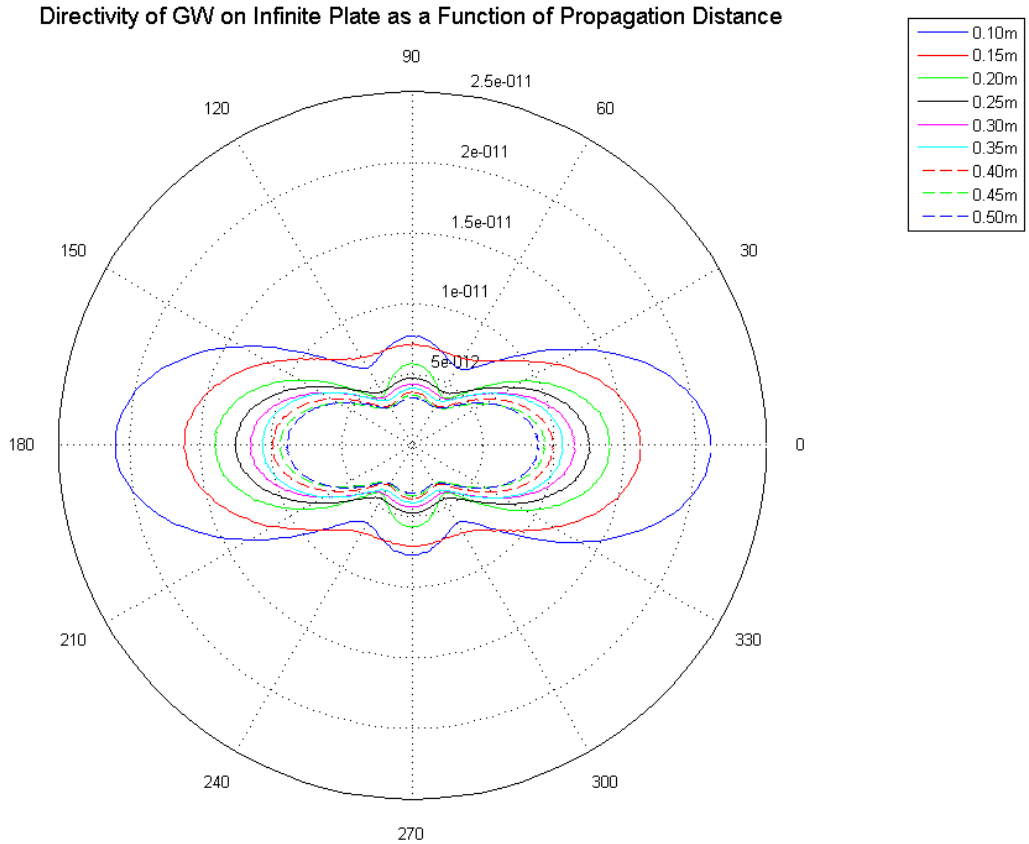

Figure 3.27
Superimposed directivity functions for a point source on a plate. Each directivity function is calculated at a mutually different distance from the source. It is seen that the shape of the directivity functions do not change with this distance, except to shrink in amplitude with distance from the source. The directivity function measured at a distance of 0.15 m from the source is different from the rest. This is due to modal interference near the source as the wave establishes itself.

The directivity functions measured by each of the rings of receivers essentially does not change with distance from the source, other than for some deviations in the shape of the directivity functions near the source. These deviations are due to modal interference as the guided wave establishes itself. The results of the x-polarized directivity functions are given in Figures 3.28 and 3.29. These plots are generated in the same fashion as Figures 3.26 and 3.27, except that they represent motion in the x-direction rather than in the y-direction. An image showing the x-polarized displacement field is given in Figure 3.25. This image represents a snapshot in time after the wave has been propagating for about 106 μs.

Figure 3.28 shows the individual, normalized directivity functions as a function of distance from the source, and Figure 3.29 shows the superposition of each of the directivity functions. Again,

nodes near the source experience greater amplitudes of displacement than do nodes further from the source due to geometric dispersion of the guided wave. Comparison of Figure 3.27 and Figure 3.29 also indicates that the displacement amplitude in the y-direction is slightly more than twice that of the displacement amplitude in the x-direction. No significant distortion is seen in the directivity functions for the displacement polarized in the x-direction, even near the source.

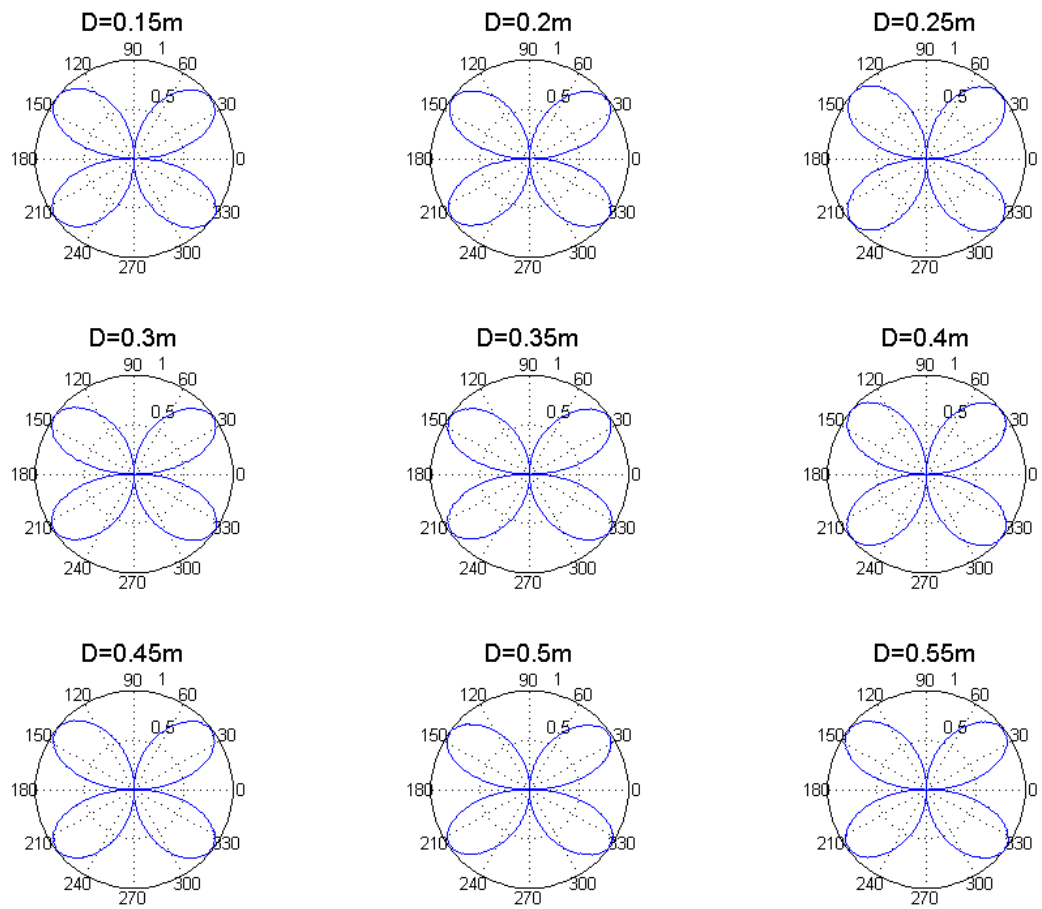

Figure 3.28
Results of an FEM model showing normalized x-displacement directivity properties of a guided wave for various distances of propagation. The functions can be seen to be invariant in shape.

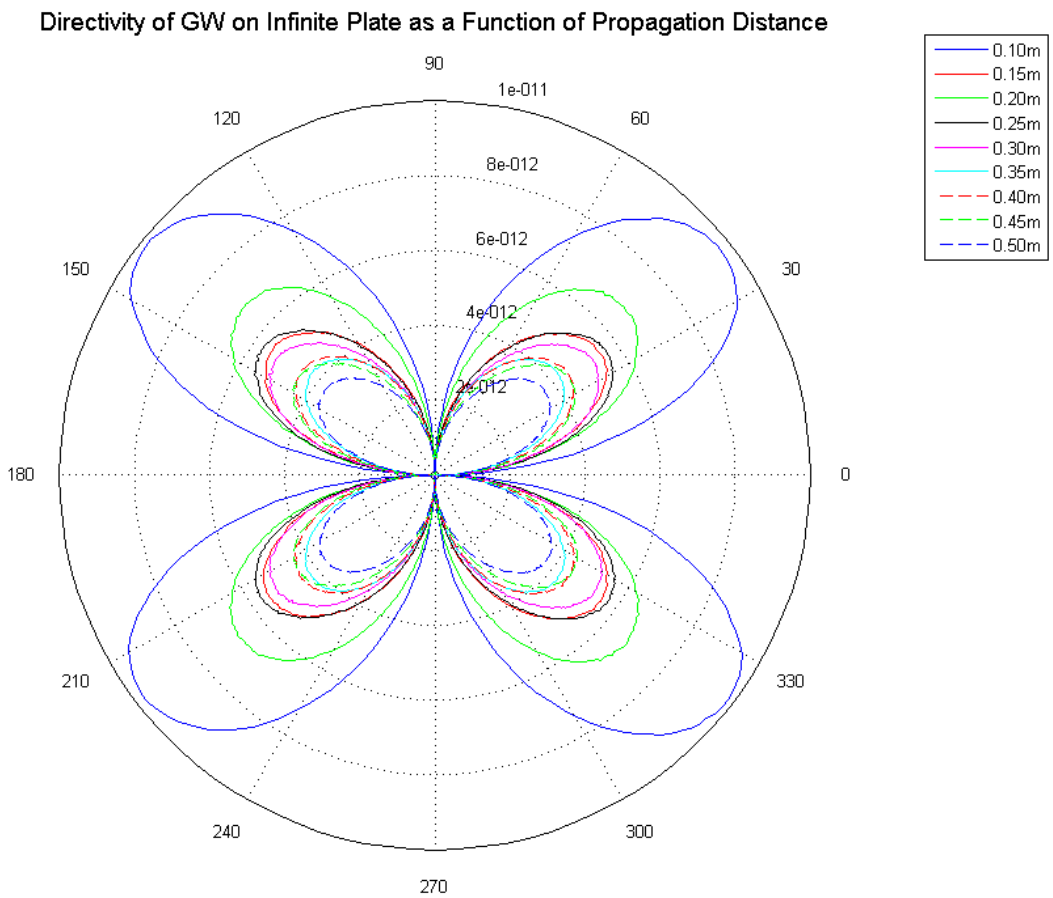

Figure 3.29
Superimposed directivity functions for a finite source on a plate. Each directivity function is calculated at a mutually different distance from the source. It is seen that the shape of the directivity functions do not change with this distance. The directivity functions measured near the source have higher energy amplitudes than those measured further away from the source, but do not change in shape.

Limitations of the Mode Following Approach and Relevant Discussion

An obvious current criticism of this technique is that it builds upon particle mechanics, while actual wave propagation is a different set of mechanics entirely. Beam spreading, for instance does not apply to particle motion, but is important to wave propagation. There are, however, paths forward for addressing such matters. For instance, the directivity function of a loading source can be found by methods of dispersion and elasticity for pipes, as shown in Appendix A or by FEM investigations, as was just discussed. Then as demonstrated in Figure 3.22, the mode tracing methods given here can be used to follow the wave energy moving in different directions from the source across the waveguide. Multiple pathways can be examined in this manner to study the properties of beam spreading. Huygen's principle can also be applied to determine

wave source behavior, at the locations of the source, or at any point along the trajectory of the wave.

Another limitation of this tool is that it does not address such matters as conversion from one mode type to another at abrupt changes in wave impedance. However, that limitation is not unique to this method, as it also applies to traditional methodologies. Such analyses sometimes fall under studies of wave scattering, which is another potential area into which the understanding developed in this work can yield insights.

Also, this method requires the knowledge of either the parametric representation of the waveguide of interest, or knowledge of the surface normals at each arbitrary point. This can lead to experimental error when applying this work to physical specimens in the field, since the geometries of these specimens could be slightly different from the theoretical nominal geometries due to age, use, or manufacturing practices. Such deviations are not possible to control in the field, but sufficiently small deviations from anticipated geometries will not seriously affect the performance of guided wave analysis in practice because of beam spreading and the coarse precision used in guided wave examinations. Additionally, the requirement of some knowledge of the system to be inspected is hardly unusual; it applies to all types of analyses and methods to one extent or another, since there is no technology that can practically inspect any structure without prior knowledge of the structure.

Another facet of this method is the fact that the derivation is based on surfaces, rather than volumes. The conventional approach applies to volumetric methods. However, this dissertation offers evidence that the new methods work well for practical structures such as pipes and bent pipes. For some structures, such as straight pipes and plates, the calculation of the transverse resonance pathway does not depend on the thickness coordinate of the waveguide. Therefore, whether the outer surface is selected as the calculation domain or the inner surface or some other radial coordinate is used, the resulting resonant pathway will be the same. The effect of the thickness of the waveguide is taken into account by the transverse resonance.

On the other hand, it can be seen that the differential equations given in Equation 2.18 and Equation 2.19 do depend on the radial coordinate selected. This means that for pipe elbow geometries, the selection of surface will make a difference to the calculated transverse resonance pathway. For thin waveguides such as practical pipes with elbows, however, modeling a waveguide as a shell does not present a problem, as will be seen in Chapters 4 and 5. It is worth

realizing that even with this approximation, the mode following technique provides a solution to guided wave propagation on an elbow while the conventional methods do not.

Now that the methods of this dissertation have been introduced and substantially validated with theoretical constructions and FEM simulations of guided wave propagation, we turn the idea of mode tracing to some important practical problems surrounding guided wave propagation on pipes with elbows. As we investigate these problems with the new methodology, we will also employ FEM simulations to support the findings of the new approach and bring increased validity to the idea of mode tracing.

Chapter 4 The Elbow as a Transfer Function for Guided Waves

The discussions up until now provide a good background for exploring ways to use this new method for practical and academic uses. The first item to be looked at here is the transfer function of the elbow. In the process of exploring the transfer function of the elbow, we will also see why 45-degree elbows disrupt axi-symmetric guided wave energy more so than do 90-degree elbows. We will also use mode tracing to look at whether we can deterministically discuss the elimination of blind spots in a guided wave examination of a pipe beyond an elbow. As described earlier, the elbow acts as a transfer function to guided wave energy, distorting axi-symmetric energy into a variety of energy packets moving in a number of different directions. When returning through the elbow from a reflector beyond the elbow, the energy is further distorted by the elbow.

The Elbow as a Guided Wave Transfer Function

To study this problem, several sets of mode traces are calculated on a pipe elbow. In each of the following cases, the elbow of interest has a bend radius of 914.4 mm (36 in) and a circumferential diameter of 609.6 mm (24 in). The pipe is schedule 20, and the bend angle of the elbow is 90 degrees. The figures from Figure 4.1 through Figure 4.8 each show a set of 23 mode traces originating from a source at some circumferential location around the elbow. The generalized coordinate θ, the bend angle of the elbow, is used as the abscissa, and the generalized coordinate ϕ, the circumferential coordinate of the pipe, is used as the ordinate for each of the plots. This location is different for the 8 figures, and is equal to $n\pi/4$ radians, where n is a different integer in each figure ranging from 0 to 7.

Each of the mode traces begins at one side of the elbow, or a θ angle of 0 radians, and terminates when it reaches a θ angle of $\pi/2$ radians. In each figure, the bounding launch angle α of the set of traces is $\pm\pi/3$ radians from the axial direction. This angle defined in Figure 1.4, and is measured as the angle on the surface of the elbow from the θ direction to the ϕ direction. Launching a mode trace at an angle of $\pi/2$ radians from the axial direction, or strictly in the ϕ direction, would result in a circumferentially oriented trace that would never reach the far end of the elbow. The color and line style selection used to draw the individual traces on each of the

following figures is arbitrary. These have no meaning, other than to make it easier to differentiate the path of one trace versus another when they cross one another.

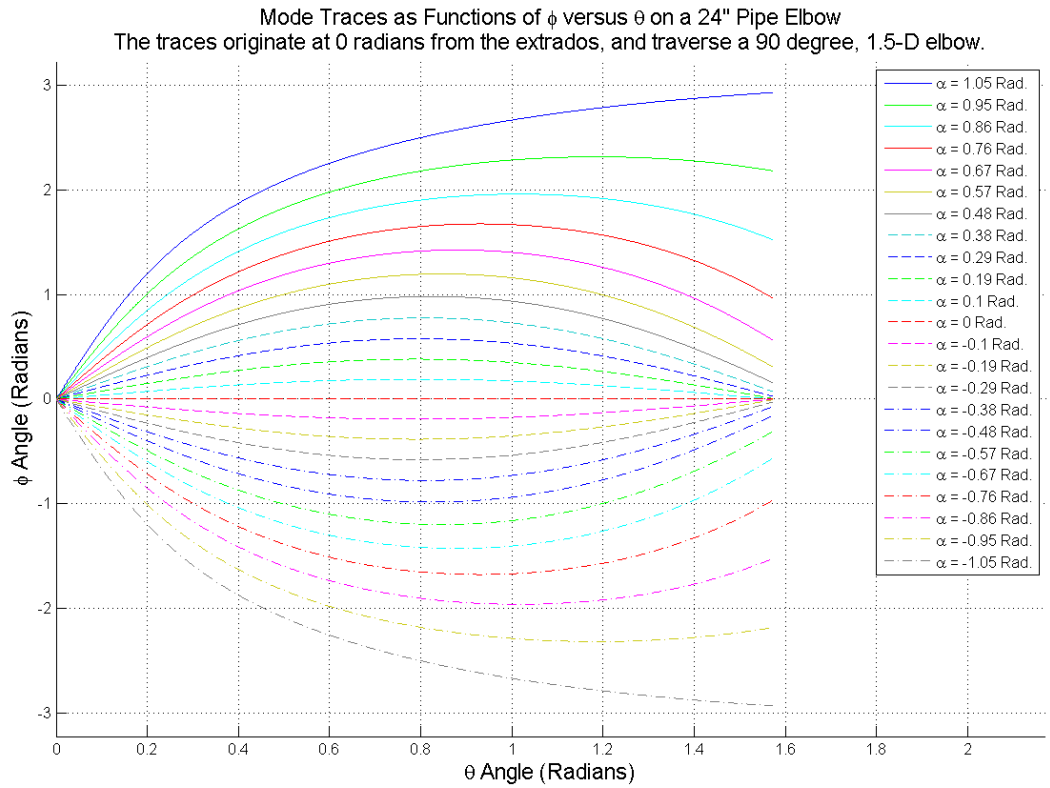

Figure 4.1
Mode traces for several angles from a source circumferentially located 0 radians from the extrados of a 90 degree elbow.

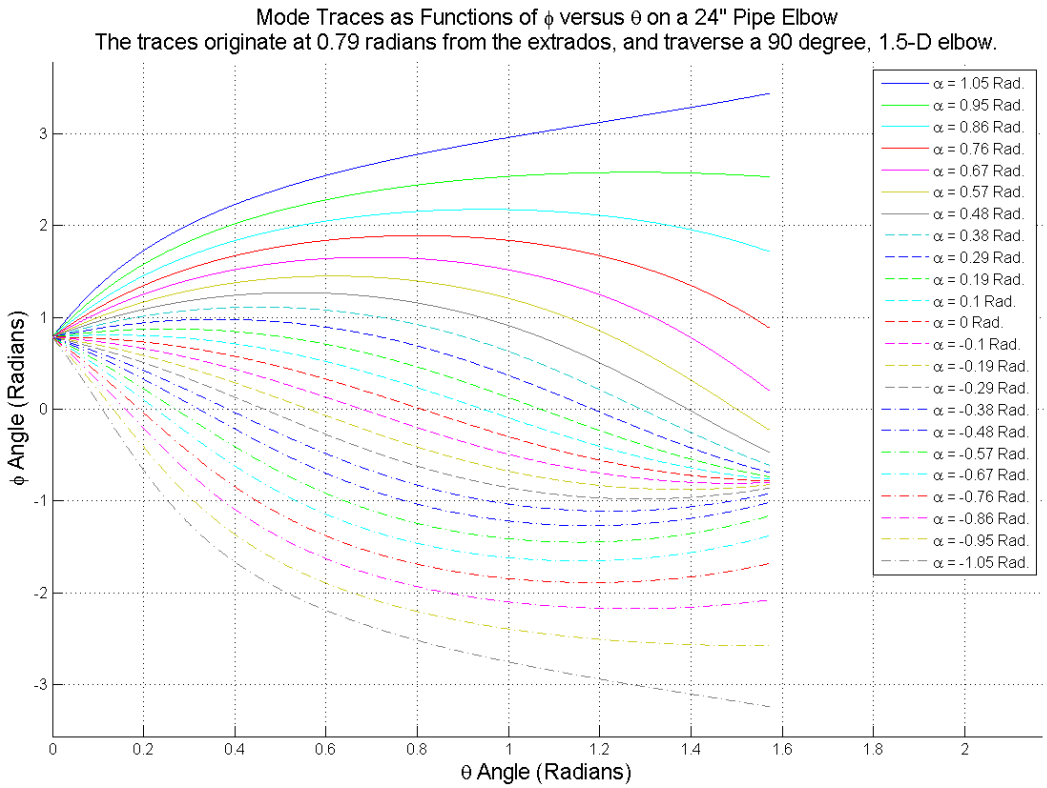

Figure 4.2
Mode traces for several angles from a source circumferentially located $\pi/4$ radians from the extrados of a 90 degree elbow.

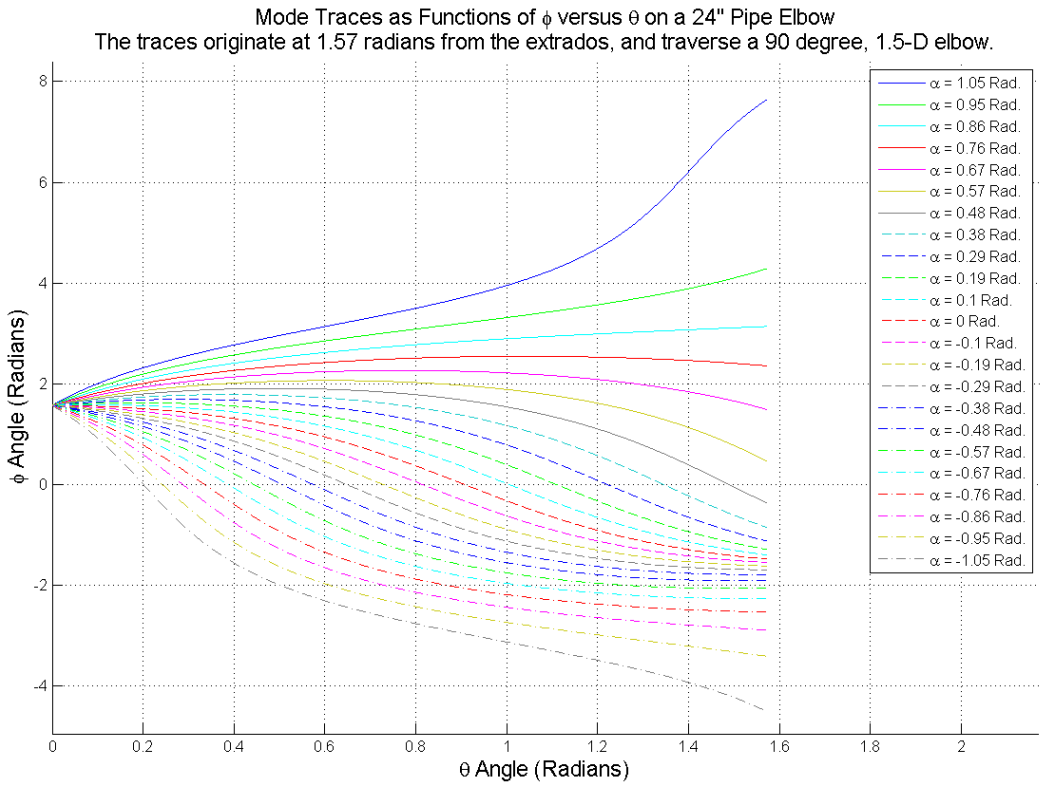

Figure 4.3
Mode traces for several angles from a source circumferentially located $\pi/2$ radians from the extrados of a 90 degree elbow.

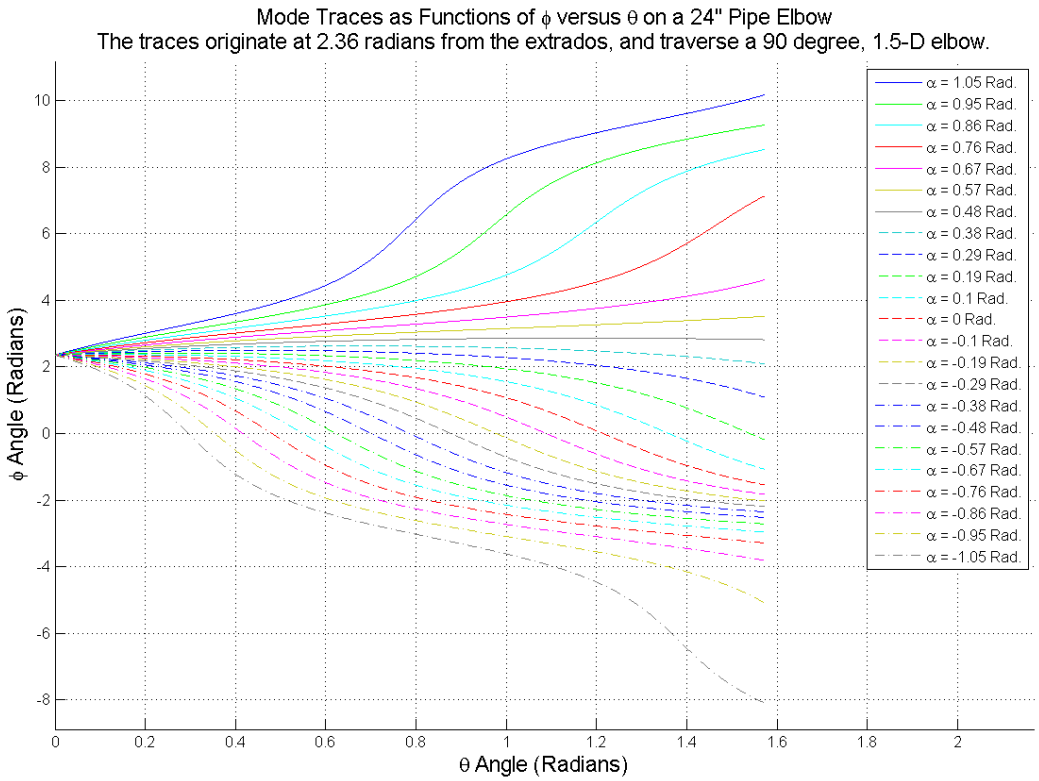

Figure 4.4
Mode traces for several angles from a source circumferentially located 3π/4 radians from the extrados of a 90 degree elbow.

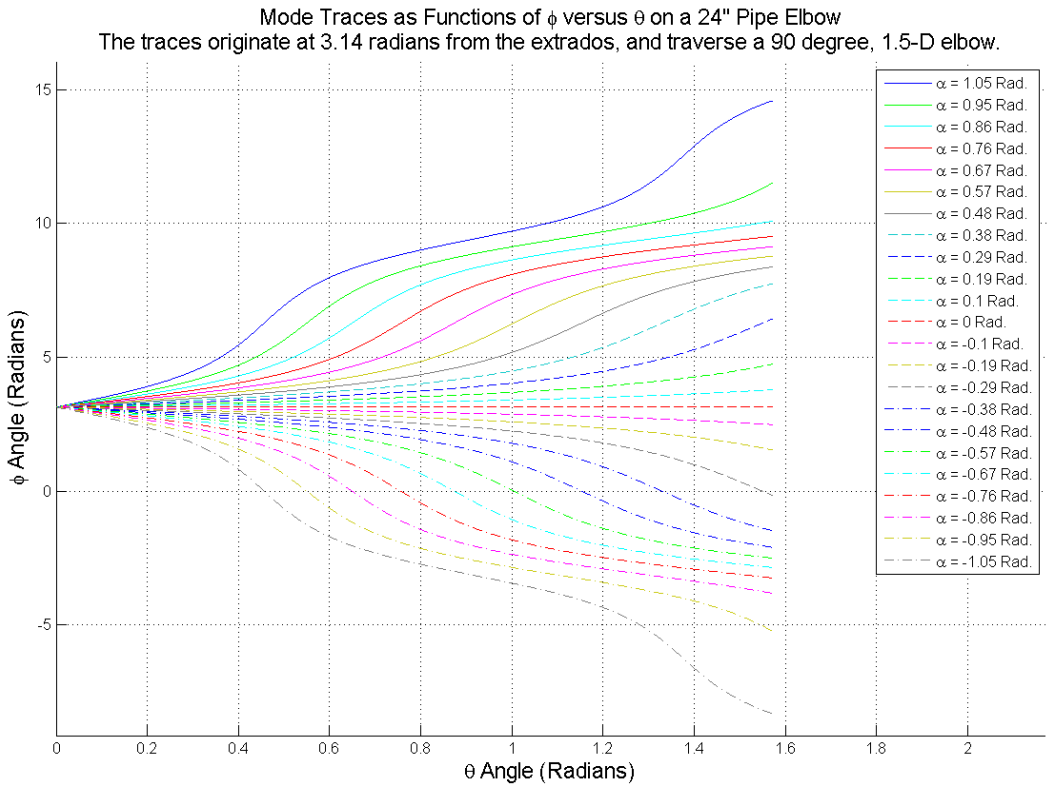

Figure 4.5
Mode traces for several angles from a source circumferentially located π radians from the extrados of a 90 degree elbow.

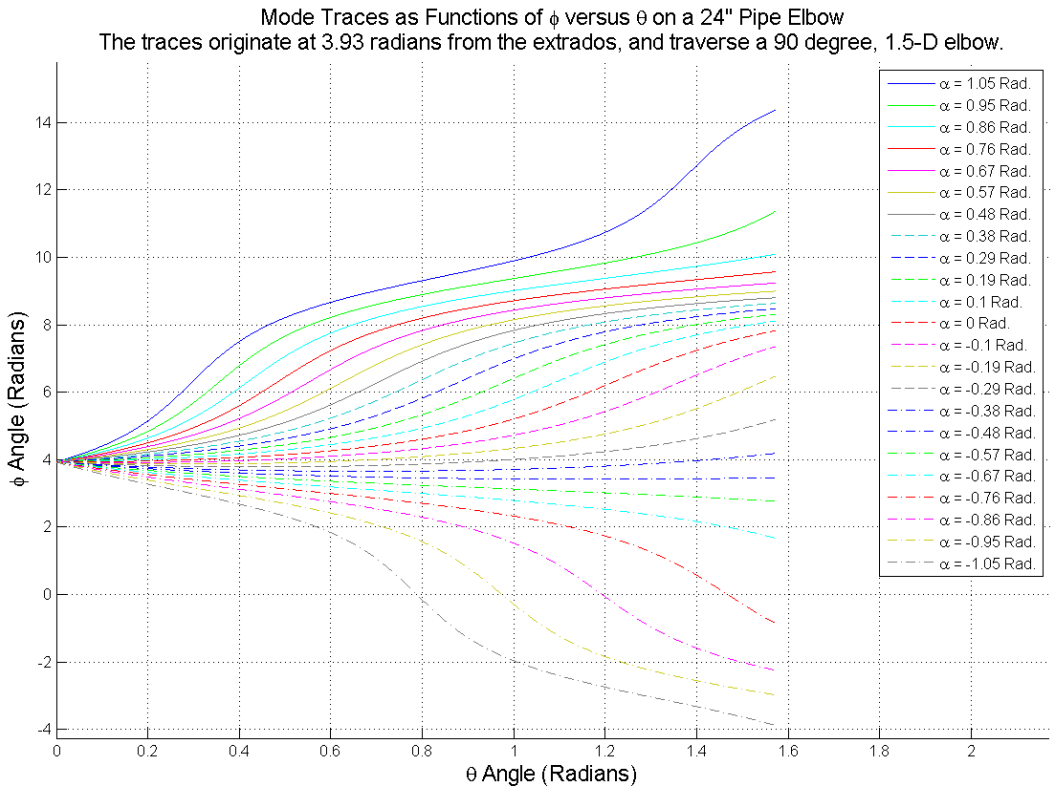

Figure 4.6
Mode traces for several angles from a source circumferentially located 5π/4 radians from the extrados of a 90 degree elbow.

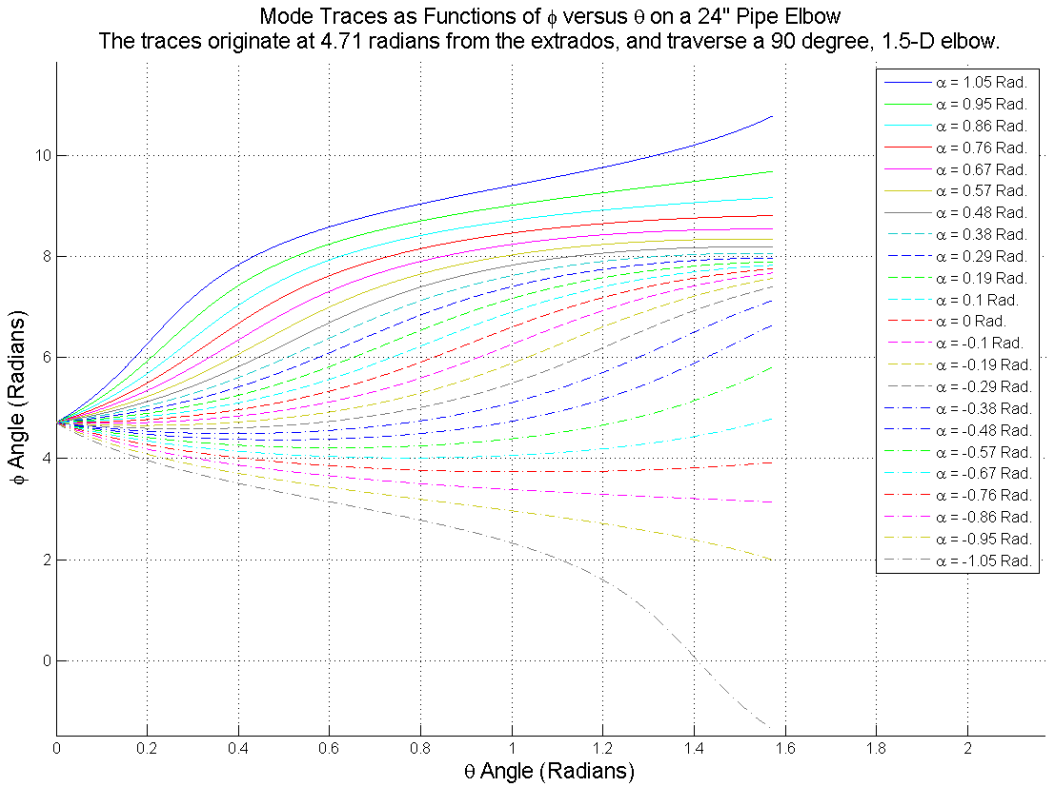

Figure 4.7
Mode traces for several angles from a source circumferentially located 3π/2 radians from the extrados of a 90 degree elbow.

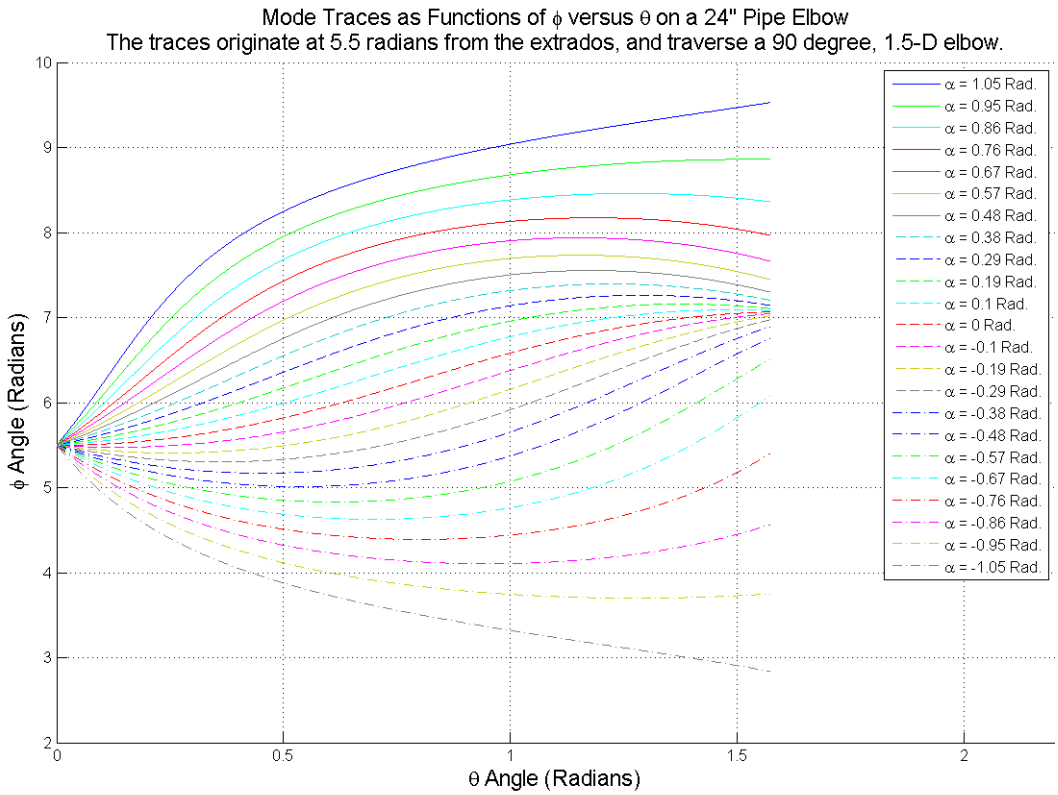

Figure 4.8
Mode traces for several angles from a source circumferentially located $7\pi/4$ radians from the extrados of a 90 degree elbow.

In each of the previous figures, the mode traces have the same set of initial directions other than their starting location. This exercise shows how the elbow changes the direction of a propagating wave as the wave traverses the elbow. It can be seen that launching a wave at different locations around the circumference of the pipe will result in very different wave properties on the far side of the elbow.

For a symmetric point source on a homogeneous, isotropic material, the wave speed will be the same in any direction. Therefore, each wave speed along each mode trace starting from the source will be mutually identical. This means that the portion of the wave moving across each trace will arrive at the other end of the elbow at an independent time, as determined by the length of the trace. Endpoints of the mode traces that are bunched together at the far side of the elbow indicate regions of natural focusing, provided the length of each trace in the bunch is of similar length. More specifically, for focusing to develop, the difference in length of the representative

traces needs to be less than half a wavelength of the energy moving along the trace, or such an amount added to an integer number of wavelengths, provided the integer number is less than the number of cycles used in the excitation of the source.

These figures show how the elbow transfers a guided wave entering the elbow at a particular circumferential location and propagation direction to another circumferential location and propagation direction on the other side of the elbow. The length of each mode trace examined can be readily obtained from the calculations, so the time needed for a wave to traverse the elbow along any pathway is also inherent in the method of mode tracing. The mode tracing calculations can be done for any choice of circumferential position and propagation direction of a wave entering an elbow. Furthermore, the calculations can be done for an elbow of any bend angle θ, any bend radius ρ, and any pipe diameter r. The ability to map guided wave propagation characteristics from one side of the elbow to the other allows us to think of the elbow as a transfer function for guided waves. As is demonstrated in this chapter, the methods introduced by this dissertation describe, for what is thought to be the first time, the transfer function of the elbow.

Following up on the discussions about directional sources and geodesic wave boundary tracing from Chapter 3, we can learn more about the results shown in Figures 4.1 through 4.8. Using the results given in Figure 4.1, for instance, we can look at how parts of a guided wave mode that enters the elbow at the extrados will move across and exit the elbow. If a sensor were placed at the location where the mode traces originate, the extrados, such a sensor may launch energy in many directions simultaneously, and the traces in Figure 4.1 show how components of the energy starting in different directions would travel across the elbow.

If the sensor were a directional sensor, such as discussed earlier, and oriented so as to launch the highest percentage of energy along the extrados line, then the largest amount of energy launched by the sensor would take the path represented by the center magenta line in Figure 4.1. There are three magenta lines in Figure 4.1, and the one referred to here is the dashed one. This line is a flat, horizontal line, and represents the mode trace that was launched with an angle of zero radians from the axial, or θ-direction. There is no circumferential travel indicated by this trace, and energy moving it will stay on the elbow extrados. Most of the energy from the directional sensor in this case, will travel along this line.

Because a real sensor, even a directional one, may also launch energy along directions other than the preferred direction, some energy introduced by the sensor may follow other traces in Figure

4.1. If a directional sensor is used and oriented so that the preferred direction of the sensor launches energy through the extrados, the energy following mode traces with non-zero angles with respect to the θ-direction would have less energy amplitude than the energy following the magenta trace identified in the previous paragraph. At some point, as the angle between the preferred direction of the sensor and the energy launch direction under consideration increases, there may be a small enough amount of energy represented that it can be neglected. The discussion surrounding Figure 3.22 offers additional context on this idea. This means that for practical uses of the elbow transfer function, only a subset of the possible energy propagation directions at the point of entry into the elbow may need to be considered.

Additionally, as the angle between the θ-direction and the energy propagation direction of interest increases, the path length of the energy traversing the elbow can become quite large before the energy reaches the far side of the elbow. For many practical uses, such long energy pathways may be of little to no interest. Furthermore, energy moving along such long pathways across an elbow can be easily differentiated from energy moving along short pathways because there will be a substantial time difference between such portions of energy after leaving the elbow. This can be useful in signal processing and in designing practical tests and experiments.

Another interesting result obtained by examining the elbow as a transfer function is obtained by looking at axi-symmetric inputs impinging on an elbow. Figure 4.9 and Figure 4.10 show these results. Figure 4.9 shows the results as functions of ϕ versus θ, and Figure 4.10 shows the same results plotted as functions of circumferential distance versus axial distance. This latter figure gives a good representation of the actual length of each pathway, since it is a plot of distance rather than of angle. This plot is constructed so that a distance of zero would be aligned with the 45-degree point along the θ-direction. It can be observed from either of these figures that natural focusing is taking place along the extrados side about half-way along the elbow. This can be seen by the increase in density of the traces along the extrados of the elbow about half way along, and the fact that the traces there are of mutually similar length.

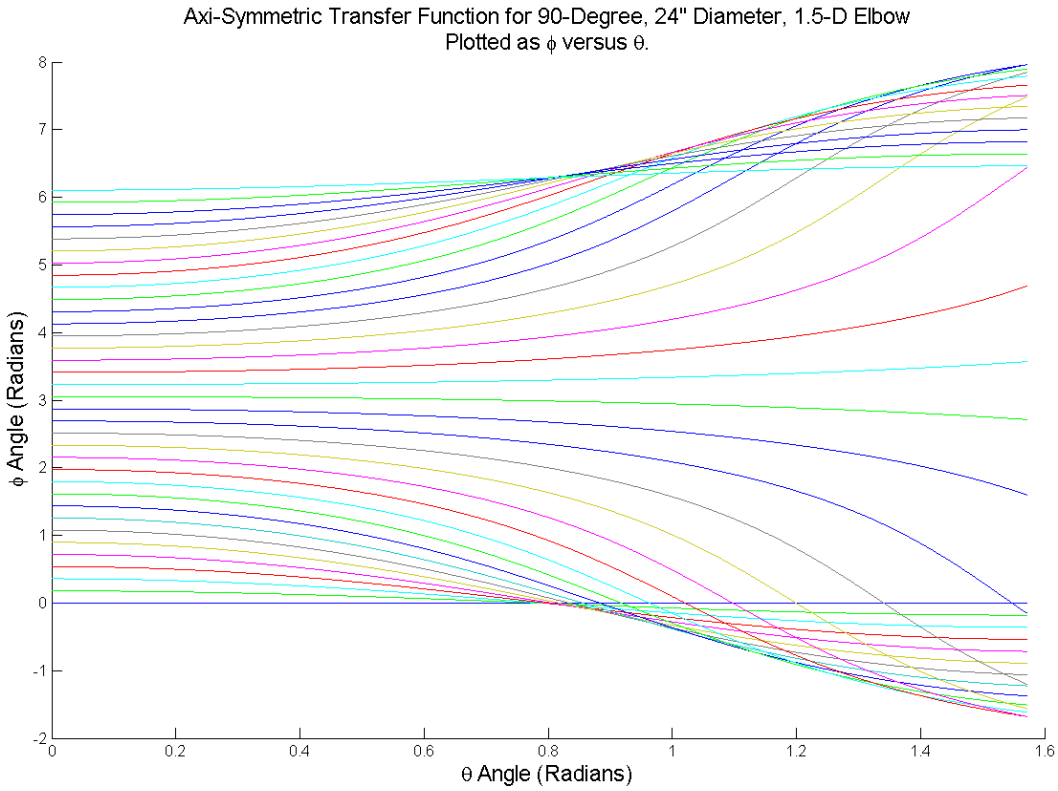

Figure 4.9
Mode tracing results plotted as functions of ϕ versus θ representing axi-symmetric energy impinging on a 90 degree elbow. Natural focusing occurs about midway through the elbow along the extrados.

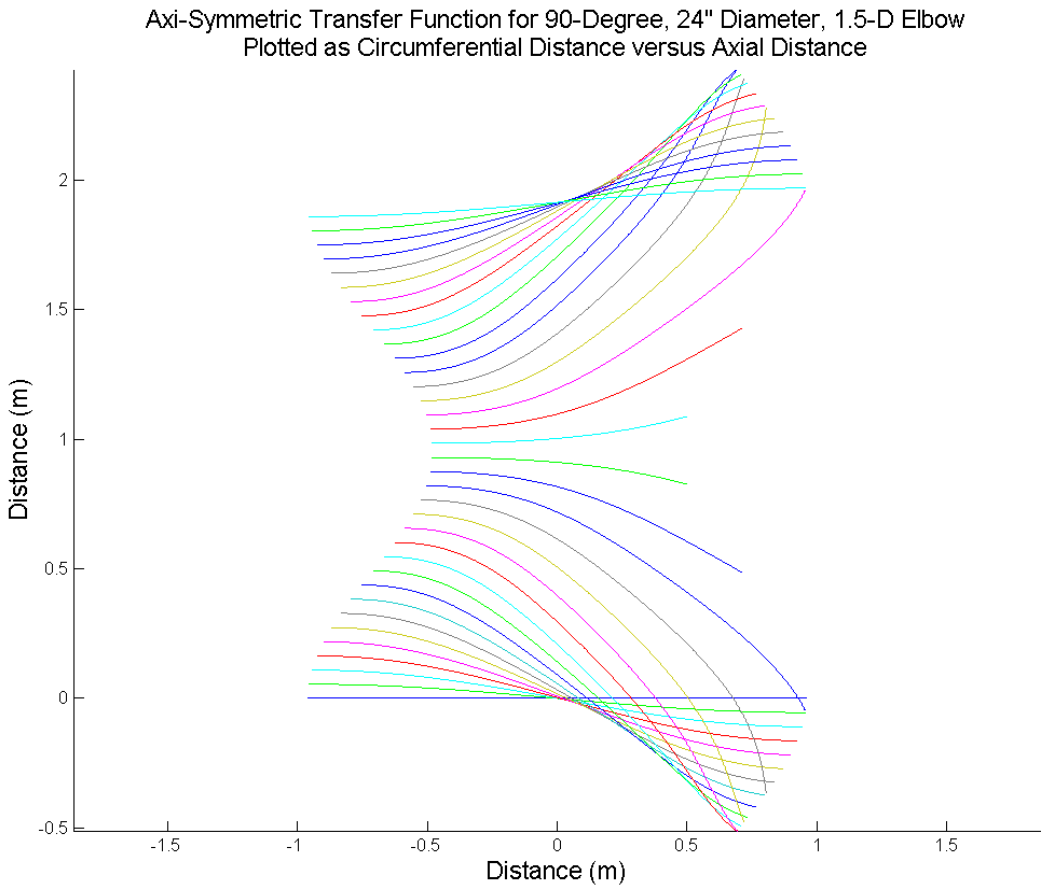

Figure 4.10
Mode tracing results plotted as functions of axial and circumferential distance representing axi-symmetric energy impinging on a 90 degree elbow. Natural focusing occurs about midway through the elbow along the extrados. The traces near the intrados are much shorter than the ones near the extrados.

A lot of the energy on the exit side of the elbow is moving with a velocity direction nearly axi-symmetric for regions near the intrados and extrados. The energy leaving the elbow at other circumferential angles leaves at very different angles. It is this energy exiting the elbow in those different angles that results in the helically-propagating energy along the straight section of pipe following an elbow. Notice also, that a large portion of the energy leaving the elbow is near the extrados. The natural focusing midway around the elbow and regions of energy concentration and de-concentration are marked in Figure 4.11. This figure is otherwise the same as Figure 4.10.

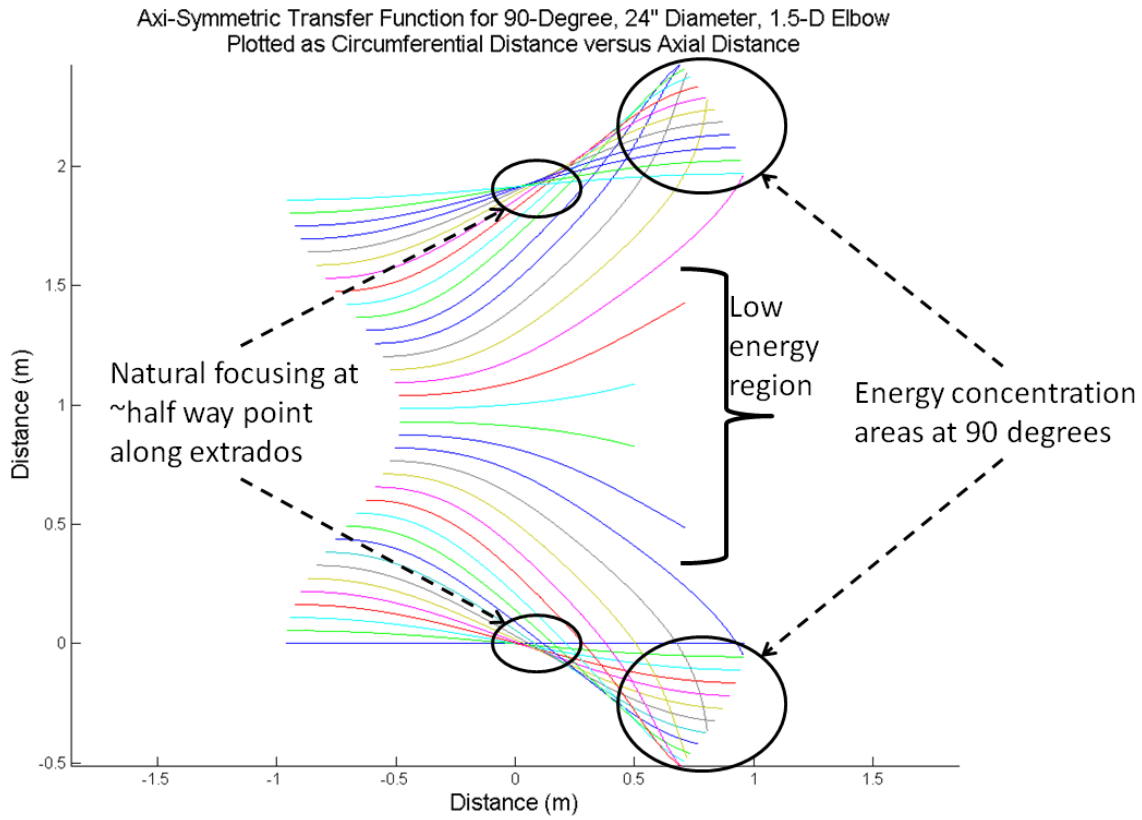

Figure 4.11
Mode tracing results showing axi-symmetric impingement on a 90-degree pipe elbow. Regions of natural focusing, energy concentrations, and a low energy region are identified in the figure. The figure is otherwise the same as Figure 4.10.

In Figure 4.10 it can be noted that the energy exiting the elbow leaves with approximately the same angle as the initial launch angle, except with different sign for those traces that exit the elbow near the extrados. This trend does not continue for traces that exit the elbow at angles near the intrados. A review of the other mode traces in this set shows that energy starting from the extrados side of the elbow tends to be the least distorted and spread out on the other side of the elbow. Energy that started above but near the extrados, however, ends up below the extrados on the other side in this case. The energy originating near the intrados, on the other hand, is the most spread out and distorted on the other side of the elbow. In several of the traces, natural focusing can be observed.

The mode traces on any part of the elbow do not depend on the geometry of other parts of the elbow not already taken in to the computation for the particular trajectory of interest. As a

consequence, shortening the elbow bend angle to, say, 60 degrees will not change the paths of the mode traces between 0 degrees and 60 degrees in any way. Therefore, the results obtained for a 90-degree elbow also contain the results of a 45-degree elbow of the same radii. This means that the natural focusing taking place midway along the extrados of the 90-degree elbow will still happen in a 45-degree elbow, only in the case of the 45-degree elbow, the focusing will occur near the end of the elbow, rather than near the center.

The 45-Degree Elbow Versus the 90-Degree Elbow

As noted in the first glance at Figure 4.10, a good portion of the mode traces exit the 90-degree elbow with a small angle from the θ-direction. This is despite having crossed the extrados part way around the elbow. Halfway along the elbow, at the 45 degree, or $\pi/4$, point on the elbow, however, very few of the traces have tangents close to the axial direction. This actually demonstrates the answer to the question of why 45-degree elbows are so much more disruptive to axi-symmetric guided waves than are 90-degree elbows.

Simply put, axi-symmetric energy tends to focus at just over 45 degrees around the elbow. If allowed to traverse more elbow, the energy straightens out somewhat, and, for a 90 degree elbow, a significant portion of the energy has become axially aligned again, resulting in less disruption in the axi-symmetry of the guided wave. Most of the this energy leaving the 90 degree elbow near the extrados, however, has crossed the extrados along the way and travels on the opposite half of the pipe from which it started.

Examining the 45-degree elbow in the same fashion as was done for the 90-degree elbow will produce the same results as for the 90-degree elbow from 0 degrees to 45 degrees along the elbow bend. However, for the sake of demonstration, such results are given in Figures 4.12 through 4.19. Again, the generalized coordinate θ, the bend angle of the elbow, is used as the abscissa, and the generalized coordinate ϕ, the circumferential coordinate of the pipe, is used as the ordinate for each plot. A look at Figure 4.12 shows that if a point source were used at the beginning of a 45-degree elbow, much of the energy would be axi-symmetric on the far side of the elbow. This is to be expected, after the discussion about the plot showing the axi-symmetric impingement on the 90-degree elbow in Figure 4.10.

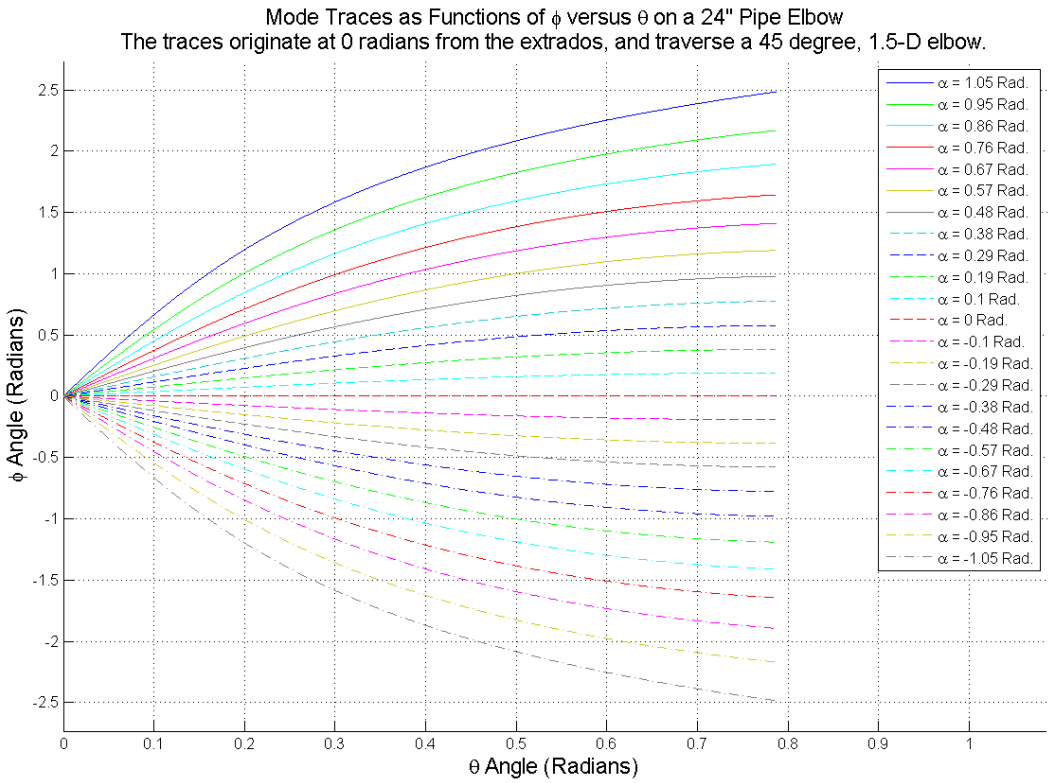

Figure 4.12
Mode traces for several angles from a source circumferentially located 0 radians from the extrados of a 45 degree elbow.

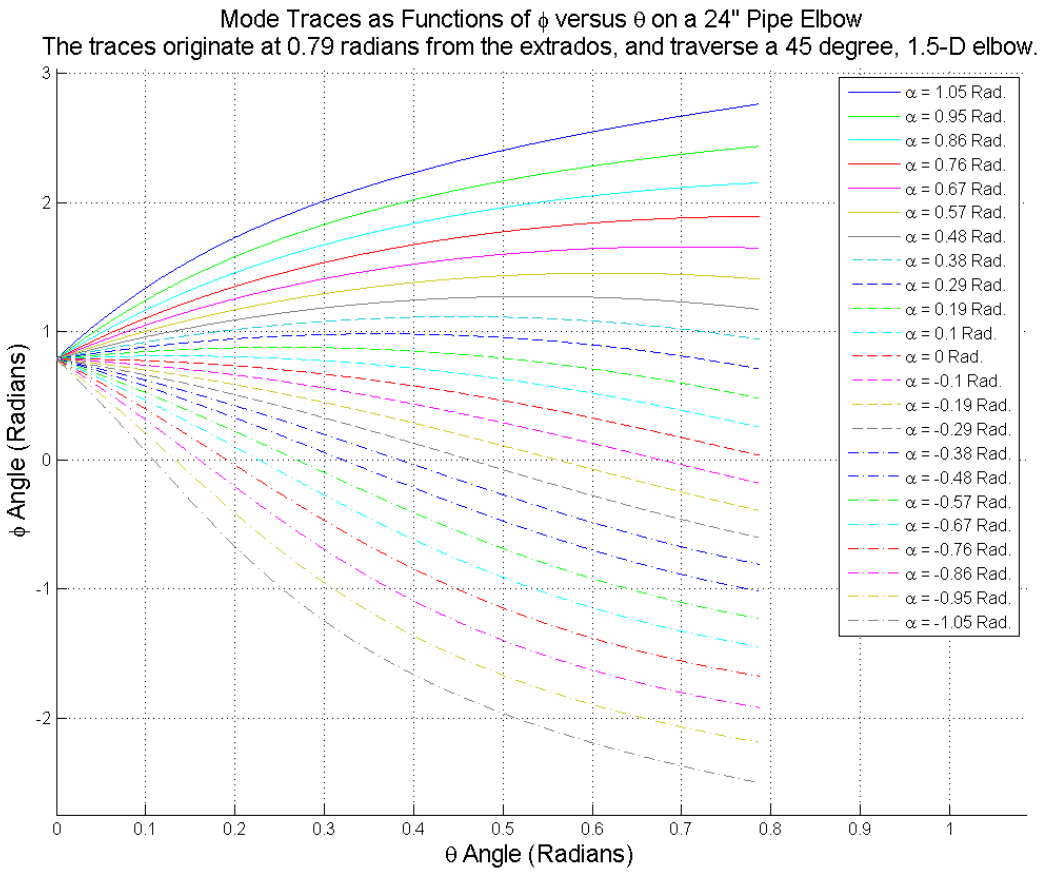

Figure 4.13
Mode traces for several angles from a source circumferentially located π/4 radians from the extrados of a 45 degree elbow.

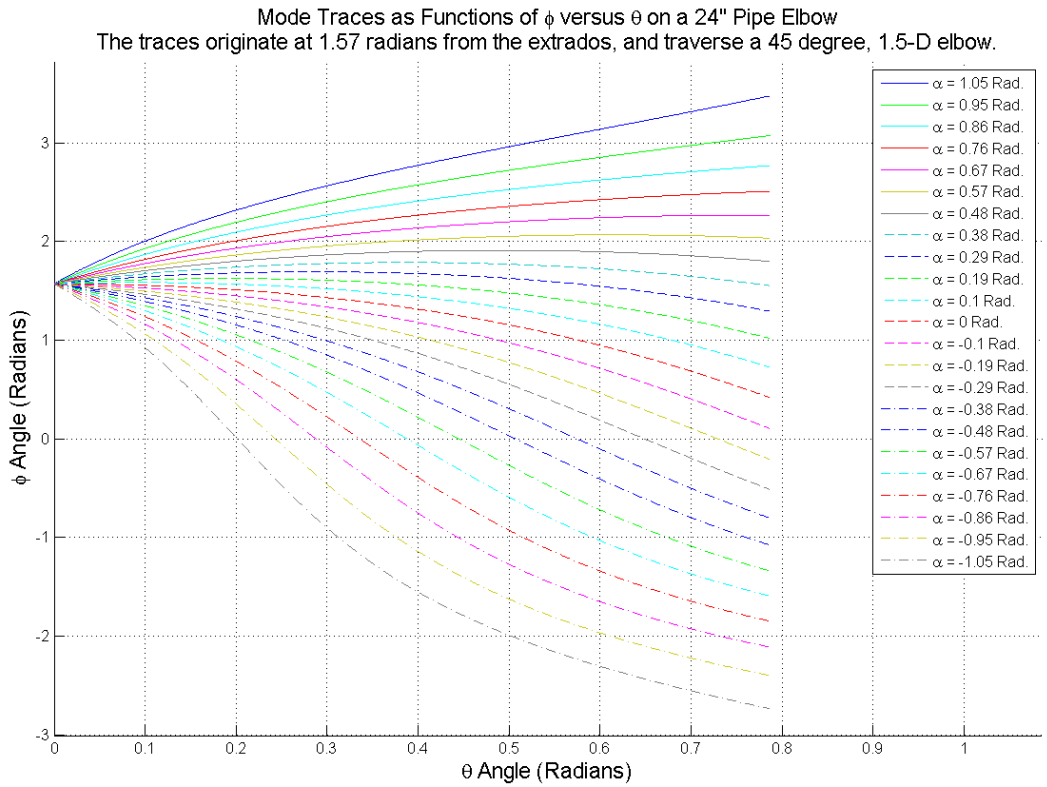

Figure 4.14
Mode traces for several angles from a source circumferentially located $\pi/2$ radians from the extrados of a 45 degree elbow.

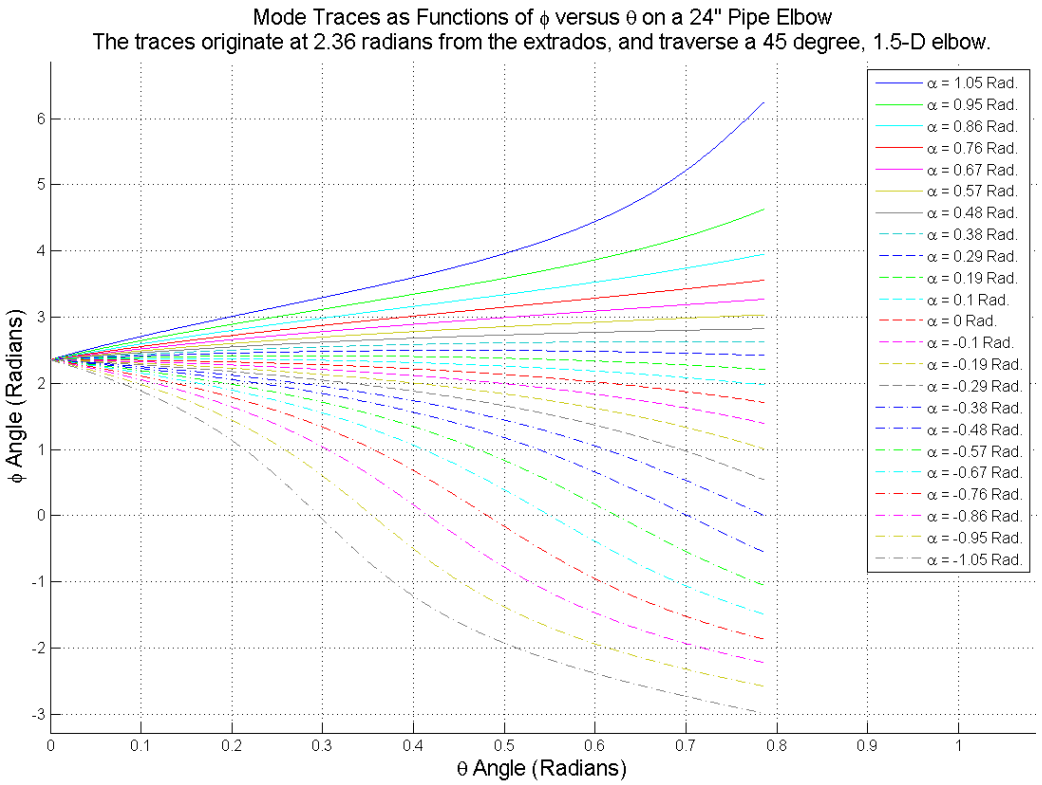

Figure 4.15
Mode traces for several angles from a source circumferentially located 3π/4 radians from the extrados of a 45 degree elbow.

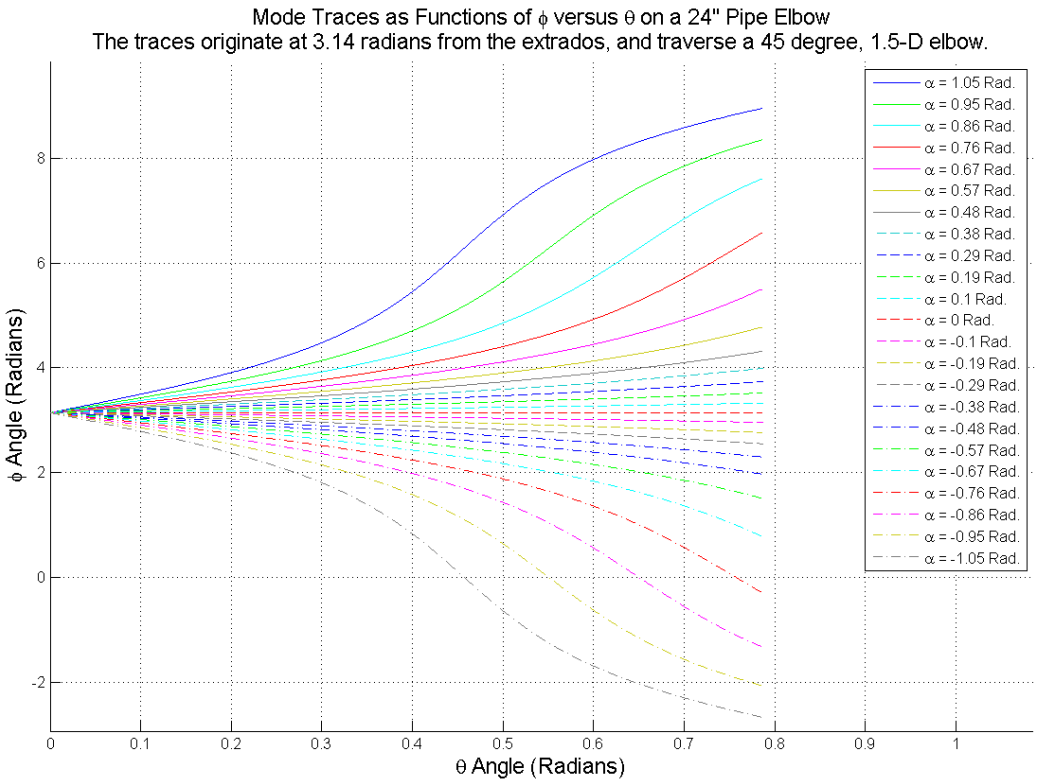

Figure 4.16
Mode traces for several angles from a source circumferentially located π radians from the extrados of a 45 degree elbow.

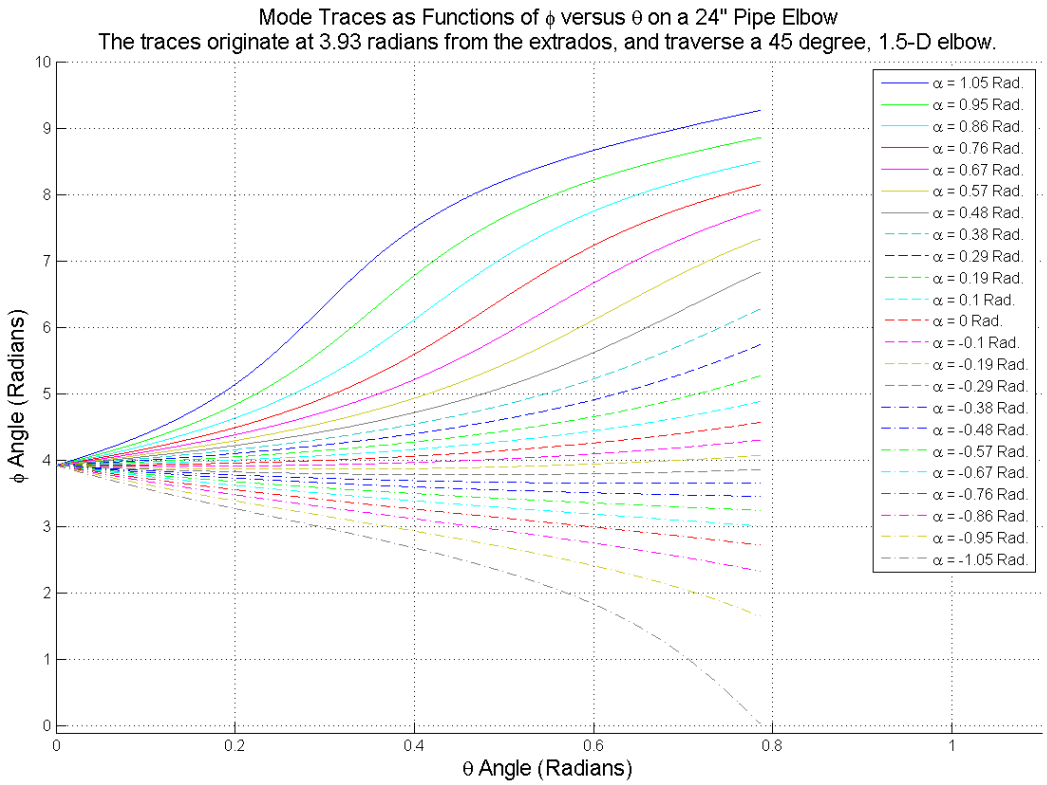

Figure 4.17
Mode traces for several angles from a source circumferentially located 5π/4 radians from the extrados of a 45 degree elbow.

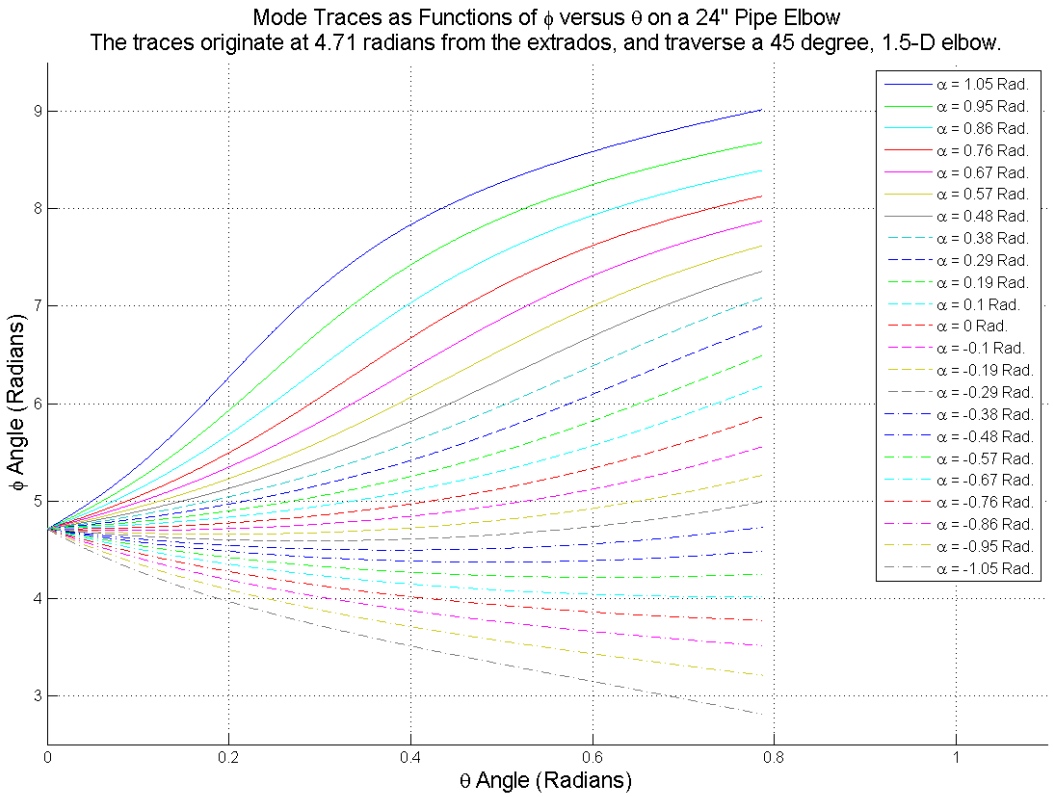

Figure 4.18
Mode traces for several angles from a source circumferentially located 3/2 radians from the extrados of a 45 degree elbow.

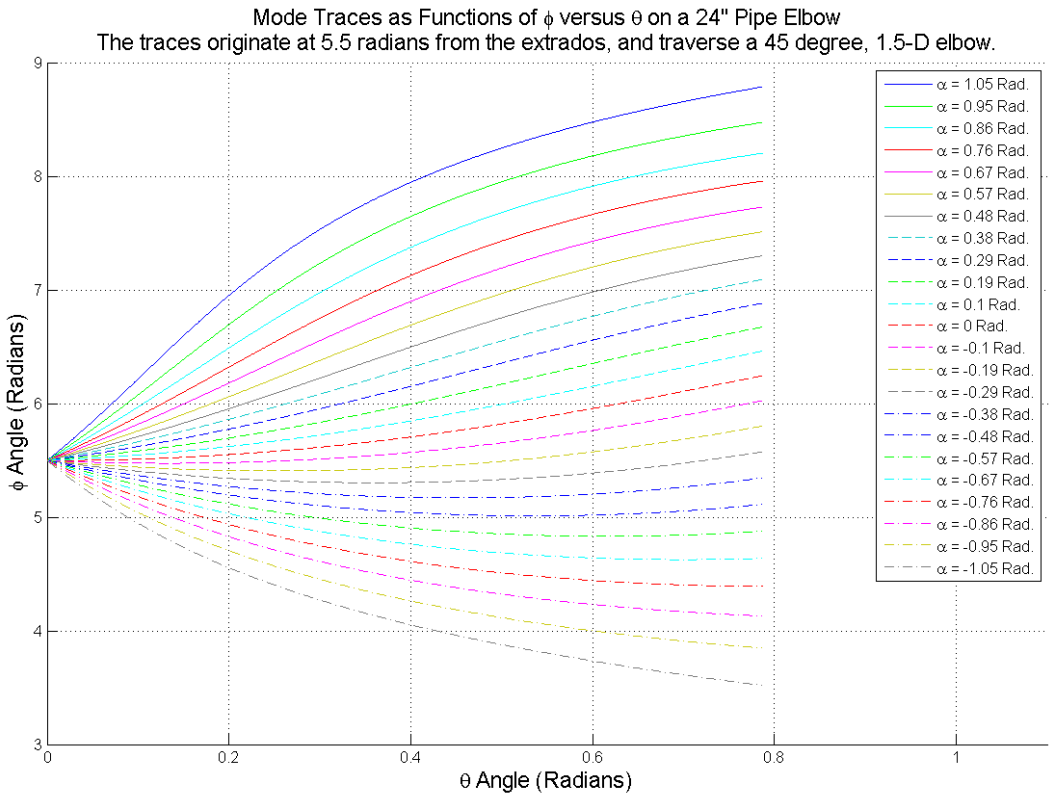

Figure 4.19
Mode traces for several angles from a source circumferentially located 7/4 radians from the extrados of a 45 degree elbow.

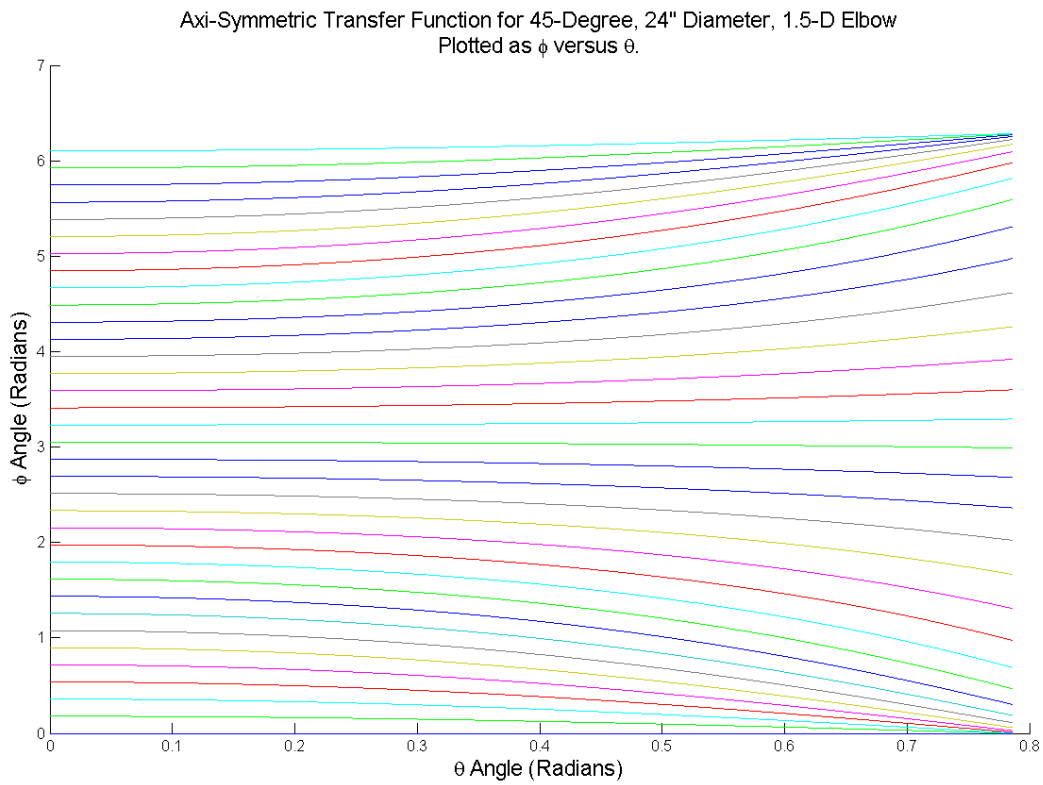

Figure 4.20
Mode tracing results representing axi-symmetric energy impinging on a 45 degree elbow. The trajectories are plotted as ϕ angles versus θ angles.

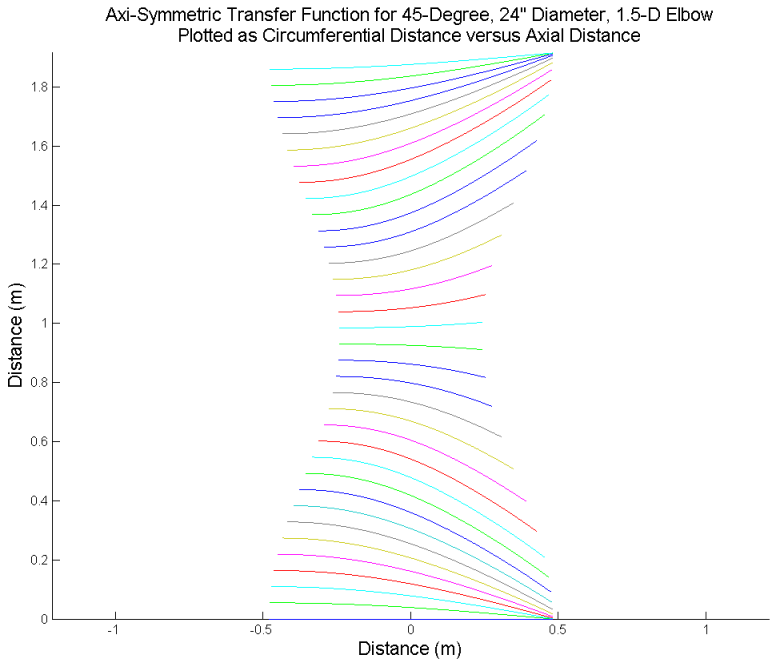

Figure 4.21
Mode tracing results plotted as functions of axial and circumferential distance representing axi-symmetric energy impinging on a 45 degree elbow. Natural focusing occurs towards the end of the elbow along the extrados. The traces near the intrados are significantly shorter than the ones near the extrados.

In contrast to Figure 4.10 showing Mode traces on the 90-degree elbow, the traces in Figure 4.20 show that a very small portion of the waves entering the 45-degree elbow axi-symmetrically actually leave the elbow with tangent directions close to the axial direction. A small amount of energy near the intrados and a small amount near the extrados remains nearly axi-symmetrically aligned throughout the elbow, but the rest of the energy tends to diverge from the intrados and produce what would become helically propagating energy in a straight pipe following a 45-degree elbow.

These figures demonstrate the transfer function of the elbow, which constitutes one of the fundamental questions about guided wave propagation answered by this work. As touched upon earlier, waves of equal speed that impinge simultaneously on the elbow and travel along different mode traces through the elbow, will arrive at the end of the elbow at different times that depend on the length of the respective trajectory followed. This produces effective time delays between the two ends of the elbow for energy starting from different circumferential angles and initial velocity directions but equal temporal coordinates.

The final spacing at the end of the elbow between mode traces that started from mutually adjacent angles at the beginning of the elbow can be used to get information about the energy density reaching the circumference of the elbow exit. The closer the trajectories are bunched together at the elbow exit, the less the energy is spreading between them. Conversely, the further the trajectories are from one another, the more the energy is spreading out between them. This can be used to map the energy density through the elbow and determine the content of the energy around the circumference of the pipe bend.

The observation of natural focusing and defocusing of axi-symmetric energy impinging on an elbow as it travels along the elbow is now demonstrated with a FEM simulation. For this simulation, a torus is modeled. The geometric dimensions of the torus represent the dimensions of a schedule 20 pipe elbow of 0.61 m (24 in) diameter. The bend radius of the torus is 0.91 m (36 in). This geometry is representative of a 1.5-diameter elbow for a 0.61 m (24 in) diameter pipe. In the FEM model, the full torus is used. This would be the effective geometry of a pipe elbow that made a full circle. Of course, such an elbow would not be useful for piping systems, but it is useful for demonstrating guided wave physics in the simulation.

A bi-directionally axi-symmetric source is used to generate guided wave energy in the torus. This is introduced as a ring sensor that excites the torus in a circumferentially polarized torsional fashion. The guided wave energy leaves this ring sensor in both the positive and negative θ-directions. For this model, the waveguide is modeled as being of aluminum, and a 40 kHz wave is generated in the component. The wave is allowed to propagate around the torus, and images showing the wave profile at the source, the 45-degree point around the torus, and the 90-degree point around the torus are shown in Figures 4.22 through 4.26.

At the source, the wave energy is evenly distributed around the circumference of the torus in the ϕ-dimension. This is shown in Figure 4.22, and a top view of the torus representing the same time is shown in Figure 4.23. At the 45-degree point along the θ-direction, as shown in Figure 4.24, the wave is focused at the extrados line, as predicted by the mode tracing algorithms shown previously. Figure 4.25 shows a top view of the torus when the wave is at the 45-degree point around the bend. Finally, at the 90-degree point around the torus in the θ-direction, the wave has mostly de-focused and has recovered a significant percentage of its original axi-symmetric profile. This is shown in Figure 4.26, and the corresponding top view is given in Figure 4.27.

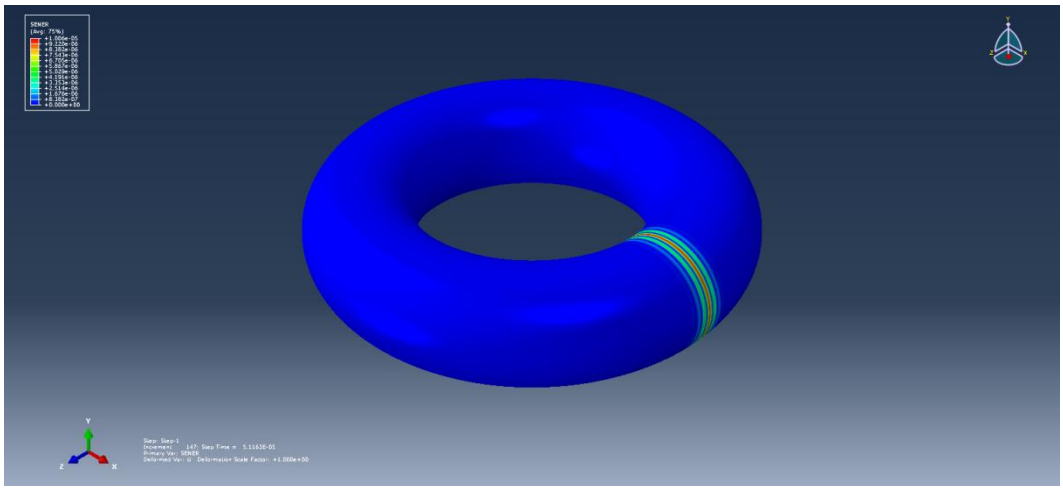

Figure 4.22
Guided wave energy 45.3 μs after launch on a torus. The energy has propagated about a pulse width, and shows little distortion.

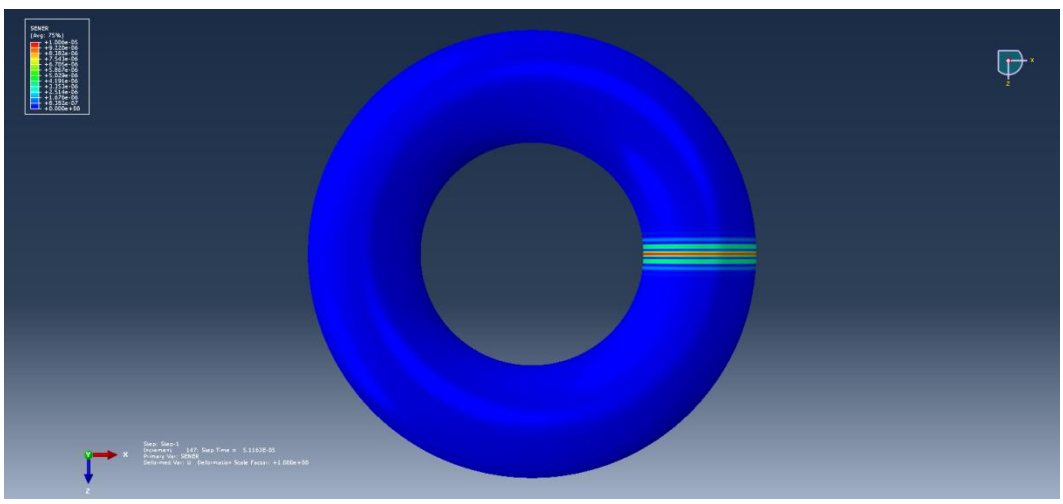

Figure 4.23
Top view of torus corresponding to Figure 4.22. This image shows the guided wave energy when it is at a reference angle of θ = 0 degrees.

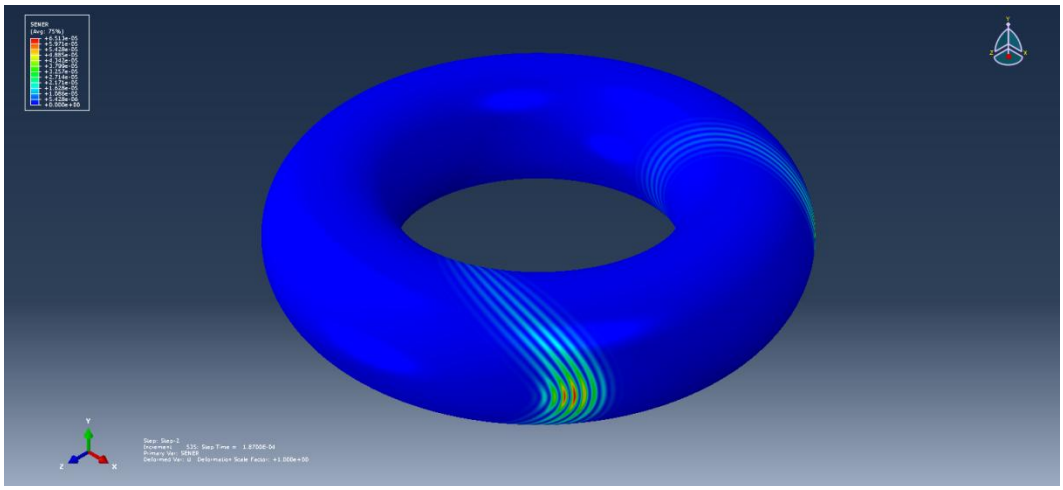

Figure 4.24
Guided wave energy 128 µs after launch on a torus. The energy is about 45 degrees from the launch location and can be seen naturally focusing on the extrados.

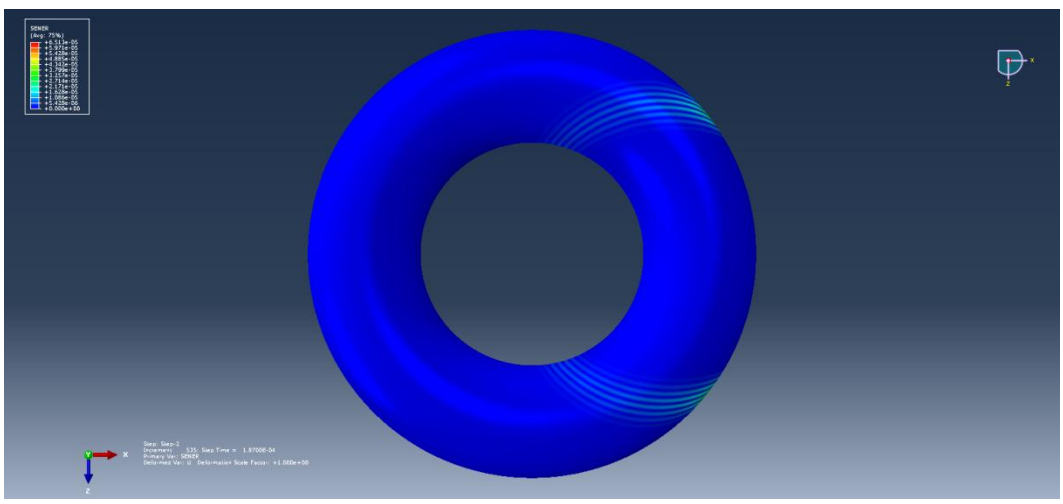

Figure 4.25
Top view of torus corresponding to Figure 4.24. This image shows the guided wave energy when it is at an angle of θ = 45 degrees at the extrados.

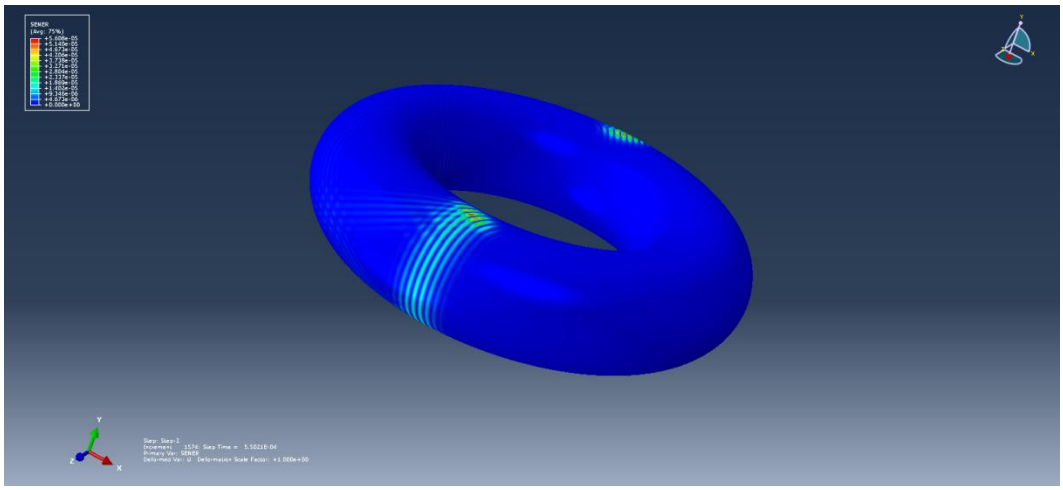

Figure 4.26
Guided wave energy 225 µs after launch on a torus. The energy is about 90 degrees from the launch location. Defocusing can be seen taking place since the wave fronts have started again to resemble axi-symmetric energy for the regions near the extrados.

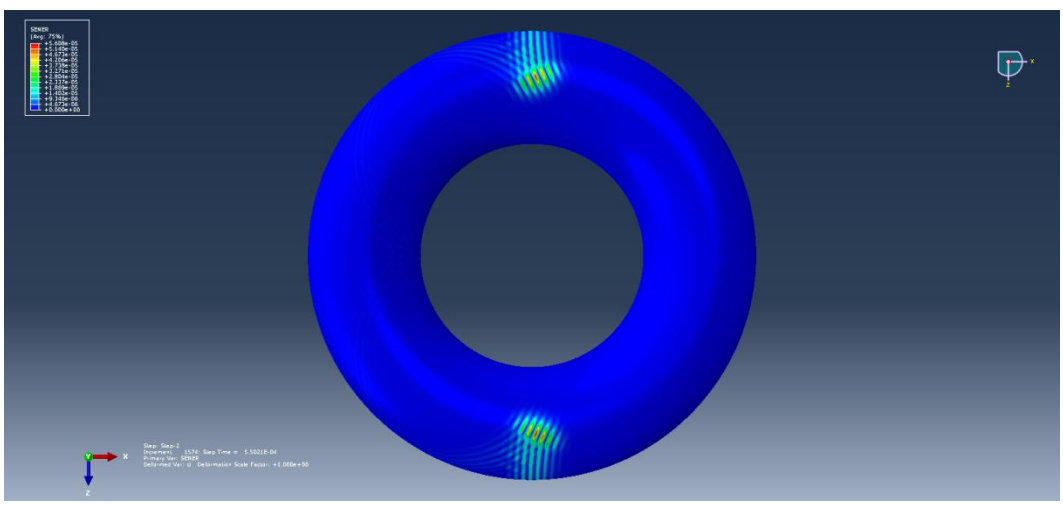

Figure 4.27
Top view of torus corresponding to Figure 4.26. This image shows the guided wave energy when it is at an angle of θ = 90 degrees on the extrados. While much of the extrados region has become defocused, or quasi axi-symmetric, again, a significant portion of the energy is traveling in the ϕ regions of $\pm$ 90 degrees, or $\pm\,\pi/2$ radians. This part of the energy exhibits a helical trajectory. Overall, this wave behavior is as predicted by the results shown in Figure 4.9 and Figure 4.10.

Figure 4.9 and Figure 4.10 show the mode tracing predictions for the wave behavior on the elbow from zero degrees to 90 degrees. Those solutions showed that natural focusing would occur near 45 degrees and partially recover near 90 degrees. Also as predicted by the mode traces, the

energy on the intrados region is much further ahead than the energy on the extrados region because the travel distance is shorter between consecutive θ angles when moving along the intrados than along the extrados. This is clearly seen in the 45 degree case shown in Figure 4.24. The energy moving along the intrados in the 90 degree case in Figure 4.26 is too small in comparison to the energy in the rest of the circumference to render in the image. In the 90 degree case shown in Figure 4.26, the energy near the extrados has become nearly axially aligned as it was when first launched. However, a significant portion of the energy has been concentrated on the top and bottom of the torus, at ϕ angles of $\pm$ 90 degrees. This energy is now moving in a helical fashion. If the model were a 90-degree pipe elbow with a straight leg following the elbow, this energy on the top and bottom of the torus/elbow would produce wave modes that spiral along the straight pipe section following the elbow.

Also, as predicted by the mode tracing, there is much more energy on the extrados side of the torus than there is on the intrados side. The energy in the FEM simulation on the intrados side at the 90-degree point of the torus is so small compared to the energy on the top, bottom, and extrados side, that it is drowned out in the rendering of Figure 4.27.

Wave Coverage Considerations

Next we will apply the idea of mode following to the problem of determining where guided wave energy will travel in the region beyond an elbow. Mode traces can be used to design guided wave excitation parameters to ensure energy coverage of any region of a waveguide that is accessible to the guided wave energy. This is another significant practical contribution of this work. It has been noted in the past that there might be blind spots in a pipeline beyond an elbow. Such blind spots, if they were to exist, would cast doubt on the reliability and applicability of guided wave methods for non-destructive testing of pipelines with elbows. Mode tracing can be used to ensure that any region of interest in a pipeline can be insonified by guided wave energy.

It is easy to realize that there exists some geodesic pathway between any two geometric points in a continuous waveguide. Therefore, we can guarantee that for a continuous waveguide, such as a pipe with one or more elbows, there is some pathway we can launch a guided wave mode along from a source point so that it crosses an arbitrarily selected geometric point elsewhere in the structure. In a structure such as a pipe with one or more elbows, there are many pathways that contain any two arbitrary geometric points in the structure. While conventional geodesic methods

determine the shortest one, other solutions may be of more interest to practical guided wave tests. Mode tracing also allows optimization for guided wave exams by enabling an operator to choose which solution to use among the many that exist.

Even without any real investigation, the problem of deterministically showing where energy will travel in a pipe system with the new methodology is very straightforward. Since mode following offers a way to project where a wave mode will travel, the problem of knowing which locations in a pipe system will be insonified by the energy is immediately answered deterministically. According to the developments of this dissertation, wherever the trajectory describing the transverse resonance pathway lies is where energy from a mode moving along that pathway will go. Because of beam spreading, areas near the pathway will also be insonified, but a consideration need only take into account the energy in the particular transverse resonance pathway of interest for a guided wave operator to know for sure that guided wave energy can be delivered to all regions of interest, provided transducer loading sources can be placed appropriately. This is further explored with mode tracing and FEM calculations next.

Several examples of how mode tracing can be used to determine which areas of a pipe will be insonified are shown in Figures 4.28 through 4.30. The first two of these figures show the trajectory of a subset of the energy resulting from a point source on a bent pipe system. Figure 4.28 illustrates that in some cases, a subset of the energy launched from the point source can have a very different trajectory than a subset of the energy from the same source that was launched in a slightly different direction.

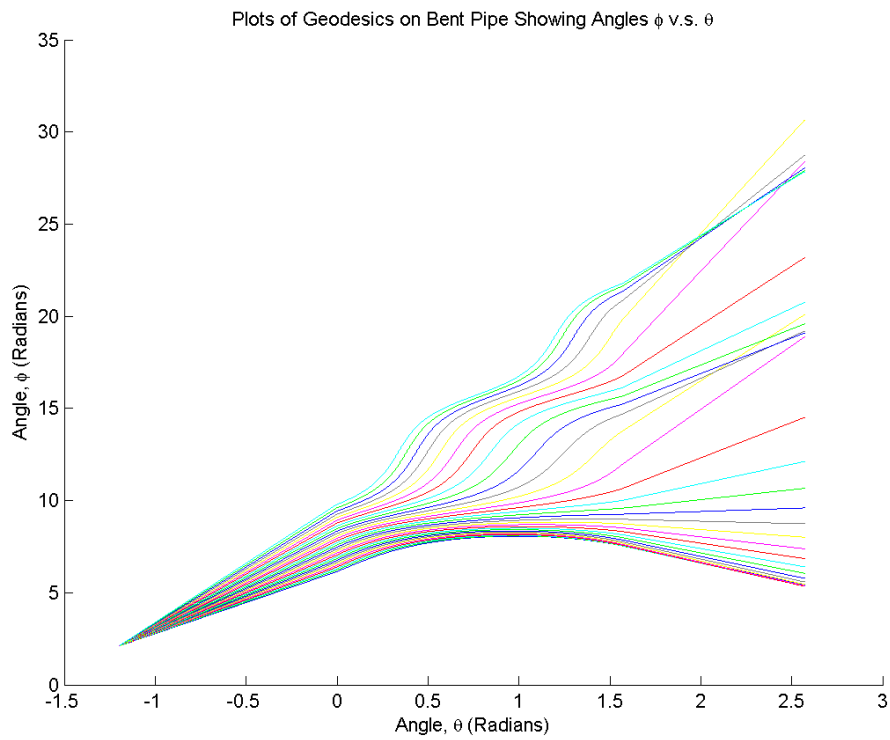

Figure 4.28
Mode tracing from a point source. The point source is located at a ϕ of $2\pi/3$ radians and includes angles α of 0.8 radians to 1.1 radians. The source is located 1.2 m (47.2 in) from an elbow and travels 1 m (39.4 in) axially past the elbow. The energy from this small sector of the source encounters a beam spreading of about 25 radians around the circumference of the pipe in this distance.

For the results shown in Figure 4.28, the point source was placed in a section of straight pipe at a ϕ angle of $2\pi/3$ radians, and a distance of 1.2 m (47.2 in) ahead of an elbow connected to the straight pipe. The energy was tracked until it traversed the elbow and reached a distance of 1m (39.4 in) in another section of straight pipe beyond the elbow. The figure shows that the energy that initially started moving from the point source at angles between $\alpha = 0.8$ radians to $\alpha = 1.1$ radians ends up covering a circumferential span of about 25 radians by the time it gets 1 m (39.4 in) past the elbow. This means wave energy moving in this location and direction in the pipe system becomes very dispersed as it propagates.

On the other hand, Figure 4.29 shows a case where a relatively large portion of energy leaving a point source does not disperse much as it travels through the pipe system. In this case, the point source is located at 0.6 m (23.6 in) ahead of the elbow, and the energy being tracked lies between $\alpha = 0.55$ radians and $\alpha = 0.95$ radians. The point source is kept at a ϕ angle of $2\pi/3$ radians. The

tracked portion of energy again travels 1 m (39.4 in) past the elbow, but this time, it only spreads about 2.5 radians as it moves through the pipe system, even though the range of initial angles is greater than for the results shown in Figure 4.28.

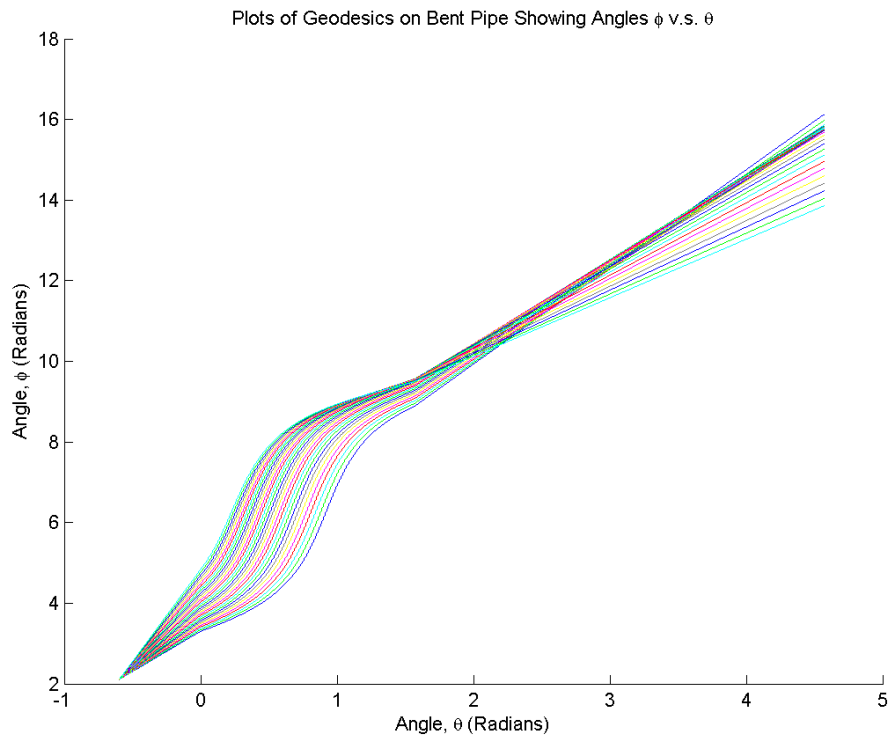

Figure 4.29
Mode tracing from a point source. The point source is located at a ϕ of $2\pi/3$ radians and includes angles α of 0.55 radians to 0.95 radians. The source is located 0.6 m (23.6 in) from an elbow and travels 1 m (39.4 in) axially past the elbow. The energy from this sector of the source encounters a beam spreading of about 2.5 radians around the circumference of the pipe in this distance.

Figure 4.30 shows yet another interesting case where a directional sensor is used. A directional sensor, unlike a point source, exhibits a preferred launch direction for the energy. While for a practical directional sensor, some energy will move in directions other than the preferred direction, most of the energy will leave the sensor in the preferred direction. The greater the percentage of energy that leaves a sensor in a preferred direction, the more directional the sensor is considered to be. Symmetric point sensors, as used at times in this dissertation, are not directional at all, since they launch energy uniformly in all directions.

For this experiment, though, the directional sensor launches energy at an α angle of $\pi/4$ radians from a circumferential location ϕ of 2π/3 radians, and an axial distance of 1 m (39.4 in) ahead of an elbow. Only the energy that leaves the sensor at the preferred angle of $\pi/4$ radians is used for this result. The energy is tracked until it reaches a distance of 0.5 m (19.8 in) past the elbow. The energy is seen to focus part way through the elbow. This source and pipe system is also modeled with a FEM simulation and discussed following the results of the mode tracing algorithm.

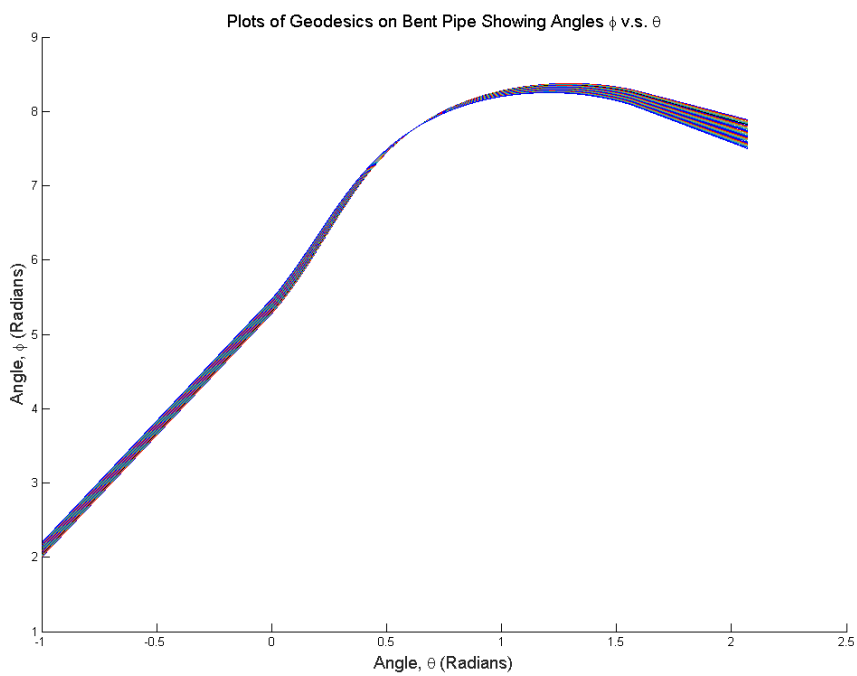

Figure 4.30
Mode tracing from a directional source. The source is centered at a ϕ of 2π/3 radians and is π/10 radians in width. the directional source launches each trace at an angle α of 0.7243 radians. The source is located 1 m (39.4 in) from an elbow and travels to a final position of 0.5 m (19.8 in) axially past the elbow. The energy from this source encounters little beam spreading around the circumference of the pipe in this distance.

The test parameters used to generate Figure 4.30 are also modeled in a FEM simulation to compare a complex and innovative result from mode tracing with numerical guided wave propagation tests. For this model, a 48 kHz wave is launched with an angle of $\pi/4$ radians from the θ-direction. A directional source that emulated the source used in generating Figure 4.30.

The edges of the model are damped to simulate infinite lengths of pipe on either side of the elbow. Several images of the simulation results at different times after launch are shown in Figure 4.31 through 4.34. These figures show the wave energy in the pipe at 210 μs, 990 μs, 1.21 ms, and 1.41 ms respectively after the wave was launched. After the analysis was completed, a field frame was created showing the maximum values of the magnitude of the displacement over all time. This frame is given in Figure 4.35. For comparison, the mode traces of Figure 4.30 have been mapped to three-dimensional space and have been superimposed over a drawing of the bent pipe used in the FEM model. This plot is shown in Figure 4.36 and does not include the damped edges used in the FEM simulation.

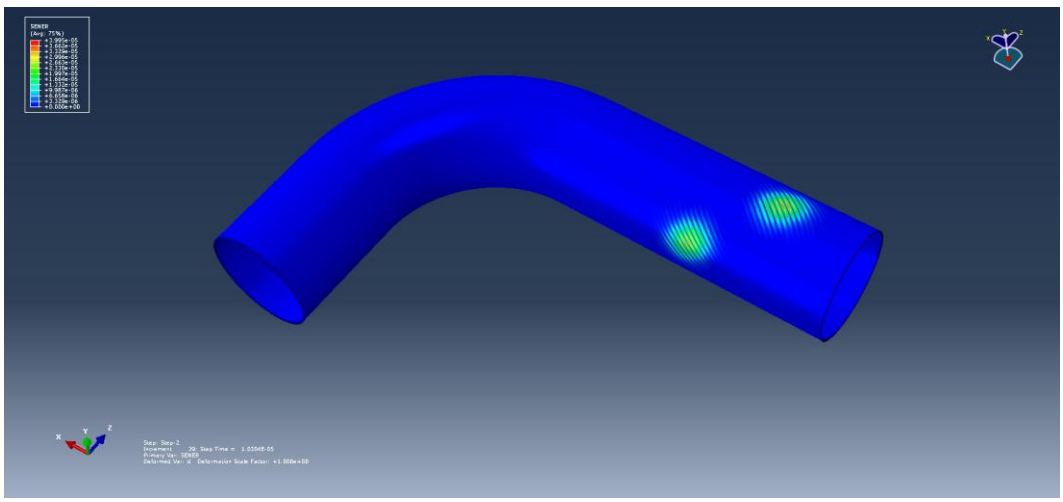

Figure 4.31
Wave mode propagating on a 0.61 m (24 in) diameter pipe with an elbow after 0.21 ms of propagation time. The source is a directional sensor that launches energy at an angle of $\pi/4$ radians from the axial direction of the pipe. Both ends of the pipe are damped so as to reduce guided wave reflection amplitudes from the pipe ends.

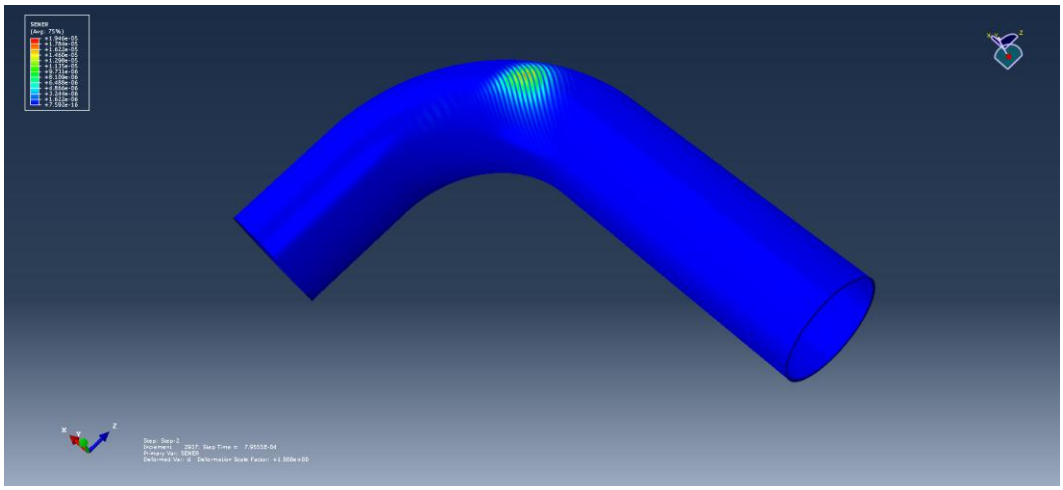

Figure 4.32
Wave mode propagating on a 0.6 m (24 in) diameter pipe with an elbow after 0.99 ms of propagation time. The source is a directional sensor that launches energy at an angle of $\pi/4$ radians from the axial direction of the pipe. Both ends of the pipe are damped so as to reduce guided wave reflection amplitudes from the pipe ends.

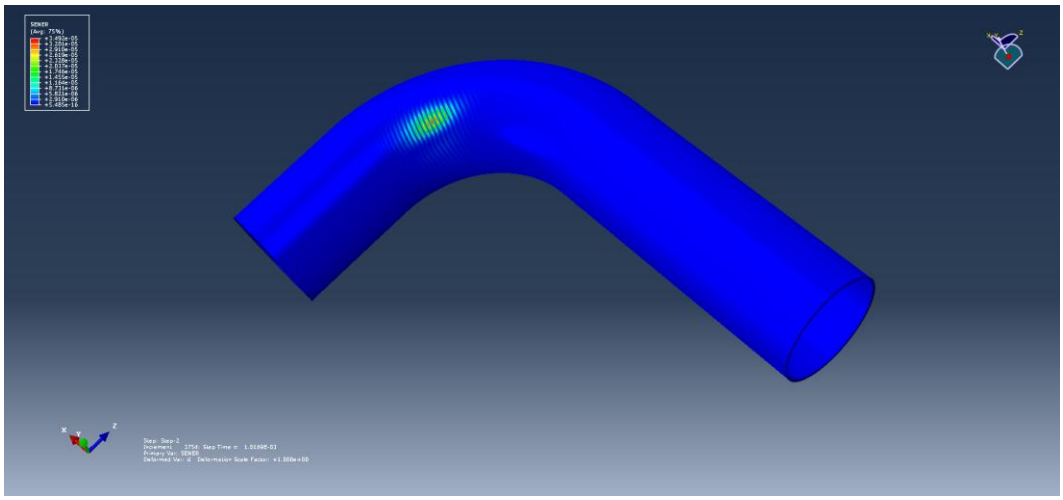

Figure 4.33
Wave mode propagating on a 0.6 m (24 in) diameter pipe with an elbow after 1.21 ms of propagation time. The source is a directional sensor that launches energy at an angle of $\pi/4$ radians from the axial direction of the pipe. Both ends of the pipe are damped so as to reduce guided wave reflection amplitudes from the pipe ends.

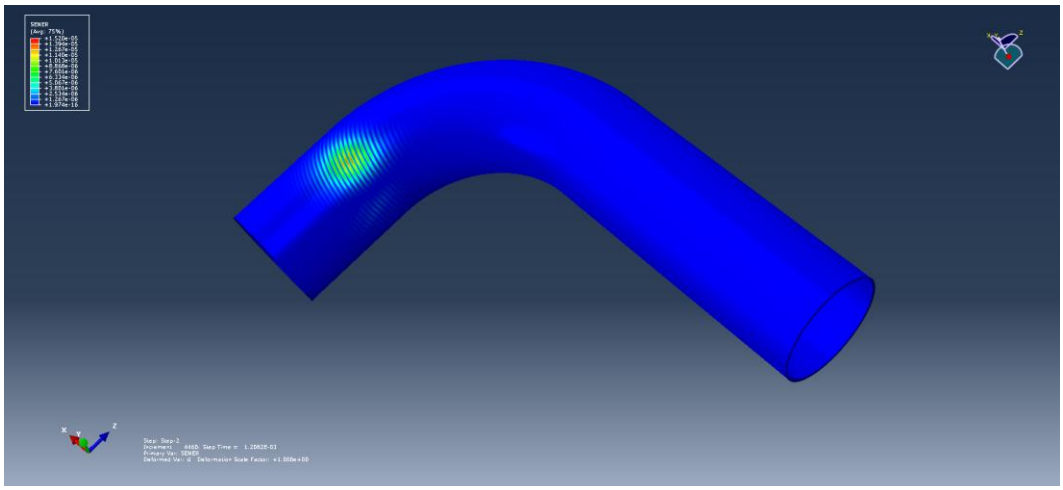

Figure 4.34
Wave mode propagating on a 0.6 m (24 in) diameter pipe with an elbow after 1.41 ms of propagation time. The source is a directional sensor that launches energy at an angle of $\pi/4$ radians from the axial direction of the pipe. Both ends of the pipe are damped so as to reduce guided wave reflection amplitudes from the pipe ends.

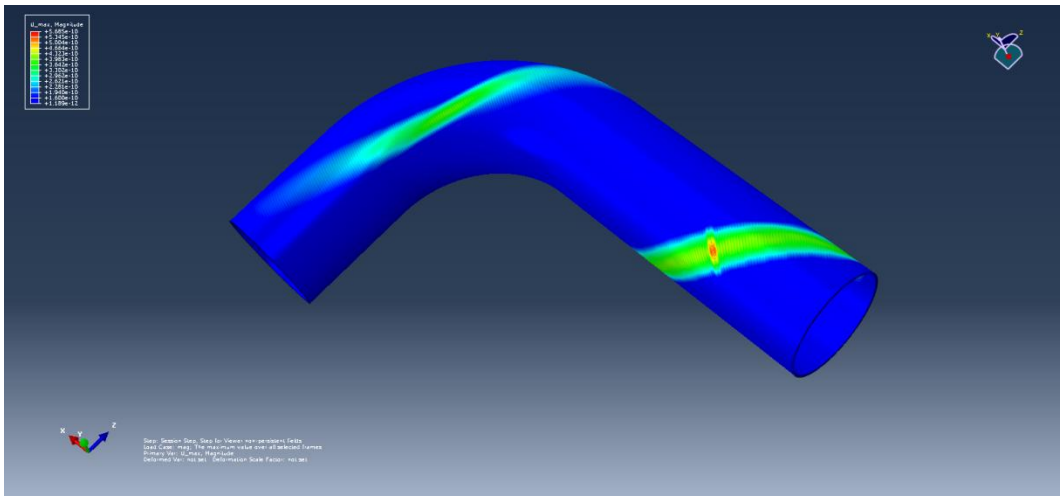

Figure 4.35
FEM simulation results showing maxima of absolute values of displacement of a wave traversing a bent pipe over all time. The model includes edge damping so that energy does not reflect off the cut ends of the pipe in either direction. The wave was launched with a directional probe from a distance of 1 m (39.4 in) from the elbow and an angle of 45 degrees.

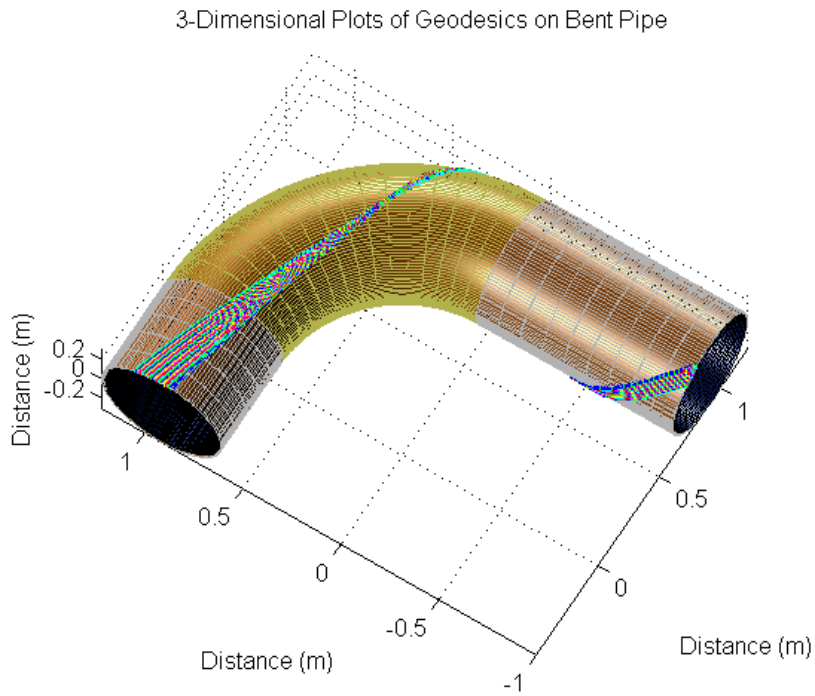

Figure 4.36
Mode tracing results showing trajectories of a wave launched at an angle α of 45 degrees from a distance of 1 m (39.4 in) from an elbow. This figure approximates the situation given in Figure 4.35.

The beam spreading and wave propagation direction seen in Figure 4.35 matches well with the same parameters in Figure 4.36. The beam spreading is actually remarkably narrow for a wave generated with the loading function used in this model on this type of structure. These two figures create a simple, yet convincing demonstration as to the validity and usefulness of mode tracing methods. The mode traces in Figure 4.30 show that a wave launched from 1 m (39.4 in) away from the elbow at an angle of 45 degrees will be mostly located at about 7.7 radians around the circumference of the pipe when it eventually reaches 0.5 m (19.8 in) beyond the elbow. This angular location of 7.7 radians represents one complete rotation from the extrados around the circumference of the pipe plus an additional 1.42 radians. This gives an angle of 1.42 radians from the extrados when the wave is at 0.5 m (19.8 in)s past the elbow.

Because mode tracing can be used to determine where guided wave energy will go, given a waveguide geometry and an initial launch direction and location, it can be used to determine the wave coverage that will be achieved when a wave is launched. This means, that mode tracing

allows the determination of wave launch parameters that will ensure that any particular location of interest is insonified.

The application of mode tracing to the practical problems shown in this chapter has produced exciting results. The new theory has lent revolutionary insights into guided wave propagation in pipes with elbows. Furthermore, finite element modeling has provided convincing validation of these insights. The value of the contributions already demonstrated in this dissertation are profound, but one additional topic will be discussed as well, as the climax of this work. While the idea of mode tracing is fundamentally the most important contribution of this dissertation, because it is foundational to the results given here, and no doubt contains great potential for other applications, we will also discuss guided wave focusing beyond an elbow as a forward technique. Such a technique represents a much-coveted improvement in guided wave mechanics. The next chapter will demonstrate this forward focusing technique and will also offer some remarks about natural focusing in and beyond an elbow.

Chapter 5 Guided Wave Focusing Beyond an Elbow

Guided waves are often used in practice for inspecting real components such as pipes and plates. However, the mechanics and mathematics of guided wave propagation has not been previously understood well enough to make significant use of guided waves that travel past an elbow. Advancing our understanding of these subjects so as to allow guided wave inspections to be done past elbows in pipelines has been an ongoing effort in the guided wave community for the past number of years [110,112-114], but satisfactory results have yet to be published.

The mode tracing concepts developed and validated in this dissertation, however, can also be used to focus guided wave energy launched from multiple sensors in an array on a pipe system to arbitrary focal spots in and beyond an elbow. The tools given here can be used for focusing in straight pipes as well, but the larger contribution of this work pertains to focusing in and beyond an elbow. Therefore, this dissertation discusses focusing in and beyond an elbow, although focusing in a straight pipe would be done the same way.

Forward Focusing by use of Mode Tracing

To discuss focusing guided waves in and beyond an elbow, we consider an array of sensors containing n number of sensors. The sensors can be positioned on the pipe in any location chosen. Many embodiments of practical sensor arrays will have all the sensors located at a shared axial location on the pipe, and the sensors equally spaced around the circumference of the pipe. This configuration is not necessary, though, as arbitrarily positioning the sensors in the array will also work for focusing the guided wave energy.

To perform the focusing with an array of sensors, a suitable transverse resonance pathway connecting the location of each guided wave source, or sensor, to the selected focal point is calculated. The initial launch angle of the these pathways will indicate the direction to launch the wave from each source so that the wave reaches the desired focal location. The length of each pathway will indicate the distance the corresponding wave mode must travel to reach the focal point. The calculated length of each pathway, when coupled with the knowledge of the wave speed, allows an appropriate time delay to be given to each source so that a wave mode launched from the source reaches the focal spot at a predetermined time.

With the set of initial launch directions and the total time needed for a wave to move from each respective sensor to the predetermined focal location obtained for each sensor, the sensor represented by the longest mode pathway between the sensor and the focal point is pulsed first. This pulse is followed by pulsing the sensor with the next-longest corresponding pathway. There is a delay between the time the first sensor is pulsed and the time the second one is pulsed. That delay is precisely calculated so that the energy launched from both sensors arrives at the focal position simultaneously. The rest of the sensors are pulsed similarly, with appropriate delays for each one, so that the energy from each of the sensors reaches the focal location simultaneously. This results in the energy launched by each of the n sensors in the array superimposing on the energy launched by each of the other sensors at the location of the focus.

This focusing strategy does not attempt to control the entire energy profile at the circumferential location containing the focal location, but it does provide a method of designing the highest percentage of energy in the entire circumference to lie at the circumferential location of the focal location. To aid in our discussion, we will introduce the variable φ as the angular distance between the desired focal location, or focal ϕ, in the circumference of a pipe, and an arbitrary point on the pipe sharing the same axial location. The variable is demonstrated in Figure 5.1.

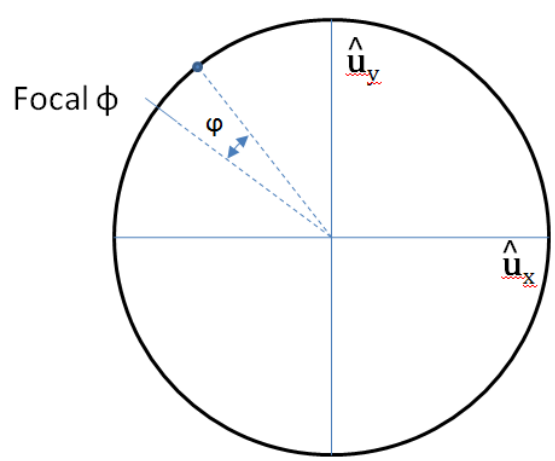

Figure 5.1
Introduction of the variable φ as the angular distance between a particular circumferential location on the edge of a pipe cross-section and an arbitrary point on the same edge. The particular circumferential location will be called the *focal* ϕ.

Due to beam spreading, some energy from the modes launched by each sensor will arrive at the axial location of the focus near the focal location, rather than exactly at it, meaning at some non-zero value of φ rather than at the focal ϕ itself. However, if the sensor is oriented so as to launch the highest percentage of its energy along the selected transverse resonance pathway, then the amount of energy traveling on either side of this transverse resonance pathway will be less than the amount of energy that arrives at the focal location.

This means that the amplitude of energy from each mode arriving at the axial location of the focus will decrease as the value of φ representing the portion of the energy under consideration increases. Furthermore, as φ changes, the time the portion of the wave front that crosses the corresponding circumferential location at the axial location of the focus also changes in the general case. The case of axi-symmetric energy impingement on the axial location of the focus could be considered a degenerate case for this consideration, but such an energy profile would not exhibit any focusing. Therefore, a good focus profile can be achieved even without directly controlling all the energy that crosses the axial location of the focus in circumferential positions other than the focal ϕ. This is demonstrated with a set of two FEM simulations later in this chapter.

However, if it is desired to directly control the energy profile in the entire circumferential plane containing the focal ϕ, another technique can also be used. This technique more closely parallels the conventional approach for focusing in straight pipes. In this focusing strategy, a number of transverse resonance pathways are used together for an individual sensor in the array to determine the circumferential profile of energy as a function of time that will exist at the desired axial focal distance as a result of pulsing that sensor. This method again uses the idea introduced with Figure 3.22. This process is employed for each source in the array, and the resulting energy profiles as functions are superimposed on one another to examine the resultant energy profile that will develop at the axial location of the focus.

Individual time delays and energy weights can be applied to each sensor profile before calculating the superposition of profiles. In this way, many candidate resultant energy profiles can be investigated, and the one that best matches the desired focal profile can be selected. The amplitudes and time delays for each load source in the array can then be adjusted based on the results of this selection process. This method is similar to the conventional techniques described in Appendix A. However, for focusing in and beyond the elbow, the mode tracing constructions developed in this dissertation offer the ability to calculate the necessary sensor profiles in a

practical way for what is thought to be the first time. This idea will be shown with an FEM simulation later in the chapter when we discuss natural focusing caused by elbows.

Numerical Focusing Demonstration

The piping system used in the simulation once again consists of a 0.6 m (24 in) diameter, schedule 20 steel pipe with a 1.5-diameter elbow. Practical directional sensors are modeled on the piping system to transmit and receive energy. The sensors represent a real data acquisition system employing magnetostrictive sensors. The sensors are 50.8 mm (2 in) wide and 203.2 mm (8 in) long, and are placed on the pipe as prescribed in the preceding discussion. A 25.4 mm (1 in) diameter side-drilled hole is placed in the pipe at an axial location of 1.52 m (60 in) from the far side of the elbow.

The angular location of the hole is placed at a ϕ angle of $5\pi/4$ radians. The sensors are placed a distance of 1 m (39.4 in) from the near side of the elbow. This is sketched in Figure 5.2. The simulation uses a guided wave of 32 kHz, a common wave frequency used in the practice of guided wave inspections of piping. In order to demonstrate the power of this focusing endeavor, a simulation of the typical current approach to inspecting a pipe with an elbow is presented before showing the effect of focusing. For this demonstration, an axi-symmetric wave is launched from one side of the elbow and is examined as it moves across the pipe domain.

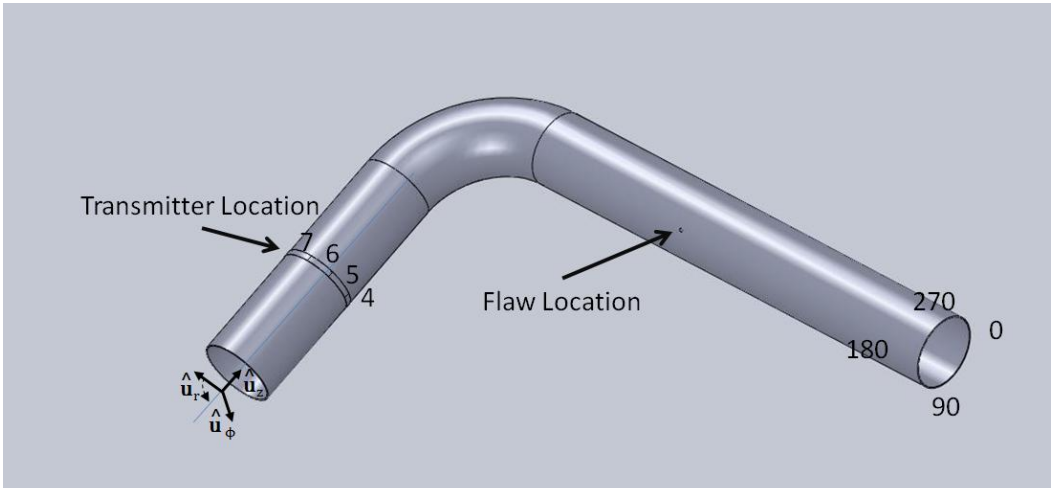

Figure 5.2
Axi-symmetric FEM simulation model setup. There are 8 sensors that make up the transmitter array. The sensor array is 1m (39.4 in) from the elbow. The Flaw Location is the position of a side-drilled hole. The angular position of the hole is 225 degrees from the extrados and the axial location of the hole is 1.52 m (60 in) from the end of the elbow.

A virtual sensor is also placed at the axial location where focusing is to take place in the next simulation. Each node lying on the outer surface of the pipe at this axial location is part of the sensor and records the displacement experienced by the node. This displacement is then plotted in a three-dimensional image that shows the displacement magnitude of each node as a function of simulation time. For this first simulation, the side-drilled hole described previously is not included in the model. This allows us to observe how an axi-symmetric wave would naturally behave in the region beyond an elbow.

Figure 5.3 and Figure 5.4 show snapshots of the FEM simulation of the axi-symmetric energy generated by the sensor array. The energy begins as a bi-directional wave in this simulation, and moves away from the sensor. The cut ends of the pipe are damped as described in Appendix C to represent infinite lengths of the pipes attached to either side of the elbow. Figure 5.3 shows the energy 105 μs after the simulation begins. In this figure, the energy pulse is still forming. Figure 5.4 shows the energy after 385 μs of propagation time. In this figure, the energy is completely formed and moving toward the elbow as an axi-symmetric wave mode. This image represents the energy profile typically used for guided wave examinations of long runs of straight pipe.

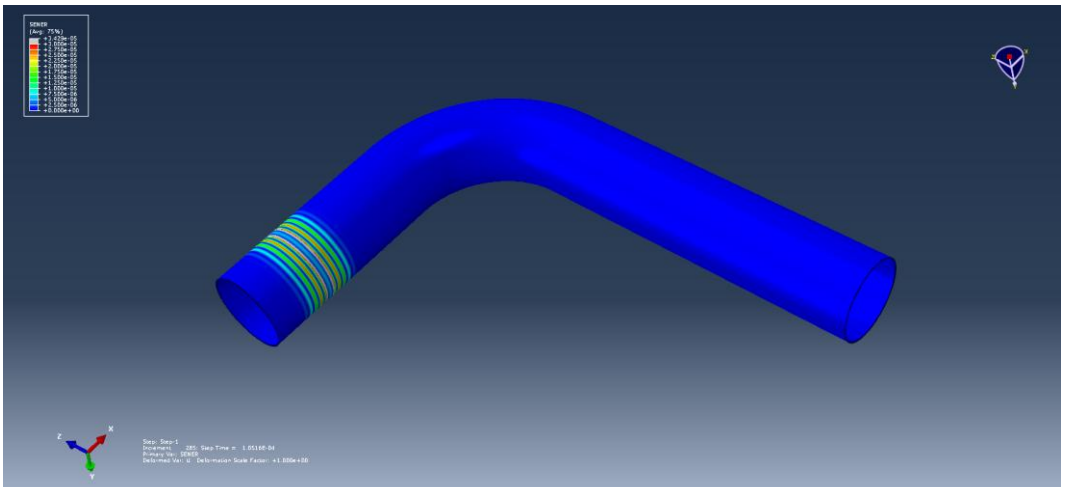

Figure 5.3
FEM simulation result showing axi-symmetric energy excitation on a pipe with an elbow. The image is taken after 105 μs of propagation time.

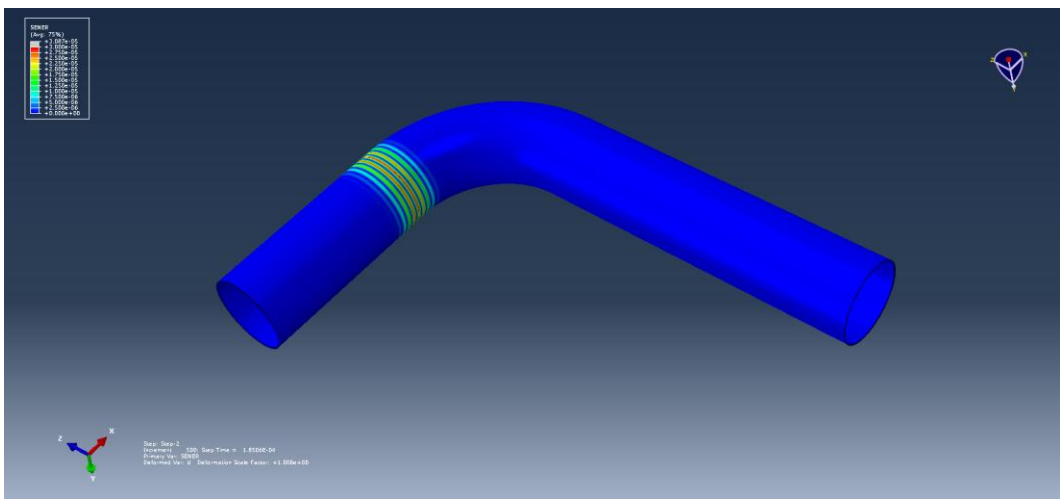

Figure 5.4
FEM simulation result showing axi-symmetric energy excitation on a pipe with an elbow. The image is taken after 385 μs of propagation time. The energy is packaged into a uniform ring before entering the elbow.

After the energy crosses the elbow, severe distortion caused by the elbow disrupts the energy from the axi-symmetric ring into a scattered profile of energy. Figure 5.5 represents the energy after it has traveled for about 886 μs, and shows the part of the energy that travels around the intrados and surrounding neighborhood. This part of the energy is still fairly smooth, but non-the-less is losing its axi-symmetry. The majority of the energy is not visible in this image

because it is still coming around the extrados side of the elbow. As noted in Chapter 4, methods of mode tracing predict that a large percentage of an axi-symmetric wave incident on a 90-degree elbow will become concentrated on the extrados region of the elbow.

Figure 5.6 shows most of the energy that was hidden by the extrados in Figure 5.5 as it begins to spiral around the pipe in the region beyond the elbow. This spiraling of the energy is also anticipated by the mode tracing results given in Chapter 4. Figures 5.5 and 5.6 demonstrate the complication that an elbow causes to axi-symmetric guided waves and show why the conventional understanding of guided wave energy that has crossed an elbow must be treated with caution.

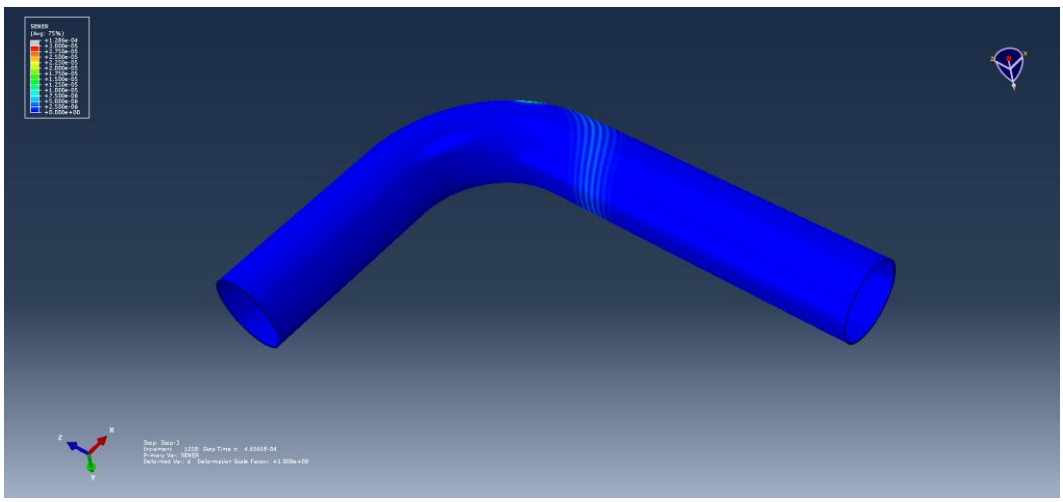

Figure 5.5
FEM simulation result showing axi-symmetric energy excitation on a pipe with an elbow. The image is taken after 866 μs of propagation time. After crossing the elbow, the energy becomes distorted, with a weak leading edge along the intrados line.

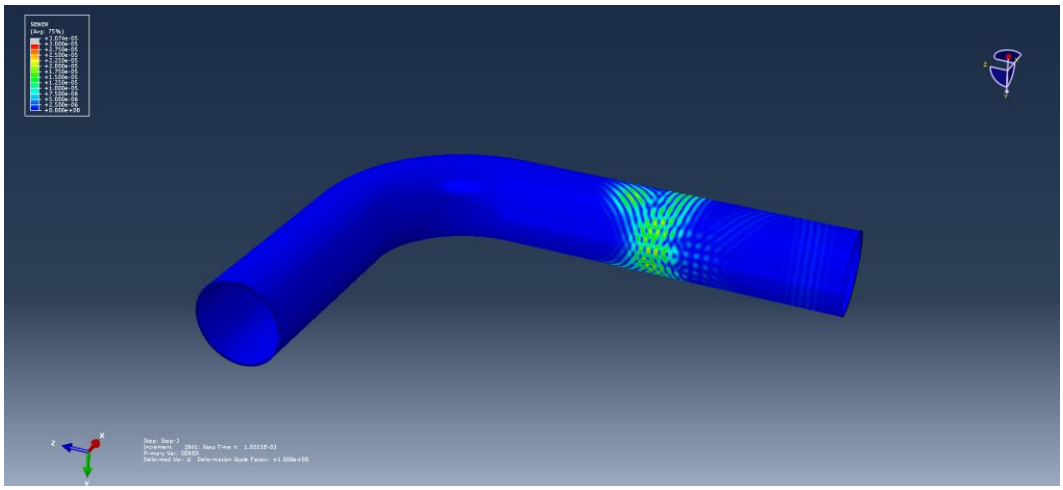

Figure 5.6
FEM simulation result showing axi-symmetric energy excitation on a pipe with an elbow. The image is taken after 1451 μs of propagation time. Following the weak leading edge is the bulk of the energy. However, after crossing the elbow, the energy loses its symmetrical form and becomes a complicated scattering of energy.

Figure 5.7 shows a three dimensional plot of the energy that has crossed the elbow. The plot shows the displacement that is experienced at the axial location of 1.52 m (60 in) past the end of the elbow. This axial location is indicated by the magenta line, and is where the side-drilled hole is placed in the focusing experiment.

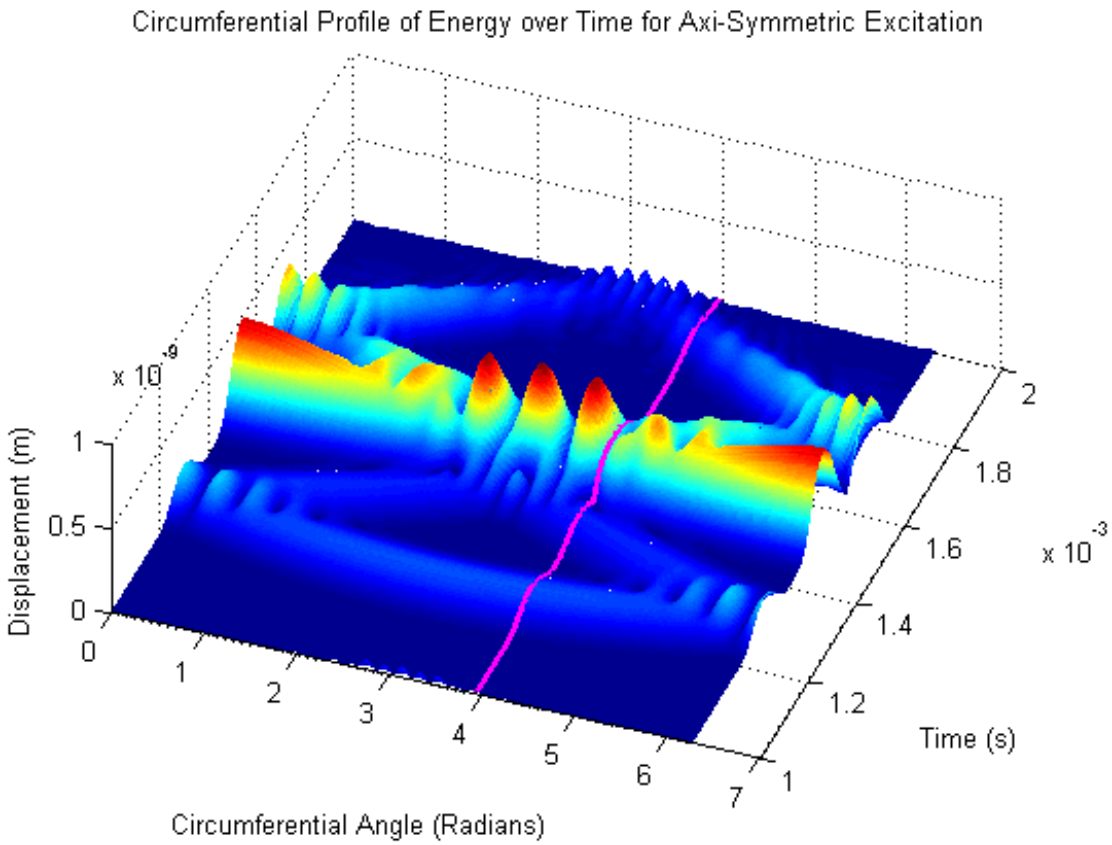

Figure 5.7
Energy profile around an axial location on the far side of the elbow as a function of time and angular position. The magenta line drawn over the plot denotes the position of the side-drilled hole in the model for comparison with the results of the focusing experiment in the next section. There is no actual hole in the model shown in the conventional sensor experiment.

The data shown in Figure 5.7 are given as displacement amplitude versus time and angular position around the pipe for a fixed axial location. Each unique time in the plot is represented by an energy envelope across the circumference of the pipe. Initially, there is no disturbance in the pipe at this axial location, as it takes some time for the guided wave to reach the position of the virtual sensor. It should be noted that for clarity and zooming purposes, Figure 5.7 does not include the first millisecond of time.

The weak leading edge of the energy on the intrados side is the first disturbance seen in the plot and arrives at about 1200 μs. This rounded leading edge is also the first energy to appear at the location of the side-drilled hole, as shown with the magenta line in the figure. The majority of the energy pulse reaches the axial location of the side-drilled hole about 200 μs later. The profile of

this portion of the energy is very strong at the extrados line and tapers off at the top and bottom of the pipe. As noted from Figure 5.6, the energy is spiraling around the pipe at this point, and due to the symmetry of the pipe and loading, the energy splits into two main lobes.

These two lobes spiral opposite ways from one another around the pipe, periodically meeting up with one another on the intrados or extrados lines. The lobes alternate meeting locations between the intrados line and the extrados line. Wherever they cross one another, they interfere with each other. This is the cause of the energy peaks along the intrados in Figure 5.7. The intrados can be envisioned by drawing an imaginary line parallel to the magenta line at a circumferential angle of π radians. The extrados is represented at both zero radians, and at 2π radians. The image shows that there is a lot of energy on the extrados line at this axial location. Also, Figure 5.7 shows that focusing is not occurring at this axial location.

The data represented in Figure 5.7 consist of many individual waveforms, each recorded by a separate node, or channel, in the FEM model. The particular time trace highlighted by the magenta line in Figure 5.7 is one such waveform. Real, contemporary, guided wave inspection systems have a comparatively small number of channels, typically one to sixteen. In many practical cases, eight channels are used.

In such a system, each of these real channels can consist of multiple sensors placed on the pipe, but the individual sensors making up each channel are typically electrically coupled to one another. This construction effectively averages the waveforms collected by individual sensors in the channel and aggregates them into a single resultant waveform. The inspection apparatus then displays a single waveform representing each channel. The channels are evenly distributed around the pipe, so each channel in an eight-channel system represents an octant of the pipe circumference.

Also, when reporting energy profiles at particular axial positions, practical guided wave inspection systems often reduce each contributing waveform or waveform subset into a single value. The Root Mean Square (RMS) is one method of performing such a reduction of a waveform into a single value. The RMS value corresponding to each channel can then be rendered on a polar plot to show a graphical representation of the energy profile.

An analogous exercise is done on the data in Figure 5.7 and shown in Figure 5.8. To do this, the RMS of each waveform in Figure 5.7 is computed, then averaged into eight virtual channels. The resulting average of RMS values corresponding to each respective virtual channel is drawn on a

polar plot. The averaged RMS value from the first octant is assigned an angular position of zero degrees. The result from the second octant is reported at 45 degrees, etc. The value corresponding to an angle of 180 degrees in Figure 5.8 is nearly co-linear with the values at 135 degrees and 225 degrees, so the corresponding data point does not produce a corner on the energy profile like the other points on the plot do.

This aggregation of data is not necessary, given that the FEM simulation provides many data points, or channels, around the pipe, but it provides a better representation of data a field technician might encounter when doing this experiment with a real pipe system. In Figure 5.8, the aggregate RMS energy value for each octant is reported 22.5 degrees below the center point of the octant. This is why the profile appears to be non-symmetric. Again, this is done here to simulate field practices of representing aggregate octant data at 45-degree intervals around the circumference of a pipe. Figure 5.8 represents a polar plot of the circumferential profile of energy in the pipe at the axial location monitored. The black outer ring in the figure is representative of the pipe wall, and the blue trace shows a map of the displacement profile as a function of circumferential angle around the pipe.

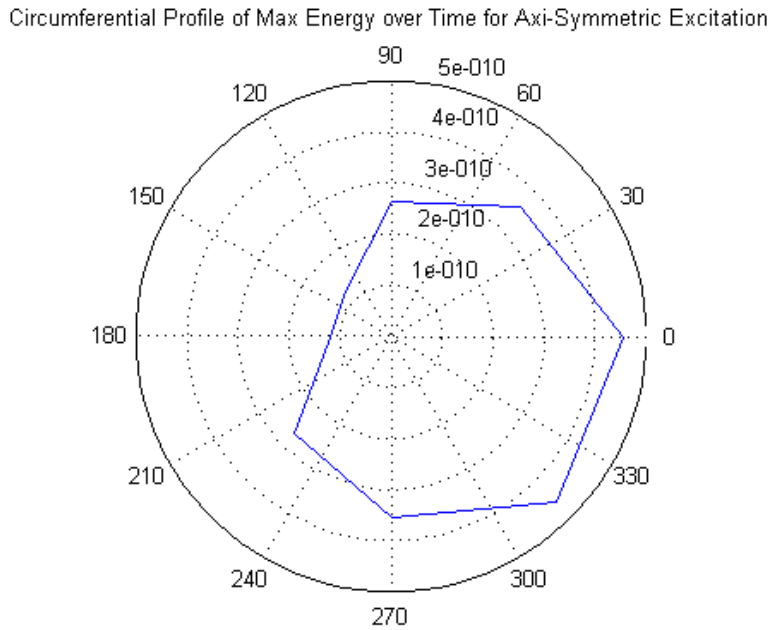

Figure 5.8
RMS energy profile around a pipe beyond an elbow resulting from an axi-symmetric loading input.

This exercise demonstrates how an axi-symmetric guided wave moves through a pipe with an elbow. Such a test is typical of a guided wave pipeline examination since knowledge of how to control guided wave energy beyond an elbow was lacking prior to this dissertation. The FEM simulation demonstrates the difficulty in predicting which regions in a pipe beyond an elbow will experience substantial guided wave energy and which regions will experience very little, extending the work of Rose, et al. [109].

From here we move on to the anticipated focusing experiment, where a FEM simulation is used to launch guided wave energy from one side of an elbow in order to focus the guided waves at a predetermined point on the other side of the elbow. In this model, the side-drilled hole, as discussed earlier, is included. This hole provides a visual marker on the pipe that represents the predetermined focal location where the focusing is to occur. The excitation parameters for each of the sensors used in this simulation are selected so that the energy focuses at the location of the side-drilled hole.

Eight independent sensors were used to excite the energy. The locations of the sensors were chosen to be 1 m (39.4 in) from the beginning of the elbow, in accordance with the previous FEM simulation. This location was then used as an input parameter to calculate the excitation requirements which would allow energy focusing at the side-drilled hole.

While in a practical experiment, sensor hardware is installed on a piping system in an optimal location, the most desirable location for sensor hardware may not be available. In such cases, the sensor is placed in a convenient location, and the ensuing testing is conducted according to the sensor placement and restrictions unique to the specific inspection.

After choosing where to place the sensors, transverse resonance pathways are calculated to connect each sensor location with the desired focal location on the far side of the elbow. As discussed previously, the calculation of these pathways also reveals the launch angle needed to move the energy from the sensor to the side-drilled hole. The length of each pathway also enables the computation of the travel time required for the energy to move from each sensor to the hole.

Each of the sensors is directional, and is installed on the model at the appropriate orientation so as to launch the energy in the required direction. The sensors are then assigned unique delay times so that the sensors further from the focal location are activated before sensors that are nearer the hole. Proper phasing of the sensors allows the energy from each sensor to reach the hole at the same time, thereby additively contributing to the RMS energy profile at the location of the side-drilled hole. The time delays and launch angles calculated from the mode tracing are indicated in Table 5.1, and were used in the focusing simulation.

Table 5.1 Time delays and launch angles for focusing FEM simulation

Octant	1	2	3	4	5	6	7	8
Time Delay (μs)	76.2	43.4	0.0	12.5	45.6	82.1	114.9	141.9
Launch Angle α (radians)	-0.423	-0.532	-0.648	0.825	0.643	0.514	0.408	0.307

Snapshots of the FEM simulation are given in Figures 5.9 through Figure 5.14. Figure 5.9 shows the model at 99μs, soon after the first few sensors begin activation. The energy from the sensors on the bottom of the model had the furthest to travel, so those sensors were activated before the ones on top. Figure 5.10 shows the energy distribution after 306 μs of simulation time.

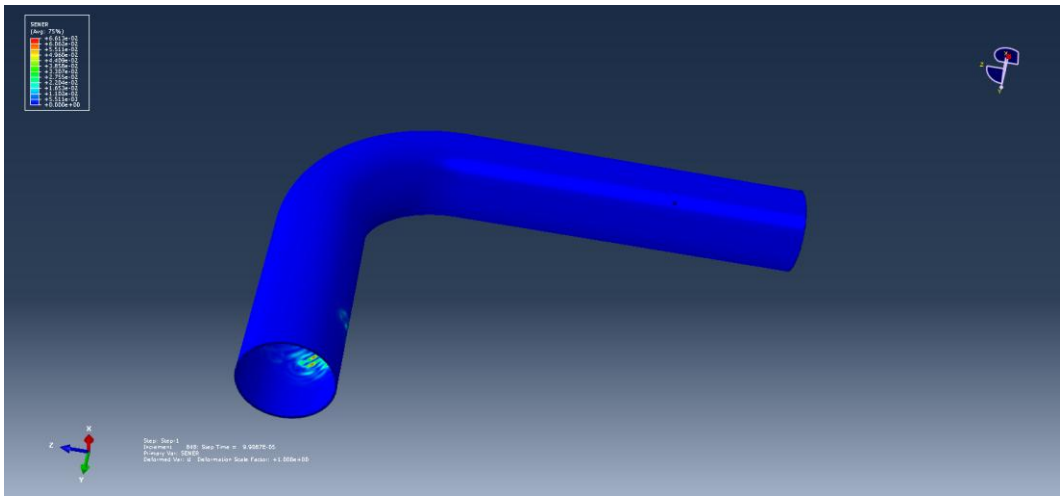

Figure 5.9
FEM simulation result showing partial loading energy excitation on a pipe with an elbow. The image was taken after 99 μs of propagation time. The eight transducers used to generate energy were not activated simultaneously. In this figure, the sensors on the bottom of the pipe were activated while those on the top were dormant.

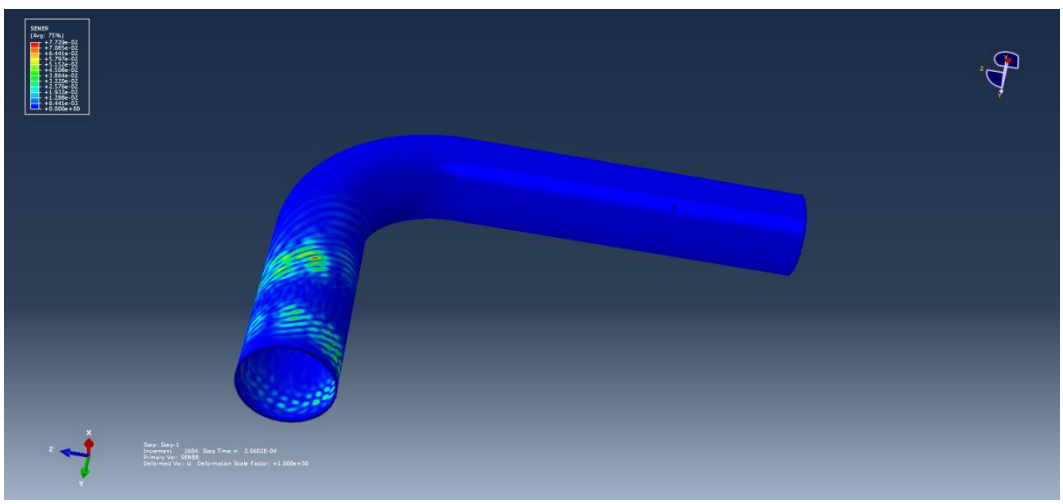

Figure 5.10
FEM simulation result showing partial loading energy excitation on a pipe with an elbow. The image was taken after 306 μs of propagation time. All eight transducers were activated and the energy from each transducer traveled along separate paths toward the side-drilled hole on the far side of the elbow.

For this simulation, the energy distribution from the loading was not uniform, or axi-symmetric, as it is in conventional loading. Instead, the inputs were carefully designed so that the energy on

the far side of the elbow could be controlled. Figure 5.11 shows the energy after 1017 μs of simulation time. The energy was once again mostly on the hidden side of the model. While some energy moved in directions other than the designed directions, this was an artifact of using finite, real, sensor types.

Figure 5.12 shows the energy at 1602 μs. The energy is now moving around the top and bottom of the pipe from the hidden side to the location of the side-drilled hole. A portion of the energy moved over the top of the pipe, and another portion of the energy converged from the bottom side of the pipe. The energy fully converged on the side-drilled hole at 1737 μs, as shown in Figure 5.13. After focusing on the side-drilled hole, the energy defocuses as it moves on through the pipe. This defocusing can be seen in Figure 5.14. Also seen in the figure is the reflection that returns from the side-drilled hole back toward the sensors.

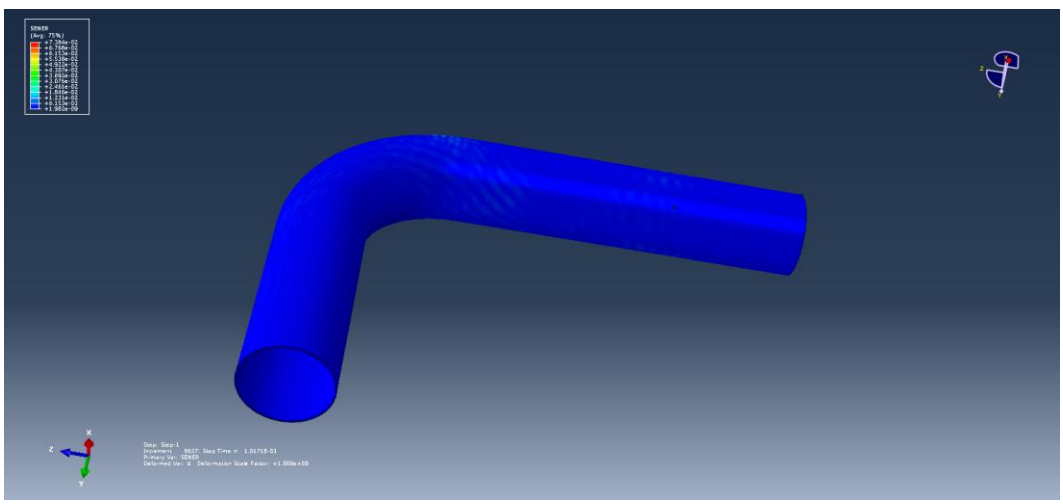

Figure 5.11
FEM simulation result showing partial loading energy excitation on a pipe with an elbow. The image was taken after 1017 μs of propagation time. Most of the energy is hidden on the concealed side of the model.

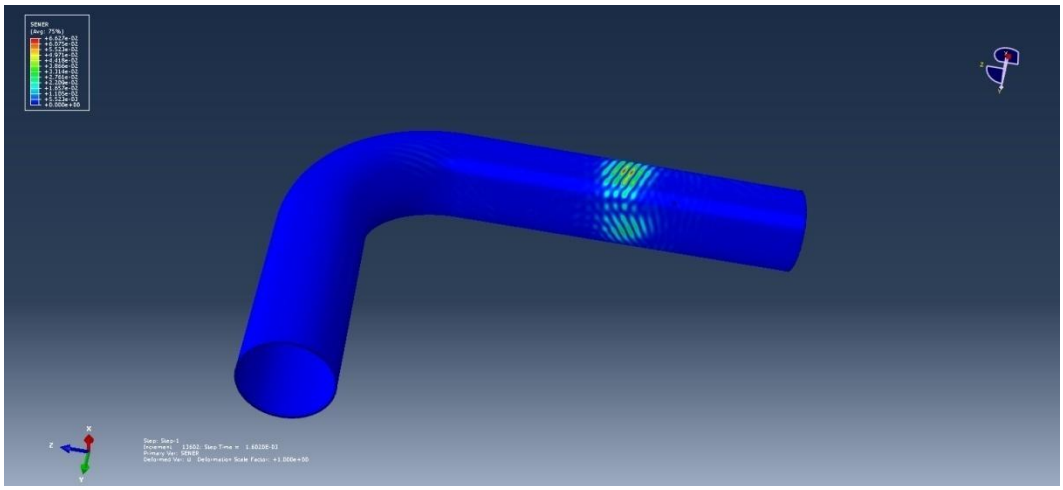

Figure 5.12
FEM simulation result showing partial loading energy excitation on a pipe with an elbow. The image was taken after 1602 μs of propagation time. The energy began to converge on the side-drilled hole. A portion of the energy moved around over the top of the pipe, and another portion of the energy converged from the bottom side of the pipe.

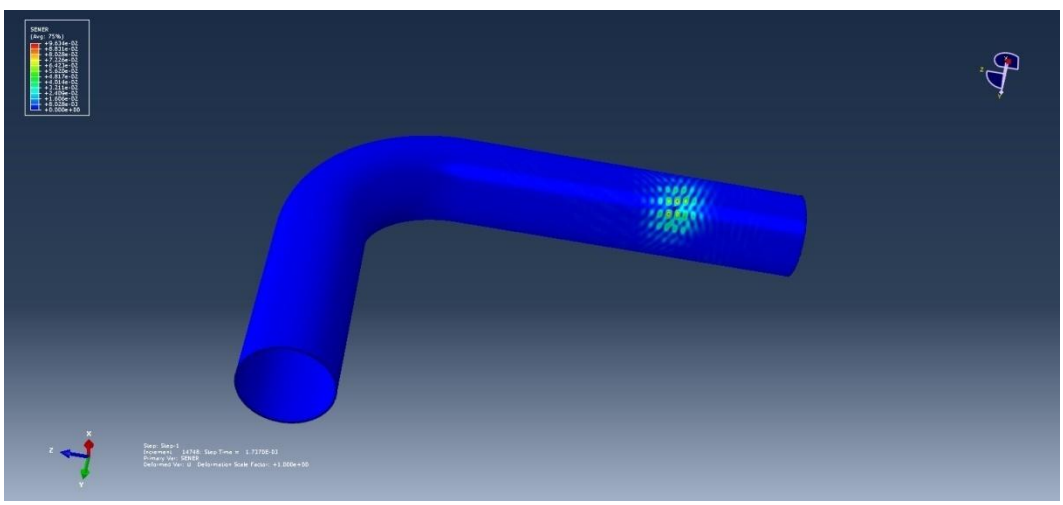

Figure 5.13
FEM simulation result showing partial loading energy excitation on a pipe with an elbow. The image was taken after 1737 μs of propagation time. The energy has converged on the side-drilled hole.

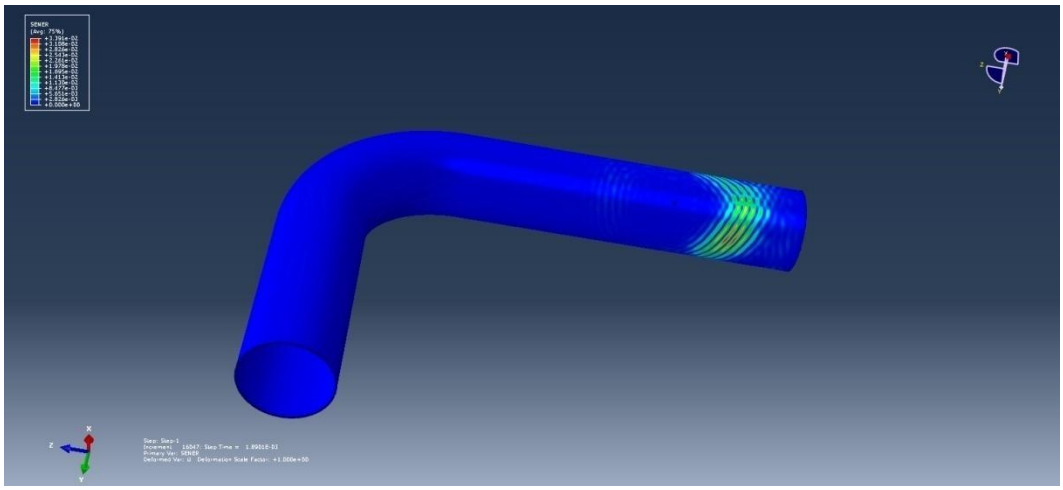

Figure 5.14
FEM simulation result showing partial loading energy excitation on a pipe with an elbow. The image was taken after 1890 μs of propagation time. The energy has moved past the side-drilled hole and has begun to de-focus.

A three-dimensional plot similar to the one shown in Figure 5.7 is given in Figure 5.15. This plot again represents the energy that travels across the axial position of the side-drilled hole. Once again, the magenta line superimposed on the plot shows the circumferential location of the side-drilled hole. This energy profile is very different from the one shown for the axi-symmetric simulation. The energy focus on the location of the side-drilled hole in this simulation is very obvious. While the peak displacement shown in Figure 5.15 focuses nicely on the side-drilled hole, there are also two other large peaks, one on each side of the hole. These peaks are part of the displacement profile, but because of the interference of the two energy packets that spiral in from different directions, there is a region of low energy immediately on each side of the hole.

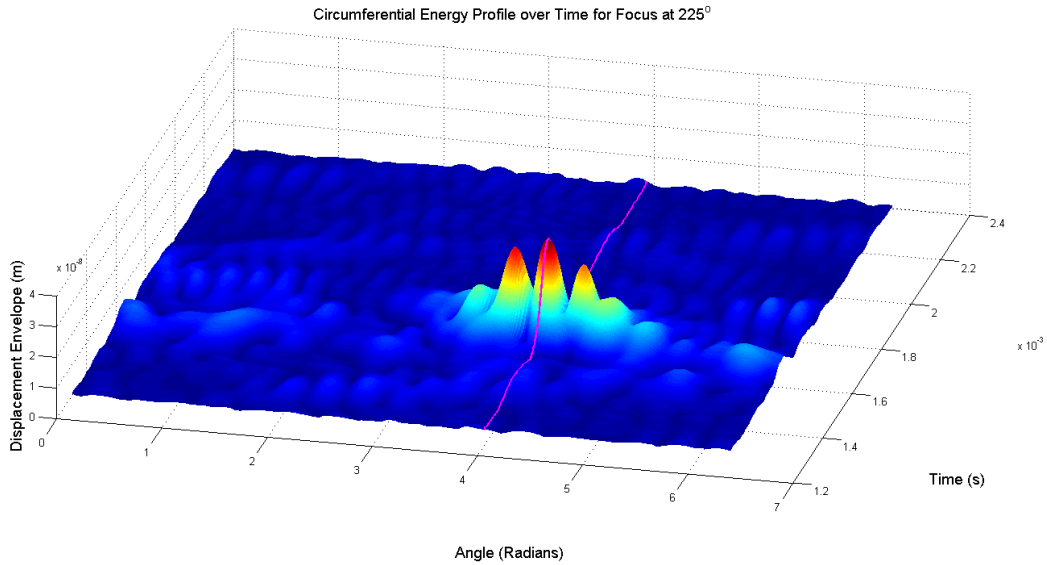

Figure 5.15
Energy profile around an axial location on the far side of the elbow as a function of time and angular position. The magenta line drawn over the plot denotes the position of the side-drilled hole in the model.

The RMS energy profile for the energy plot given in Figure 5.15 is shown in Figure 5.16. This figure can be compared with the RMS energy profile shown in Figure 5.8. Again, the energy distribution is aggregated into eight sections, together representing the energy profile a typical sensor would observe in a practical experiment. The aggregate energy measurement for each octant is again given at 45-degree intervals around the pipe. This energy profile also shows a very definite focus at the location of the side-drilled hole.

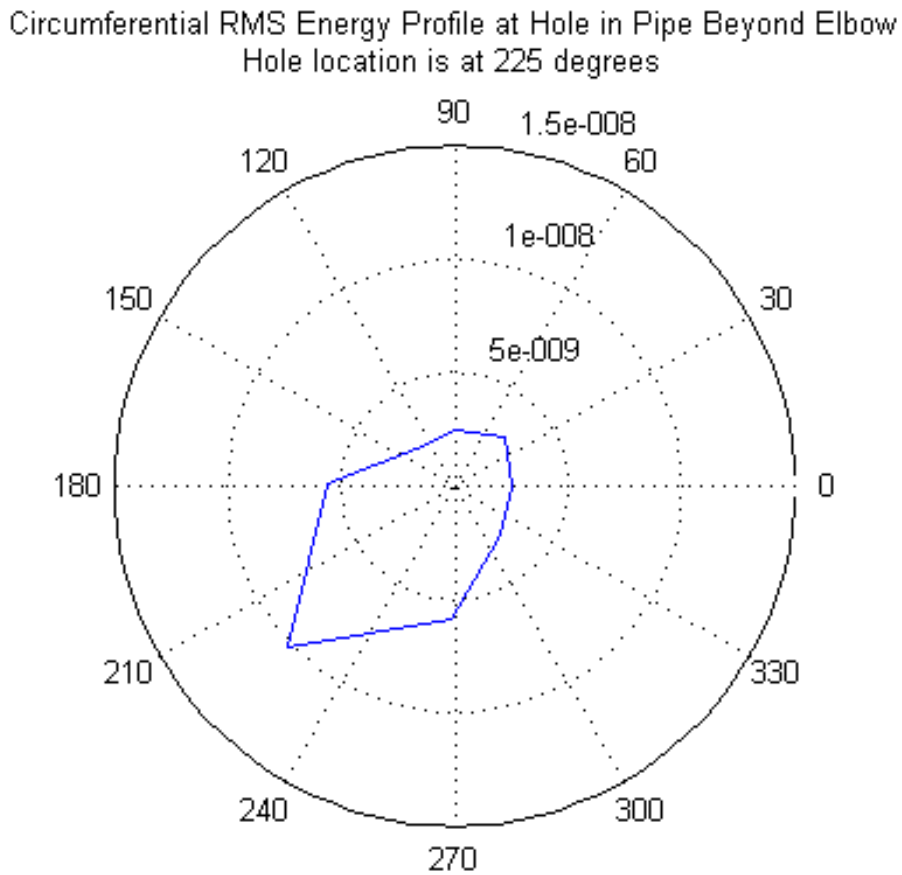

Figure 5.16
RMS energy profile around a pipe at an axial position beyond an elbow. The energy is launched so as to focus the energy at this location.

The results of these two FEM simulations demonstrate the power of the new mode tracing tools for focusing guided wave energy in pipes beyond elbows. As can be seen in this work, the use of informed sensor phasing and energy control brings about a revolution in how guided waves can be used in piping applications. In addition to being able to predict how an axi-symmetric wave will behave after entering an elbow, these tools allow us to actually design guided wave tests that cause guided waves to behave in a desired manner, even in a geometrically complex waveguide. As one final example of the knowledge gained by the tools delivered in this dissertation, we will next discuss natural focusing caused by a pipe elbow.

Natural Focusing Caused by a Pipe Elbow

The curvature of a pipe elbow can cause natural guided wave focusing. Prior to this research, tools for studying such natural focusing were not well established. Specific configurations could be modeled in FEM analyses to examine the consequence of a particular pipe geometry on a particular input, but such investigations are slow and not parametrically based. Methods of mode tracing, however, can also be used to investigate situations that cause natural focusing in a pipe configuration. To demonstrate this, we will begin with a FEM simulation of a pipe with an elbow that exhibits natural focusing caused by the elbow when using a point source.

Figures 5.17 through Figure 5.21 show a finite element simulation of a 0.61 m (24 in) diameter pipe with a 1.5-diameter, 90 degree bend. A point source is located 457 mm (18 in) ahead of the elbow at a circumferential angle of $2\pi/3$ radians. A virtual ring receiver, similar to that used in the previous FEM simulation, is placed in the model 457 mm (18 in) past the elbow. The receiver ring covered the entire circumference of the pipe. Figure 5.17 shows a three-dimensional plot of the signal envelopes obtained by the ring receiver as a function of circumferential location. This plot is analogous to Figure 5.7 and Figure 5.15. Figure 5.18 shows the same information, but the regions of the most intense natural focusing are outlined with a white ellipse.

As shown in Figure 5.18, natural focusing occurs several times between roughly 1.2 ms and 1.8 ms, in the circumferential zone of about 3.5 radians to 6 radians. Figure 5.19 shows a top view of the image in Figure 5.17, zoomed to show the region of natural focusing. The same information is given in Figure 5.20 with the natural focusing again outlined with a white ellipse.

Mode tracing is also used to model the point source on the pipe system. In Figure 5.21, red dots show the circumferential location, ϕ, and the effective time where wave energy traveling along mode traces originating from the point source land at the axial location of the receiver beyond the elbow. The locations of these dots denote the energy map that predicts where energy leaving the source will arrive at the receiver location. The dots represent the anticipated leading edge of the wave energy.

Regions with high densities of red dots represent regions where the mode tracing map predicts that significant guided wave energy will appear. Conversely, regions with few dots represent regions where little guided wave energy is expected. As seen in Figure 5.21, some regions containing a high density of dots, and therefore high guided wave energy, exhibit destructive wave interference. This tends to occur when a high density of red dots fall near one another and

trace out a curved or cusped profile. Two examples are shown in the outlined region of Figure 5.20. In particular, they are the curved profile of dots from approximately 3.5 radians to 6 radians near 1.2 ms, and the cusp in the dot profile that appears at approximately 4.1 radians and 1.4 ms.

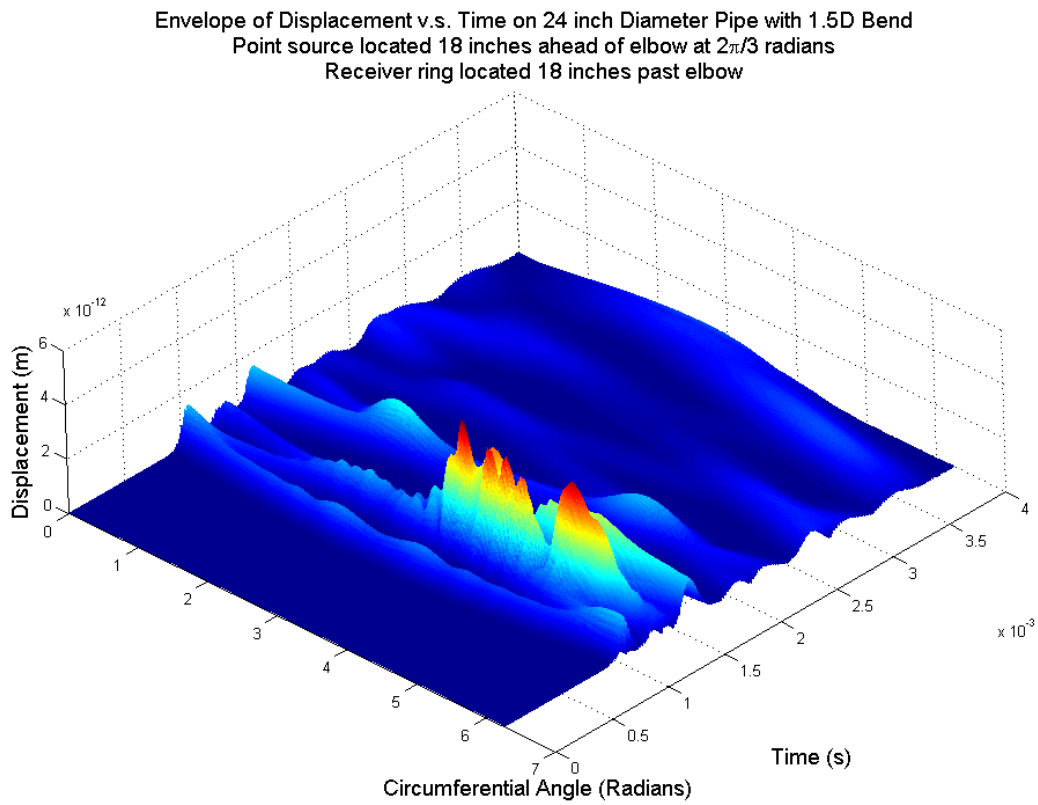

Figure 5.17
Envelope of time versus displacement signals obtained by the FEM ring receiver on the far side of the elbow. The loading for this model is a point source located 457 mm (18 in) ahead of the elbow and at a circumferential angle of $2\pi/3$ radians. The elbow causes natural focusing to occur between approximately 1.2 ms and 1.8 ms in the region between 3.5 radians and 6 radians around the circumference.

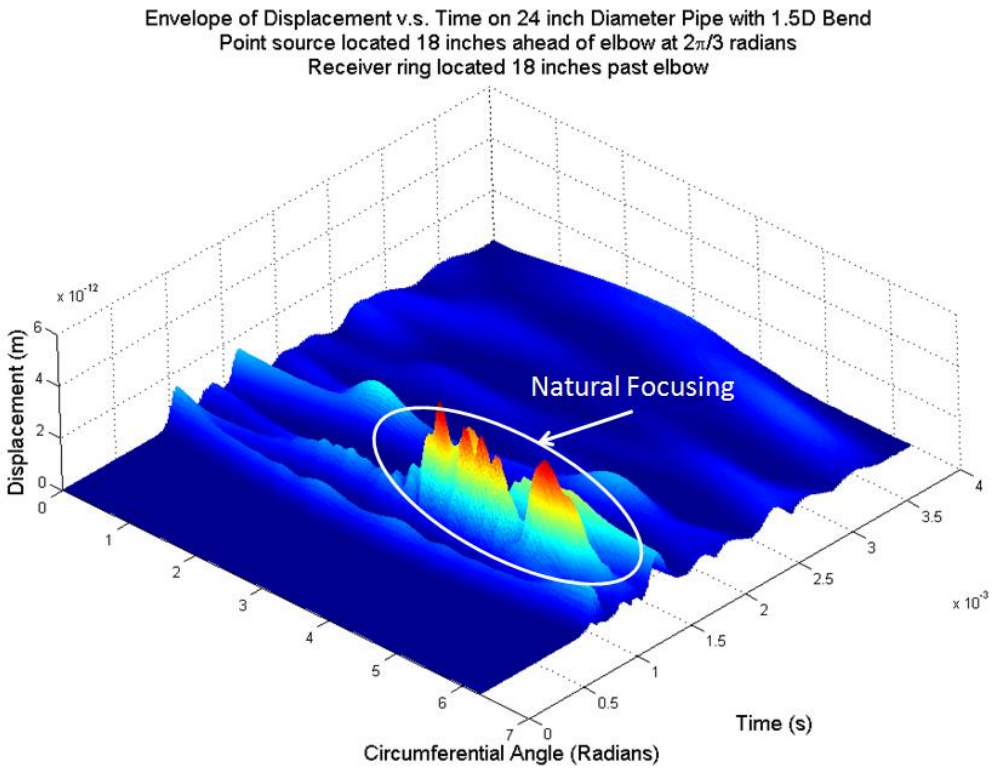

Figure 5.18
Envelope of time versus displacement signals obtained by the FEM ring receiver on the far side of the elbow. The figure is the same as Figure 5.17 except that the region containing the naturally focused energy is outlined with a white ellipse.

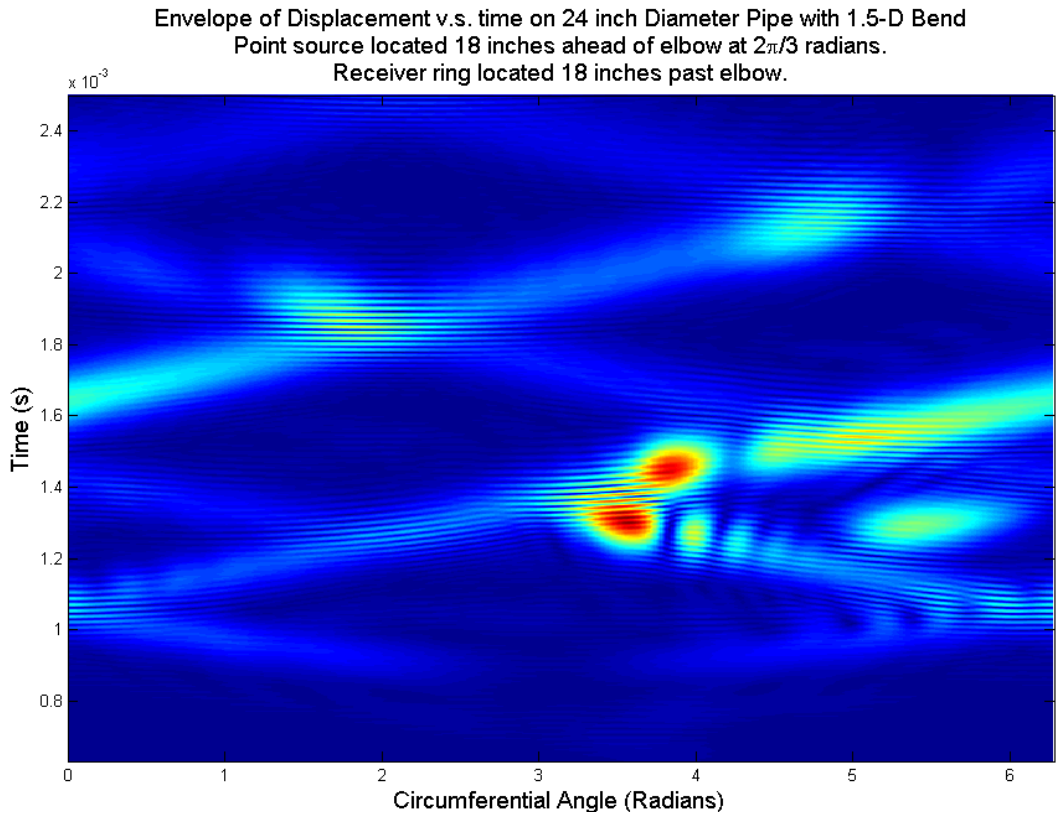

Figure 5.19
Top view image showing a zoomed section of Figure 5.17. Several spots of natural focusing can be seen.

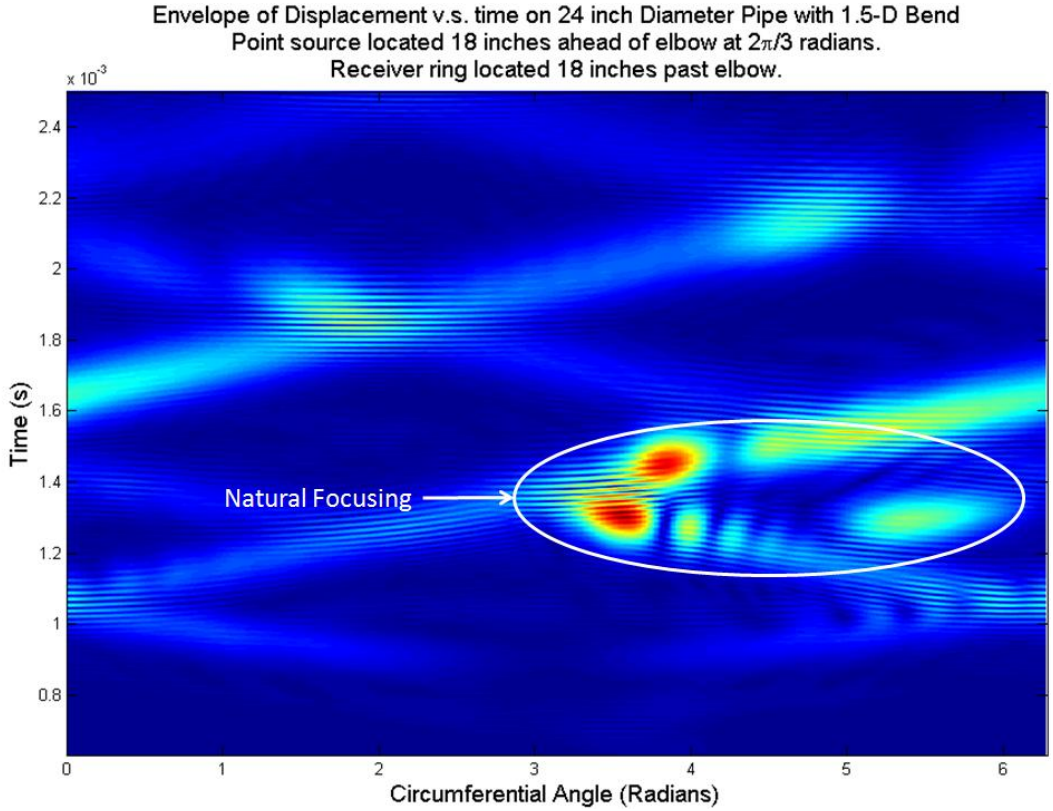

Figure 5.20
Natural focusing from a point source on a pipe with an elbow. The figure is the same as Figure 5.19, except that the region with the focused energy is outlined with a white ellipse.

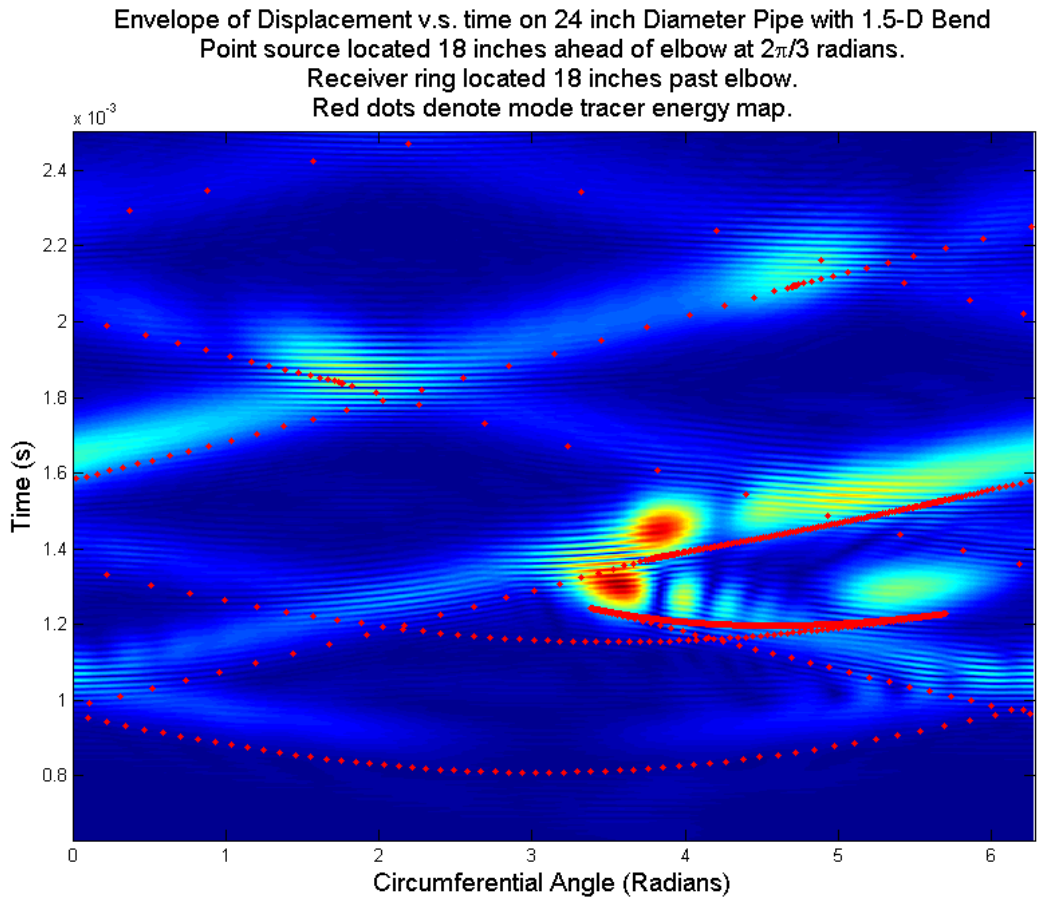

Figure 5.21
Image showing natural focusing on an FEM model of a pipe with an elbow. This image contains the same FEM information as that of Figure 5.19, but this image also contains red dots that represent mode tracing predictions of how the energy of the point source placed ahead of the elbow will map to this location past the elbow. Regions of high densities of red dots denote predictions of greater wave energy. Regions of sparse red dots denote regions of low wave energy.

Once again, there is outstanding agreement between the results obtained by the mode tracing techniques of this dissertation and FEM simulations of guided wave propagation. It is anticipated that the contribution of this work to guided wave mechanics and understanding will lead to further innovations. The methods described here are applicable to many facets of guided wave propagation besides those discussed in this dissertation and are expected to provide a basis for future research studies.

Chapter 6 Summary and Concluding Remarks

A new understanding of guided wave propagation has been developed in this dissertation. The innovative ideas in this research were first introduced as intuitive and hypothetical, and then fleshed out by linking to relevant and established theories. Validation was then brought about using of finite element analyses. The tools were applied to important current problems related to pipes with elbows to gain valuable insights accompanied by numerical proofs.

This new understanding made use of the fact that guided waves require a thickness resonance in order to exist, and that they do not change their direction of propagation without a physical driver. It was shown that the direction a guided wave mode would take across a waveguide can be deterministically calculated. This work represents a breakthrough for guided wave understanding and answers some important questions surrounding guided wave propagation in pipes with elbows for the first time.

This dissertation describes a new tool for studying guided wave propagation in geometrically complex structures. As the tool has not yet been developed to the same level as prior analytical approaches, there is opportunity for future work. The new understanding lays a foundation for additional breakthroughs in guided wave inspection technology. For instance, the method has been shown to focus guided wave energy at arbitrary regions of a pipeline in and beyond an elbow. It also enables guided wave energy to be steered to arbitrary regions of interest in a waveguide with complex geometry.

Prior to this research, it was not fully understood if and when full guided wave coverage occurred in bent pipe waveguides. The new tool explains why 45-degree elbow bends are more detrimental to axi-symmetric wave propagation than are 90-degree elbow bends. It also provides a foundation for new abilities in signal processing, and will potentially become a design instrument for more capable sensor hardware systems.

Perhaps the most important derivative contribution of the discoveries included in this dissertation is the introduction of the elbow transfer function that maps energy impinging on one side of an elbow to the configuration it will take when exiting the elbow. This transfer function is a function of the bend radius of the pipe elbow, the pipe diameter, and the bend angle of the elbow, and is independent of frequency and wave speed. It can be consulted to determine how axi-

symmetric or other profiles of energy impinging on an elbow will behave throughout the elbow and how they will exit the elbow.

This research demonstrates a forward focusing model for controlling guided wave energy beyond elbows in pipelines. As such, it represents significant contributions to guided wave inspection practice in real piping systems, and may be the first forward focusing apparatus for guided wave examinations of piping beyond elbows.

Furthermore, the developments here were given as independent of wave frequency, wave speed, and excitation properties such as source shape, actuation characteristics, pulse width, etc. An assortment of frequencies, source types, geometries, and structural materials, have been modeled with Finite Element Method simulations to compare numerical studies with the results obtained in this dissertation. Remarkable convergence was shown for the respective scenarios.

In summary, the major contributions of this work are as follows:

- introduction of new, validated, methods for understanding guided wave propagation that enable the investigation of geometrically complex waveguides such as pipes that contain elbows;
- introduction of the elbow as a transfer function;
- explanation as to why 45-degree elbows are more disruptive to practical guided wave tests than are 90-degree elbows;
- introduction of determinacy and control as to where guided wave energy will travel in a waveguide of complex geometry—the elimination of blind spots in guided wave inspections;
- new ability to focus guided wave energy at arbitrary locations of interest in pipes in and beyond an elbow;
- ability to control guided waves in waveguides of complex geometries; and
- introduction of a foundation for many future improvements to guided wave inspection technology such as but not limited to:
    - signal processing improvements;
    - increased understanding of guided wave mechanics for a broad range of generic waveguide geometries;
    - responsible implementation of guided wave technology for piping and other applications; and

- improvements to guided wave inspection hardware and software systems.

This work was theoretically driven and was demonstrated through FEM simulations with ABAQUS EXPLICIT. It offers:

- insights into the governing physics of guided waves as applied to pipeline systems with elbows;
- determination of the elbow transfer function; and
- unlocks new advancements for signal processing to accommodate analysis of regions beyond an elbow in a pipeline.

The developments here represent a new approach to understanding guided wave physics and will no doubt form the basis for new advances in guided wave inspection technologies and tooling. Several such advances include focusing beyond an elbow, signal design for maximizing wave coverage, understanding of wave coverage in complex shapes, signal processing in waveguides of complex shapes, and improved resolution and characterization of detected flaws. The progress made gives rise to many new exciting ways to further our understanding and practical implementation of guided wave technologies.

References

[1] The Electric Power Research Institute, "Testing of Ultrasonic Guided Waves for Pipe Evaluation," EPRI1000445, The Electric Power Research Institute, 2000.

[2] W. Zhu, J. L. Rose, J. N. Barshinger, and V. S. Agarwal, "Ultrasonic Guided Wave NDT for Hidden Corrosion Detection," Res Nondestr Eval, vol. 10, pp. 206-225, 1998.

[3] David N Alleyne and Peter Cawley, "Optimization of Lamb Wave Inspection Techniques," NDT&E International, vol. 25, no. 1, pp. 11-22, 1992.

[4] Bastien Chapuis, Nicolas Terrien, and Daniel Royer, "Excitation and Focusing of Lamb Waves in a Multilayered Anisotropic Plate," Journal of the Acoustical Society of America, vol. 127, no. 1, pp. 198-203, 2010.

[5] Y. Chen and L. Guo, "On Group Velocity of Elastic Waves, in an Anisotropic Plate," Journal of Sound and Vibration, vol. 254, no. 4, pp. 227-232, 2005.

[6] Lingyu Yu and Victor Giurgiutiu, "In Situ 2-D Piezoelectric Wafer Active Sensors Arrays for Guided Wave Damage Detection," Ultrasonics, vol. 48, pp. 117-134, 2008.

[7] Fei Yan and Joseph L. Rose, "Guided Wave Phased Array Beam Steering in Composite Plates," Health Monitoring of Structural and Biological Systems, vol. 6532, 2007.

[8] Fei Yan, Ultrasonic Guided Wave Phased Array for Isotropic and Anisotropic Plates; Ph.D Dissertation.: The Pennsylvania State University, 2008.

[9] Paul D. Wilcox, "Omni-Directional Guided Wave Transducer Arrays for the Rapid Inspection of Large Areas of Plate Structures," IEEE Transactions on Ultrasonics, Ferroelectrics, and Frequency Control, vol. 50, no. 6, pp. 699-709, 2003.

[10] Zhongqiing Su, Lin Ye, and Ye Lu, "Guided Lamb waves for identification of damage in composite structures: A review," Journal of Sound and Vibration, vol. 295, pp. 753-780, 2006.

[11] Francesco and Cawley, Peter Simonetti, "On the Nature of Shear Horizontal Wave Propagation in Elastic Plates Coated with Viscoelastic Materials," Proceedings of the Royal Society A, vol. 460, pp. 2197-2221, 2004.

[12] F Simonetti and P. Cawley, "A Guided Wave Technique for the Characterization of Highly Attenuative Viscoelastic Materials," in Review of Quantitative Nondestructive Evaluation, vol. 22, 2003, pp. 1235-1242.

[13] Yijun Shi, Analysis of Optimum Lamb Wave Tuning; Ph.D Dissertation.: Massachusetts Institute of Technology, 2001.

[14] K.I. Salas and C.E.S. Cesnik, "Guided Wave Structural Health Monitoring Using CLoVER Transducers in Composite Materials," Smart Materials and Structures, vol. 19, 2009.

[15] Joseph L. Rose, "Ultrasonic Guided Waves in Structural Health Monitoring," Key Engineering Materials, vol. 270-273, pp. 14-21, 2004.

[16] Joseph L Rose, "A Baseline and Vision of Utrasonic Guided Wave Inspection Potential," Journal of Pressure Vessel Technology, vol. 124, pp. 273-282, 2002.

[17] J.L. Rose, S.P. Pelts, and M.J. Quarry, "A Comb Transducer Model for Guided Wave NDE," Ultrasonics, vol. 36, pp. 163-169, 1998.

[18] S.I. Rokhlin and L. Wang, "Ultrasonic Waves in Layered Anisotropic Media: Characterization of Multidirectional Composites," International Journal of Solids and Structures, vol. 39, pp. 4133-4149, 2002.

[19] S. Mahadev Prasad, Krishnan Balasubramaniam, and C.V. Krishnamurthy, "Structural Health Monitoring of Composite Structures Using Lamb Wave Tomography," Smart Materials and Structures, vol. 13, pp. N73-N79, 2004.

[20] R.S.C. Monkhouse, P.W. Wilcox, M.J.S. Lowe, R.P. Dalton, and P. Cawley, "The Rapid Monitoring of Structures Using Interdigital Lamb Wave Transducers," Smart Mater. Struct., vol. 9, pp. 304-309, 2000.

[21] Kritsakorn Luangvilai, Wonsiri Punurai, and Laurence J. Jacobs, "Guided Lamb Wave Propagation in Composite Plate/Concrete Component," Journal of Engineering Mechanics, pp. 1337-1341, 2002.

[22] Jaya Prakash Koduru and Joseph L. Rose, "Guided Wave Annular Array Sensor Design for Improved Tomographic Imaging," Review of Quantitative Nondestructive Evaluation, vol. 28, pp. 658-665, 2009.

[23] Doyoun Kim, Younho Cho, and Joonhyun Lee, "Assessment of Wall-Thinning in Carbon Steel Pipe by Using Laser-Generated Guided Wave," Nuclear Engineering and Technology, vol. 42, no. 5, pp. 546-551, 2010.

[24] Hayashi, Takahiro; Kawashima, Koichiro; Sun, Zongqi; Rose, Joseph L., "Guided Wave Dispersion Curves for a Bar with an Arbitrary Cross-Section, A Rod and Rail Example," Ultrasonics, vol. 41, pp. 175-183, 2003.

[25] Takahiro and Kawashima, Koichiro Hayashi, "Multiple Reflections of Lamb Waves at a Delamination," Ultrasonics, pp. 193-197, 2002.

[26] Thomas R. Hay, Lou Wei, and Joseph L. Rose, "Rapid Inspection of Composite Skin-Honeycomb Core Structures with Ultrasonic Guided Waves," Journal of Composite Materials, vol. 37, no. 10, pp. 929-939, 2003.

[27] Thomas R. Hay, Aspects of Guided Waves in Structural Health Monitoring; Ph.D Dissertation.: The Pennsylvania State University, 2004.

[28] N. Guo and P. Cawley, "The interaction of Lamb waves with delaminations in composite laminates," The Journal of the Acoustical Society of America, vol. 94, no. 4, pp. 2240-2246, 1993.

[29] Sebastien Grondel, Christophe Paget, Christophe Delebarre, Jamal Assaad, and Klas Levin, "Design of Optimal Configuration for Generating A Lamb Mode in a Composite Plate Using Piezoceramic Transducers," J. Acoustical Soc. Am., vol. 112, no. 1, pp. 84-90, 2002.

[30] Victor Giurgiutiu, "Tuned Lamb Wave Excitation and Detection with Piezoelectric Wafer Active Sensors for Structural Health Monitoring," Journal of Intelligent Material Systems and Structures, vol. 16, pp. 291-305, 2005.

[31] Huidong Gao and Joseph L. Rose, "Impact of Ultrasonic Guided Wave Transducer Design on Health Monitoring of Composite Structures," Health Monitoring of Structural and Biological Systems, vol. 6532, 2007.

[32] Huidong Gao, Ultrasonic Guided Wave Mechanics for Composite Material Structural Health Monitoring; Ph.D Dissertation.: Pennsylvania State University, 2007.

[33] Takashi Furukawa and Ichiro Komura, "Simulation and Visualization of Guided Wave Propagation by Large-Scale 3D FEM," E-Journal of Advanced Maintenance, vol. 3, no. 3, 2011.

[34] J.J. Ditri and J.L. Rose, "Excitation of Guided Waves in Generally Anisotropic Layers Using Finite Sources," Transactions of the ASME, vol. 61, pp. 330-338, 1994.

[35] Vinay Dayal and Vikram K. Kinra, "Leaky Lamb Waves in an Anisotropic Plate. I: An Exact Solution and Experiments," Journal of the Acoustical Society of America, vol. 85, no. 6, pp. 2268-2276, 1989.

[36] D.E. Chimenti and Adnan H. Nayfeh, "Ultrasonic Reflection and Guided Wave Propagation in Biaxially Laminated Composite Plates," Journal of the Acoustical Society of America, pp. 1409-1415, 1990.

[37] P. Cawley, "The Rapid Non-Destructive Inspection of Large Composite Structures," Composites, vol. 25, no. 5, pp. 351-357, 1994.

[38] Luke Breon, Ultrasonic Guided Wave Thickness Measurement of Isotropic Plate-Like Structures; M.S. Thesis.: The Pennsylvania State University, 2008.

[39] David N. Alleyne, The Nondestructive Testing of Plates Using Ultrasonic Lamb Waves; Ph.D Dissertation. London: University of London, 1991.

[40] Shi-Chang Wooh and Yijun Shi, "Synthetic Phase Tuning of Guided Waves," IEEE Transactions of Ultrasonics, Ferroelectrics, and Frequency Control, vol. 48, no. 1, pp. 209-223, 2001.

[41] Viktorov, Rayleigh and Lamb Waves. New York: Plenum Press, 1967.

[42] T.R. Hay, R.L. Royer, Huidong Gao, Xiang Zhao, and J.L. Rose, "A comparison of embedded sensor Lamb wave ultrasonic tomography approaches for material loss detection," Smart Materials and Structures, vol. 15, pp. 946-951, 2006.

[43] Filippo Bellan et al., "A New Design and Manufacturing Process for Embedded Lamb Waves Interdigital Transducers Based on Piezopolymer Film," Sensors and Actuators, vol. A, no. 123-124, pp. 379-387, 2005.

[44] Ismael Nunez, Ros K. Ing, Carlos Negreira, and Mathias Fink, "Transfer and Green function based on Modal Analysis for Lamb Waves Generation," Journal of the Acoustical Society of America, pp. 2370-2378, 2000.

[45] Buli Xu and Victor Giurgiutiu, "Single Mode Tuning Effects on Lamb Wave Time Reversal with Piezoelectric Wafer Active Sensors for Structural Health Monitoring," Journal of Nondestructive Evaluation, vol. 26, pp. 123-134, 2007.

[46] P.D. Wilcox, M.J.S. Lowe, and P. Cawley, "Mode and Transducer Selection for Long Range Lamb Wave Inspection," Journal of Intelligent Material Systems and Structures, vol. 12, pp. 553-565, 2001.

[47] Ajay Raghavan and Carlos E.S. Cesnik, "Modeling of Piezoelectric-based Lamb-wave Generation and Sensing for Structural Health Monitoring," Smart Structures and Materials, vol. 5391, pp. 419-430, 2004.

[48] C.W. and Cawley, P. Chan, "Lamb Waves in Highly Attenuative Plastic Plates," Journal of the Acoustical Society of America, vol. 104, no. 2, pp. 874-881, 1998.

[49] D. P., Hutchins, D. A. Jansen, "Lamb Wave Tomography," 1990 Ultrasonics Symposium, pp. 1017-1020, 1990.

[50] Younho Cho, Derrick D. Hongerholt, and Joseph L. Rose, "Lamb Wave Scattering Analysis for Reflector Characterization," IEEE Transactions on Ultrasonics, Ferroelectrics and Frequency Control, vol. 44, no. 1, pp. 44-52, 1997.

[51] Wenhao Zhu and Joseph L. Rose, "Lamb Wave Generation and Reception with Time-Delay Periodic Linear Arrays: A BEM Simulation and Experimental Study," IEEE Transactions on Ultrasonics, Ferroelectrics, and Frequency Control, vol. 46, no. 3, pp. 654-664, 1999.

[52] Sung-Ho Joh et al., "Joint Inversion for Apparent Phase Velocities of Rayleigh and Love Waves," GeoCongress 2006, 2006.

[53] Victor Giurgiutiu and JingJing Bao, "Embedded-ultrasonics Structural Radar for In Situ Structural Health Monitoring of Thin-wall Structures," Structural Health Monitoring, vol. 3, no. 2, pp. 121-140, 2004.

[54] P.A. Doyle, "Depth Measurement for Cracks in Corners Using Ultrasonic Rayleigh Waves," Journal of Nondestructive Evaluation, vol. 5, no. 3/4, pp. 179-187, 1986.

[55] I.G. Scott and C.M. Scala, "A Review of Non-destructive Testing of Composite Materials," NDT International, pp. 75-86, 1982.

[56] J.L. Rose, A. Pilarski, and J.J. Ditri, "An Approach to Guided Wave Mode Selection for Inspection of Laminated Plate," Journal of Reinforced Plastics and Composites, vol. 12, pp. 536-544, 1993.

[57] Bernard Hosten and Michel Castaings, "Transfer matrix of multilayered absorbing and anisotropic media. Measurements and simulations of ultrasonic wave propagation through composite materials," The Journal of the Acoustical Society of America, vol. 94, no. 3, pp. 1488-1495, 1993.

[58] Adnan H. Nayfeh, "The General Problem of Elastic Wave Propagation in Multilayered Anisotropic Media," Journal of the Acoustical Society of America, vol. 89, no. 4, pp. 1521-1531, 1991.

[59] J. Vishnuvardhan, Ajith Muralidharan, C.V. Krishnamurthy, and Krishnan Balasubramaniam, "Structural Health Monitoring of Anisotropic Plates Using Ultrasonic Guided Wave STMR Array Patches," NDT&E International, vol. 42, pp. 193-198, 2009.

[60] Calvin S. Wang, Fan Wu, and Fu-Kuo Chang, "Structural Health Monitoring from Fiber-reinforced Composites to Steel-reinforced Concrete," Smart Materials and Structures, vol. 10, pp. 448-552, 2001.

[61] S.P. Pelts and J.L. Rose, "Source Influence Parameters on Elastic Guided Waves in an Orthotropic Plate," Journal of the Acoustical Society of America, vol. 99, no. 4, pp. 2124-2129, 1996.

[62] Alexander Velichko and Paul D. Wilcox, "Modeling the excitation of guided waves in generally anisotropic multilayered media," The Journal of the Acoustical Society of America, vol. 121, no. 1, pp. 60-69, 2007.

[63] K.S. Tan, N. Guo, and B.S. Wong, "Experimental Evaluation of Delaminations in Composite Plates by the Use of Lamb Waves," Composites Science and Technology, vol. 53, pp. 77-84, 1995.

[64] M.J.S. Lowe and P. Cawley, "The Applicability of Plate Wave Techniques for the Inspection of Adhesive and Diffusion Bonded Joints," Journal of Nondestructive Evaluation, vol. 13, no. 4, pp. 185-200, 1994.

[65] Victor Giurgiutiu, Andrei N. Zagrai, and Jing Jing Bao, "Piezoelectric Wafer Embedded Active Sensors for Aging Aircraft Structural Health Monitoring," Structural Health Monitoring, vol. 1, no. 1, pp. 41-60, 2002.

[66] Paul Fromme, Paul D. Wilcox, Michael J.S. Lowe, and Peter Cawley, "On the Development and Testing of a Guided Ultrasonic Wave Array for Structural Integrity Monitoring," IEEE Transactions on Ultrasonics, Ferroelectrics, and Frequency Control, vol. 53, no. 4, pp. 777-785, 2006.

[67] Victor Giurgiutiu and Adrian Cuc, "Embedded Non-destructive Evaluation for Structural Health Monitoring, Damage Detection, and Failure Prevention," The Shock and Vibration Digest, vol. 37, no. 2, pp. 83-105, 2005.

[68] Jeong-Beom Ihn and Fu-Kuo Chang, "Detection and Monitoring of Hidden Fatigue Crack Growth Using a Built-in Piezoelectric Sensor/Actuator Network: I. Diagnostics," Smart Materials and Structures, vol. 13, pp. 609-620, 2004.

[69] E. Rhian Green and W.A. Green, "A Computational Method for Wave Propagation from a Point Load in an Anisotropic Material," Ultrasonics, vol. 38, pp. 262-266, 2000.

[70] L. Knopoff, "A Matrix Method for Elastic Wave Problems," Bulletin of the Seismological Society of America, vol. 54, no. 1, pp. 431-438, 1964.

[71] Philip W. Loveday and Craig S. Long, "Time Domain Simulation of Piezoelectric Excitation of Guided Waves in Rails Using Waveguide Finite Elements," Sensors and Smart Structures Technologies for Civil, Mechanical and Aerospace Systems, vol. 6529, 2007.

[72] J.D. Achenbach and Y. Xu, "Wave Motion in an Isotropic Elastic Layer Generated by a Time-harmonic point load of arbitrary direction," J. Acoustic Soc. Am., vol. 106, no. 1, pp. 83-90, 1999.

[73] Ali Khojasteh, Mohammad Rahimian, Ronald Y.S. Pak, and Morteza Eskandari, "Asymmetric Dynamic Green's Functions in a Two-Layered Transversely Isotropic Half-Space," Journal of Engineering Mechanics, pp. 777-787, 2008.

[74] William T. Thompson, "Transmission of Elastic Waves Through a Stratified Solid Medium," Journal of Applied Physics, Vol. 21, 1950.

[75] Adnan H. Nayfeh, "Elastic Wave Propagation in Fluid-loaded Multiaxial Anisotropic Media," Journal of the Acoustical Society of America, vol. 88, no. 2, pp. 542-549, 1991.

[76] R. Long, K Vine, M.J.S Lowe, and P. Cawley, "The Effect of Soil Properties on Acoustic Wave Propagation in Buried Iron Water Pipes," Review of Quantitative Nondestructive Evaluation, vol. 21, pp. 1310-1317, 2002.

[77] Bert A. Auld and Gordon S. Kino, "Normal Mode Theory for Acoustic Waves and its Application to the Interdigital Transducer," IEEE Transactions on Electron Devices, vol. 8, no. 10, pp. 898-908, 1971.

[78] Ivan Bartoli, Alessandro Marzani, Fransesco Lanza di Scalea, and Erasmo Viola, "Modeling Wave Propagation in Damped Waveguides of Arbitrary Cross-Section," Journal of Sound and Vibration, vol. 295, pp. 685-707, 2006.

[79] Michael J.S. Lowe, "Matrix Techniques for Modeling Ultrasonic Waves in Multilayered Media," IEEE Transactions on ULtrasonics, Ferroelectrics, and Frequency Control, vol. 42, no. 4, pp. 525-542, 1995.

[80] B.N. Pavlakovic, M.J.S. Lowe, and P. Cawley, "High Frequency Low-Loss Ultrasonic Modes in Imbedded Bars," Journal of Applied Mechanics, vol. 68, pp. 67-75, 2001.

[81] Joseph, L. Rose, "Guided Wave Nuances for Ultrasonic Nondestructive Evaluation," IEEE Transactions on Ultrasonics, Ferroelectrics, and Frequency Control, vol. 47, no. 3, pp. 575-583, 2000.

[82] L.P. Soli and B.A. Auld, "Elastic Waves in Free Anisotropic Plates," The Journal of the Acoustical Society of America, vol. 54, no. 1, pp. 50-65, 1973.

[83] Takahiro and Murase, Morimasa Hayashi, "Defect Imaging with Guided Waves in a Pipe," J. Acoustical Soc. Am., vol. 117, no. 4, pp. 2134-2140, 2005.

[84] E.C. Shang, "Source Depth Estimation in Waveguides," The Journal of the Acoustical Society of America, vol. 77, no. 4, pp. 1413-1418, 1985.

[85] Carlos H.F. Alves, Kevin Snook, Timothy Ritter, and K. Kirk Shung, "High Frequency Single Element and Annular Array Transducers Incorporating PVDF," Medical Imaging 2000: Ultrasonic Imaging and Signal Processing, vol. 3982, pp. 116-121, 2000.

[86] Jenifer E. Michaels Michaels and Thomas E., "An Integrated Strategy for Detection and Imagin of Damage Using a Spatially Distributed Array of Piezoelectric Sensors," in Health Monitoring of Structural and Biological Systems, vol. 6532, 2007.

[87] J. Pena-Macias, M.C. Perez, R. Martinez-Ona, Y. Gomez-Ullate, and F Montero De Espinosa, "Phased-array Transducers for Damage Detection in Aircraft Structures," Fatigue and Fracture of Engineering Materials & Structures, vol. 31, pp. 1019-1030, 2008.

[88] Li Zhang, Guided Wave Focusing Potential in Hollow Cylinders; Ph.D Dissertation.: The Pennsylvania State University, 2005.

[89] Li Yibo, Sun Liying, Song Zhidong, and Zhang Yuankai, "Study on Energy Attenuation of Ultrasonic Guided Waves Going Through Girth Welds," Ultrasonics, vol. 44, pp. 1111-1116, 2006.

[90] Li-ying Sun, "Study on Excitation Frequency of Longitudinal and Torsional Guided Waves," 2009 Chineese Control and Decision Conference (CCDC 2009), 2009.

[91] Siqueira, M.H.S.;Gatts, C.E.N.;DaSilva, R.R.;Rebello, J.M.A., "The use of Ultrasonic Guided Waves and Wavelets Analysis in Pipe Inspection," Ultrasonics, vol. 41, pp. 785-797, 2004.

[92] Shin, Hyeon Jae; Rose, Joseph L., "Guided Waves by Axisymmetric and Non-Axisymmetric Surface Loading on Hollow Cylinders," Ultrasonics, vol. 37, pp. 355-363, 1999.

[93] Hyeon Jae Shin and Joseph L. Rose, "Guided Wave Tuning Principles for Defect Detection in Tubing," Journal of Nondestructive Evaluation, vol. 17, no. 1, pp. 27-36, 1998.

[94] Hideo Nishino, Yasuhiro Tanaka, Yasuhisa Kato, and Kenichi Yoshida, "Efficient Generation and Detection of a Guided Wave in a Pipe Using Guided Wave Reflectors," Journal of Solid Mechanics and Materials Engineering, vol. 3, no. 2, pp. 267-277, 2009.

[95] Jing Mu and Joseph L. Rose, "Guided Wave Propagation and Mode Differentiation in Hollow Cylinders with Viscoelastic Coatings," Journal of the Acoustical Society of America, vol. 124, no. 2, pp. 866-874, 2008.

[96] Jing Mu, Guided Wave Propagation and Focusing in Viscoelastic Multi-Layered Hollow Cylinders; Ph.D Dissertation.: The Pennsylvania State University, 2008.

[97] Mohr, Wolfgang; Holler, Paul, "On Inspection of Thin-Walled tubes for Transverse and Longitudinal Flaws by Guided Ultrasonic Waves," vol. SU-23, no. 5, pp. 369-374, 1976.

[98] Wei Luo and Joseph L. Rose, "Phased Array Focusing with Guided Waves in a Viscoelastic Coated Hollow Cylinder," The Journal of the Acoustical Society of America, vol. 121, no. 4, pp. 1945-1955, 2007.

[99] John M. Liu, Carrie E. Davis, and Terri M. Regin, "Ultrasonic Guided Wave Technology for Non-invasive Assessment of Corrosion-induced Damage in Piping for Pollution Prevention in DOD Fuel Storage Facilities," 2011.

[100] Li, Jian; Rose, Joseph L., "Natural Beam Focusing of Non-Axisymmetric Guided Waves in Large-Diameter Pipes," Ultrasonics, vol. 44, pp. 35-45, 2006.

[101] Li, Jian; Rose, Joseph L., "Excitation and Propagation of Non-Axisymmetric Guided Waves in a Hollow Cylinder," Journal of the Acoustical Society of America, vol. 109, no. 2, pp. 457-464, 2001.

[102] Li, Jian; Rose, Joseph L., "Angular-Profile Tuning of guided Waves in Hollow cylinders Using a Circumferential Phased Array," IEEE Transactions on ultrasonics, ferroelectrics, and frequency control, vol. 49, no. 12, pp. 1720-1729, 2002.

[103] Jian Li, Longitudinal Flexural Mode Utility in Quantitative Guided Wave Evaluation; Ph.D Dissertation.: The Pennsylvania State University, 2001.

[104] John J. and Rose, Joseph L. Ditri, "Excitation of Guided Elastic Wave Modes in Hollow Cylinders by Applied Surface Tractions," vol. 72, no. 7, 1992.

[105] A Demma, P. Cawley, M. Lowe, A.G. Roosenbrand, and B. Pavlakovic, "The Reflection of Guided Waves From Notches in Pipes: A guide for interpreting corrosion measurements," NDT&E International, vol. 37, pp. 167-180, 2004.

[106] Davies, Jacob, and Cawley, Peter, "The Application of Synthetic Focusing for Imaging Crack-Like-Defects in Pipelines Using Guided Waves," vol. 56, no. 4, 2009.

[107] Jyin-Wen Cheng, Shiuh-Kuang Yang, Ping-Hung Lee, and Chi-Jen Huang, Attenuation of Guided Wave Propagation by the Insulation Pipe, 2012.

[108] Thomas R. Hay and Joseph L. Rose, "Flexible PVDF Comb Transducers for Excitation of Axisemmetric Guided Waves in Pipe," Sensors and Actuators, vol. 100, pp. 18-23, 2002.

[109] Joseph L. Rose, Li Zhang, Michael J. Jr. Avoili, and Peter J. Mudge, "A Natural Focusing Low Frequency Guided Wave Experiment for the Detection of Defects Beyond Elbows," in ASME Pressure Vessels and Piping Conference (PVP2003), vol. 127, 2005, pp. 310-316.

[110] Rose, Joseph L. and Zhao, Xiaoliang, "Pipe Elbow Inspection with Guided Waves," in Roma 2000 15th WCNDT, vol. 15, Roma, 2000.

[111] Hayashi, Takahiro; Kawashima, koichiro; Sun, Zongqi; Rose, Joseph L., "Guided Wave Propagation Mechanics Across a Pipe Elbow," vol. 127, no. 322, 2005.

[112] Demma, A.;Cawley, P.; Lowe, M.J.S., "Guided Waves in Curved Pipes," Review of Quantitative Nondestructive Evaluation, vol. 21, pp. 157-164, 2002.

[113] Demma, A.; Cawley, P.; Lowe, M.J.S., "Mode Conversion of Longitudinal and Torsional Guided Modes due to Pipe Bends," Review of Progress in Quantitative Nondestructive Evaluation, vol. 20, 2001.

[114] Demma, A.; Cawley, P.; Lowe M.;Pavlakovic, B., "The Effect of Bends on the Propagation of Guided Waves in Pipes," vol. 127, no. 322, 2005.

[115] A. J. Brath, F. Simonetti, P. B. Nagy, and G. Instanes, "Guided Wave Radiation from a Point Source in the Proximity of a Pipe Bend," 40th Annual Review of Progress in Quantitative Nondestructive Evaluation, vol. 40, pp. 316-323, 2014.

[116] Luke Breon, Michael Quarry, Ehsan Khajeh, and Joseph Rose, "System and method for focusing guided waves beyond curves in test structures," Application US 20140278193 A1, March 15, 2013.

[117] M. El Bakkali, A. Lhemery, V Baronian, and S Grondel, "A modal formulation for the propagation of guided waves in straight and curved pipes and the scattering at their junction," in 12th Anglo-French Physical Acoustics Conference (AFPAC2012), 2014.

[118] R. M. Sanderson, D. A Hutchins, D. R. Billson, and P. J. Mudge, "The Investigation of Guided Wave Propagation Around a Pipe Bend Using an Analytical Modeling Approach," vol. 133, no. 3, pp. 1404-1414, 2013.

[119] M.J.S. Lowe and P. Cawley, Long Range Guided Wave Inspection Usage - Current Comercial Capabilities and Research Directions, 2006.

[120] Lawrenson, Christopher C.;Lafleur, Dwynn L.; Shields, Douglas F., "The Solution for the Propagation of Sound in a Toroidal Waveguide with Driven Walls (The Acoustitron)," vol. 103, no. 3, 1998.

[121] Dong-Lai Liu and Robert C. Waag, "Propagation and Backpropagation for Ultrasonic Wavefront Design," IEEE Transactions on Ultrasonics, Ferroelectrics, and Frequency Control, vol. 44, no. 1, 1997.

[122] B.A. Auld and J.C. Moulder, "Review of Advances in Quantitative Eddy Current Nondestructive Evaluation," Journal of Nondestructive Evaluation, vol. 18, no. 1, pp. 3-36, 1999.

[123] D. Bates, G Smith, D. Lu, and J. Hewitt, "Rapid Thermal Non-destructive Testing of Aircraft Components," Composites Part B: engineering, vol. 31, pp. 175-185, 2000.

[124] George A. Matzkanin and H. Thomas Yolken, "Nondestructive Evaluation Techniques for Detecting Hidden Corrosion," The AMMTIAC Quarterly, vol. 2, no. 2.

[125] Dong Fei, D.E. Chimenti, and Sorin V. Teles, "Material Property Estimation in Thin Plates Using Focused, Synthetic-aperture Acoustic Beams," J. Acoustical Soc. Am., vol. 113, no. 5, pp. 2599-2610, 2003.

[126] Chen Ciang Chia, Jung-Ryul Lee, and He-Jin Shin, "Hot Target Inspection Using a Welded Fibre Acoustic Wave Piezoelectric Sensor and a Laser-Ultrasonic Mirror Scanner," Measurement Science and Technology, vol. 20, 2009.

[127] Na Young Lee, Seung Gi Lee, Kyung Ha Ryu, and Il Soon Hwang, "On-Line Monitoring System Development for Single-Phase Flow Accelerated Corrosion," Transactions of the 17th International Conference on Structural Mechanics in Reactor Technology, pp. 761-767, 2007.

[128] Jung-Ryul Lee, Junji Takatsubo, Nobuyuki Toyoma, and Dong-Hoon Kang, "Health Monitoring of Complex Curved Structures Using an Ultrasonic Wavefield Propagation Imaging System," Measurement Science and Technology, vol. 18, pp. 3816-3824, 2007.

[129] B. Hosten and M. Castaings, "Comments on the Ultrasonic Estimation of the Viscoelastic Properties of Anisotropic Materials," Composites, vol. 39, pp. 1054-1058, 2008.

[130] J.D. Achenbach, Wave Propagation in Elastic Solids. Amsterdam: Elsevier Science Publishers B.V., 1975.

[131] B.A. Auld, Acoustic Fields and Waves in Solids, 2nd ed. Malabar, FL: Kreiger Publishing Company, Inc., 1990, vol. I.

[132] B.A. Auld, Acoustic Fields and Waves in Solids, 2nd ed. Malabar, FL: Krieger Publishing Company, Inc, 1990, vol. II.

[133] Karl F. Graff, Wave Motion in Elastic Solids. new York: Dover Publications, Inc., 1991.

[134] Joseph L. Rose, Ultrasonic Waves in Solid Media. Cambridge: Cambridge University Press, 1999.

[135] Martin Redwood, Mechanical Waveguides. New York: Pergamon Press LTD., 1960.

[136] Yoseph Bar-Cohen, "Emerging NDE Technologies and Challenges at the Beginning of the 3rd Millenium -- Part 2, Part 1," vol. 5, no. 1, 2000.

[137] Mathias Fink, "Time-Reversal Mirrors," Journal of Physics D: Applied Physics, vol. 26, pp. 1333-1350, 1993.

[138] Chakroun, Najet; Fink, Mathias; Wu, Francois, "Ultrasonic non-Destructive Testing with Time Reversal Mirrors," SPIE, vol. 1773, no. 191, pp. 191-199, 1992.

[139] Prada, Claire; Fink, Mathias, "Eigenmodes of the Time Reversal Operator: A Solution to Selective Focusing in Multiple-Target Media," Wave Motion, vol. 20, pp. 151-163, 1994.

[140] Prada, Claire; Kerbrat, Estelle; Cassereau, Didier; Fink, Mathias, "Time Reversal Techniques in Ultrasonic Non-Destructive Testing of Scattering Media," Inverse Problems, vol. 18, pp. 1761-1773, 2002.

[141] Hak-Joon Kim, Sung-Jin song, Jung-Ho Seo, Jae-Hee Kim, and Heung-Sup Eom, "Time Reversal Technique for Ultrasonic Guided Wave Inspections," vol. 321-323, 2006.

[142] H. C. Song, W. A. Kuperman, W. S. Hodgkiss, T. Akal, and C. Ferla, "Iterative Time Reversal in the Ocean," Journal of the Acoustical Society of America, vol. 105, no. 6, pp. 3176-3184, 1999.

[143] Jean-Louis Thomas, Philippe Roux, and Mathias Fink, "Inverse Scattering Analysis with an Acoustic Time-Reversal Mirror," Physical Review Letters, vol. 72, no. 5, pp. 637-640, 1994.

[144] Hyun Woo Park, Seung Bum Kim, and Hooon Sohn, "Understanding a Time Reversal Process in Lamb Wave Propagation," Wave Motion, pp. 1-17, 2009.

[145] Yunus A. Cengel and John M. Cimbala, Fluid Mechanics; Fundamentals and Applications. New York, NY: McGraw-Hill, 2006.

[146] D. Reilly, P. Leggat, and A. McNab, "3D Ultrasonic Ray Tracing in AutoCAD," in Review of Progress in Quantitative Nondestructive Evaluation, vol. 20, 2001, pp. 587-594.

[147] A. Balvantin, A. Baltazar, and P. Rodriquez, "Characterization of Laser Generated Lamb Wave Modes after Interaction with a Thickness Reduction Discontinuity Using Ray Tracing Theory," Experimental Mechanics, vol. 54, pp. 743-752, 2013.

[148] Thomas E. Barnard, Franz J. Klein, and Lorenzo Resca, "Ray Theory Results and Ray Wavefront Diagrams for the Hyperbolic Cosine Propagation Sound-Speed Profile," IEEE Journal of Oceanic Engineering, 2015.

[149] R. Breeuwer, "Backward Ray Tracing for Ultrasonic Imaging," Ultrasonics Symposium, pp. 401-404, 1990.

[150] A. Gardahaut, K. Jezzine, D. Cassereau, and N. Leymarie, "Simulation of Ultrasonic Wave Propagation in Welds Using Ray-Based Methods," Journal of Physics: Conference Series 498, vol. 498, 2014.

[151] D. Hemzal, R. Jirik, and J. Jan, "Analytical Ray Propagation in FEM Modelling of Ultrasonic Transmission Tomography," IWSSIP 2012, pp. 580-583, 2012.

[152] S. R. Kolkoori et al., "A comparative Study of Ray Tracing and CIVA Simulation for Ultrasonic Examination of Anisotropic Inhomogeneous Austenitic Welds," in Review of Progress in Quantitative Nondestructive Evaluation, vol. 39, 2013, pp. 1043-1050.

[153] G. Muller, "Exact Ray Theory and its Application to the Reflection of Elastic Waves from Vertically Inhomogeneous Media," Geophys. J. R. astr Soc., vol. 21, pp. 261-283, 1970.

[154] J. A. Ogilvy, "An Iterative Ray Tracing Model for Ultrasonic Nondestructive Testing," NDT & E International, vol. 25, no. 1, pp. 3-10, 1992.

[155] J.A Ogilvy, "Ultrasonic Beam Profiles and Beam Propagation in an Austenitic Weld Using a Theoretical Ray Tracing Model," Ultrasonics, vol. 24, pp. 337-347, 1986.

[156] J.A. Ogilvy, "Ultrasonic Reflection Properties of Planar Defects Within Austenitic Welds," Ultrasonics, vol. 26, pp. 318-327, 1988.

[157] S. R. Seshadri, "Ray Theory of the Love Wave Interactions," Journal of Applied Physics, vol. 55, no. 7, pp. 2676-2684, 1984.

[158] Luke J. Breon, Guided Wave Thickness Measurement Tomography for Structural Health Monitoring in Critical Zones of Pipelines; B.S. Thesis. State College: The Pennsylvania State University, 2007.

[159] Zhang Haiyan, Chen Xianhua, Yu Jianbo, and Cao Yaping, "Ultrasonic Guided Wave Tomography of Pipes," ICALIP2010, pp. 1729-1733, 2010.

[160] Kevin R. and Hinders, Mark K. Leonard, "Guided Wave Helical Ultrasonic Tomography of Pipes," Journal of the Acoustical Society of America, vol. 114, no. 2, pp. 767-774, 2003.

[161] Kevin R. Leonard and Mark K. Hinders, "Lamb Wave Tomography of Pipe-like Structures," Ultrasonics, vol. 43, pp. 574-583, 2005.

[162] Erwin Kreyszig, Differential Geometry. New York: Dover Publications Inc., 1991.

[163] D. F. Lawden, Introduction to Tensor Calculus, Relativity and Cosmology. Mineola, New York: Dover Publications, Inc., 2002.

[164] Brian F. Martin and Clyde F. Doolin, Introduction to Differential Geometry for Engineers. New York: Marcel Dekker, 1990.

[165] Absos Ali Shaikh and Joydeep Sengupta, Tensor Calculus. Oxford: Alpha Science International Ltd., 2008.

[166] Clifford Henry Taubes, Differential Geometry Bundles, Connections, Metrics and Curvature. New York: Oxford University Press, Inc., 2011.

[167] Daniel Zwillinger, CRC Standard Mathematical Tables and Formulae. New York: Chapman & Hall/CRC, 2003.

[168] Richard L. Bishop and Samuel I. Goldberg, Tensor Analysis on Manifolds. New York: Dover Publications, Inc, 1980.

[169] Jerry Ginsberg, Engineering Dynamics. New York: Cambridge University Press, 2008.

[170] Li, Jian; Rose, Joseph L., "Implementing Guided Wave Mode Control by Use of a Phased Transducer Array," IEEE Transaction on Ultrasonics, Ferroelectrics, and Frequency Control, vol. 48, no. 3, pp. 761-768, 2001.

[171] Denos C. Gazis, "Three Dimensional Investigation of the Propagation of Waves in Hollow Circular Cylinders. I. Analytical Foundation," vol. 31, no. 5, 1959.

[172] Denos C Gazis, "Exact Analysis of the Plane-Strain Vibration of Thick-Walled Hollow Cylinders," The Journal of the Acoustical Society of America, vol. 30, no. 8, pp. 786-794, 1958.

[173] Leonard Meirovitch, Analytical Methods in Vibrations. New York: Macmillan Publishing Co. Inc., 1967.

[174] Martin H. Sadd, Elasticity Theory, Applications, and Numerics. Burlington: Elsevier Butterworth-Heinemann, 2005.

[175] Pei Chi Chou Pagano and Nicholas J., Elasticity Tensor, Dyadic, and Engineering Approaches. New York: Dover Publications, Inc., 1992.

[176] Philip M. Morse and Herman Feshbach, Methods of Theoretical Physics. Minneapolis: Feshback Publishing, LLC, 1953.

[177] R. C. Hibbler, Engineering Mechanics Dynamics, 10th ed. Upper Saddle River, New Jersey: Pearson Prentice Hall, 2004.

[178] R. Prabhu, M. Drozdz, E. A. Skelton, M. J. S Lowe, and R. V. Craster, "On the use of absorbing layers to simulate the propagation of elastic waves in unbounded isotropic media using commercially available Finite Element packages," NDT&E International, vol. 51, pp. 30-40, 2012.

APPENDIX A

Conventional Theory for Guided Wave Mechanics in Straight Pipes

The conventional approach to guided wave propagation in hollow cylinders is outlined in this appendix. First is a derivation of the dispersion curves for straight pipes. Following this derivation is a brief discussion of the effect of partial loading of a hollow cylinder on the circumferential profile of stress and particle velocity. These constructs form the basic essentials of the conventional understanding of guided wave behavior in straight pipes, particularly for practical examinations of piping and for focusing guided waves in pipes.

While these basics have been built upon and expanded by others such as [96], they will suffice for the purposes of demonstrating the conventional approach to understanding guided wave behavior. The discussion begins with the theory governing torsional wave modes in straight pipes, then covers the generic derivation of conventional guided wave theory for pipes. The derivation follows the work of Gazis [171], Rose [134], and Ditri [104]. This appendix will also serve as a good reference for the theory, as it concatenates the work of these various authors into an annotated summary.

Torsional Wave Modes

First, consider Navier's equation that governs the motion of isotropic elastic media. This foundational relationship is shown in A.1.

$$\mu\nabla^2\boldsymbol{u}+(\lambda+\mu)\nabla\nabla\cdot\boldsymbol{u}=\rho(\partial^2\boldsymbol{u}/\partial t^2) \tag{A.1}$$

The variables μ and λ represent Lame's constants, t represents time, ρ is the density of the medium and $\boldsymbol{u}$ is the displacement vector. Several kinds of modes (longitudinal, torsional, and flexural) exist in pipes, and their mathematical description will be introduced separately. For torsional modes, the displacement vector $\boldsymbol{u}$ will be a function of the radius r and the

circumferential angle θ. It will not depend on the axial distance z. The displacement vector can be represented in terms of the potential functions ϕ and ψ as given in A.2 and A.3.

$$\boldsymbol{u}_r = \frac{\partial \phi}{\partial r} + \frac{1}{r}\frac{\partial \psi}{\partial \theta}$$

A.2

$$\boldsymbol{u}_{\boldsymbol{\theta}} = \frac{1}{r}\frac{\partial \phi}{\partial r} - \frac{\partial \psi}{\partial r}$$

A.3

The potentials ϕ and ψ have to satisfy the wave equations such that A.4 and A.5 hold.

$$\left(\frac{\partial^2}{\partial r^2} + \frac{1}{r}\frac{\partial}{\partial} + \frac{1}{r^2}\frac{\partial^2}{\partial \theta^2}\right)\phi + \frac{\varpi^2}{c_L^2}\phi = 0$$

A.4

$$\left(\frac{\partial^2}{\partial r^2} + \frac{1}{r}\frac{\partial}{\partial} + \frac{1}{r^2}\frac{\partial^2}{\partial \theta^2}\right)\psi + \frac{\varpi^2}{c_T^2}\psi = 0$$

A.5

The variable ω is the angular frequency and C_L and C_T are the longitudinal and transverse wave velocities respectively. Hooke's law then provides A.6 through A.8.

$$\sigma_{rr} = \lambda\left(\frac{\partial u_r}{\partial r} + \frac{u_r}{r} + \frac{1}{r}\frac{\partial u_\theta}{\partial \theta}\right) + 2\mu\frac{\partial u_r}{\partial r}$$

A.6

$$\sigma_{\theta\theta} = \lambda\left(\frac{\partial u_r}{\partial r} + \frac{u_r}{r} + \frac{1}{r}\frac{\partial u_\theta}{\partial \theta}\right) + 2\mu\left(\frac{u_r}{r} + \frac{1}{r}\frac{\partial u_\theta}{\partial \theta}\right)$$

A.7

$$\sigma_{r\theta} = \lambda\left(\frac{\partial u_\theta}{\partial r} - \frac{u_\theta}{r} + \frac{1}{r}\frac{\partial u_r}{\partial \theta}\right)$$

A.8

The variable σ here represents stress. On the boundaries of the hollow cylinder, that is along the inside and outside radii of the hollow cylinder, (referred to here as a and b respectively) the stresses are zero. This is noted as A.9.

$\sigma_{rr} = \sigma_{r\theta} = 0$ when $r = a$ and when $r = b$

A.9

Since circumferentially propagating waves will behave similarly to waves traveling in a plate, they will be dependent on the circumferential angle θ as given in the term $e^{i\theta kb}$. Here the k coefficient is the analog of the wave number related to wave propagation in a plate. In the case of a hollow cylinder, k is the angular wave number. The value of k is found by satisfying the boundary conditions. The functions Φ(r) and Ψ(r) will be introduced as shown in A.10 and A.11.

$$\phi = \Phi(r)e^{i(kb\theta - t\varpi)}$$

A.10

$$\psi = \Psi(r)e^{i(kb\theta - t\varpi)}$$

A.11

For simplicity the term $e^{-i\varpi t}$ will be dropped for the remainder of this derivation.

Making the substitution of A.10 and A.11 into A.4 and A.5 respectively, yields A.12 and A.13.

$$\Phi'' + \frac{1}{\mathrm{r}}\Phi' + \left(\left(\frac{\varpi}{\mathrm{c_L}}\right)^2 - \left(\frac{\mathrm{kb}}{\mathrm{r}}\right)^2\right)\Phi = 0$$

A.12

$$\Psi'' + \frac{1}{\mathrm{r}}\Psi' + \left(\left(\frac{\varpi}{\mathrm{c_T}}\right)^2 - \left(\frac{\mathrm{kb}}{\mathrm{r}}\right)^2\right)\Psi = 0$$

A.13

The solutions to A.12 and A.13 are A.14 and A.15 respectively, where A_1, A_2, B_1, and B_2 are unknown constants that will be solved for by satisfying the four traction-free boundary equations introduced as A.9. $J_h(z)$ and $Y_h(z)$ are Bessel functions of order h of the first and second kind respectively. Substituting A.14 and A.15 into the appropriate equations found earlier with Hooke's law it is found that the radial stress and the shear stress in the plane of the cross-section can be written as A.16 and A.17 respectively.

$$\Phi(r) = A_1 J_{kb}\left(\frac{\varpi r}{c_L}\right) + A_2 Y_{kb}\left(\frac{\varpi r}{c_L}\right)$$

A.14

$$\Psi(r) = B_1 J_{kb}\left(\frac{\varpi r}{c_T}\right) + B_2 Y_{kb}\left(\frac{\varpi r}{c_T}\right)$$

A.15

$$\sigma_{rr} = \frac{\mu e^{ikb\theta}}{r^2}\left(\left(\frac{c_L}{c_T}\right)^2 r^2\Phi'' + \left(\left(\frac{c_L}{c_T}\right)^2 - 2\right)\mathrm{r}\Phi' - \left(\left(\frac{c_L}{c_T}\right)^2 - 2\right)\mathrm{k}^2\mathrm{b}^2\Phi + 2\mathrm{ikb}(\mathrm{r}\Psi' - \Psi)\right)$$

A.16

$$\sigma_{r\theta} = \frac{\mu e^{ikb\theta}}{r^2}\left(-r^2\Psi'' + \mathrm{r}\Psi' - \mathrm{k}^2\mathrm{b}^2\Psi + 2\mathrm{ikb}(\mathrm{r}\Phi' - \Phi)\right)$$

A.17

Solving for the four unknown constants discovered in A.14 and A.15 by making use of A.16 and A.17, four equations involving homogeneous linear equations are produced. Each of these equations has four terms and will be represented here in matrix form where the four-by-four matrix name will be **D**. In describing the sixteen terms of this **D** matrix, the simplifications given in A.18 will be used.

$$h = b - a, M = \frac{kh}{1-\gamma}, \varepsilon = \frac{\varpi h}{c_T(1-\gamma)}, \chi = \frac{c_L}{c_T}, \text{and } \gamma = \frac{a}{b}$$

A.18

The terms in the **D** matrix then are shown as A.19 through A.34.

$$D_{11} = \left[J_{M-2}\left(\frac{\varepsilon}{\chi}\right) + J_{M+2}\left(\frac{\varepsilon}{\chi}\right) - 2(\chi^2 - 1)J_M\left(\frac{\varepsilon}{\chi}\right)\right]\chi^{-2}$$

A.19

$$D_{12} = i[J_{M-2}(\varepsilon) - J_{M+2}(\varepsilon)]$$

A.20

$$D_{13} = \left[Y_{M-2}\left(\frac{\varepsilon}{\chi}\right) + Y_{M+2}\left(\frac{\varepsilon}{\chi}\right) - 2(\chi^2 - 1)Y_M\left(\frac{\varepsilon}{\chi}\right)\right]\chi^{-2}$$

A.21

$$D_{14} = i[Y_{M-2}(\varepsilon) - Y_{M+2}(\varepsilon)]$$

A.22

$$D_{21} = i\left[J_{M-2}\left(\frac{\varepsilon}{\chi}\right) - J_{M+2}\left(\frac{\varepsilon}{\chi}\right)\right]\chi^{-2}$$

A.23

$$D_{22} = -i[J_{M-2}(\varepsilon) + J_{M+2}(\varepsilon)]$$

A.24

$$D_{23} = i\left[Y_{M-2}\left(\frac{\varepsilon}{\chi}\right) - Y_{M+2}\left(\frac{\varepsilon}{\chi}\right)\right]\chi^{-2}$$

A.25

$$D_{24} = -i[Y_{M-2}(\varepsilon) + Y_{M+2}(\varepsilon)]$$

A.26

$$D_{31} = \left[J_{M-2}\left(\frac{\gamma\varepsilon}{\chi}\right) - J_{M+2}\left(\frac{\gamma\varepsilon}{\chi}\right) - 2(\chi^2 - 1)J_M\left(\frac{\gamma\varepsilon}{\chi}\right)\right]\gamma^2\chi^{-2}$$

A.27

$$D_{32} = i[J_{M-2}(\gamma\varepsilon) - J_{M+2}(\gamma\varepsilon)]\gamma^2$$

A.28

$$D_{33} = \left[Y_{M-2}\left(\frac{\gamma\varepsilon}{\chi}\right) + Y_{M+2}\left(\frac{\gamma\varepsilon}{\chi}\right) - 2(\chi^2 - 1)Y_M\left(\frac{\gamma\varepsilon}{\chi}\right)\right]\gamma^2\chi^{-2}$$

A.29

$$D_{34} = i[Y_{M-2}(\gamma\varepsilon) - Y_{M+2}(\gamma\varepsilon)]\gamma^2$$

A.30

$$D_{41} = i\left[J_{M-2}\left(\frac{\gamma\varepsilon}{\chi}\right) - J_{M+2}\left(\frac{\gamma\varepsilon}{\chi}\right)\right]\gamma^2\chi^{-2}$$

A.31

$$D_{42} = -i[J_{M-2}(\gamma\varepsilon) + J_{M+2}(\gamma\varepsilon)]\gamma^2$$

A.32

$$D_{43} = i\left[Y_{M-2}\left(\frac{\gamma\varepsilon}{\chi}\right) - Y_{M+2}\left(\frac{\gamma\varepsilon}{\chi}\right)\right]\gamma^2\chi^{-2}$$

A.33

$$D_{44} = -i[Y_{M-2}(\varepsilon) + Y_{M+2}(\varepsilon)]\gamma^2$$

A.34

The solution to these equations will be non-trivial only when the determinant of the **D** matrix is zero. The angular phase velocity is found by dividing the angular frequency by the product of k and b. This is demonstrated in A.35 as the variable α. The linear phase velocity c_p is then found as A.36.

$$\alpha = \frac{\varpi}{kb}$$

A.35

$$c_p = r\alpha = \frac{\varpi}{k}\frac{r}{b}$$

A.36

General Matrix Equations for all Propagating Wave Modes on Hollow Cylinders

The development so far is for torsional waves, but the more general case of wave propagation in a hollow cylinder can be obtained similarly. Again, the stresses are set to zero on the outside and inside boundaries of the hollow cylinder. This yields A.37 where a is again the inside radius and b is still the outside radius of the hollow cylinder. The assumed displacements for this wave are given in A.38 through A.40 where $u_{r,\theta,z}$ are the components of the wave in the radial, circumferential, and axial directions respectively, and $U_{r,\theta,z}$ are the amplitude functions and contain Bessel functions and modified Bessel functions in the same directions as $u_{r,\theta,z}$.

$$\sigma_{rr} = \sigma_{rz} = \sigma_{r\theta} = 0 \text{ at } r = a \text{ and at } r = b$$

A.37

$$u_r = U_r(r)cos(n\theta)cos(\varpi t + kz)$$

A.38

$$u_\theta = U_\theta(r)sin(n\theta)cos(\varpi t + kz)$$

A.39

$$u_z = U_z(r)cos(n\theta)sin(\varpi t + kz)$$

A.40

The solution for $U_{r,\theta,z}$ will contain six unknowns and can be represented in a matrix form involving Bessel functions and modified Bessel functions. The matrix **C** will be used here to represent this matrix. The **C** matrix will be a six-by-six matrix and the entries are C_{ij} where i and j are indices that range from 1 to 6. The entries for the index i ranging from 1 to 3 and the index j ranging from 1 to 6 are given in A.42 through A.59. The rest of the entries are the same except that every a in the first set of equations is replaced by b. For simplification, the identities shown in A.41 will be used. Also, Z will be used to represent Bessel functions and W will be used to represent modified Bessel functions.

$$\alpha^2 = \frac{\varpi^2}{c_L^2} - k^2,\ \beta^2 = \frac{\varpi^2}{c_T^2} - k^2,\ \alpha_1 r = |\alpha r|, \beta_1 r = |\beta r|$$

A.41

$$C_{11} = [2n(n-1) - (\beta^2 - k^2)a^2]Z_n(\alpha_1 a) + 2\lambda_1\alpha_1 a Z_{n+1}(\alpha_1 a)$$

A.42

$$C_{12} = 2k\beta_1 a^2 Z_n(\beta_1 a) - 2ka(n+1)Z_{n+1}(\beta_1 a)$$

A.43

$$C_{13} = -2n(n-1)Z_n(\beta_1 a) + 2\lambda_2 n\beta_1 a Z_{n+1}(\beta_1 a)$$

A.44

$$C_{14} = [2n(n-1) - (\beta^2 - k^2)a^2]W_n(\alpha_1 a) + 2\alpha_1 a W_{n+1}(\alpha_1 a)$$

A.45

$$C_{15} = 2k\lambda_2\beta_1 a^2 W_n(\beta_1 a) - 2ka(n+1)W_{n+1}(\beta_1 a)$$

A.46

$$C_{16} = -2n(n-1)W_n(\beta_1 a) + 2n\beta_1 a W_{n+1}(\beta_1 a)$$

A.47

$$C_{21} = 2n(n-1)Z_n(\alpha_1 a) - 2\lambda_1 n\alpha_1 a Z_{n+1}(\alpha_1 a)$$

A.48

$$C_{22} = -k\beta_1 a^2 Z_n(\beta_1 a) + 2ka(n+1)Z_{n+1}(\beta_1 a)$$

A.49

$$C_{23} = -[2n(n-1) - \beta^2 a^2]Z_n(\beta_1 a) - 2\lambda_2\beta_1 a Z_{n+1}(\beta_1 a)$$

A.50

$$C_{24} = 2n(n-1)W_n(\alpha_1 a) + 2n\alpha_1 a W_{n+1}(\alpha_1 a)$$

A.51

$$C_{25} = -k\lambda_2\beta_1 a^2 W_n(\beta_1 a) + 2ka(n+1)W_{n+1}(\beta_1 a)$$

A.52

$$C_{26} = -[2n(n-1) - \beta^2 a^2]W_n(\beta_1 a) - 2\beta_1 a W_{n+1}(\beta_1 a)$$

A.53

$$C_{31} = 2nk\alpha_1 Z_n(\alpha_1 a) - 2k\alpha_1\lambda_1 a^2 Z_{n+1}(\alpha_1 a)$$

A.54

$$C_{32} = n\beta_1 a Z_n(\beta_1 a) - (\beta^2 - k^2)a^2 Z_{n+1}(\beta_1 a)$$

A.55

$$C_{33} = -nkaZ_n(\beta_1 a)$$

A.56

$$C_{34} = 2nkaW_n(\alpha_1 a) - 2k\alpha_1 a^2 W_{n+1}(\alpha_1 a)$$

A.57

$$C_{35} = n\lambda_2\beta_1 a W_n(\beta_1 a) - (\beta^2 - k^2)a^2 W_{n+1}(\beta_1 a)$$

A.58

$$C_{36} = -nkaW_n(\beta_1 a)$$

A.59

The determination of the values of α, α_1, α_2, λ, λ_1, λ_2, Z, and W depend on the frequency interval of the arguments of the Bessel functions and are given in Table A.1. In Table A.1, **J** and **Y** represent Bessel functions of the first and second kind respectively, and **I** and **K** represent the modified Bessel functions of the first and second kind respectively.

Table A.1
Bessel functions and variable values used based on argument range of equations A.42 through A.59.

Argument Range	Bessel Functions Used	Values Used
$kC_L<\varpi$	**J**(αr),**J**(βr),**Y**(αr),**Y**(βr)	$\lambda_1=1$, $\lambda_2=1$
$kC_T<\varpi<kC_L$	**I**(α_1r),**K**(α_1r),**J**(βr),**Y**(βr)	$\lambda_{1=}-1$, $\lambda_2=1$
$\varpi<kC_T$	**I**(α_1r),**K**(α_1r),**I**(β_1r),**K**(β_1r)	$\lambda_1=-1$, $\lambda_2=-1$

Setting the determinant of the **C** matrix to zero as Shown in A.60 yields the frequency equation for waves in a hollow cylinder. Setting n=0 in the **C** matrix will yield the frequency equation for axisymmetric longitudinal and torsional modes. In the case when n=0, the frequency equation, referred to here as **F**, can be decomposed into the product of two sub determinants as given in A.61 through A.63.

$$\det(\boldsymbol{C}) = \begin{vmatrix} c_{11} & c_{12} & c_{13} & c_{14} & c_{15} & c_{16} \\ c_{21} & c_{22} & c_{23} & c_{24} & c_{25} & c_{26} \\ c_{31} & c_{32} & c_{33} & c_{34} & c_{35} & c_{36} \\ c_{41} & c_{42} & c_{43} & c_{44} & c_{45} & c_{46} \\ c_{51} & c_{52} & c_{53} & c_{54} & c_{55} & c_{56} \\ c_{61} & c_{62} & c_{63} & c_{64} & c_{65} & c_{66} \end{vmatrix} = 0$$

A.60

$$\boldsymbol{F} = \boldsymbol{S_1} \cdot \boldsymbol{S_2} = 0$$

A.61

$$\boldsymbol{S_1} = \begin{vmatrix} c_{11} & c_{12} & c_{14} & c_{15} \\ c_{31} & c_{32} & c_{34} & c_{35} \\ c_{41} & c_{42} & c_{44} & c_{46} \\ c_{61} & c_{62} & c_{64} & c_{66} \end{vmatrix}$$

A.62

$$\boldsymbol{S_2} = \begin{vmatrix} c_{23} & c_{26} \\ c_{53} & c_{56} \end{vmatrix}$$

A.63

Setting the determinant in A.62 equal to zero gives the longitudinal modes for a pipe. Doing the same for A.63 yields the torsional modes for a pipe. Again, these determinants are meaningful for the case when n=0 in the more general **C** matrix. It is common to name modes with the

following convention. Axisymmetric longitudinal modes (those corresponding to setting A.62 to zero) are referred to as L(0,m) modes, where the 0 index refers to the index of n that was set to zero. Axisymmetric torsional modes are referred to as T(0,m). Other modes that are obtained when n is not equal to zero are generically called flexural modes and are referred to as F(n,m). Solving A.60 for all values of n and for all frequencies, although not numerically possible because of the infinite range of frequency and the indices n and m, would produce all the modes in a pipe including the axisymmetric modes and all the flexural modes. An example of the solution to A.60 for the value of n equal to zero and for a frequency range of 0 to 800 kHz is shown in Figure A.1 and Figure A.2. For Figure A.1, the pipe diameter is 406 mm (16 in) and the pipe is schedule-30. Figure A.2, shows the roots for 0.61 m (24 in) diameter schedule 20 pipe.

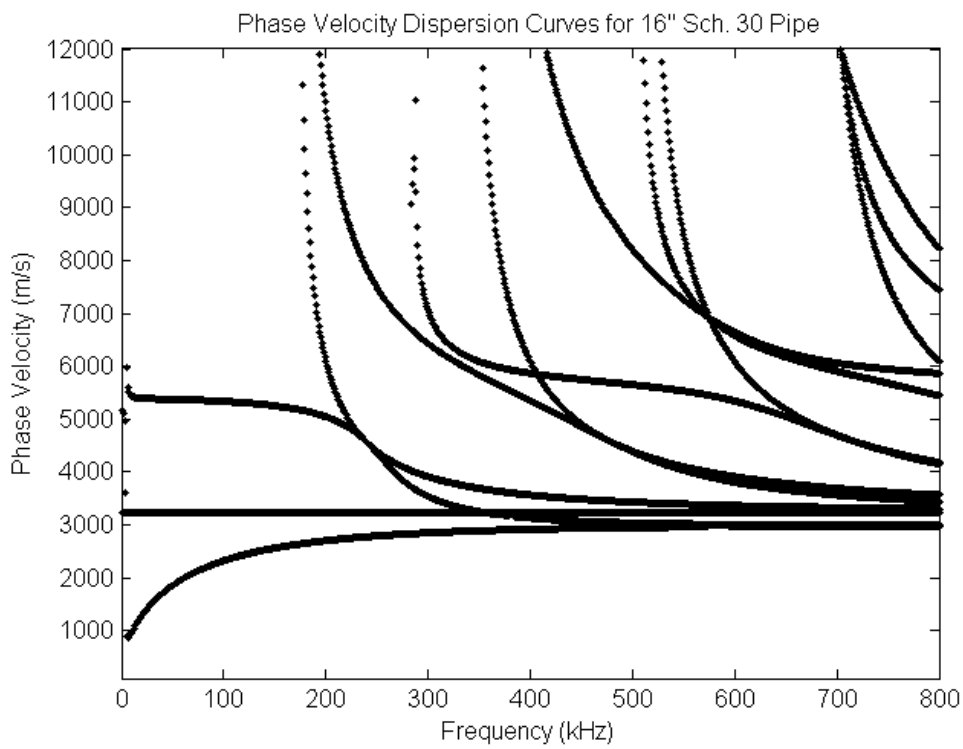

Figure A.1
Axi-symmetric phase velocity dispersion curves for schedule 30 pipe of 406 mm (16 in) diameter.

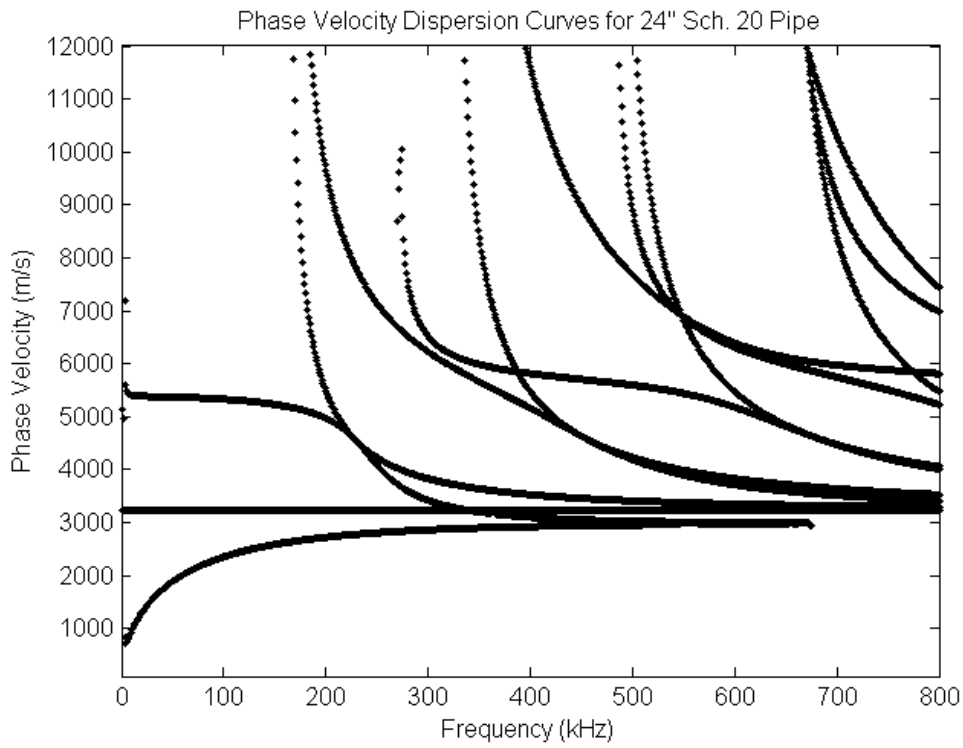

Figure A.2
Axi-symmetric phase velocity dispersion curves for schedule 20 pipe of 0.6 m (24 in) diameter.

Particle Displacement Field in a Partially Loaded Hollow Cylinder

Source influence is an important factor in the actual excitement of a guided wave in any media. The size and shape of a transducer will, in part, control what modes are generated and which directions they will propagate. Normal mode expansion provides an excellent method for calculating the stress field generated by a particular loading source. The following discussion is based on the work of Ditri [104]. The velocity field, $\boldsymbol{V}_m^n(r,\theta)$,established by a particular wave mode can be written as A.64.

$$\boldsymbol{V}_m^n(r,\theta)e^{i(\varpi t-k_m^n z)} = \sum_{\alpha=r,\theta,z} R_{m\alpha}^n(r)\Theta_\alpha^n(\mathrm{n}\theta)\mathrm{e}^{\mathrm{i}(\varpi \mathrm{t}-\mathrm{k}_\mathrm{m}^\mathrm{n}\mathrm{z})}\,\hat{u}_\alpha$$

A.64

Here $R_{n\alpha}^m(r)$and $\Theta_\alpha^n(\mathrm{n}\theta)$ represent the radial and circumferential field distributions respectively of the velocity component of the nth mode of the mth family indexed by α. The stress field, $\boldsymbol{T}_m^n(r,\theta)$, can then be written as in A.65.

$$\boldsymbol{T}_m^n(r,\theta)e^{i(\varpi t-k_m^n z)} = \sum_{\alpha}\sum_{k} R_{m\alpha k}^n\ (r)\Theta_{\alpha k}^n(n\theta)e^{i(\varpi t-k_m^n z)}\hat{u}_\alpha \otimes \hat{u}_k;\ \alpha, k \in \{r,\theta,z\}$$

A.65

Here $R_{m\alpha k}^n\ (r)$and $\Theta_{\alpha k}^n(n\theta)$ are the respective radial and circumferential distributions of the αk^{th} component of stress caused by the mth mode of the nth family. The circumferential function contains sines and cosines using the argument $n\theta$ for modes of circumferential order n. The radial component of the stress contains Bessel functions and modified Bessel functions of the first and second kind. Ditri [104] showed that these modes are orthogonal, and developed a relationship for the amplitudes needed for the normal mode expansion of them for calculating the stress field as a function of boundary tractions. His result for forward propagating waves is shown in A.66.

$$A_m^n(z) = \frac{e^{-izk_m^n}}{4P_{mm}^{nn}}\int_c^z e^{-i\eta k_m^n}\left(\oint_{\partial\mathfrak{D}} \boldsymbol{v}_m^{n*}\cdot(\boldsymbol{T}\cdot\hat{\boldsymbol{n}})ds\right)d\eta$$

A.66

In A.66, $\boldsymbol{T}\cdot\hat{\boldsymbol{n}}$ represents the applied traction. **T** is the stress found from A.65, $\hat{\boldsymbol{n}}$ is the surface unit normal vector, $\boldsymbol{v}_m^{n*}$ is the complex conjugate of the velocity field found from A.64, $\partial\mathfrak{D}$ is the surface of the cylinder, and P_{mm}^{nn} is defined in A.67.

$$P_{mm}^{nn} = -\frac{1}{4}\int\int_{\mathfrak{D}}(\boldsymbol{v}_m^{n*}\cdot\boldsymbol{T}_n^m + \boldsymbol{v}_n^m\cdot\boldsymbol{T}_m^{n*})\cdot\hat{\boldsymbol{u}}_z d\sigma$$

A.67

After finding the normal mode amplitudes, the respective velocity and stress fields produced by a loading function can be found using the normal mode expansion technique shown in A.68 and A.69.

$$\boldsymbol{v}(r,\theta,z) = \sum_{n=0}^{\infty}\sum_{m} A_m^n(z)\boldsymbol{v}_m^n(r,\theta)$$

A.68

$$\boldsymbol{T}(r,\theta,z) = \sum_{n=0}^{\infty}\sum_{m} A_m^n(z)\boldsymbol{T}_m^n(r,\theta)$$

A.69

The total stress field caused by an array of transducers at some distance away from the array will be given as the simple superposition of the stress field caused by each individual transducer. The stress field caused by each transducer can be calculated using A.69. Thus, for an array of N identical transducers arranged in the same plane around the circumference of a pipe, the stress field G(θ) at a distance d from the array as a function of circumferential angle θ on the outside of the pipe will be given as A.70, where $A(\theta_i)$ is a complex weighting function representing the amplitude and phase of the waveform produced by the ith transducer. The θ_i term denotes the angular position of the ith transducer around the circumference of the pipe. Refer to Figure 1.5 for a sketch of the geometry of the transducer array under discussion here. In that figure, however, the θ angle is denoted by ϕ.

$$G(\theta) = \sum_{i=1}^{N} A(\theta_i)\boldsymbol{T}(b,\theta-\theta_i,d)$$

A.70

Because the circumferential profile of stress caused by a phased array of transducers depends on time and the exact waveform inputted to each transducer, these input waveforms can be given electronic time delays and weighted as a method of controlling what the circumferential profile of stress will be at some location of interest in a pipe. The ability to predict and control this profile of stress resulting from each sensor in the array forms the basis for the conventional methodology for focusing in pipes. Focusing allows the control of the circumferential guided wave energy profile at some axial distance in a pipe. The usual concept in focusing guided wave energy is to concentrate the bulk of the guided wave energy at a particular circumferential location around the pipe wall. While there will still be some amount of energy in other circumferential locations around the pipe at the same axial location, those energy amplitudes are suppressed by the design of the focusing parameters.

The use of focusing enables at least two important tools in practical pipe inspections using guided waves. One such tool is the reduction of reflection amplitudes resulting from circumferential locations around the pipe other than the location where the focusing is designed to happen.

Another tool is the ability to increase the overall energy level at specific circumferential locations in a pipe compared to the energy level that would exist in an axi-symmetric condition. To perform focusing in this manner, the effect of each transducer in the array on a particular axial position in the pipe is examined.

Because this effect depends on time, the time dependent energy profile that best lends itself to contributing to the desired focusing profile is selected for each sensor. A time delay is designed for each sensor in the array relative to the other sensors so that, at a particular time, the circumferential energy profile at the focal distance caused by each sensor is the previously selected profile. Each such energy profile from each individual sensor is also weighted so that the profile amplitude can be controlled as well.

The ultimate energy profile at the focal distance and time of the focus is the superposition of all the individual circumferential energy profiles from each sensor. With the correct selection of time delays and weights for each sensor, the resulting superimposed energy profile at the focal distance can be designed to concentrate a significant portion of energy at a desired circumferential position. The weighting functions are found as an inverse problem that solves the complex values of $A(\theta_i)$ in A.70 for a particular desired energy profile $G(\theta)$.

APPENDIX B

Derivation of Geodesics on a Torus

Calculating the geodesics for a torus is a tedious and lengthy process. It is therefore moved from the relevant discussion of geodesics in Chapter 2 to this appendix. To keep the appendix as a stand-alone reference to the development of geodesics on a torus, the equations given in Chapter 2 are repeated here. The construction presented here follows the style of [167]. Pipe elbow geometries, or toroidal geometries, are smooth and continuous throughout their domain, so the manifold W representing the torus is affine. Also, in this development, r will be allowed to vary. The map between global Cartesian coordinates {x,y,z} and generalized coordinates $\{r, \theta, \phi\}$ are given as B.1. Here, the elbow bend radius is denoted as ρ, the pipe radius is r, the circumferential pipe coordinate is ϕ, and the elbow bend angle is θ.

$$x = (\rho + r\cos\phi)\cos\theta$$
$$y = r\sin\phi$$
$$z = (\rho + r\cos\phi)\sin\theta$$

B.1

The covariant tensor, g_{ij}, can be found using the metric equation shown as B.2. The square of the arc-length drawn across the manifold W by varying each of the generalized coordinates $\{r, \theta, \phi\}$ is ds^2, and is the sum of $dx^2+dy^2+dz^2$ as shown in B.3. The differentials {dx,dy,dz} are given in B.4.

$$ds^2 = g_{ij}\,dx_i\,dx_j$$

B.2

$$ds^2 = \dot{x}^2 + \dot{y}^2 + \dot{z}^2$$

B.3

$$dx = \dot{x} = \cos\phi\cos\theta\,\dot{r} - r\sin\phi\cos\theta\dot{\phi} - (\rho + r\cos\phi)\sin\theta\,\dot{\theta}$$
$$dy = \dot{y} = \sin\phi\,\dot{r} + r\cos\phi\,\dot{\phi}$$
$$dz = \dot{z} = \cos\phi\sin\theta\dot{r} - r\sin\theta\sin\phi\dot{\phi} + (\rho + r\cos\theta)\cos\phi\,\dot{\theta}$$

B.4

Applying B.4 into B.3 and simplifying yields the equation given in B.5.

$$ds^2 = \dot{r}^2 + (\rho + r\cos\phi)^2\dot{\theta}^2 + r^2\dot{\phi}^2$$

B.5

Solving B.2 for g_{ij} given B.5 yields the covariant tensor shown in B.6. There are no cross-differential terms in B.5, so all the off-diagonal entries in g_{ij} are zero. This is expected for geometries in orthogonal coordinate systems as noted in Chapter 2. The covariant tensor g_{ij} multiplied by the contravariant tensor g^{ij} results in the Kronnecker Delta tensor, as shown in B.7. Since g_{ij} is diagonal, g^{ij} can be found by taking the reciprocal of each of the diagonal terms in g_{ij} and keeping the off-diagonal entries zero. The contravariant tensor is given in B.8

$$g_{ij} = \begin{bmatrix} 1 & 0 & 0 \\ 0 & (\rho + r\cos\phi)^2 & 0 \\ 0 & 0 & r^2 \end{bmatrix}$$

B.6

$$g_{ij}g^{ij} = \begin{bmatrix} 1 & 0 & 0 \\ 0 & 1 & 0 \\ 0 & 0 & 1 \end{bmatrix}$$

B.7

$$g_{ij} = \begin{bmatrix} 1 & 0 & 0 \\ 0 & \dfrac{1}{(\rho + r\cos\phi)^2} & 0 \\ 0 & 0 & \dfrac{1}{r^2} \end{bmatrix}$$

B.8

The form of the geodesic equation for local coordinates on W is given as B.9, where the Christoffel symbols, Γ^{i}_{jk}, are defined in B.10. In B.10, commas denote the derivative of the component of the covariant tensor indicated to the left of the comma with respect to the coordinate indicated to the right of the comma.

$$\frac{d^2x_i}{dt^2} + \Gamma^{i}_{jk}\frac{dx_j}{dt}\frac{dx_k}{dt} = 0$$

B.9

$$\Gamma^{i}_{jk} = \frac{1}{2} g^{im} \left(g_{mj,k} + g_{mk,j} - g_{jk,m} \right)$$

B.10

So, solving B.9 for the first generalized coordinate, r, involves the summation of nine Γ^{i}_{jk} terms, each multiplied by the corresponding time derivatives that appear to the right of the Christoffel symbol in B.9. Each Γ^{i}_{jk} term also involves the summation of three terms involving the contravariant tensor and derivatives of the covariant tensor. The generic equation representing Γ^{1}_{11} is given in B.11, and the nine terms of Γ^{1}_{jk} that represent the r coordinate are given in B.12 through B.20.

$$\Gamma^{1}_{11} = \frac{1}{2}\left(g^{11}\left(g_{11,1} + g_{11,1} - g_{11,1} \right) + g^{12}\left(g_{21,1} + g_{21,1} - g_{11,2} \right) + g^{13}\left(g_{31,1} + g_{31,1} - g_{11,3} \right) \right)$$

B.11

$$\Gamma^{1}_{11} = \frac{1}{2}\left(1(0 + 0 - 0) + 0(0 + 0 - 0) + 0(0 + 0 - 0) \right) = 0$$

B.12

$$\Gamma^{1}_{12} = \frac{1}{2}\left(1(0 + 0 - 0) + 0(0 + 2(\rho + r\cos\phi)\cos\phi - 0) + 0(0 + 0 - 0) \right) = 0$$

B.13

$$\Gamma^{1}_{13} = \frac{1}{2}\left(1(0 + 0 - 0) + 0(0 + 0 - 0) + 0(0 + 2r - 0) \right) = 0$$

B.14

$$\Gamma^{1}_{21} = \frac{1}{2}\left(1(0 + 0 - 0) + 0(2(\rho + r\cos\phi)\cos\phi + 0 - 0) + 0(0 + 0 - 0) \right) = 0$$

B.15

$$\Gamma^{1}_{22} = \frac{1}{2}\left(1(0 + 0 - 2(\rho + r\cos\phi)\cos\phi) + 0(0 + 0 - 0) + 0(0 + 0 + 2r(\rho + r\cos\phi)\sin\phi) \right)$$
$$= -(\rho + r\cos\phi)\cos\phi$$

B.16

$$\Gamma^1_{23} = \frac{1}{2}\big(1(0+0-0) + 0(-2r(\rho + r\cos\phi)\sin\phi - 2r(\rho + r\cos\phi)\sin\phi + 2r(\rho + r\cos\phi)\sin\phi) + 0(0+0-0)\big) = 0$$

B.17

$$\Gamma^1_{31} = \frac{1}{2}\big(1(0+0-0) + 0(0+0-0) + 0(2r+0-0)\big) = 0$$

B.18

$$\Gamma^1_{32} = \frac{1}{2}\big(1(0+0-0) + 0(0 - 2r(\rho + r\cos\phi)\sin\phi - 0) + 0(0+0-0)\big) = 0$$

B.19

$$\Gamma^1_{33} = \frac{1}{2}\big(1(0+0-2r) + 0(0+0-0) + 0(0+0-0)\big) = -r$$

B.20

The only nonzero Christoffel symbols are Γ^1_{22} and Γ^1_{33} as shown in B.16 and B.20. Placing these in B.9 yields B.21. Using the dot notation to represent a time derivative and solving for $\ddot{r}$, we can rewrite B.21 as B.22.

$$\frac{d^2r}{dt^2} - (\rho + r\cos\phi)\cos\phi\left(\frac{d\theta}{dt}\right)^2 - r\left(\frac{d\phi}{dt}\right)^2 = 0$$

B.21

$$\ddot{r} = (\rho + r\cos\phi)\cos\phi\,\dot{\theta}^2 + r\dot{\phi}^2$$

B.22

Continuing the derivation for the remaining coordinates of θ and ϕ, we obtain the values for the remaining Christoffel symbols next in B.23 through B.40. For these equations, however, we will not evaluate the derivatives of the covariant tensor for those that are pre-multiplied by an off-diagonal entry in the contravariant tensor, since such terms will ultimately compute to zero.

$$\Gamma_{11}^{2} = \frac{1}{2}\left(\frac{1}{(\rho + r\cos\phi)^2}(0 + 0 - 0)\right) = 0$$

B.23

$$\Gamma_{12}^{2} = \frac{1}{2}\left(\frac{1}{(\rho + r\cos\phi)^2}(0 + 2(\rho + \mathrm{r}\cos\phi)\cos\phi - 0)\right) = \frac{\cos\phi}{(\rho + \mathrm{r}\cos\phi)}$$

B.24

$$\Gamma_{13}^{2} = \frac{1}{2}\left(\frac{1}{(\rho + r\cos\phi)^2}(0 + 0 - 0)\right) = 0$$

B.25

$$\Gamma_{21}^{2} = \frac{1}{2}\left(\frac{1}{(\rho + r\cos\phi)^2}(2(\rho + \mathrm{r}\cos\phi)\cos\phi + 0 - 0)\right) = \frac{\cos\phi}{(\rho + \mathrm{r}\cos\phi)}$$

B.26

$$\Gamma_{22}^{2} = \frac{1}{2}\left(\frac{1}{(\rho + r\cos\phi)^2}(0 + 0 - 0)\right) = 0$$

B.27

$$\Gamma_{23}^{2} = \frac{1}{2}\left(\frac{1}{(\rho + r\cos\phi)^2}(-2\mathrm{r}(\rho + \mathrm{r}\cos\phi)\sin\phi + 0 - 0)\right) = -\frac{\mathrm{r}\sin\phi}{(\rho + \mathrm{r}\cos\phi)}$$

B.28

$$\Gamma_{31}^{2} = \frac{1}{2}\left(\frac{1}{(\rho + r\cos\phi)^2}(0 + 0 - 0)\right) = 0$$

B.29

$$\Gamma_{32}^{2} = \frac{1}{2}\left(\frac{1}{(\rho + r\cos\phi)^2}(0 + -2\mathrm{r}(\rho + \mathrm{r}\cos\phi)\sin\phi - 0)\right) = -\frac{\mathrm{r}\sin\phi}{(\rho + \mathrm{r}\cos\phi)}$$

B.30

$$\Gamma_{33}^{2} = \frac{1}{2}\left(\frac{1}{(\rho + r\cos\phi)^2}(0 + 0 - 0)\right) = 0$$

B.31

$$\Gamma_{11}^{3} = \frac{1}{2}\left(\frac{1}{r^2}(0+0-0)\right) = 0$$

B.32

$$\Gamma_{12}^{3} = \frac{1}{2}\left(\frac{1}{r^2}(0+0-0)\right) = 0$$

B.33

$$\Gamma_{13}^{3} = \frac{1}{2}\left(\frac{1}{r^2}(0+2\mathrm{r}-0)\right) = \frac{1}{\mathrm{r}}$$

B.34

$$\Gamma_{21}^{3} = \frac{1}{2}\left(\frac{1}{r^2}(0+0-0)\right) = 0$$

B.35

$$\Gamma_{22}^{3} = \frac{1}{2}\left(\frac{1}{r^2}(0+0+2\mathrm{r}(\rho+\mathrm{r}\cos\phi)\sin\phi)\right) = \frac{(\rho+\mathrm{r}\cos\phi)\sin\phi}{\mathrm{r}}$$

B.36

$$\Gamma_{23}^{3} = \frac{1}{2}\left(\frac{1}{r^2}(0+0-0)\right) = 0$$

B.37

$$\Gamma_{31}^{3} = \frac{1}{2}\left(\frac{1}{r^2}(2\mathrm{r}+0-0)\right) = \frac{1}{\mathrm{r}}$$

B.38

$$\Gamma_{32}^{3} = \frac{1}{2}\left(\frac{1}{r^2}(0+0-0)\right) = 0$$

B.39

$$\Gamma_{33}^{3} = \frac{1}{2}\left(\frac{1}{r^2}(0+0-0)\right) = 0$$

B.40

Examining equations B.23 through B.40 shows that the only nonzero Christoffel terms for equation B.9 when looking at the coordinate θ, are those given in B.24, B.26, B.28, and B.30. Using these results in the geodesic equation and employing the dot notation yields B.41.

$$\ddot{\theta} = -2\frac{\cos\phi}{(\rho + r\cos\phi)}\dot{r}\dot{\theta} + 2\frac{r\sin\phi}{(\rho + r\cos\phi)}\dot{\theta}\dot{\phi}$$

B.41

Similarly, only the terms given in B.34, B.36, and B.38 are nonzero for the Christoffel symbols in B.9 for the coordinate ϕ. The use of these results in the geodesic equation yields B.42.

$$\ddot{\phi} = -\frac{2}{r}\dot{r}\dot{\phi} - \frac{(\rho + r\cos\phi)\sin\phi}{r}\dot{\theta}^2$$

B.42

Holding the r coordinate constant in order to restrict the domain of interest to lie on the surface of the torus means that the first and second derivatives of the r coordinate become zero. Using this restriction allows us to rewrite B.41 and B.42 as B.43 and B.44 respectively. These are the familiar equations seen in Chapter 2.

$$\ddot{\theta} = \frac{2r\sin\phi}{(\rho + r\cos\phi)}\dot{\theta}\dot{\phi}$$

B.43

$$\ddot{\phi} = -\frac{(\rho + r\cos\phi)\sin\phi}{r}\dot{\theta}^2$$

B.44

For the sake of reference, the generic version of the accelerations obtained for each of the three generalized coordinates are collected here and given as B.45.

$$\ddot{r} = (\rho + r\cos\phi)\cos\phi\,\dot{\theta}^2 + r\dot{\phi}^2$$

$$\ddot{\theta} = -2\frac{\cos\phi}{(\rho + r\cos\phi)}\dot{r}\dot{\theta} + 2\frac{r\sin\phi}{(\rho + r\cos\phi)}\dot{\theta}\dot{\phi}$$

$$\ddot{\phi} = -\frac{2}{r}\dot{r}\dot{\phi} - \frac{(\rho + r\cos\phi)\sin\phi}{r}\dot{\theta}^2$$

B.45

APPENDIX C

Finite Element Modeling

For all the numerical Finite Element Method (FEM) modeling used in this work, ABAQUS EXPLICIT was used. The explicit solver is chosen here because of the transient wave solutions desired. While the explicit method is not as theoretically elegant as its implicit counterpart, the explicit method is comparatively fast, and capable of capturing the desired transient components of the wave.

Some of the work shown in this dissertation made use of ABAQUS version 6.9.2, while most of the work was done with version 6.10-EF. The mesh elements for each model consisted of some combination of three-dimensional hexahedral brick mesh elements, and three-dimensional tetrahedral elements. The element size was designed such that the longest edge of an element was about one fifteenth or one twentieth of a wavelength of the guided wave energy modeled. A minimum of four elements was used through the thickness of the waveguide under simulation.

Unless otherwise noted in the text all the models employed in this work represented steel waveguides and had the material properties given as C.1, where ρ_s is the material density, υ_s is Poisson's ratio, and E_s is the modulus of elasticity.

$$\rho_s = 7860\ \frac{kg}{m^3}$$
$$\upsilon_s = 0.3$$
$$E_s = 200\ GPa$$

C.1

One model used aluminum for the waveguide material. The material properties used to model aluminum were similarly defined as given in C.2, where ρ_a, υ_a, and E_a are again the material density, Poisson's ratio, and the modulus of elasticity respectively.

$$\rho_a = 2700\ \frac{kg}{m^3}$$
$$\upsilon_a = 0.33$$
$$E_a = 70\ GPa$$

C.2

To reduce edge reflections from the ends of the models, some of the simulations included viscous damping to dissipate the energy moving near these regions. An interesting exploration of damping strategies in FEM solvers is given by Prabhu et al. [178]. The models exhibiting this damping more or less followed the so-called 'absorbing layers using increasing damping' technique described by Prabhu et al. [178]. These models were constructed with multiple adjacent sections of viscous damping with progressively higher alpha damping coefficients. The relationship between the damping coefficient of one layer and the previous one followed a cubic relationship with the width of the layer. The layer with the highest damping coefficient was placed along the extreme end of the model and had an alpha value of 20,000 to 2,000,000.

The layers further from the ends of the model had decreasing values of alpha damping, until reaching the nominal material sections of the geometry, where the alpha damping was set to zero. This damping system was typically comprised of 40 layers, and was very effective. The damping reduced the energy reflecting from the edges of the model geometry by two or three orders of magnitude.

Depending on the model, either a force loading was applied to a sub-section of the model surface to represent the loading function, or a displacement loading was applied. Most of the modeling was done using displacement loading, as this type of boundary condition tended to yield more consistent results with the versions of ABAQUS used. In particular, ABAQUS 6.10-ef usually did not produce an axi-symmetric wave mode in a pipe with an elbow when used with an axially symmetric force loading. When using an axi-symmetric displacement load, though, ABAQUS produced a simulated wave that was axi-symmetric in the same pipe geometry before the elbow, as would be expected.

The use of displacement loading has several drawbacks. One drawback of the displacement loading is that mode cancelation cannot be used with this method. If two transducer rings are used with phase delays between them, the first ring to be excited will generate a bi-directional mode, and the second will create a clamped boundary condition or will excite a new bi-directional mode, depending on the loading of the second ring. Either case does not simulate an experimental system. To establish mode control of backwards propagating energy, the source can be set at the end of the model so that the model excludes a backwards direction, or viscous damping can be applied to dissipate the energy along one direction.

For high-frequency wave generation, the use of displacement loading can create another difficulty, because the forces generated by the forced displacements may not sum to zero even if the displacement amplitude does. This can allow the load to introduce a net force into the modeled simulation, causing the geometry to drift through space over time. Pinning the ends of the model does not typically help, as this only introduces unrealistic deformation in the geometry. The drifting caused by this effect can be filtered out of the results by either looking at model stresses rather than displacement, or filtering the displacement results through a high pass filter during post processing.

Finally, when using a displacement boundary condition in ABAQUS EXPLICIT, care must be taken that the load does not introduce unwanted fixed displacement boundary conditions. After the loading function is finished in a model, ABAQUS ramps the last specified displacement in the loading function to zero over the rest of the model simulation time. This means that if the last specified displacement in the loading function is not zero, that the loaded region has a non-zero displacement for the duration of the rest of the simulation. Also, if the last value of the loading function is zero, ABAQUS effectively clamps the degrees of freedom specified by the load for the rest of the model simulation time.

In either case, the use of displacement boundary conditions can cause problems in the wave propagation after the loading has been applied. Also, if ABAQUS forces a displacement, whether zero or non-zero, at the loading region, this makes the loaded region a dead zone that cannot be used as a receiver. To solve this problem, the displacement boundary condition can be deactivated after the load has been applied.

When using a single, non-phased transducer, displacement boundary conditions can work very well. However, when using phased array of transducers with displacement boundary conditions, many loading steps must be used and the calculation of the displacement amplitudes to be used for each transducer over each step can become very cumbersome to create and apply.

Force loads, on the other hand, do not create any special requirements after the load has been applied, provided that the last value in the force load is zero. Imposing a traction free boundary after the load has been applied is, after all, the same as not applying a traction, and therefore does not affect the wave propagation. Force loads are also more accommodating for such exercises as mode cancellation, since they can be used to counteract a wave traveling in some direction

without imposing a clamped boundary. Unfortunately, force loads in ABAQUS EXPLICIT do not always work correctly.

For the work demonstrated here, force loading is used for models having phased array sensors, and displacement conditions are used elsewhere. Also, in all the models, the input loading function represents a hanning-windowed pulse of a specified number of cycles and frequency. In many cases involving partial loading, the loaded region is spatially weighted with a cosine function so that the edges of the loaded region have zero load and the center of the loaded region has the maximum amplitude. This weighting scheme reduces the excitation of unwanted modes, such as L(m,2).

Receivers are placed at various strategic positions throughout the different models. These receivers consist of a set of mesh nodes, whose identity is determined prior to running the simulation. ABAQUS can be requested to retain various quantities of energy, displacement, stress, etc. at these locations. In the results given in this work, the quantity retained by the receiver nodes is displacement. ABAQUS reports the displacement obtained at each node for each requested time interval in terms of global Cartesian {X,Y,Z} coordinates. These values can be mapped to cylindrical and toroidal coordinates during post processing to obtain the displacement amplitudes in the radial, circumferential, and axial directions $\{r,\phi,(z=\theta)\}$ respectively.

The time intervals used when requesting the displacement outputs from the receivers was designed to afford a sampling frequency of at least ten times the frequency of the guided wave of interest in the model. Plotting the displacement over time of the wave sampled at the receivers allowed the extracted data to be viewed as a simulated signal. Receivers placed in coincidence with the loading source then represented a pulse-echo transceiver configuration, and receivers placed elsewhere on the model represented a pitch-catch sensor configuration.

Another type of receiver was also used for each node and element for the entire model. This receiver was used to generate qualitative measurements of the propagating wave. The data retained by this receiver was a combination of strain energy, velocity, and nodal displacement. Typically, strain energy was selected as the rendered quantity for the results given showing field frames of the entire model.

Using the convention established in Figure 1.2, the mapping from the global {X,Y,Z} coordinates in the ABAQUS modeling can be obtained as the rotation tensors given in C.3, C.4, and C.5 for the regions before, in, and after the elbow region respectively.

$$\begin{Bmatrix} \hat{u}_r \\ \hat{u}_\phi \\ \hat{u}_z \end{Bmatrix} = \begin{bmatrix} 0 & -\sin\phi & \cos\phi \\ 0 & -\cos\phi & -\sin\phi \\ 1 & 0 & 0 \end{bmatrix} \begin{Bmatrix} X \\ Y \\ Z \end{Bmatrix}$$

C.3

$$\begin{Bmatrix} \hat{u}_r \\ \hat{u}_\phi \\ \hat{u}_z \end{Bmatrix} = \begin{bmatrix} \cos\phi\cos\theta & \sin\phi & -\cos\phi\sin\theta \\ -\cos\phi\sin\theta & \cos\phi & \sin\phi\sin\theta \\ -\sin\theta & 0 & -\cos\theta \end{bmatrix} \begin{Bmatrix} X \\ Y \\ Z \end{Bmatrix}$$

C.4

$$\begin{Bmatrix} \hat{u}_r \\ \hat{u}_\phi \\ \hat{u}_z \end{Bmatrix} = \begin{bmatrix} \cos\phi & -\sin\phi & 0 \\ -\sin\phi & -\cos\phi & 0 \\ 0 & 0 & -1 \end{bmatrix} \begin{Bmatrix} X \\ Y \\ Z \end{Bmatrix}$$

C.5

Vitae

Luke J. Breon
Technical Leader
The Electric Power Research Institute
1300 West WT Harris Blvd
Charlotte, NC, 28262
Phone: (704) 595-2802 Fax: (704) 595-2865

Citizenship: United States Citizen

Education:

Ph.D. Engineering Science and Mechanics, 2016
The Pennsylvania State University, University Park, PA

M.S. Engineering Mechanics, 2008
The Pennsylvania State University, University Park, PA

B.S. Engineering Science, 2007
The Pennsylvania State University, University Park, PA

Professional Experience:

2011 - Present: Practical research and project management at the Electric Power Research Institute
Significant scripting and graphical programming;
Extensive experience with Finite Element Modeling

Selected Publications:

1. **Breon, L.**, Feng, Y., Principle Investigators: "Nondestructive Evaluation: Methods for Characterizing Residual Stress in Metals and Thermal Aging in Cast Austenitic Stainless Steel: Technology Survey for Stress Measurement and NDE for CASS" EPRI document 3002005454. published December 2015
2. **Breon, L.**, Principle Investigator: "Nondestructive Evaluation: Novel Ultrasonic Sensor Technology for Structure Monitoring" EPRI document 3002003031, published December 2014
3. Quarry, M., **Breon, L.**, Principle Investigators: "Obtaining Credit for Guided Wave as a Buried Pipe Direct Examination" EPRI document 3002000468, published December 2013
4. **Breon, L.**, Quarry, M., Rassler, B., Dennis, M., Yu, F., Stafford, T., Principle Investigators: "Nondestructive Evaluation: Development of NDE Techniques for Detection of Outside Diameter Stress Corrosion Cracking on Stainless Steel Under Pipe Clamps" EPRI document 3002000448, published December 2013
5. **Breon, L.**, Quarry, M., Principle Investigators: "Nondestructive Evaluation: Buried Pipe Structural Health Monitoring periodic monitoring using permanently attached sensors" EPRI document 1025213, published November 2012
6. **Breon, L.**, Kenefick, S., Quarry, M., Principle Investigators: "Nondestructive Evaluation: Guided Wave Status Update" EPRI document 1022929, published November 2011
7. Hohmann, Brian P., Crosson, Joseph P., Esselman, Thomas C., Wall, James J., Quarry, Mike, **Breon, Luke** "Flaw Detection Capability and Sensitivity in the Inspection of Nuclear Containment Liner and Shell Mock-ups Utilizing a Magnetostrictive Sensor (MsS) Guided Wave UT Technique" Journal of Modern Physics Vol. 5, No. 13, 2014
8. **Breon, Luke**, *Ultrasonic Guided Wave Thickness Measurement of Isotropic Plate-Like Structures* The Pennsylvania State University, Master of Science Dissertation, May 2008

Patent Publications:

1. **Breon, Luke;** Quarry, Michael; *System and method for focusing guided waves beyond curves in test structures*
Patent publication US 20140278193 A1, Filed March 15, 2013

Awards / Honors:

2008 Best paper of the year award for **L J Breon**, J K Van Velsor, J L Rose, "Guided Wave Damage Detection Tomography for Structural Health Monitoring in Critical Zones of Pipelines" Materials Evaluation 65(12) 1215-1219

2007 First Place in college of engineering poster contest at PSU for **Luke Breon**; *Tomographic Imaging of Wall Thinning in Pipes*